

AD-A157 609

THIN FILM RESEARCH

VOL. 2

Contract: N60530-81-C-0158
Effective date of contract: 1 August 1981
Expiration date of contract: 31 July 1984

Final Report

Principal Investigator: H. Angus Macleod
(602-621-2449)

Optical Sciences Center
University of Arizona
Tucson, AZ 85721

Sponsored by:
Defense Advanced Research Projects Agency (DoD)
ARPA Order No.: 3343

Monitored by Dr. James L. Stanford
under Contract N60530-81-C-0158

DTIC
SELECTE
AUG 9 1985
A

The views and conclusions contained in this document are those of the authors and should not be interpreted as representing the official policies, either expressed or implied, of the Defense Advanced Research Projects Agency of the US Government.

May 30, 1985

DTIC FILE COPY

This document has been approved
for public release and sale; its
distribution is unlimited.

85

7

18

00

24

UNCLASSIFIED
SECURITY CLASSIFICATION OF THIS PAGE

ADA 157 609

REPORT DOCUMENTATION PAGE

1a. REPORT SECURITY CLASSIFICATION UNCLASSIFIED		1b. RESTRICTIVE MARKINGS	
2a. SECURITY CLASSIFICATION AUTHORITY		3. DISTRIBUTION/AVAILABILITY OF REPORT Approved for public release; distribution unlimited.	
3b. DECLASSIFICATION/DOWNGRADING SCHEDULE		5. MONITORING ORGANIZATION REPORT NUMBER(S)	
4. PERFORMING ORGANIZATION REPORT NUMBER(S)		5. MONITORING ORGANIZATION REPORT NUMBER(S)	
5a. NAME OF PERFORMING ORGANIZATION Optical Sciences Center University of Arizona	5b. OFFICE SYMBOL (If applicable)	7a. NAME OF MONITORING ORGANIZATION Naval Weapons Center	
6a. ADDRESS (City, State and ZIP Code) Optical Sciences Center University of Arizona Tucson, AZ 85721		7b. ADDRESS (City, State and ZIP Code) China Lake, California 93555	
8a. NAME OF FUNDING/SPONSORING ORGANIZATION DARPA	8b. OFFICE SYMBOL (If applicable)	9. PROCUREMENT INSTRUMENT IDENTIFICATION NUMBER N60530-81-C-0158	
6c. ADDRESS (City, State and ZIP Code) 1400 Wilson Blvd Arlington, Virginia 22204		10. SOURCE OF FUNDING NOS.	
11. TITLE (Include Security Classification) Thin Film Research, Vols. 1 and 2		PROGRAM ELEMENT NO.	PROJECT NO.
12. PERSONAL AUTHOR(S) H. Angus Macleod		TASK NO.	WORK UNIT NO.
13a. TYPE OF REPORT Final	13b. TIME COVERED FROM 1/8/81 TO 7/31/84	14. DATE OF REPORT (Yr., Mo., Day) May 30, 1985	
15. PAGE COUNT 77 + Appendices		15. PAGE COUNT 77 + Appendices	

6. SUPPLEMENTARY NOTATION		
7. COSATI CODES		
FIELD	GROUP	SUB. GR.
18. SUBJECT TERMS (Continue on reverse if necessary and identify by block number) Thin films, coatings, physical vapor deposition, PVD, ion-assisted deposition, IAD, ion bombardment, electron-assisted deposition, electron bombardment, optical thickness monitor.		

9. ABSTRACT (Continue on reverse if necessary and identify by block number)
Optical thin films are critical components in a broad range of technologies, ranging from energy conversion to information storage. In response to the demand for increasingly specialized and durable coatings, enquiry into the basic nature of these coatings has intensified. Such efforts are necessary because assumptions that thin films were similar to nominally identical bulk materials have proven unreliable. For example, while most bulk materials show a high degree of isotropy, thin films display pronounced anisotropy. Another distinction between bulk and thin film materials is the lower density of the latter, with the resulting porosity. Both anisotropy and porosity often contribute to the unpredictable performance and durability of optical coatings. This report covers three years of fruitful research aimed at better understanding and modifying film microstructure in the direction of greater isotropy and density through novel deposition techniques. We have supported this effort with an array of analysis techniques and with a major effort in film growth simulation and in the theoretical description of anisotropic films. Our

10. DISTRIBUTION/AVAILABILITY OF ABSTRACT UNCLASSIFIED/UNLIMITED <input checked="" type="checkbox"/> SAME AS RPT. <input type="checkbox"/> DTIC USERS <input type="checkbox"/>		21. ABSTRACT SECURITY CLASSIFICATION Unclassified	
2a. NAME OF RESPONSIBLE INDIVIDUAL H. Angus Macleod		22b. TELEPHONE NUMBER (Include Area Code) (602) 621-2449	

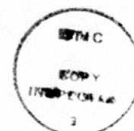
Reproduced from
best available copy.

APPENDIX D

DEVELOPMENT OF AN AUTOMATED SCANNING

MONOCHROMATOR FOR MONITORING THIN FILMS

Accession For	
NTIS GRA&I	<input checked="checked" type="checkbox"/>
DTIC TAB	<input type="checkbox"/>
Unannounced	<input type="checkbox"/>
Justification	
By	
Distribution/	
Availability Codes	
Dist	Avail and/or Special
A1	



85 7 18 002

DEVELOPMENT OF AN AUTOMATED SCANNING MONOCHROMATOR
FOR MONITORING THIN FILMS

F.J. Van Milligen, Bertrand Bovard, Michael R. Jacobson,
James Mueller, Ross Potoff, Richard L. Shoemaker, H. Angus Macleod

University of Arizona
Optical Sciences Center
Tucson, Arizona 85721

ABSTRACT

A scanning monochromator system for the monitoring of thin film deposition in a box coater is described. The system employs data from both a quartz crystal oscillator and a wide band transmission spectrometer. The spectrometer uses a holographic grating as its dispersive element and a CCD array to collect the data. All data is sent to a microcomputer where the information is displayed, stored, and analyzed. Several applications, including measurement of optical constants of inhomogeneous films and characterization of moisture adsorption, are discussed.

1. INTRODUCTION

After an optical filter has been satisfactorily designed, it must be implemented in a production facility. For anything but the simplest of multilayer stacks, this involves the selection of the proper process parameters for a specific set of materials in a particular vacuum chamber. The length of time required to control this process fully depends upon the efficiency and fidelity of the monitoring techniques available to the operator. In general, there are two means of monitoring film deposition:

1) Optical monitoring: This technique is more appropriate in realizing coatings consisting of quarterwave layers by detecting the extrema of transmission or reflectance at a particular wavelength. This method is extremely stable for the control wavelength and only slightly less stable around it.¹ Therefore, it is used for coatings designed for performance over a narrow wavelength region.

2) Physical Mass Monitoring: By observing the natural resonance frequency of a quartz crystal, it is possible to determine the mass deposited on its surface; assuming densities for the film materials, one can compute the thickness of the layers. With this technique one can monitor layers of any thickness with high sensitivity. Unfortunately, since it does not include any measurements of the optical performance, it does not provide the stability of optical monitoring, and demands accurate calibration and reliable density data.

In this paper, we will describe a scanning monochromator system which employs both of these techniques in parallel with the added advantage of measuring the optical transmission of the sample over a wide wavelength range. We continue by discussing relevant features of the system and considering some of its applications.

2. IMPLEMENTATION

It is appropriate to begin by mentioning that our system was inspired by one built by the group led by Pelletier in Marseilles, France.^{2,3} Our scanning monochromator system was intended to augment the capabilities of a Balzers 760 box coater, which was delivered with an automated process controller (Balzers Model KB 181) based on a quartz crystal monitor and a second, unautomated, single wavelength optical monitor (Balzers Model GSM 218). The front end of the first subsystem was left intact; the second subsystem was replaced with our wideband optical monitoring portion of the scanning monochromator system.

Figure 1 is a descriptive flow diagram of the scanning monochromator system. To ensure that the signal reaching the CCD array is adequate, the original Balzers light source was replaced with a much brighter, 500 W tungsten-halogen lamp. This source met the required criteria: enough light to saturate the detectors and sufficient stability to rely on a single 100% reference line for an entire coating run. Unfortunately, its spectral profile, shown in Figure 2A, varies excessively and does not extend into the important

ultraviolet region. To solve this problem, we are currently replacing the tungsten-halogen with a xenon arc lamp which will have both a flatter spectrum and output in the ultraviolet, shown in Figure 2B.

Immediately adjacent to the source, the beam is modulated by a four sector chopper, which also provides a reference signal to the lock-in amplifier, part of the detector electronics beyond the detector. After the chopper, the light is projected by a lens into the chamber via a port in the baseplate, through the witness, or reference sample, and back out through a port in the chamber roof. For some experiments, a rotating fixture moves more than one sample through the monitor beam, permitting in situ coating comparisons. Figure 3 depicts the overall arrangement of the scanning monochromator with respect to the original box coater.

After exiting the chamber, the beam is turned by a flat mirror into the main scanning monochromator optics. First, it is refocused by a lens onto a slit, which is 1 cm high and approximately 30 μ m wide. After the slit, the beam encounters the dispersive element of the scanning monochromator, a Jobin-Yvon holographic, reflective grating, ruled at 300 lines/mm and designed to disperse light into a spectrum ranging from 400 to 800 nm, of which we use 440 to 800 nm due to our light source. The grating has sufficient optical power to image the slit onto the Fairchild 122 CCD array, which is reached after a final bounce from a flat folding mirror. The CCD intercepts the beam at an image of the grating's negative first order; the one-

inch long CCD array matches the one-inch flat field of the CCD at that point.⁴ A view of this part of the monochromator appears in Figure 4.

The CCD array consists of 1728 elements; our signal processing electronics averages sets of ten adjacent elements, providing us with 172 data points. These data levels are sent on to a dedicated IBM-PC, which records the data on five inch floppy disks and displays them on an Amdek video monitor for real time feedback to the plant operator. At the same time, information from the original process controller, based on the quartz crystal monitor, is sent through an interface module to the IBM-PC.

A flowchart showing how the computer handles the data appears in Figure 5. The IBM-PC incorporates a Tecmar A/D board, which accepts 12-bit data from both the quartz crystal monitor and the CCD array. Although the electronics are capable of running at a rate of four spectra per second, we generally take one spectrum every three seconds. This is quite adequate, since at our typical deposition rates (primarily of oxides), we deposit ten to twenty Angstroms of material in three seconds. The potential for data rates at least an order of magnitude higher would permit us to monitor extremely rapid changes, should the need arise. Table 1, below, summarizes important characteristics of the scanning monochromator monitor.

Before each run, wavelengths are calibrated by inserting a piece of didymium glass in the light path and then setting zero readings in the data to the didymium's known absorption lines. For

readings other than those given by the absorption lines the wavelength is determined by linear interpolation between known points. We estimate an accuracy of 2 to 4 nm over the range we have tested with available spectral line sources.

3. APPLICATIONS

Several examples of applications for the scanning monochromator monitor follow:

1) A sequence of transmission spectra for each run can be stored for later analysis of the effects of various process parameters. A 360K double-density 5.25 inch disk can accommodate about 50 minutes of continuously monitored spectral data.

2) The wideband transmission spectra that appear on the monitor provide the plant operator with a much broader view of coating progress; should problems arise, the operators can base their decisions during deposition on a larger data base.

3) Monitoring done in situ permits testing and observation of coatings without removing them from the system. One example of this feature's utility appears in Figure 6: It examines the effect of water adsorption on a filter. ⁵

4) The larger data base available to the computer permits better characterization of a film's optical constants. Figure 7 shows one such calculation for a film of TiO_2 as it grows. We note that this illustrates the dispersion of n and k with thickness at a particular wavelength. The system can also derive the dispersion with wave-

length at a particular thickness. ⁶

4. ACKNOWLEDGMENTS

The development of our scanning monochromator system was inspired by a pioneering system constructed at the Laboratoire d'Optique de l'Ecole Nationale Supérieure de Physique in Marseille, France, led by E. Pelletier and including F. Flory, A. Fornier, and R. Richier. One other member of that group is among the authors of this paper; we were fortunate enough to have B. Bovard as a post-doctoral scientist for one year at the Optical Sciences Center. His visit had an extremely stimulating influence on the construction and completion of the instrument. The Air Force Office of Scientific Research [AFOSR] provided salary support for his year in Arizona. We would also like to thank T. D. Ferguson and Russell Chipman of the Optical Sciences Center for their helpful discussions. M. Osgood skillfully executed the figures. We also would like to thank the Defense Advanced Research Projects Agency [DARPA] for their generous support of basic thin films research through a three-year contract monitored by the Naval Weapons Center.

5. REFERENCES

1. H.A. Macleod, "Turning Value Monitoring of Narrow-Band All-Dielectric Thin Film Optical Filters, " *Optical Acta*, 19, 1-28 (1972).
2. P. Bousquet and E. Pelletier, "Optical Thin Film Monitoring - Recent Advances and Limitations," *Thin Solid Films*, 77, 165-79 (1981).
3. B. Vidal, A. Fornier, and E. Pelletier, "Wideband Optical Monitoring of Non-Quarterwave Multilayer Filters," *Applied Optics*, 18, 22, 3851-56 (1979).
4. J.M. Lerner, J. Flamand, J.P. Laude, G. Passereau, and A. Thevenon, "Diffraction Gratings Ruled and Holographic - A Review," *SPIE* 240, 82-88 (1980).
5. S.G. Saxe, M.J. Messerly, B. Bovard, L. Desandre, F. J. Van Milligen, and H.A. Macleod, "Ion Bombardment-Induced Retarded Moisture Adsorption in Optical Thin Films," *Applied Optics*, 23, 20, 3633-3637 (1984).
6. B. Bovard, S.G. Saxe, M.J. Messerly, F.J. Van Milligen, and H.A. Macleod, "Techniques for Thin-Film Optical Constant Derivation from In Situ Transmission Measurements," presented at the OSA 1984 Annual Meeting, San Diego, California, October 29 - November 2, 1984.

TABLE 1: SYSTEM PERFORMANCE

Wavelength Range	440 - 800 nm
Wavelength Resolution	2 nm
Resolving Power	300
Etendu of System	$1 \times 10^{-3} \text{ cm}^2\text{-sr}$
Minimum Transmission	2%
Signal Level of CCD	70% of saturation at 650 nm

FIGURE CAPTIONS

1. Scanning Monochromator Flow Diagram
- 2a. Spectral Profile of Tungsten Halogen Lamp
- 2b. Spectral Profile of Xenon Arc Lamp
3. Appearance of Scanning Monochromator system
4. Top view of Scanning Monochromator
5. Flowchart of Computer Data Handling Program
6. Example of Water Adsorption in a TiO_2 , SiO_2 Fabry-Perot Filter
7. Variation of optical constants of TiO_2 as the film is being deposited. Upper curve corresponds to n , lower curve to k .

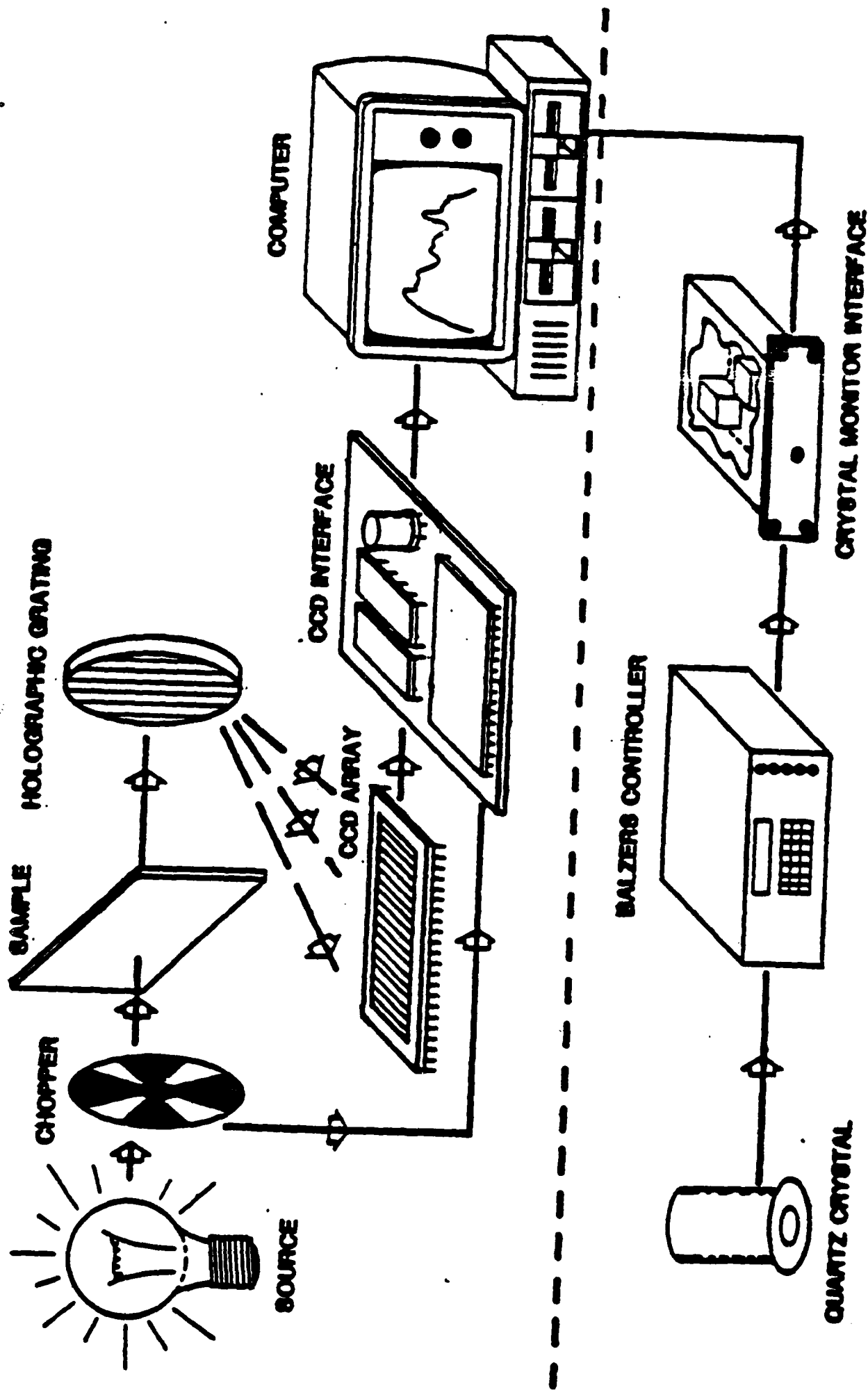


Fig 1. Scanning Monochromator Flow Diagram.

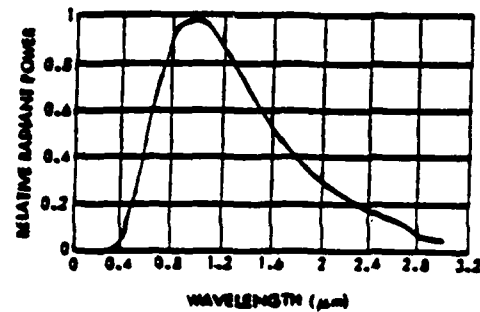


Fig 2a. Spectral Profile of Tungsten Halogen Lamp.

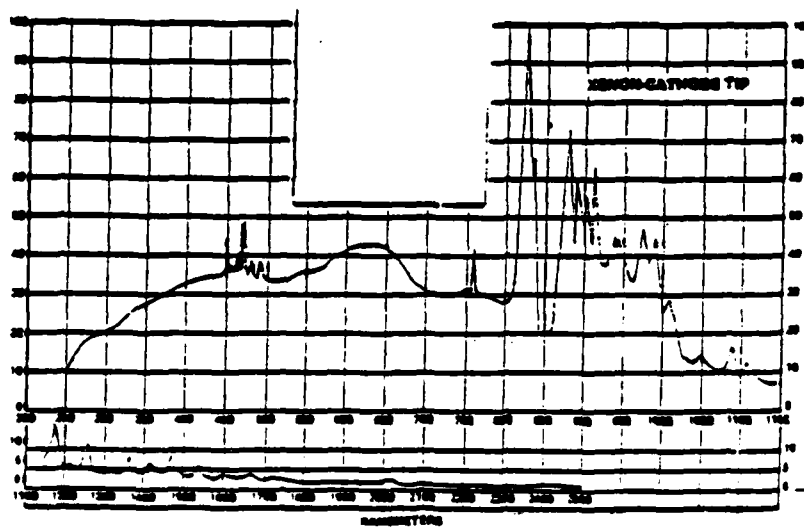


Fig 2b. Spectral Profile of Xenon Arc Lamp.

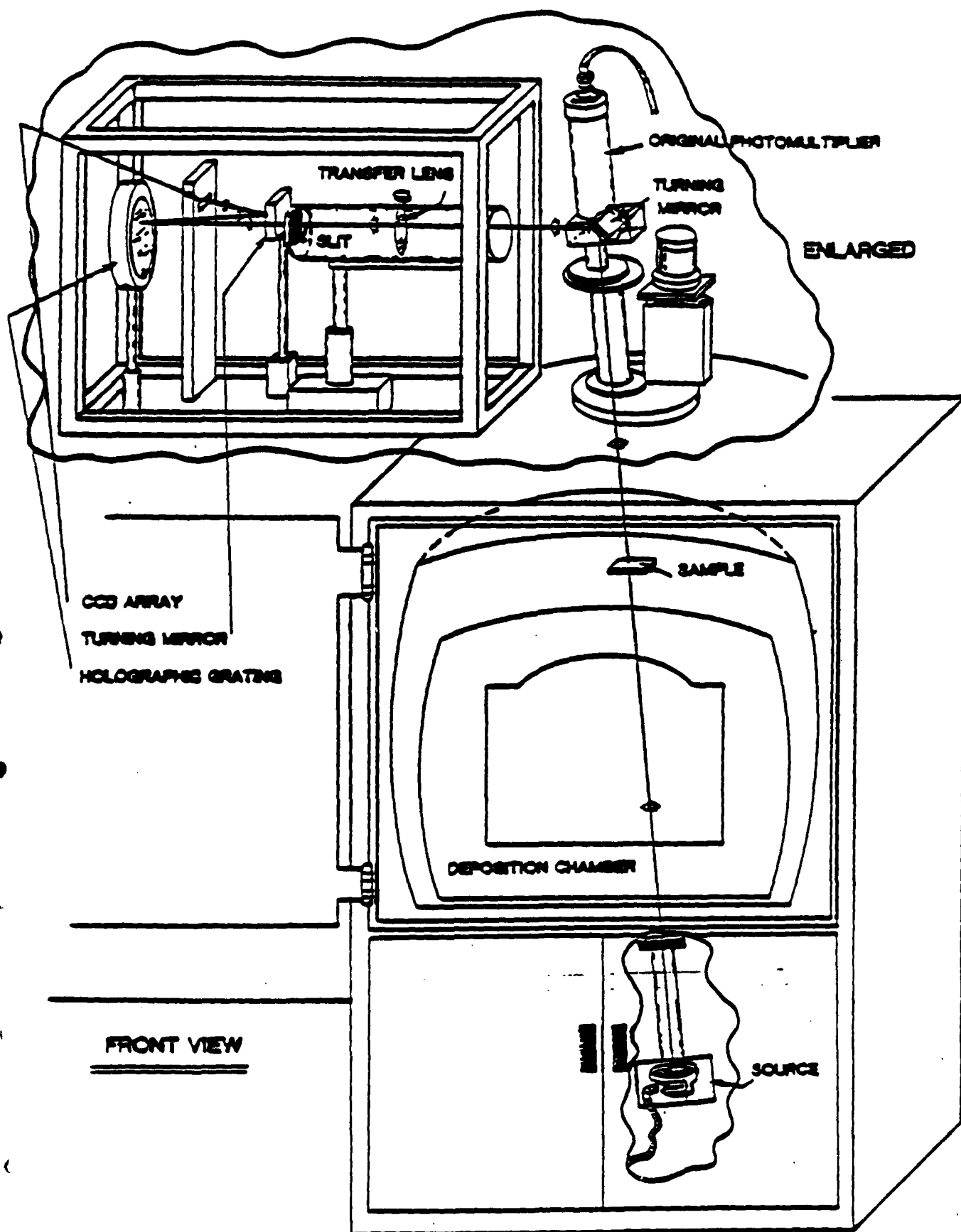


Fig 3. Appearance of Scanning Monochromator system.

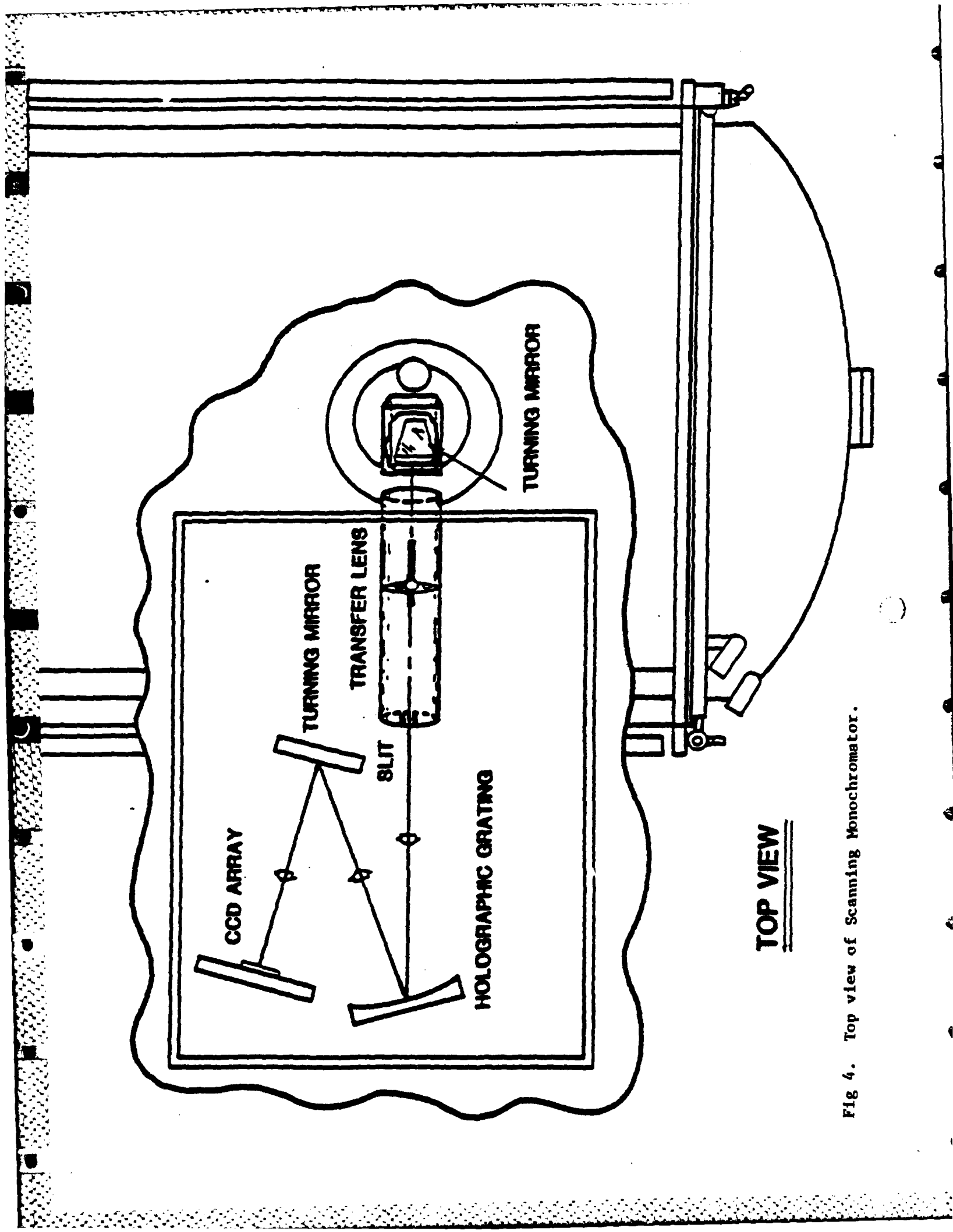


Fig 4. Top view of Scanning Monochromator.

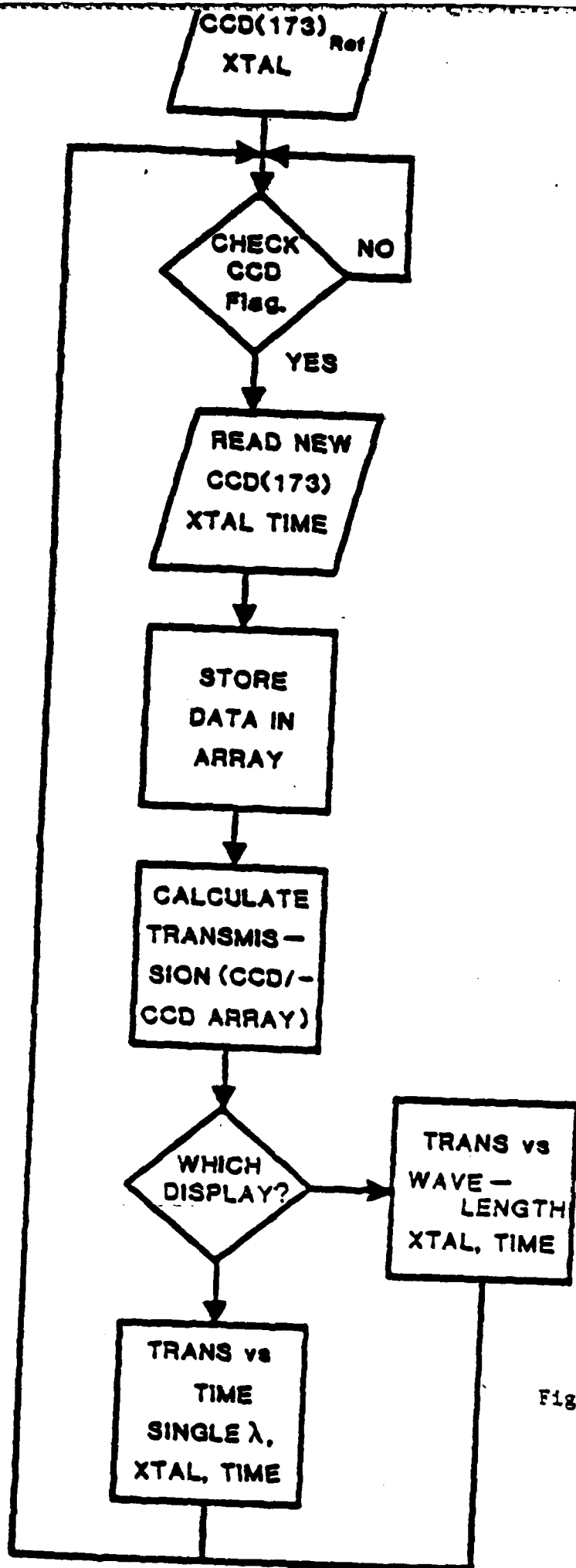


Fig 5. Flowchart of Computer Data Handling Program.

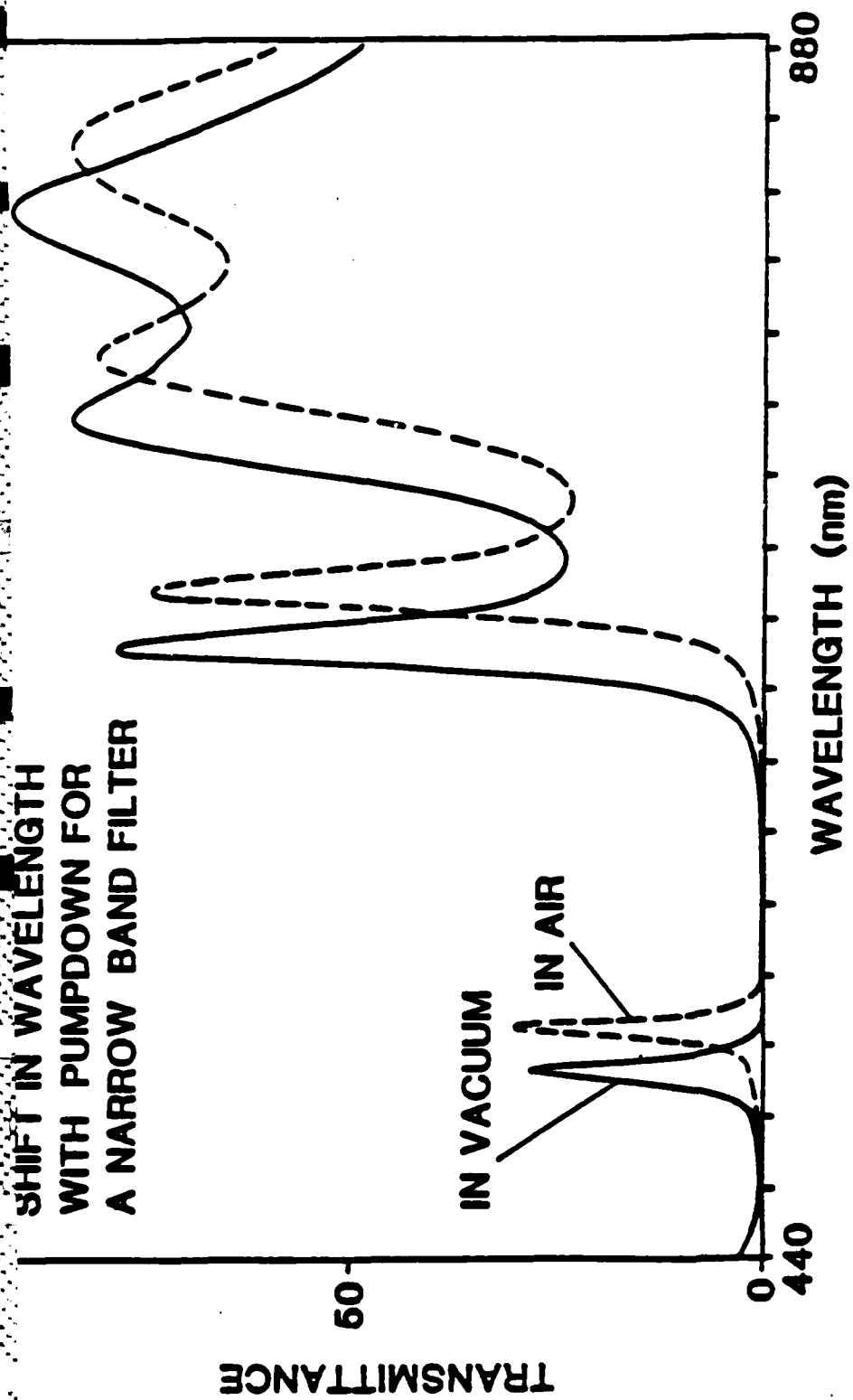


Fig 6. Example of Water Adsorption in a TiO_2 , SiO_2 Fabry-Perot Filter

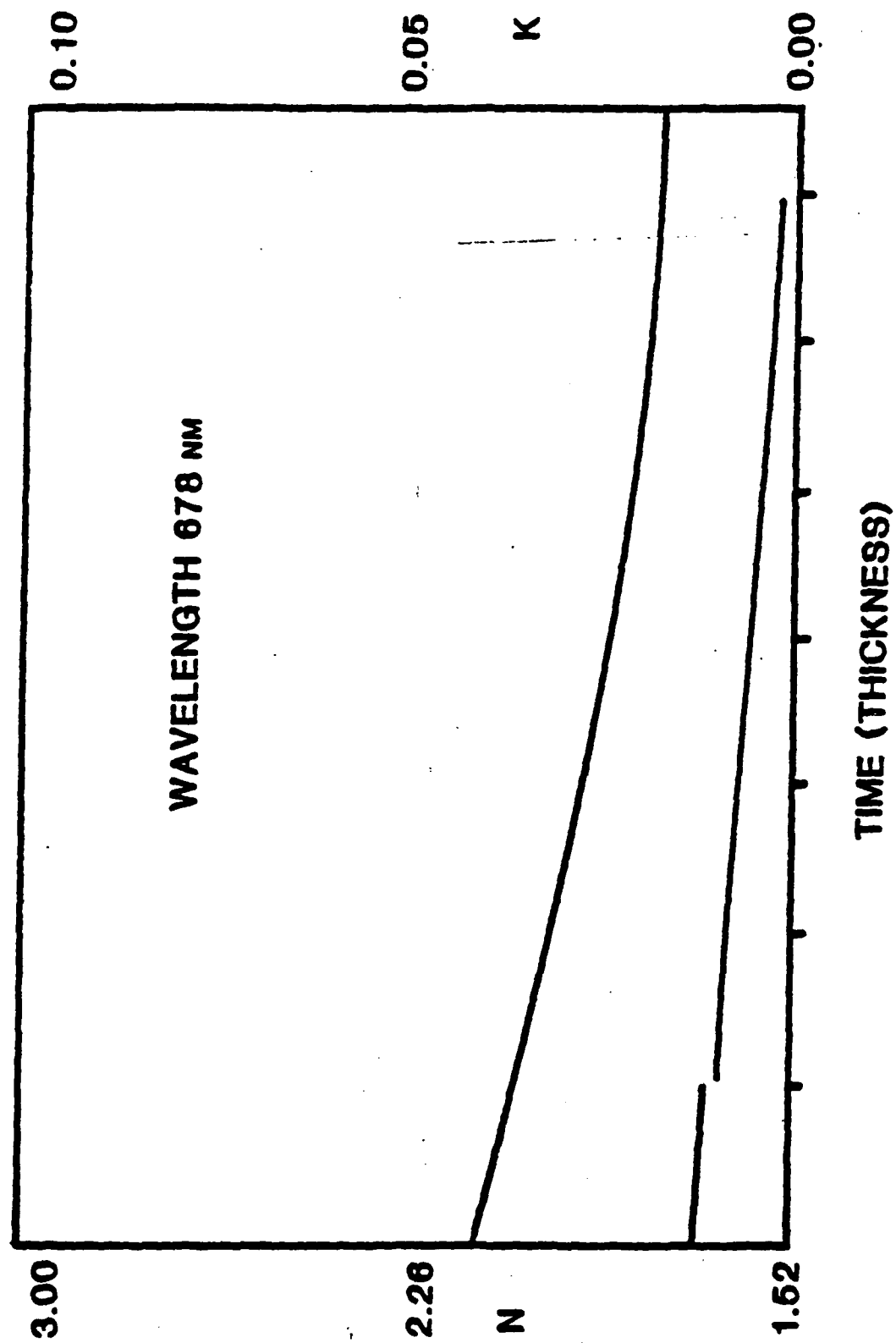


Fig 7. Variation of optical constants of TiO_2 film as the film is being deposited.
Upper curve corresponds to n, lower curve to k.

APPENDIX E

**OPTICAL CONSTANTS DERIVATION FOR AN INHOMOGENEOUS
THIN FILM FROM IN SITU TRANSMISSION MEASUREMENTS**

Optical constants derivation for an inhomogeneous
thin film from in situ transmission measurements

B. Bovard, F.J. Van Milligen, M.J. Messerly, S.G. Saxe and H.A. Macleod

University of Arizona
Optical Sciences Center
Tucson, Arizona 85721

ABSTRACT

The optical constants of a thin film depend upon its structure. A technique, based on transmission measurements carried out in vacuo, has been developed to derive the profiles of the refractive index and extinction coefficient. The interpretation of the profiles gives information on the layer structure in vacuo. The technique can be used as a means of monitoring the variations of the optical constants with changes in the deposition parameters. This paper presents the technique, which is based on an envelope method, and gives some experimental results.

I. Introduction

The refractive index and the extinction coefficient of a thin film depend upon the conditions of deposition and, as a consequence, upon the structure of the film itself. In the case of oxides, inhomogeneities are largely due to the film's columnar structure¹ and to the variations in degree of oxidation throughout the layer. The derivation of their profiles as a function of depth is difficult once the layer has been deposited. Furthermore, most techniques developed to measure the refractive index are carried out under atmospheric conditions. Exposure of a film to the air modifies its optical properties: the voids existing in its structure tend to adsorb moisture and an oxidation process may occur for a suboxidized layer, changing the refractive index and the extinction coefficient.^{2,3} Therefore a technique taking into account the evolution of the transmission of a layer growing in vacuo has great advantages. To achieve such measurements we have used a scanning monochromator system⁴ which provides us with the transmission over the visible spectrum versus time, during deposition. Using these data we have developed a technique for deriving the profiles of the optical constants. After a verification of the optical constants determination technique by computer simulation, we have applied the method to various layers of titanium dioxide. This technique can then be used as a means of monitoring the effect on the optical constants of a change in any of the parameters used for the coating process.

II. Determination of the profile of the optical constants of an inhomogeneous film

In the case of negligible extinction coefficients the derivation of the refractive index can be achieved using an admittance circle method based on transmission measurements during the growth of the layer⁵. But since our interests lie more in slightly absorbant materials such as oxides, we have developed a technique that has its origins in the envelope method described by Manifacier et al (6,7). We have used an inhomogeneous model of a thin film to derive the refractive index and the extinction coefficient profiles.

II.1. Envelope method in the inhomogeneous case

Manifacier et al⁶ developed the envelope method for the limiting case of an homogeneous thin film where only transmission measurements are required for the derivation of n and k . A generalization to an inhomogeneous model was presented by Arndt et al⁸ to derive the optical constants from measurements of reflectance and transmittance. In these studies reflection and transmission are considered as functions of wavelength and their envelopes are used to calculate the optical constants. To obtain the profiles of the optical constants, as in this study, we considered the envelopes of the curve of transmittance as functions of thickness for a chosen wavelength. We were able to obtain the dispersion by applying the same method to a range of wavelengths.

We now demonstrate the principle of the method and give the analytical expressions for the optical constants.

A lossless inhomogeneous layer, where the inhomogeneity can be considered a perturbation of otherwise homogeneous behaviour and not the dominant factor, can be represented by the characteristic matrix⁹:

$$\begin{bmatrix} (n_{in}/n_{out})^{1/2} \cos \delta & i \sin \delta / (n_{out} n_{in})^{1/2} \\ i(n_{in} n_{out})^{1/2} \sin \delta & (n_{out}/n_{in})^{1/2} \cos \delta \end{bmatrix}$$

where n_{out} is the index at the outer surface (away from substrate) of the film

n_{in} is the index at the inner surface of the film, and

δ is the phase thickness.

n_{out} and n_{in} should not be too close to the indices of the incident medium and of the substrate, respectively

If we assume that the absorption is very small, the amplitude reflection coefficients at the interfaces are scarcely affected if we neglect it. The absorption in the layer is determined principally by δ . Thus we can include the effects of small extinction coefficient k by inserting it in δ so that

$$\delta = 2\pi(\bar{n} - i\bar{k})d/\lambda$$

where \bar{n} is the mean index of the film (i.e. $\bar{n} = \frac{1}{d} \int_0^d n(z)dz$),

\bar{k} is the mean extinction coefficient (i.e. $\bar{k} = \frac{1}{d} \int_0^d k(z)dz$),

λ is the wavelength and

d the thickness of the layer.

Let us assume that the incident medium has a refractive index n_0 and that the substrate is nonabsorbing and of index n_s . After some tedious calculation, we find the expression for the transmission of the coated substrate:

$$T = \frac{16n_s n_0 n_{in} n_{out} e^{2\delta_2}}{C_1^2 + C_2^2 e^{4\delta_2} + 2C_1 C_2 e^{2\delta_2} \cos 2\delta_1}$$

where

$$C_1 = (n_{out} + n_0)(n_s + n_{in}) \quad , \quad C_2 = (n_{out} - n_0)(n_s - n_{in})$$

$$\delta_1 = 2\pi\bar{n}d/\lambda$$

$$\delta_2 = -2\pi\bar{k}d/\lambda$$

In the following we shall assume that we are dealing with a high index layer so that C_2 is negative. Then the two expressions of the envelopes become:

$$T_{\max} = \frac{16n_0n_s n_{in} n_{out} e^{2\delta_2}}{(C_1 + C_2 e^{2\delta_2})^2}$$

$$T_{\min} = \frac{16n_0n_s n_{in} n_{out} e^{2\delta_2}}{(C_1 - C_2 e^{2\delta_2})^2}$$

These two equations are used to determine the outermost index for each instant during film deposition. They are also used to calculate the extinction coefficient at the quarterwave points.

However, all these derivations are possible only if we make a very basic assumption about the stability of the layer during deposition. This assumption is simply that the innermost index does not vary during the growth of the film. The profiles of the optical constants can then be derived and considered as functions of thickness instead of time.

We shall not go through the details of the derivation and we shall only give the analytical expressions for the innermost and outermost refractive index, the geometrical thicknesses and the extinction coefficient profile.

The expression of the innermost refractive index is obtained by setting

$n_{in} = n_{out}$ when $d = 0$ so that:

$$n_{in} = [N + (N^2 - n_0^2 n_s^2)^{1/2}]^{1/2} \text{ where } N = \frac{n_0^2 + n_s^2}{2} + 2n_0 n_s \left(\frac{T_{\max} - T_{\min}}{T_{\max} T_{\min}} \right)$$

The expression of the outermost refractive index is then:

$$n_{out} = \frac{2n_{in}n_s n_0}{n_{in}^2 - n_s^2} \left(\frac{T_{max} - T_{min}}{T_{max} T_{min}} \right) + n_0 \left[1 + 4n_{in}^2 n_s^2 \frac{\left(\frac{T_{max} - T_{min}}{T_{max} T_{min}} \right)^2}{(n_{in}^2 - n_s^2)^2} \right]^{1/2}$$

which is calculable only if we know the innermost index value.

Provided we assume the innermost index is stable we can calculate the profile of the refractive index of an inhomogeneous layer. Note that it requires the knowledge of the substrate refractive index, which can be measured independently, but it does not require the value of wavelength.

We also need to determine the geometrical thickness. Since we are dealing with low-absorption materials, the extrema of transmission occur when the optical thickness of the layer is a multiple of a quarterwave.

If m is the order of the extremum ($m=1$ indicating the first minimum) the corresponding geometrical thickness is

$$d = m \frac{\lambda}{4\bar{n}} \text{ where } \bar{n} = \frac{1}{d} \int_0^d n(z) dz$$

since calculation of $\frac{1}{d} \int_0^d n(z) dz$ is impossible, we make an

approximation and write that $\bar{n} = \frac{1}{t} \int_0^t n(u) du$ where t is the instant

when the extremum occurs.

This is equivalent to assuming that the rate of deposition (change in thickness per unit time) is constant. The assumption is reasonable because our deposition rate is automatically controlled.

With regard to the profile of extinction coefficient we note first that a mean value of the extinction coefficient can be derived each time we reach a new quarterwave:

$$\bar{k} = -\frac{\lambda}{4\pi d} \text{Log } a(d) \text{ with } a(d) = \frac{C_1[1-(T_{\max}/T_{\min})^{1/2}]}{C_2[1+(T_{\max}/T_{\min})^{1/2}]} = \exp\left(-4\pi \frac{\bar{k}d}{\lambda}\right)$$

but since the function a is available at any instant during the growth of the layer, we can also calculate its derivative versus time and obtain an expression giving the profile of extinction coefficient.

$$k(z) = -\frac{\lambda}{4\pi} \frac{1}{a(z)} \frac{da}{dz} \text{ where } z \text{ is the thickness of the layer.}$$

Because of the derivative, this expression is somewhat sensitive to errors but can still be used to obtain an indication of the absorption of the material.

II.2. Stability of deposition and conclusion

Provided we know the envelopes of a curve of transmission, using these analytical expressions we are able to derive the optical constants. But the necessity of knowing the envelopes as functions of thickness leads us to a very basic assumption concerning the stability of growth of the layer. The envelopes calculated using the measured transmission versus time are usable if they do not shift during the deposition process, which means that an earlier part of the layer is not modified during the deposition of a later part.

It is easy to foresee the importance of having an accurate way of determining extrema of the transmission curves. Their precise estimation, both value and position, demanded that we consider some numerical treatments of the raw data before calculating the envelopes fitting these points. We present in the next section the data processing techniques developed together with a justification of their validity and of the expressions presented above.

III. Data Processing and Simulation

The envelope computation requires an accurate knowledge of the extrema together with a method to fit curves to these points. It was thought possible that the data processing used for the calculation of the envelopes might introduce a bias in the results given by the program of optical constant determination. However, we are able to show that it is not the case so that our results are free from such effects.

III. 1. Smoothing the curve of transmission versus time

Many methods are available for smoothing, but our major concern is to smooth without distorting the curve. For this reason, we decided to use a filtering method based on a finite impulse response filter calculated to have a linear phase and an extremely flat low-pass band. We thus avoid any distortion introduced by a nonlinear phase and the attenuation due to a nonflat passband. The filter does still introduce a delay equal to the derivative of its phase versus frequency, but this delay is constant and is corrected in the computation by an entire shift of the curve. Details of this type of approach are given in reference 10, which inspired the present design and so we limit our description to demonstrating its application to a real signal in Figs. 1 and 2.

III. 2. Envelope Computation

The equations of the envelopes are computed by segments. The first group of three points, corresponding to the first three maxima or first three minima depending upon which curve is being drawn, gives a parabola which is used to describe the segment of the curve between the first two points. Next the first point is discarded and replaced by the fourth point. A new parabola is now calculated and used to describe the segment between the second and third points. This operation is repeated until the entire curve is produced.

III. 3. Verification and precision of the technique

The validity of the expressions for the refractive indices and the extinction coefficient has been checked by some simulations, the results of which are presented here.

A program able to handle variable optical constants has been developed to compute the evolution of the transmission of a coated substrate during growth of a thin film. The profiles of the optical constants are fed into the program which divides the inhomogeneous layer into a stack of homogeneous sublayers each of thickness 1 nm . The transmittance is then recorded on disk files exactly as when the scanning monochromator is used. The optical constant determination program is then used to compute the index and extinction coefficient profiles. Their comparison with the original ones verifies the accuracy of the technique. Our goal was also to show it is possible to separate the inhomogeneity of the refractive index from that of the extinction coefficient. Of the many computations that have been performed we simply show two of the most characteristic ones.

The simplest case is that of a homogeneous layer. Taking starting values of $n = 2.3$ and $k = 10^{-3}$, the optical constants were calculated for two wavelengths 400 and 800 nm and the indices found were to be within 0.03% of the initial value. As foreseen, the efficiency of the calculation of the extinction coefficient was not as good, leading to a 10% relative error.

To test the derivation in the case of an inhomogeneous layer, an arbitrary curve of refractive index was chosen to compute the evolution of transmission : $n(d) = 2 + 0.3 \exp(-d/200)$ where d is the thickness of the layer. The extinction coefficient was assumed constant equal to 10^{-3} . Table 1 shows the calculated results for two wavelengths. The columns $\Delta n_{1n}/n_{1n}$ etc. list the error in the determination expressed as a percentage.

These results indicate that we can expect acceptable accuracy in the refractive index profile using this technique. It is important to note that the higher accuracy corresponds to the shorter wavelength. This is due to the greater number of extrema at the shorter wavelength, which provides more information so the envelopes calculated have a more exact position. This inaccuracy of the envelopes leads to questionable values of extinction coefficient for the longer wavelength. These results are rigorously true only for the cases considered but they strongly suggest what we can generally expect from this method. The relative accuracy of the refractive index depends also upon the quality of the transmittance measurements: it ranges from $\Delta T/T$ to $5\Delta T/T$ where $\Delta T/T$ is the relative accuracy achieved in the transmittance measurements.

IV. Experimental results

The optical constant determination has been carried out for titanium dioxide layers only. We will present the results obtained with two different layers, the first layer fitting the model used in this derivation and the second being unstable.

The starting material used in our experiments was Ti_2O_3 , evaporated by electron bombardment onto a glass substrate.

For the first layer we consider, the oxygen partial pressure was 4.4×10^{-7} mbar and the chamber temperature varied from 204° to $227^\circ C$ during the deposition.

The profile of refractive index and of extinction coefficient are plotted in Fig. 3 for the wavelength 678 nm. The thickness of the layer is 670 nm, the inner index is 2.135 and the outermost index 1.794. The layer is inhomogeneous, as expected for an oxide layer, and slightly absorbant. The correlation between index and extinction coefficient can be interpreted as an increase of the degree of oxidation with the thickness of the layer and as a decrease of the packing density due to a conical form of the columnar structure. It is difficult to decide which has the primary effect.

Fig. 4 gives the dispersion of the innermost and outermost refractive indices. A high dispersion for the outermost index suggests a more absorbant outer part of the layer.

The layer appears to be stable and therefore our results indicate that it is an inhomogeneous layer showing a decrease in its packing density and a decrease in its oxidation degree in the direction of growth.

We now examine an unstable layer. This layer was deposited in a chamber at a temperature of 260°C in the presence of oxygen at a partial pressure of $1.3 \cdot 10^{-4}$ mbar.

This atmosphere was intentionally deficient in oxygen compared with the usual conditions for the deposition of titanium dioxide and we expected

some absorption in the layer. We are not disappointed as shown Fig. 5 but furthermore another phenomenon seems to occur. The curve of the extinction coefficient falls with thickness towards a value which could even become negative. This is almost certainly the effect of instability in the oxidation of the layer: starting with a high deficiency of oxygen the inner part of the film is gradually oxidized as the layer grows. This defeats the technique presented here since the extrema used to calculate the envelopes are changing with the oxidation of the layer and also because we have assumed the innermost refractive index to be constant. Any change in the properties after deposition is interpreted by the model as entirely due to the fresh material added. The real curve is impossible to obtain but we can expect that it would present a less inhomogeneous profile.

Other experiments have been carried out to understand the limitations of this method. The instability of the layer can manifest itself by the occurrence of negative extinction coefficients, by thicknesses varying with wavelength or by very misshapen profiles of index. Nevertheless, the application of this technique to stable layers gives very interesting results. These can give information on the structure of the layer in terms of packing density as well as in terms of degree of oxidation. It is also important to know that layers can be unstable and to be able to recognise such an instability. Further work is required in this area. We hope that eventually it may be possible to distinguish an instability

caused by a structural rearrangement from a reoxidation of some innermost portions of the film.

V. Conclusion

This method has been developed for layers presenting a high index, a small inhomogeneity, and a small extinction coefficient. It permits the determination of the profiles of the optical constants and the dispersion of index in vacuo provided the assumption of stability is fulfilled. It identifies layers that are unstable. It makes possible the study of the variations of the optical constants with changes in the deposition parameters.

Major support for this work was provided by the Defense Advanced Research Projects Agency (DARPA) through a contract with the Naval Weapons Center, China Lake. Additional support was also given by DARPA through a contract with the Naval Ocean Systems Center, San Diego. Bovard was supported by the Air Force Office of Scientific Research and Saxe by a fellowship from the U.S. Army Research Office.

References

1. H.A. Macleod, "Microstructure of optical thin films," Proc SPIE 325 21-28 (1982).
2. Cheng-Chung Lee, "Moisture adsorption and optical instability in thin film coatings," Ph.D. Dissertation, University of Arizona (1983).
3. J. P. Borgogno, P. Bousquet, F. Flory, B. Lazarides, E. Pelletier and P. Roche, "Inhomogeneities in films: limitation of the accuracy of optical monitoring of thin films," Applied Optics 20 90-94 (1981).
4. F. Van Milligen, B. Bovard, M.R. Jacobson, J. Mueller, R. Potoff, H.A. Macleod, R. Shoemaker, University of Arizona, "Development of an Automated Scanning Monochromator for a Balzers 760 Evaporation System,." Paper presented at OSA Annual Meeting, San Diego, October 1984.
5. B. Schmitt, Thèse de docteur ingénieur, "Problèmes de réalisation des filtres spectraux multidiélectriques: contrôle simultané de l'indice de réfraction et de l'épaisseur des couches en cours de formation," Ecole Nationale Supérieure de Physique, Marseille (1983).
6. J.C. Manifacier, J. Gasiot, J.P. Fillard, "A Simple method for the determination of the optical constants n , k and the thickness of a weakly absorbing thin film," Journal of Physics E: Scientific Instruments, 9 1002-4 (1976).

7. R. Swanepool. "Determination of the thickness and optical constants of amorphous silicon." *Journal of Physics E: Scientific Instruments*, 16, 1214 (1983).
8. D.P. Arndt, R.M.A. Azzam, J.M. Bennett, J.P. Borgogno, C.K. Carniglia, W.E. Case, J.A. Dobrowski, U.J. Gibson, T. Tuttlehart, F.C. Ho, V.A. Hodgkin, W.P. Klapp, H.A. Macleod, E. Pelletier, M.K. Purvis, D.M. Quinn, D.E. Strone, R. Swenson, P.A. Temple, T.F. Thonn, "Multiple Determination of the Optical Constants of Thin Film Coating Materials," *Applied Optics*, 23 3571-3596 (1984)
9. R. Jacobsson, "Inhomogeneous and coevaporated homogeneous films for optical Applications," *Physics of Thin Films*, ed. G. Hass, M.H. Francombe and R.W. Hoffman, 8 51-98 Academic Press (1975).
10. S.M. Bozic, "Digital and Kalman Filtering. An Introduction to Discrete Time Filtering and Optimum Linear Estimation," Edward Arnold, London (1979).

FIGURE CAPTIONS

1. Plot of noisy signal. The extrema are difficult to determine with accuracy.
2. After filtering, the extrema have been extracted from the noise without distorting or attenuating the transmission curve.
3. Profile of refractive index and extinction coefficient for a stable titanium dioxide layer. (Upper curve represents n , lower curve k).
4. Dispersion of innermost and outermost refractive index for a stable layer of titanium dioxide.
5. Example of result given by the method when applied to an unstable layer. Titanium dioxide layer deposited in an oxygen deficient atmosphere.

TRANSMISSION vs TIME FOR WAVELENGTH 803 nm

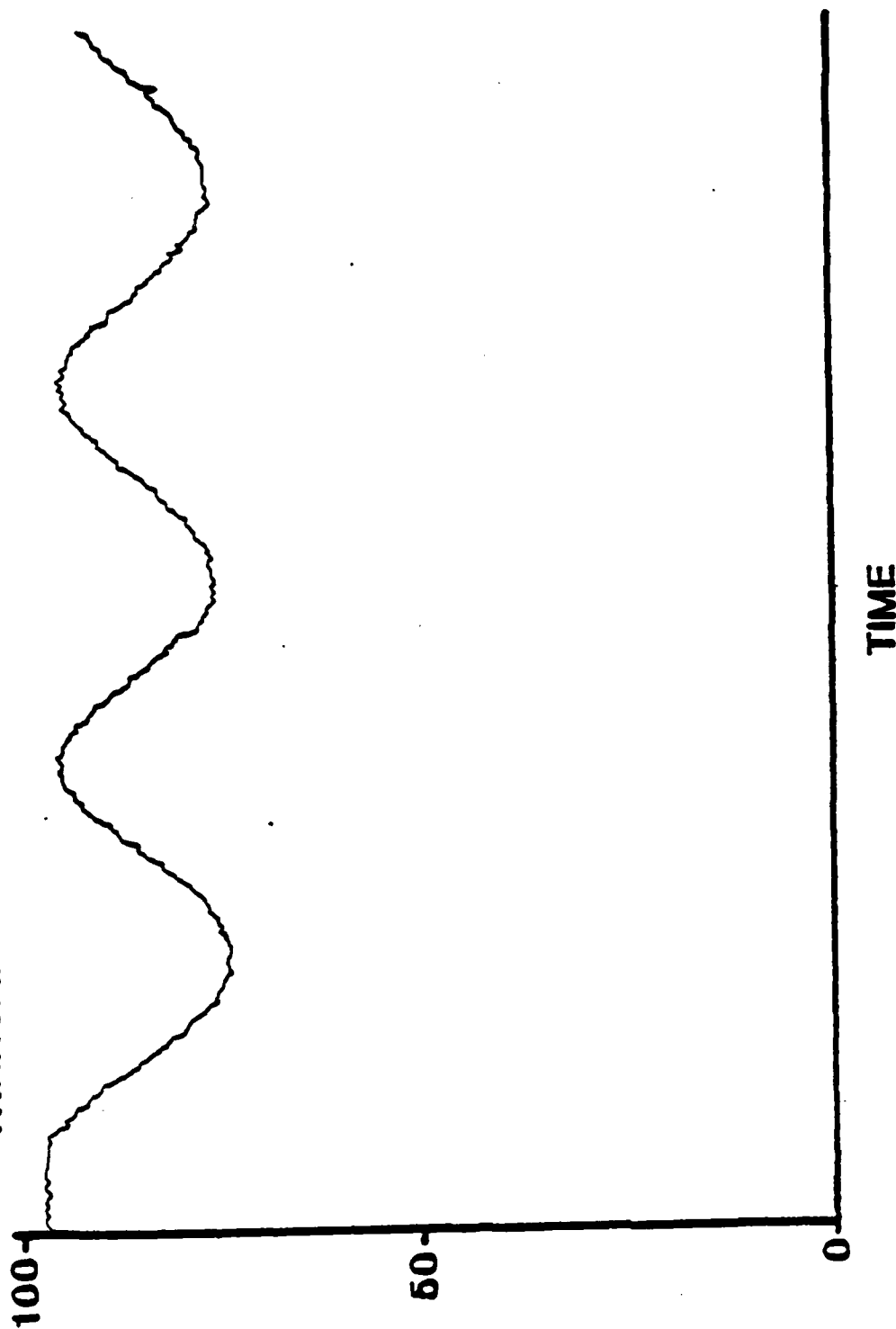


Fig 1. Plot of noisy signal. The extrema are difficult to determine with accuracy.

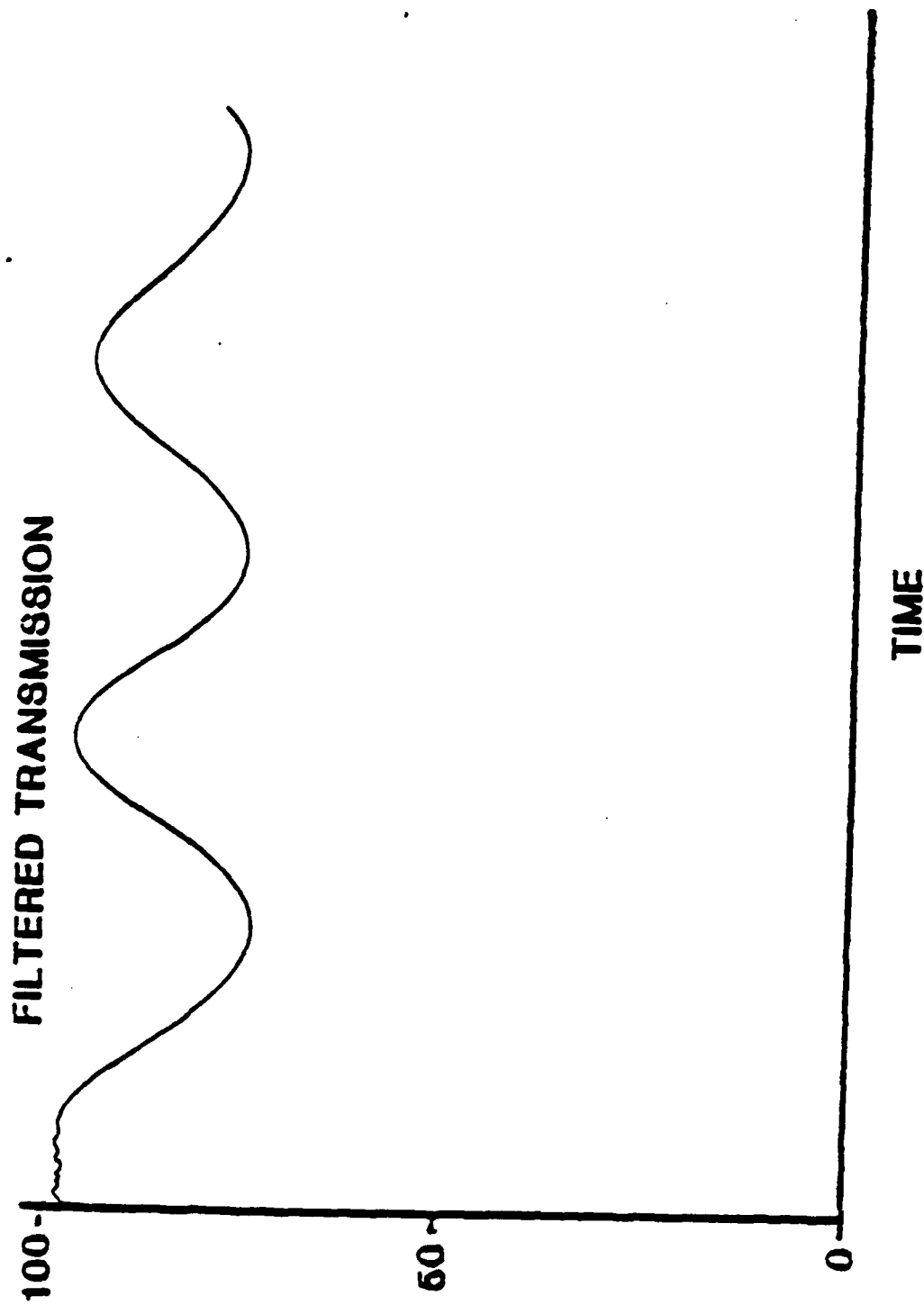


Fig 2. After filtering, the extrema have been extracted from the noise without distorting or attenuating the transmission curve.

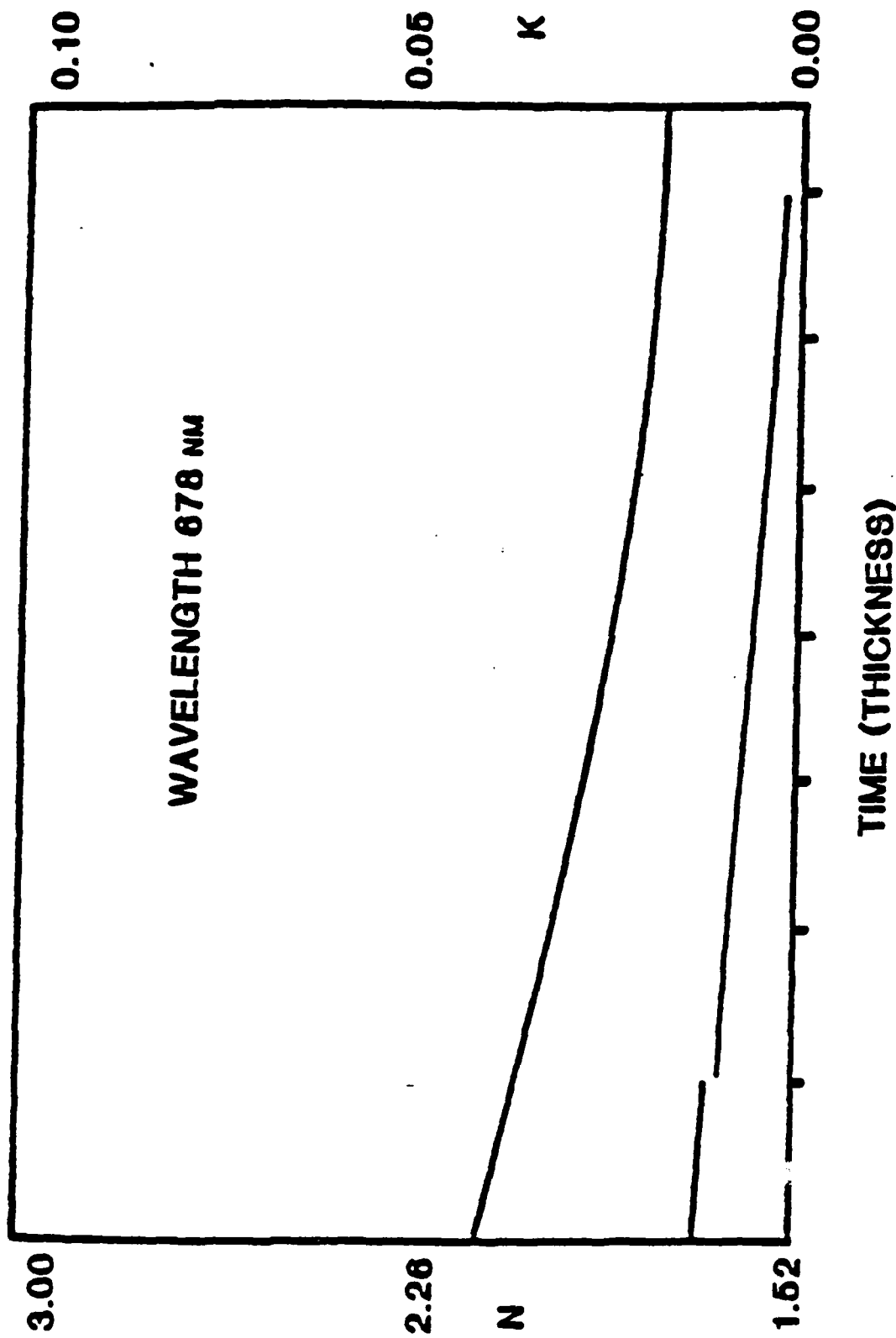


Fig 3. Profile of refractive index and extinction coefficient for a stable Titanium Dioxide layer. (Upper curve represents n, lower curve k).

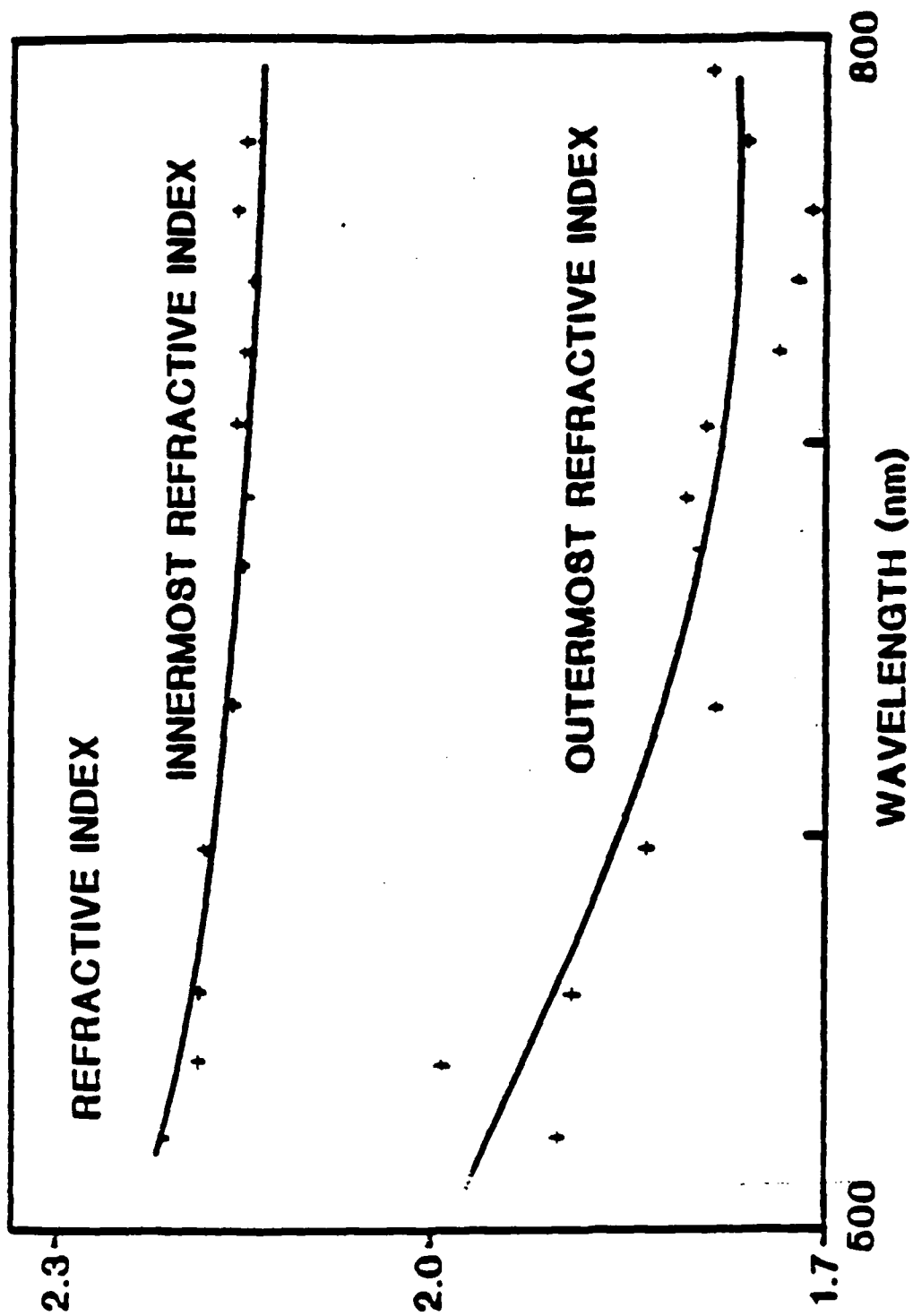


Fig 4. Dispersion of innermost and outermost refractive index for a stable layer of titanium dioxide.

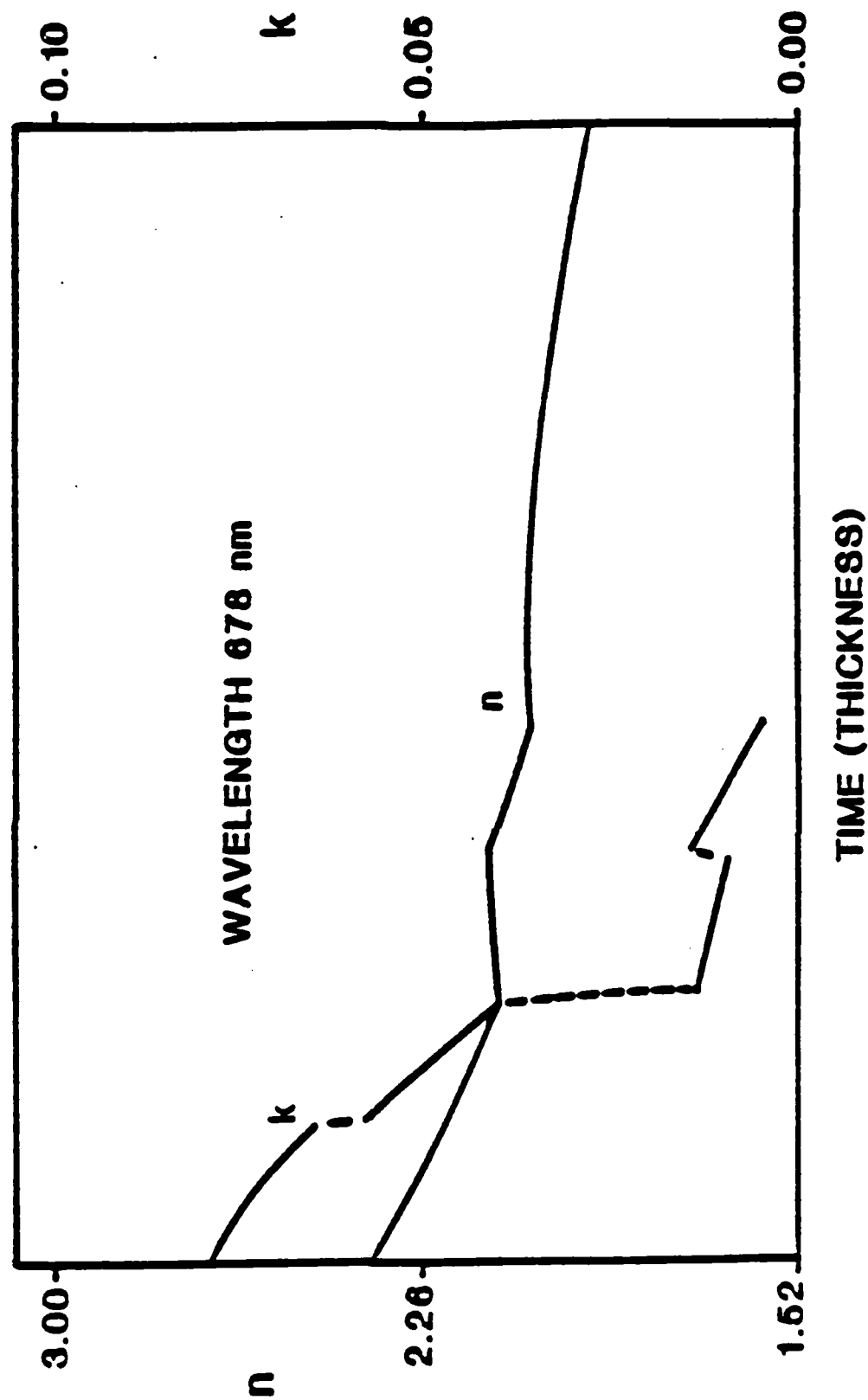


Fig 5. Example of result given by the method when applied to an unstable layer. Titanium dioxide layer deposited in an oxygen deficient atmosphere.

TABLE 1

Wavelength

(nm)	n_{in}	$\Delta n_{in}/n_{in}$	n_{out}	$\Delta n_{out}/n_{out}$	k	$\Delta k/k$
400	2.297	0.15%	2.012	0.09%	1.03×10^{-3}	7%
800	2.283	1%	2.025	0.7%	$0-1.7 \times 10^{-3}$	-

Results of simulation calculations

APPENDIX F

MICROSTRUCTURE RELATED PROPERTIES OF OPTICAL THIN FILMS

PhD Dissertation by John Wharton

2	BACKGROUND	
3	EXPERIMENTAL APPARATUS	33
	High Vacuum Coating Plant.	33
	Ultraviolet Source	54
	Ion Source	61
	Substrate Preparation	63
	Source Materials	65
4	METHODS OF ANALYSIS	67
	Dektak Profilometer	67
	Spectrophotometer Analysis	67
	FECO Interferometer	76
	Adhesion, Hardness, and Durability	78
	X-Ray Diffraction	79
	Transmission Electron Microscope	82
5	RESULTS	84
	X-Ray Diffraction	84
	Spectrophotometer Analysis for Narrowband Filters	96
	Optical Analysis of Single-Layer Samples	103
	Optical Birefringence	108
	Transmission Electron Microscope	111
	Adhesion, Hardness, and Durability	114
6	CONCLUSIONS AND RECOMMENDATIONS	117

TABLE OF CONTENTS--Continued

	Page
APPENDIX A. OPERATIONS CHECKLIST FOR BALZERS BAK 760 AND RELATED EQUIPMENT.	120
APPENDIX B. TYPICAL AUTOMATIC DEPOSITION PARAMETERS	133
APPENDIX C. THE INVERTED MAGNETRON ION SOURCE	134
APPENDIX D. SAMPLES AND DEPOSITION CONDITIONS	140
APPENDIX E. TURNING POINT DATA FOR SINGLE MATERIAL COATINGS	142
REFERENCES	143

One of these methods, UV irradiation during deposition, is of particular interest because of studies of post-deposition UV irradiation and its effect upon film properties. Bradford et al. (1965) have irradiated SiO_2 films with quartz UV lamps and have noted two effects. First, the initial high absorptance of the films in the far UV has been essentially eliminated as shown in Figure 2-8. Second, the index of refraction of the films has been decreased by about 8% based upon measurements of the reflectance of the films at their interference minima. Bradford and his co-workers have attributed these effects to two entirely different processes. The first is a rearrangement of the oxygen atoms or molecules getterred during the deposition process and the formation of well defined silicon oxide molecules with low UV absorptance. The second is a further oxidation of the deposited film when the UV treatment is applied in air or oxygen.

Mickelsen (1968) has also studied the effects of post-deposition UV irradiation and noted the elimination of absorption in the 200- to 400-nm region. He has attributed this to the photorelease of electrons trapped at oxygen-ion vacancies, the trapped electrons being responsible for the UV absorption. In addition he has noted that UV-irradiated samples show greater stability of the dielectric constant with time than nonirradiated samples. This he attributes to a decrease in the migration of oxygen ions within the film.

Hodgkinson and Walker (1973) have studied the effect of post-deposition UV irradiation of SiO_2 but have concentrated on the change in mechanical properties. They have used the cantilever method of

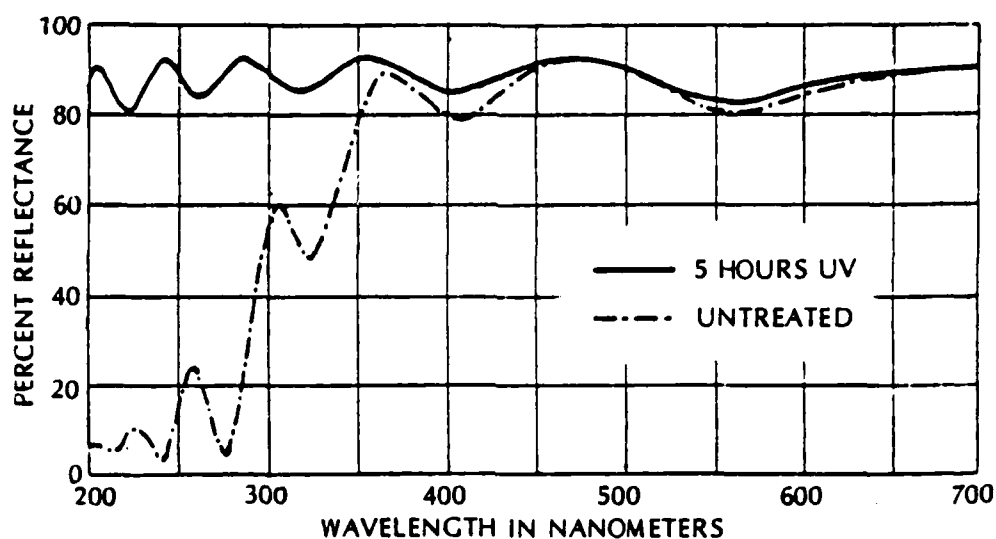


Figure 2-8. Reduction of absorption due to post-deposition UV irradiation.

Effect of UV irradiation on the visible and UV reflectance of aluminum protected with 4100 Å of SiO₂. SiO₂ evaporated at 9×10^{-5} torr of oxygen and deposited at a rate of 6 Å/sec. Irradiation performed with Hanovia lamp. (From Bradford et al., 1965.)

measuring stress by clamping one end of a film-coated substrate and measuring the deflection of the other end. When air has been admitted to the vacuum chamber, they have noted a large increase in the compressive stress. However, for samples irradiated by UV in a vacuum, they have noted a change from compressive stress to tensile stress, and after air has been allowed into the vacuum chamber, the stress again becomes compressive. Their explanation for this is that, prior to irradiation, the film has a loose structure with many oxygen molecules not bonded in the silicon oxide structure. The UV rearranges the oxygen molecules, producing well defined silicon oxide molecules and reducing the stress. Oxidation in an atmosphere, on the other hand, involves the addition of oxygen molecules to the film and an increase in compressive stress.

All of these studies show that UV irradiation has an impact on films already deposited. The influence of the UV irradiation should have a greater influence during the deposition process while columns are growing and before oxygen molecules are trapped. Another method of adding energy to the film growth process would be bombardment by either electrons or ions. Browning (1983) has studied the effect of bombarding growing films with electrons. Based on x-ray diffraction observations, he has found that for potassium hexafluorozirconate, electron bombardment during deposition eliminates crystal structure. On the other hand, he has found that electron bombardment has no effect on thin film growth of SiO_2 . Because post-deposition electron bombardment shows no effect, he has concluded that the electrons are

not able to transfer energies to the molecules greater than the lattice bonding energies. This suggests that bombardment by ions heavier than the electrons might have a greater effect.

The use of ion bombardment is not a new area of study for the deposition of thin films. Hirsch and Varga (1980) have examined the improvement of film adherence by argon ion bombardment. Cuomo et al. (1982) have examined the modification of film stress by low-energy argon ion bombardment. Martin et al. (1983) were the first to investigate ion bombardment as a means of improving packing density. They have used ion bombardment of refractory oxide films and reported significant changes in packing densities of TiO_2 and ZrO_2 . X-ray diffraction of the ZrO_2 films has shown that the ion bombardment promotes film growth in the face-center-cubic phase, while electron microscopy has revealed a disruption of columnar growth and an increase in surface roughness. Most significantly, they have found that narrow-band filters made during ion bombardment show an increased resistance to moisture penetration due to increased packing densities. In addition, there are many studies concerning sputtering that also involve ion bombardment and are thus of interest. These include Gautherin and Weissmantel (1978), Weissmantel et al. (1979), and Pawlewicz et al. (1982). Thus, ion bombardment also appears to be a way of influencing thin film growth.

CHAPTER 3

EXPERIMENTAL APPARATUS

High Vacuum Coating Plant

Because of the importance of controlling as many deposition parameters as possible, a state-of-the-art high vacuum coating plant was obtained for this research from the Balzers Company of Liechtenstein. The coating plant and its auxiliary equipment are collectively called the Balzers BAK 760 (Figures 3-1, 3-2, and 3-3). Putting the coating plant into operation and establishing the operating parameters was a time consuming process. Feedthroughs were added, support structures were installed, and procedures of operation were established. Calibration of the source materials and determination of the deposition conditions were critical to this research. For example, there is a tradeoff among oxygen pressures, substrate temperature, and deposition rates that determines the ideal conditions for the deposition of any one source material. As a result, a long series of test runs was necessary before any UV irradiation or ion bombardment could be attempted. Since this was the first project involving the use of the plant, points of operation needed to be detailed as a reference for future researchers. Rather than cover the operating details in this chapter, Appendix A has been included as an operating checklist. However, a description of the coating plant is included

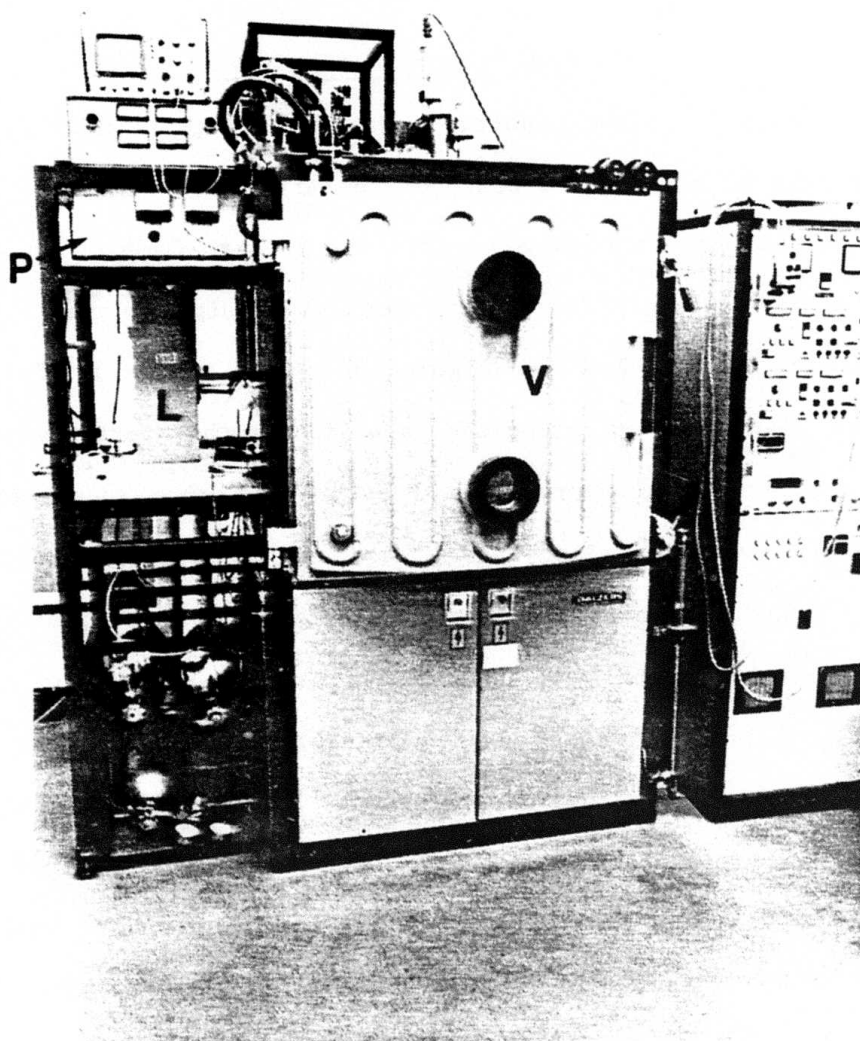


Figure 3-1. Balzers BAK 760 high vacuum coating plant.

V = vacuum chamber; P = power supply;
L = UV lamp housing

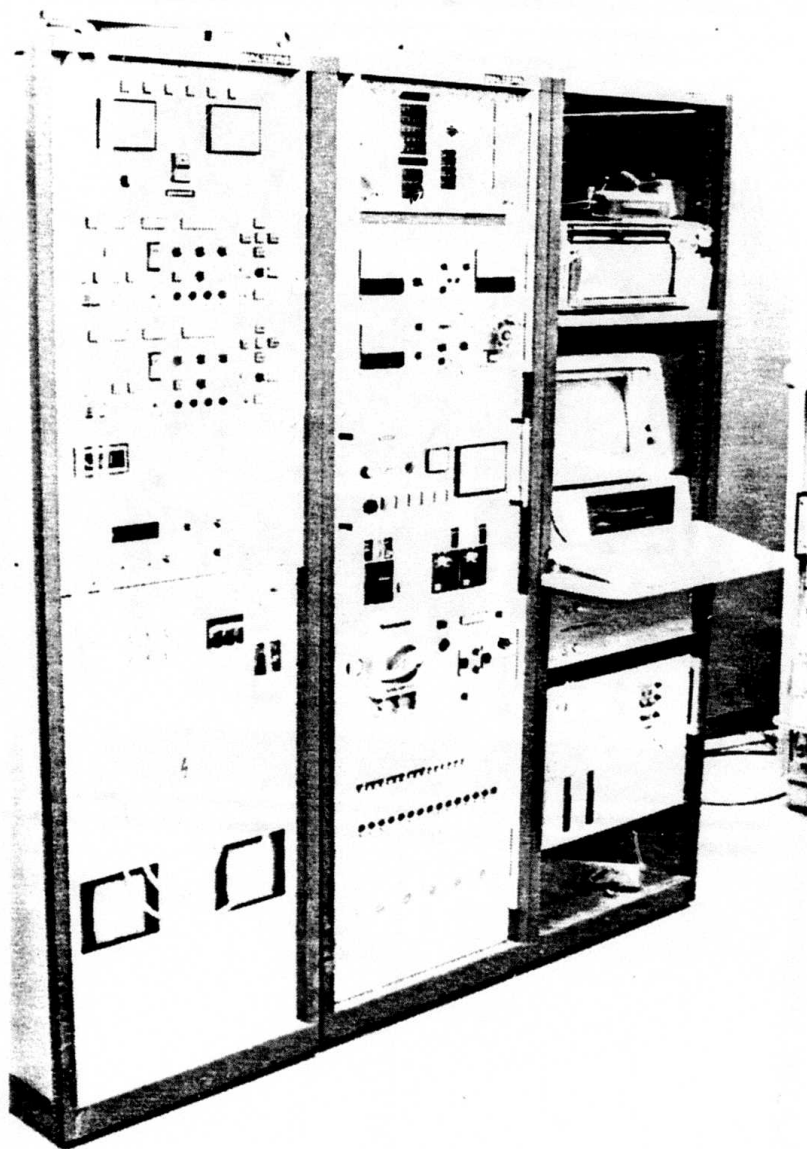


Figure 3-2. Balzers BAK 760 power supplies and digital controller.

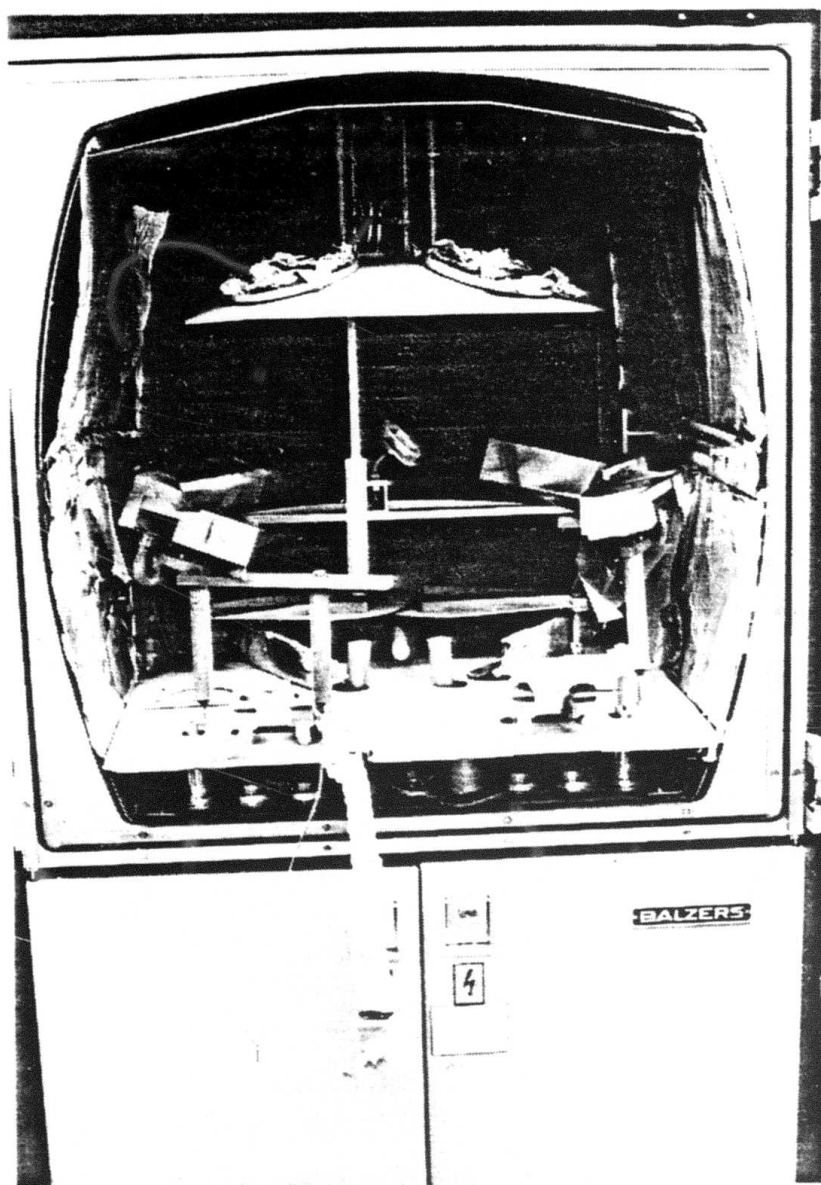


Figure 3-3. Interior of vacuum chamber.

here in order to document the conditions under which the thin films for this research were made.

The vacuum chamber itself is made of stainless steel and has a working area 888 mm wide, 923 mm high, and 950 mm deep. Tube coils are welded to the exterior walls and door to provide for heating and cooling of the vacuum chamber. A plate valve housing is attached to the rear of the chamber. A protective chevron is mounted in the opening between the working area and the valve housing to protect the valve plate from evaporants. Two large sight glasses are mounted in the door for visual monitoring of the coating process. Opening the door frees the entire cross section of the chamber, thus affording good accessibility to all internal equipment.

The roughing pump is a two-stage arrangement consisting of a Roots pump in series with a single-stage rotary vane pump with gas ballast (Balzers UNO 100). It is capable of reaching a pressure of 3×10^{-2} mbar without gas ballast and a pressure of 5×10^{-1} mbar with gas ballast. About 15 minutes is required for the roughing pump to rough down the chamber. High vacuum is obtained by a refrigerator cryo-pump (Balzers RKP 500), which uses liquid nitrogen. The advantage of using a cryo-pump is the elimination of an oil mist found when using a diffusion pump. The compressor unit is separated from the cryo-generator by means of flexible, high-pressure connecting lines in order to eliminate vibrations as much as possible. The cryo-pump is capable of obtaining pressures below 10^{-6} mbar. In practice, the cryo-pump is normally allowed to operate overnight in order to reach

this pressure. A pumping station control system (Balzers PC 101) is used to control the pumping and venting of the system. It monitors the pressure at various points in the system as well as the condition of the roughing pump and the cryo-pump. It automatically opens or closes the necessary valves by means of control signals. The pumping station control system also controls the flow of hot or cold water through the chamber wall tubes.

Pressure inside the chamber is monitored using an ionization vacuum gauge (Balzers IMG 060B). The pressure-dependent ion current of a hot-cathode gauge head is used for measurement. The electrons emitted from the cathode ionize the existing gas molecules on their way to the positive electron collector. The resultant positively charged ions are drawn off by an ion collector, and the measuring current is converted into a corresponding voltage by an electrometer amplifier which is displayed on the gauge. The emission current is held constant by a control circuit, and the ion current is proportional to the pressure within the measuring range. An alternative would have been a cold-cathode gauge, but these are not as accurate at very low pressures. Care must be taken not to operate hot-cathode gauges at too high a pressure, so a protection circuit is built into the ionization gauge control that automatically turns the filament of the gauge off at higher pressures. A manual switch is also provided for turning the filament on and off.

A regulating valve (Balzers RME 010) is mounted to the side of the coating chamber, and for this research was used to admit oxygen

at a controlled pressure during film deposition. A valve control unit (Balzers RVG 040) monitors a pressure-dependent electrical signal from the ionization gauge control and sends a control signal to the regulating valve. A precision potentiometer is used to select the desired pressure (called the "set point"), and a gauge on the control unit displays the valve voltage.

Four 2-kW quartz halogen lamps are mounted inside the coating chamber and used for heating substrates. The surfaces of the substrates to be coated are directly exposed to the radiant heat of the quartz lamps. This method of heating substrates is now becoming more popular than the old rear-surface type. The substrate temperature is preset on a control unit that controls two power controllers. Each controller supplies power to a pair of quartz lamps. The temperature inside the coating chamber is monitored using a thermocouple and is displayed on a digital unit. By comparing this temperature with the preset temperature, the control unit maintains the proper current for the quartz lamps. During this research, it was found that the location of the quartz lamps was critical for film deposition on a stationary substrate. The location of the lamps is shown in Figure 3-4.

Also shown in Figure 3-4 is the location of a glow discharge bar at the base of the coating chamber. This is the basis of a 700-W glow discharge system and is used as the final step in cleaning substrates. It will be covered in more detail under the topic of substrate preparation. Part of the glow discharge system is a regulating valve (Balzers RVE 016), which maintains the proper discharge current

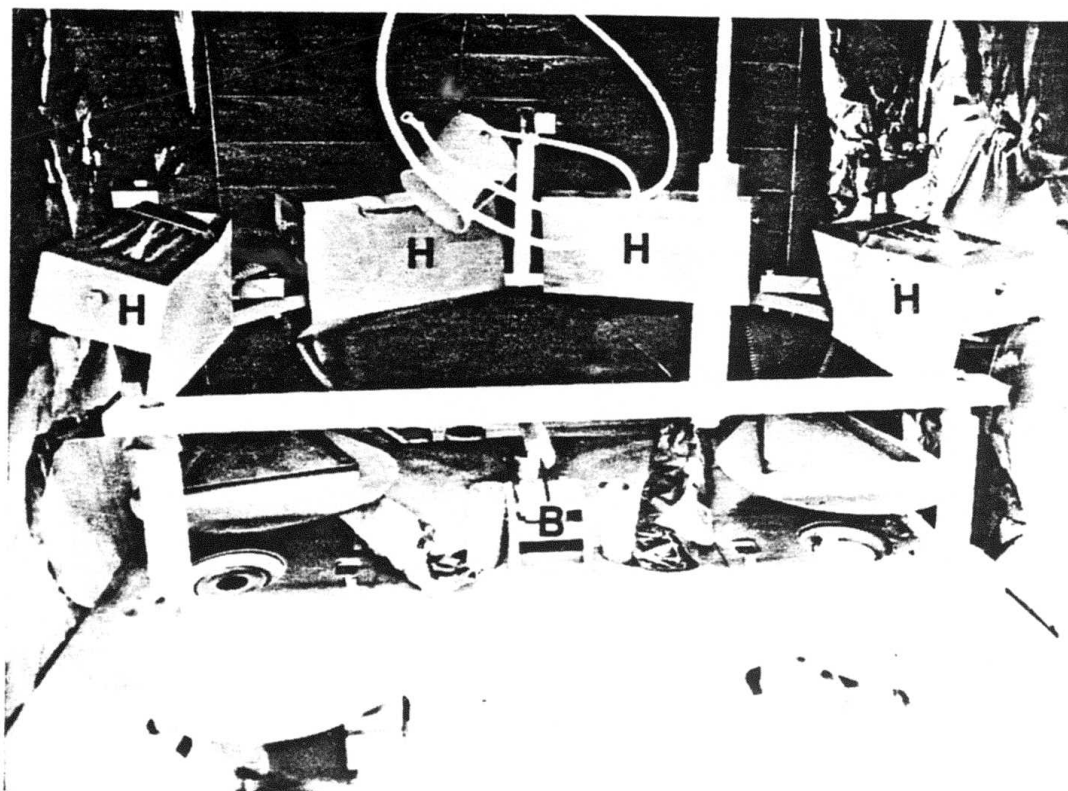


Figure 3-4. Location of substrate heaters and glow discharge bar.

H = heater; B = bar

for the glow discharge by maintaining the proper gas pressure. Air is admitted to the coating chamber and maintained at a pressure of 4×10^{-2} mbar. To control the rate at which the air is admitted, a throttling valve is built into the outlet end of the regulating valve. Although normally operated automatically, the throttling valve can be operated manually.

There are four evaporation sources mounted in the coating chamber; two of these use thermal heating and two use electron-beam heating (see Figure 3-5). In both cases, the thin film deposition process is called vacuum evaporation. An understanding of this evaporation process is necessary for understanding the formation of the microstructure of thin films. If a material is heated in air it will eventually vaporize, provided it does not decompose or react with its environment. The vapor is given off in a turbulent stream that is not uniform in time. When it strikes a cold surface and condenses, it produces a porous deposit that is generally not suitable for optical purposes. However, when the evaporation takes place in a vacuum, such is not the case. Most important, at sufficiently low pressures the evaporant will not react with the atmosphere. In addition, the vapor stream given off is even, and the evaporant molecules appear to travel in a straight line. If a cold substrate is properly prepared and inserted in the path of the evaporant, a useful film will be deposited (Macleod, 1969).

For vacuum evaporation, the first step necessary is the heating of the source material to change it from a condensed phase,

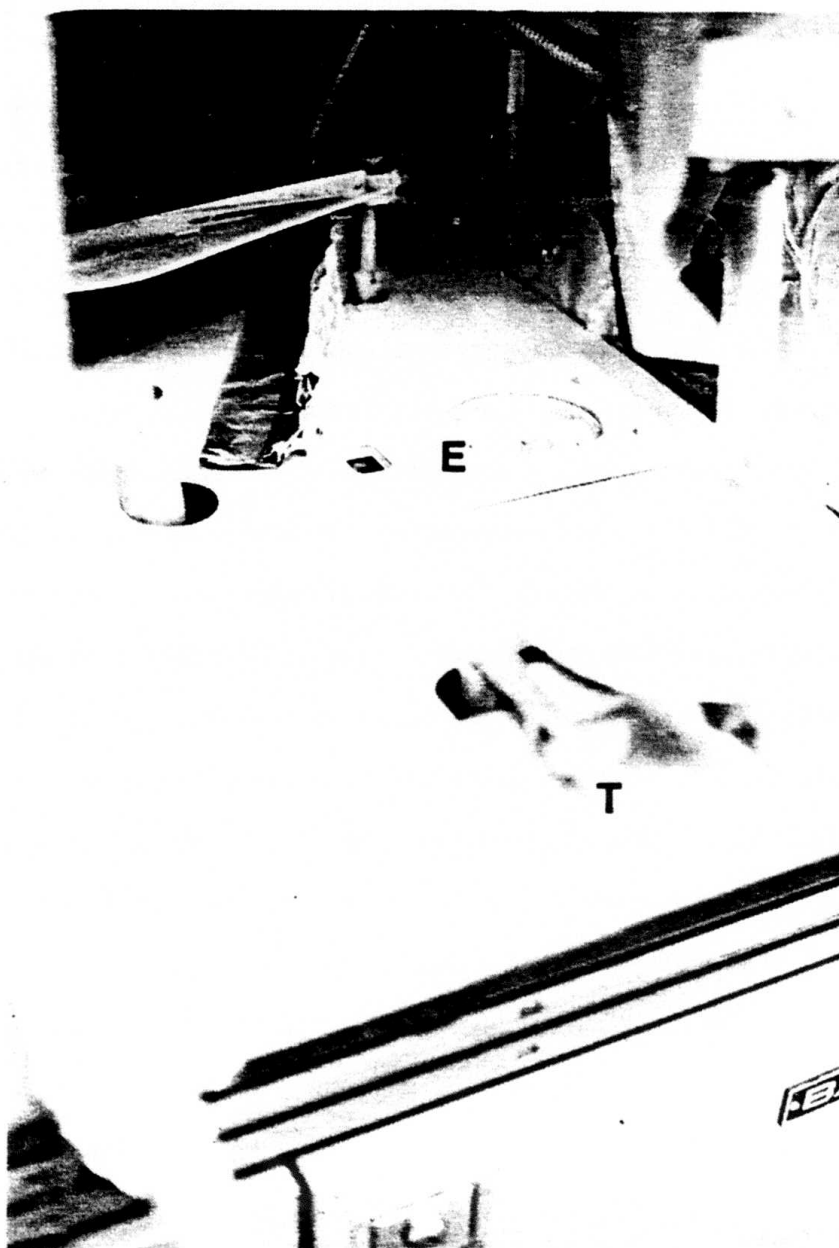


Figure 3-5. Location of thermal sources and electron beam sources.

(a) Right side view. T = thermal source;
E = electron beam source

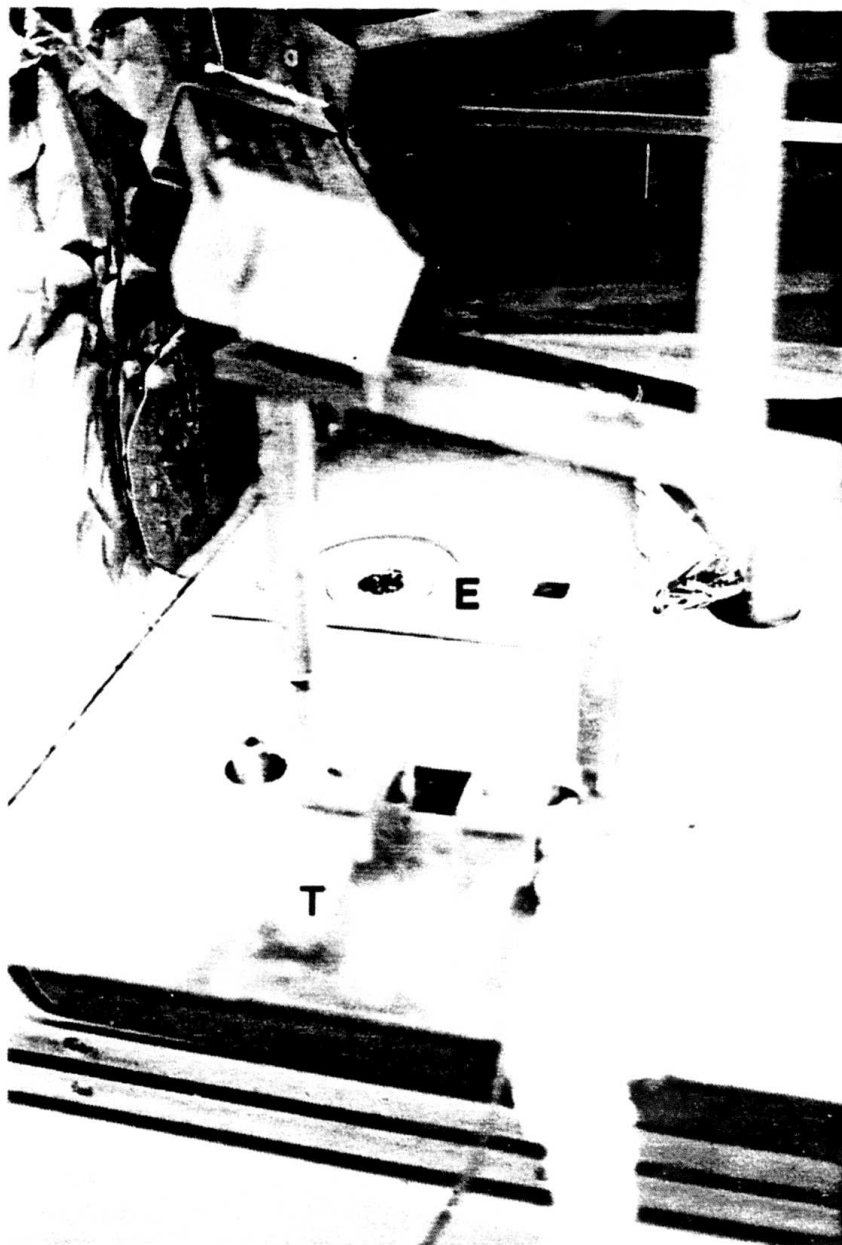


Figure 3-5--Continued

(b) Left side view. T = thermal source;
E = electron beam source

either solid or liquid, to a gaseous state. The choice of heating method depends largely on the vaporization temperature of the source material. The most easily controlled method is thermal heating. In this method the source material is placed in a "boat" made of a refractory metal, such as tungsten, tantalum, or molybdenum. The boat serves the function of a crucible to contain the source material, and when an electric current is passed through it, it provides the heat necessary to vaporize the material. For this research, a tungsten coil was used to hold aluminum for deposition. Each thermal evaporation source has a 4-kVA high current transformer and is controlled by a digital system controller (Balzers BPU 100E), which will be discussed later. By use of the controller, the rate of deposition can be held constant.

Also in the coating chamber are two electron-bombardment-heated sources, more simply called electron-beam sources. Instead of being heated by resistance or induction heating, the source material is heated by an electron beam focused onto its surface. Most of the kinetic energy of the electrons is converted into heat, and higher evaporation temperatures can be reached. This is the biggest advantage to using electron-beam sources. Another advantage is that there is less interaction between the source material and its container. This is because the electron beam is focused onto the surface of the source material, and the portion of the source material in contact with the container is maintained at a lower temperature. Even materials that are very reactive, such as silicon which is hard to evaporate by any other method, can be used.

The two electron-beam guns (Balzers ESQ 310U) are designed for maximum flexibility. Three interchangeable crucibles can be selected, based on the number of materials needed for the film design and the amount of material needed. When two source materials are required in quantity, a large (80-cc), single-pocket, or pot, crucible is used. A crucible control unit (Balzers ETS 110) rotates the crucible to use the source material uniformly. A separate molybdenum liner is used for each source material, and placed inside the single-pocket crucible; this allows for easily changing source materials within one crucible. When many source materials are needed, a four-way crucible containing four separate 8-cc pockets is used. It is mounted with a crucible cap that exposes only one pocket at a time to the electron-beam gun. The crucible control unit is used to select which pocket is exposed. An oscillating crucible is similar to the four-way crucible except that two of the pockets are replaced by a 20-cc, crescent-shaped pocket that is oscillated during use. This crucible combines the advantage of a larger amount of one source material with the availability of several other source materials.

Each electron-beam gun has a separate 15-kW power supply (Balzers EHV 110A) and is controlled by a separate control unit (Balzers EKS 110A). The control unit provides power for the cathode in order to control the electron beam output and control the position of the beam spot on the evaporant. Electrons are produced by the heated cathode of the electron gun, extracted by an electric field potential, and focused by means of a voltage applied to a Wehnelt shutter. The electrons are deflected through approximately 270° by

means of a magnetic field, and strike the evaporant in the crucible. The y-sweep of the electron beam is controlled by a periodic variation of the deflection field, and the frequency can be adjusted from 2 to 40 Hz. The x-sweep of the electron beam is controlled by an additional electromagnetic field; the sweep frequency is 50 Hz. With a 10-kV acceleration voltage, the density of the electron beam at the crucible is 40 kW/cm^2 . Since a very much lower density of 1 kW/cm^2 is needed for the evaporation of dielectrics, the beam is defocused by means of an electromagnetic AC field superimposed on the deflection field. A hand-held remote control allows for adjustment of the beam position, for fine control of the crucible position, and for remote switching off of the filament current. This is essential as a safety device since the beam can be controlled while the operator is looking at the source material in the crucible through the sight windows of the vacuum chamber door.

The electron-beam gun control unit can be operated either manually or automatically. The advantage of manual operation is that the power can be controlled while the operator is watching the material in the crucible. For automatic operation, it is necessary to determine both the power levels and the deposition rates that will be used. This must be done by making several trial runs under manual operation. The greatest advantage to automatic operation is that the deposition rate can be held constant more accurately than can be done manually. Another advantage is that a coating design can be repeated with coating parameters held as close to the same values as possible.

For automatic operation, the power supplies for the thermal evaporation sources and the electron gun control units are controlled by a microprocessor unit (Balzers QSR 101). This unit relies on information from a quartz crystal to accurately control film thicknesses and deposition rates. It also controls such auxiliary functions as shutter opening and closing, substrate rotation, and glow discharge. As shown in Figure 3-6, process parameters are entered through a keyboard, and can be displayed and updated at any time. For each of the four sources, the following information must be entered into the microprocessor: thickness of the layer in angstroms, deposition rate in angstroms per second, a material constant in grams per cubic centimeter which is proportional to the specific density of the coating material, four control times, and four power levels.

The control times and power levels are shown diagrammatically in Figure 3-7. The time T1 is the glow discharge time; time T2 is the recovery period after the glow discharge; time T3 is the rise time during which the power is increased from zero to power P1; and time T4 is the degassing time. The power settings are given as a percentage of the maximum power that can be achieved for a given source, and must be determined manually. Power P1 is the rise power and is the power level at which degassing begins. The degassing period is necessary to allow the source material to outgas and the system to return to the pressure required for deposition. Power P2, which may be higher or lower than power P1, is the degassing power and is the power reached at the end of time T4. Power P3 is the maximum power

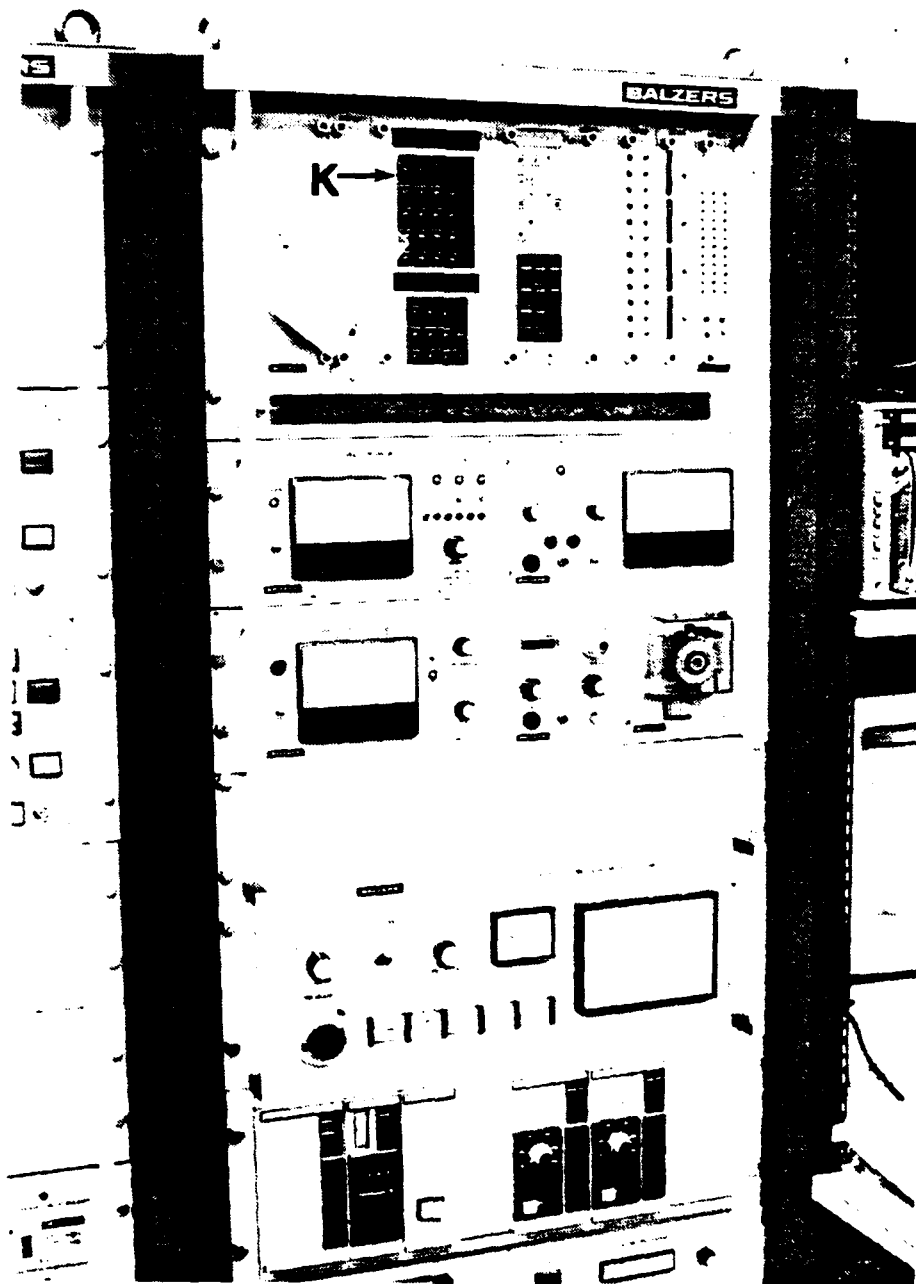


Figure 3-6. Digital controller.

K = keypad

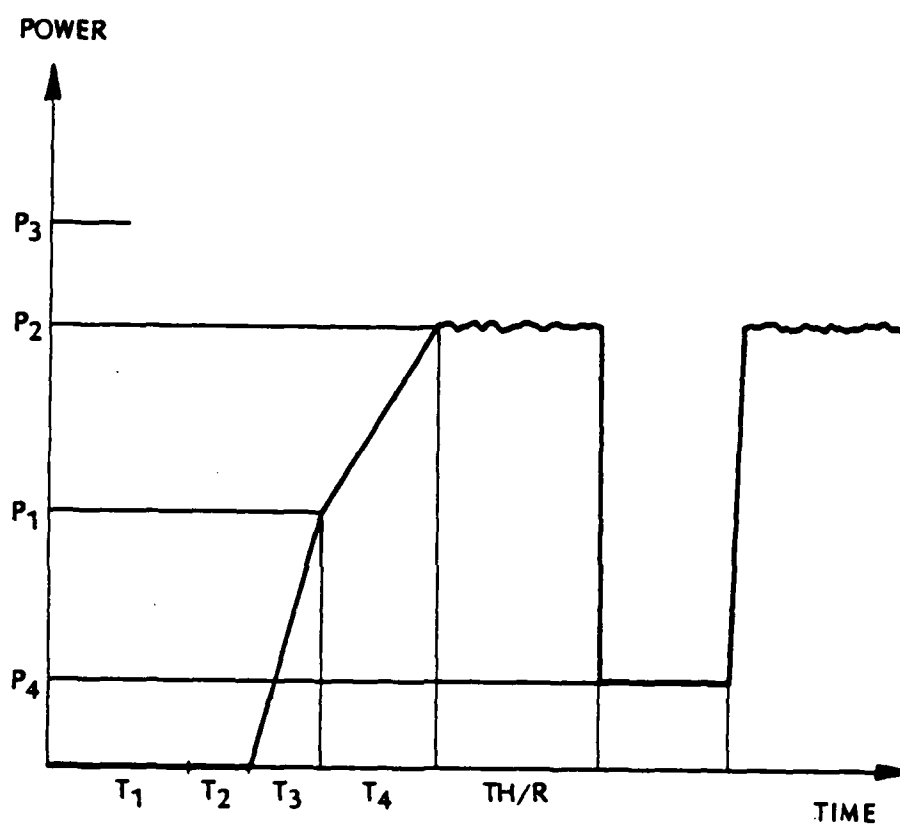


Figure 3-7. Control times and power levels.

that can ever be applied for a given source, and is selected for safety reasons. Finally, power P_4 is a holding power that maintains the source material at a temperature below the vaporization temperature. Typical values for these parameters as used during this research are given in Appendix B.

The quartz crystal is mounted in a water-cooled copper shield in the vacuum chamber just below a rotating substrate holder. As material is being evaporated, it condenses on an exposed portion of the quartz crystal just as it condenses on the substrate. The frequency of the quartz crystal changes from its natural frequency owing to the additional mass, and the change of frequency is given by

$$\frac{df}{f} = - \frac{m}{\rho A d}$$

where f is the natural frequency, d is the thickness of the quartz, ρ is the density of the quartz, A is the area of the quartz, and m is the mass covering the quartz. The thickness of the coated layer is then given by

$$th = \frac{K}{\rho'} * \left(\frac{1}{f} - \frac{1}{f_0} \right)$$

where th is the thickness of the layer, ρ' is the density of the coating material, f_0 is the starting frequency, f is the measured frequency, and K is a constant. In the microprocessor, the value M is used to input the constant for this equation.

The actual frequency change of the quartz crystal not only depends on the mass of the material being deposited, but is affected by temperature stability and the kind of holder used for the crystal.

In this case, the crystal holder is water cooled to assure a high temperature stability of the quartz. The holder is also designed to put a minimum amount of mechanical pressure on the quartz so as not to distort the frequency.

To calibrate the material constant for each material, the thickness of a layer being deposited must be determined by a means additional to the quartz crystal. For this reason, and for manual operation, an optical thin film monitoring system (Balzers GSM 210) is used. The components of the optical monitoring system are shown in Figure 3-8. A light source, powered by a stabilized voltage source, produces a light beam that is modulated or chopped at 80 Hz by a rotating chopper blade. The light beam enters through a window in the base of the vacuum chamber and strikes a monitor plate positioned in the plane of the substrates to be coated. For this research the monitor plateholding assembly was modified to hold a stationary substrate, so that the substrate itself acts as a monitoring plate. The modulated light that is reflected from or transmitted through the substrate is detected by separate four-stage blue photomultipliers, whose spectral sensitivity is shown in Figure 3-9. An alternating current proportional to the light intensity is then sent to a monitoring instrument that displays both the amount of total light and the percentage of reflection or transmission. To ensure that light from the evaporation sources, substrate heaters, room lights, etc., is not included in the measurements, the amplifier in the monitoring instrument is selectively matched to the modulation frequency. A filter

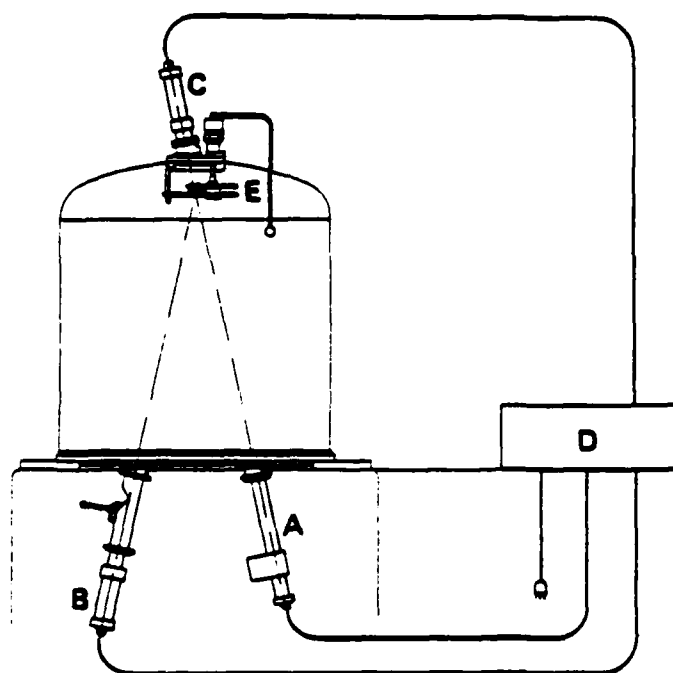


Figure 3-8. Optical monitoring system.

- A Light source
- B,C Photomultiplier tubes
- D Monitoring instrument
- E Monitor plateholder

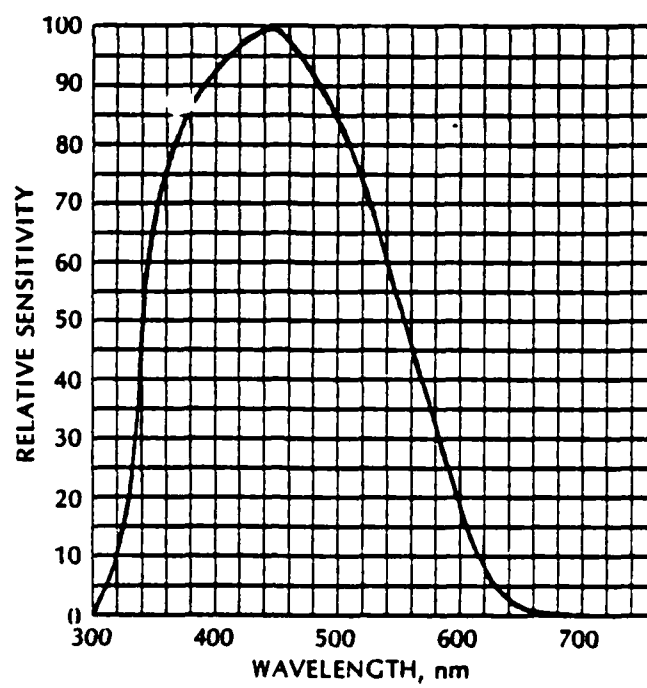


Figure 3-9. Spectral sensitivity of photomultiplier tube.

holder is mounted in the photomultiplier tube assembly, and a pair of interference filters is used to select the monitoring wavelength. The spectral transmission of the pair of filters is shown in Figure 3-10.

Ultraviolet Source

A 1000-W mercury-xenon lamp was used as a UV source for this research. As shown in Figure 3-11, the lamp house (Kratos LH151) was mounted on the side of the coating chamber. Although it would be desirable to mount the UV source under the coating chamber so that the beam of light could be directly aimed at the substrates, space limitations under the coating chamber prevented this choice. The walls of the lamp house are of heavy duty construction as a safety precaution in the event the arc lamp explodes. The lamp housing has an internal blower to provide cooling ventilation for the lamp. However, as an additional safety measure, an external blower system was connected to the output vent to remove ozone from the laboratory area. The condensing system of the lamp house uses 3.81 cm (1-1/2 in.) optics with an f-number of 1.5.

A mercury-xenon lamp was chosen in preference to pure mercury because it should have a longer life and be more stable in use. However, xenon has the disadvantage of a high output in the near infrared. Figure 3-12 shows the spectral output of the mercury-xenon lamp. To limit the purely thermal effects of the long-wavelength light, a Schott UG-5 spectral filter was used to filter out the visible and infrared portions of the spectrum. The spectral transmission of this filter is shown in Figure 3-13. The light from the lamp

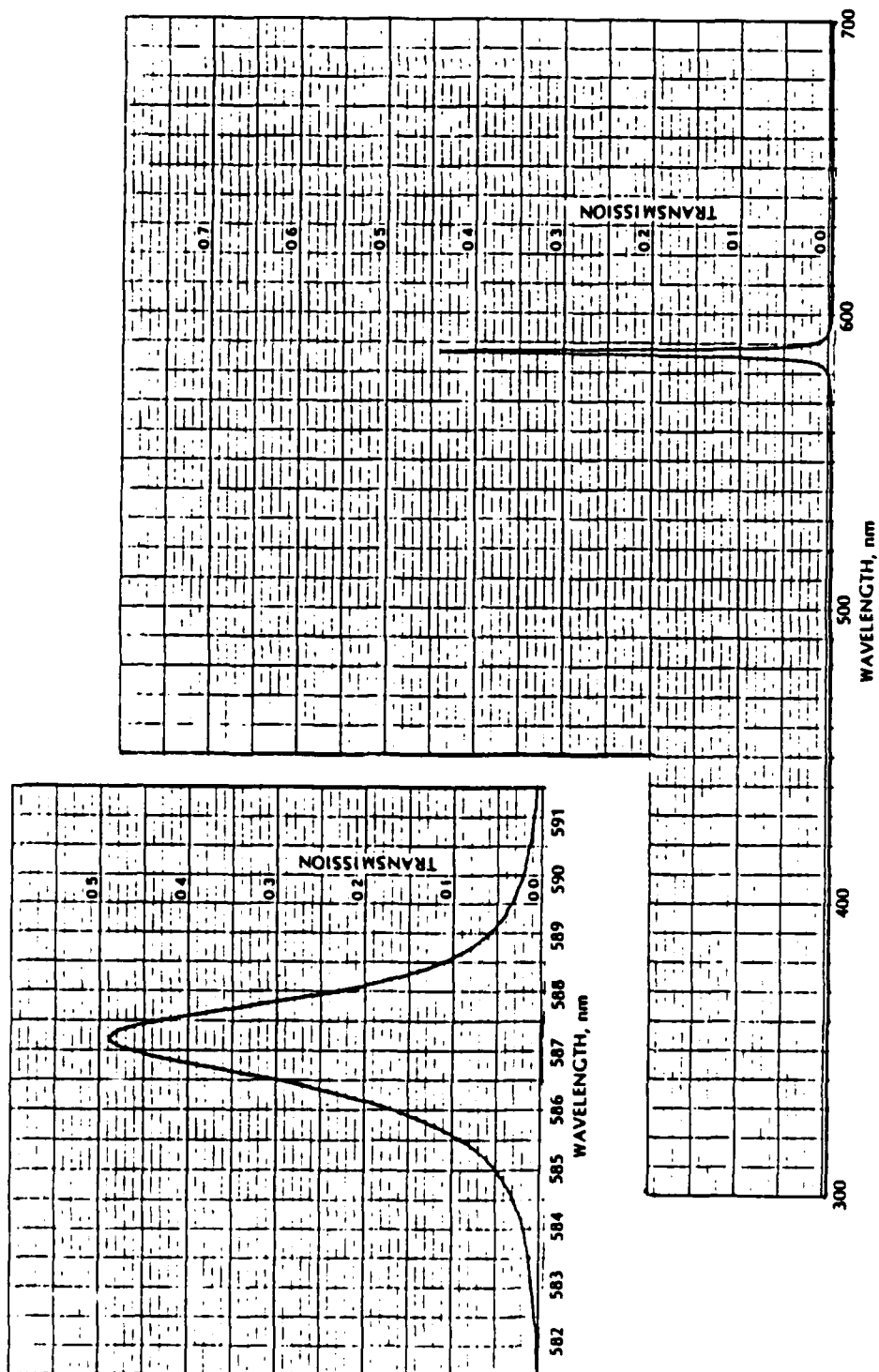


Figure 3-10. Spectral transmission of monitoring filters.

Expanded plot of peak region is shown at upper left.

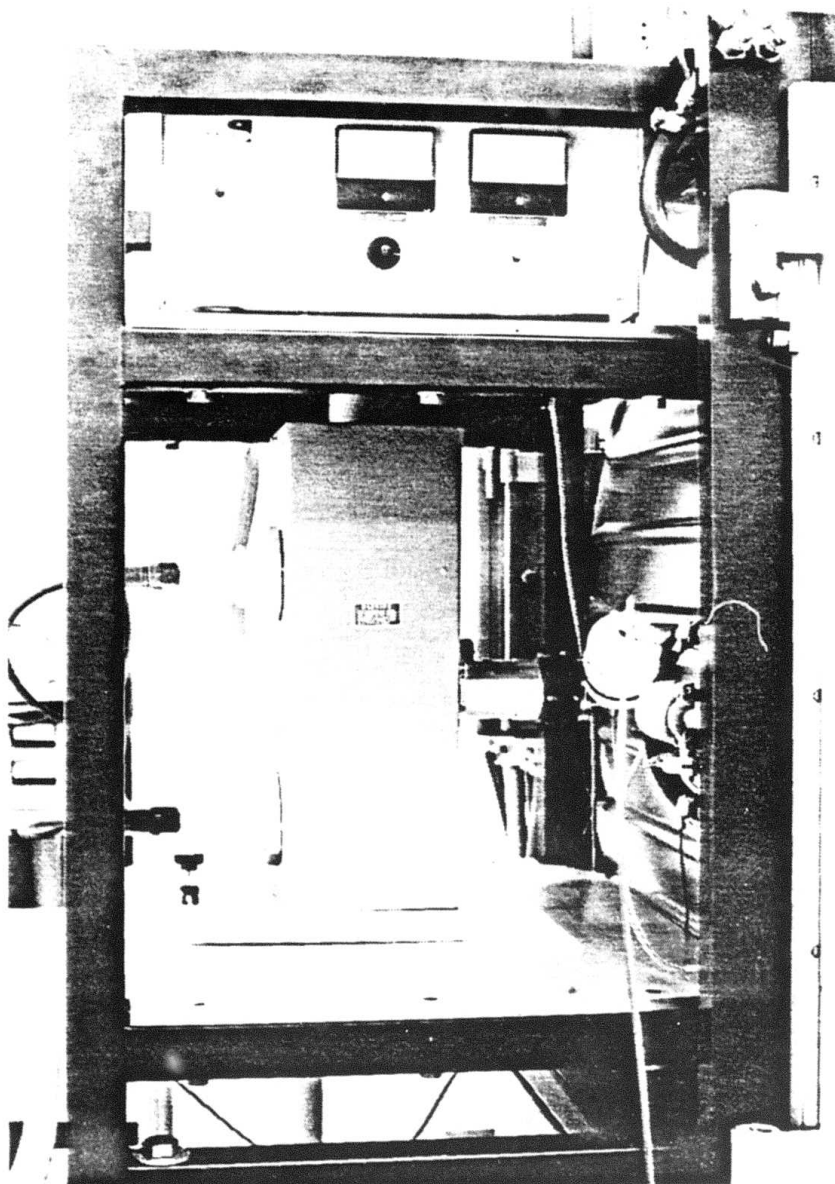


Figure 3-11. UV lamp house and power supply.

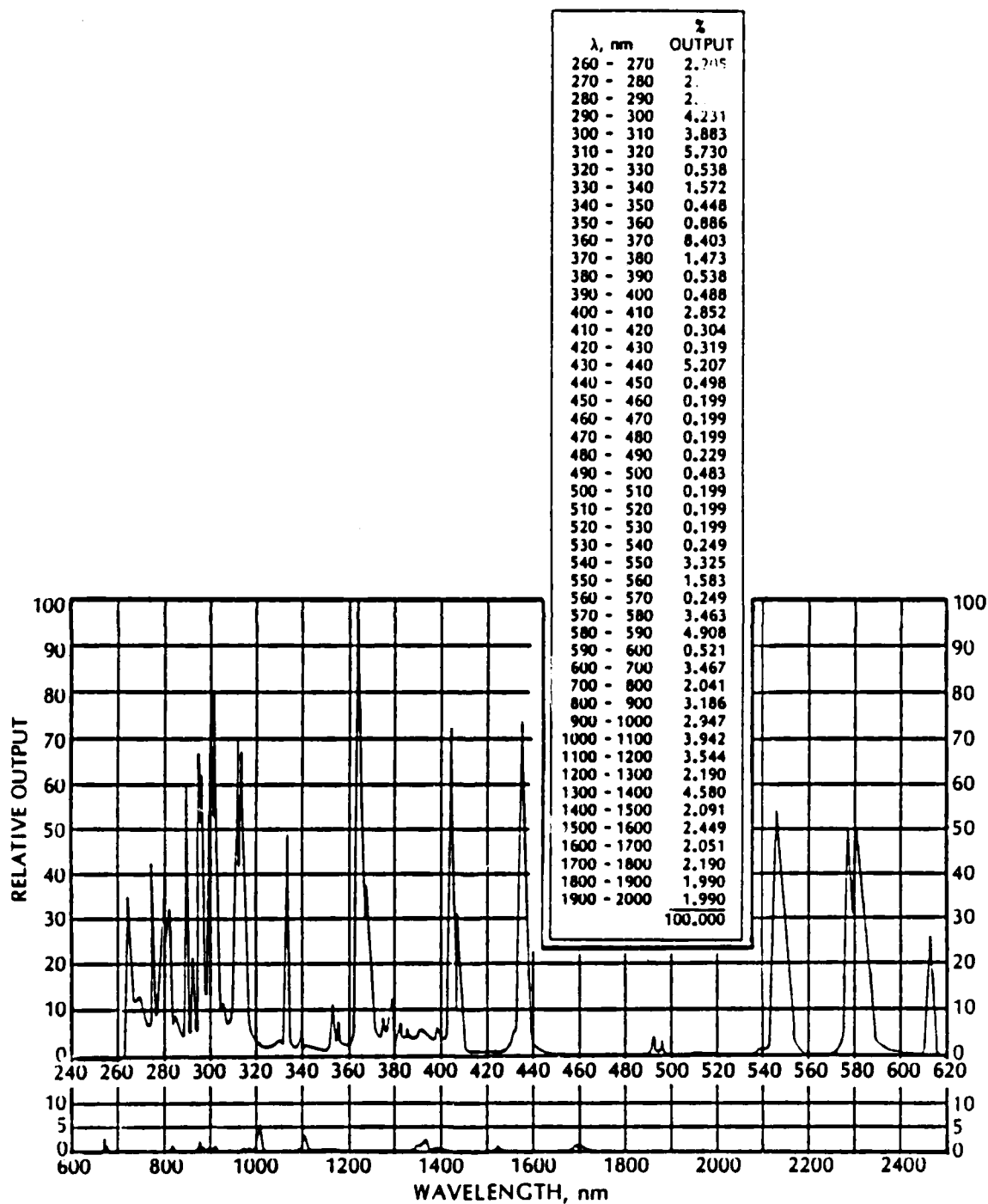


Figure 3-12. Spectral output of mercury-xenon lamp.

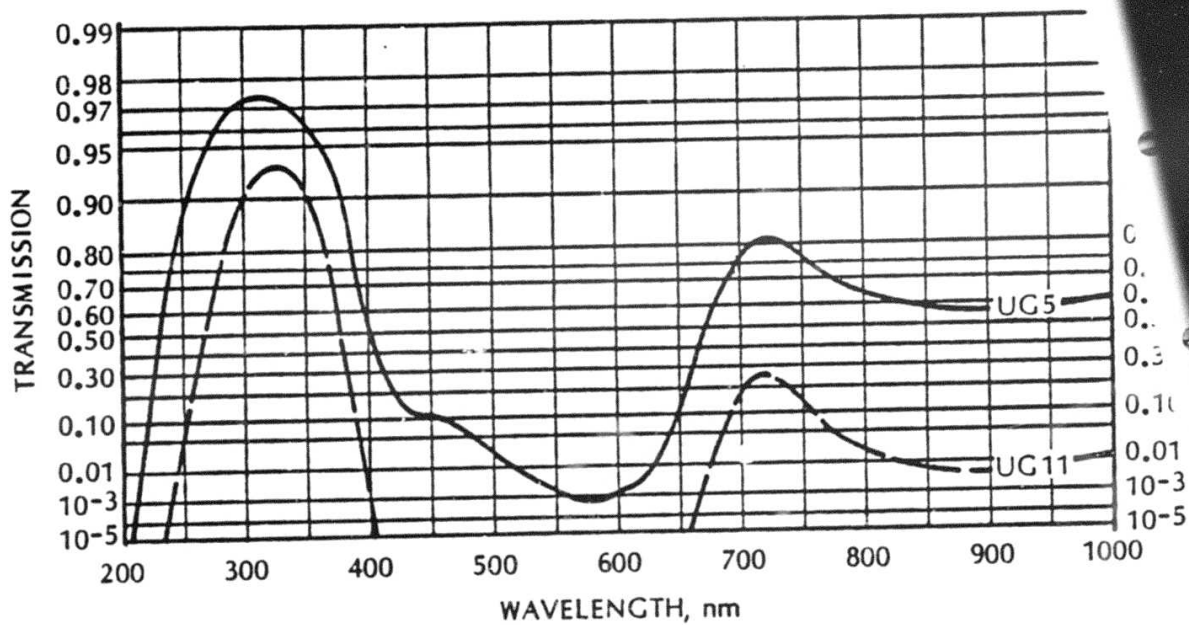


Figure 3-13. Spectral transmission of UG-5 filter.

is transmitted into the vacuum chamber through a sapphire window, chosen because of its high ultraviolet transmittance, and onto a mask with a slit. Then the light is directed onto the stationary substrate by means of two aluminized folding mirrors. The components of the UV system are shown in Figure 3-14.

The amount of UV radiation reaching the samples should be enough to increase the mobility slightly. The energy of a UV photon is on the order of the bonding energy of the material, and it is necessary to ensure a photon arrival rate comparable to the material arrival rate. For the UV system selected for this research, it was difficult to calculate this rate because of losses in transmission through the sapphire window of the vacuum chamber and the losses due to reflection from the two mirrors. However, a measurement of the UV irradiation reaching the sample was made using a Coherent Model 210 Power Meter.

With the Schott UG-5 filter present in the system, a power of 0.5 W or J/s was measured at the substrate location. The energy of each photon was calculated using the simple equation

$$E = h \frac{c}{\lambda}$$

where the wavelength λ is some average wavelength within the UV region. For a value of 3×10^{-7} m, the result was 6.62×10^{-19} J/photon. Thus, the rate at which photons arrive at the substrate is 7.5×10^{17} per second.

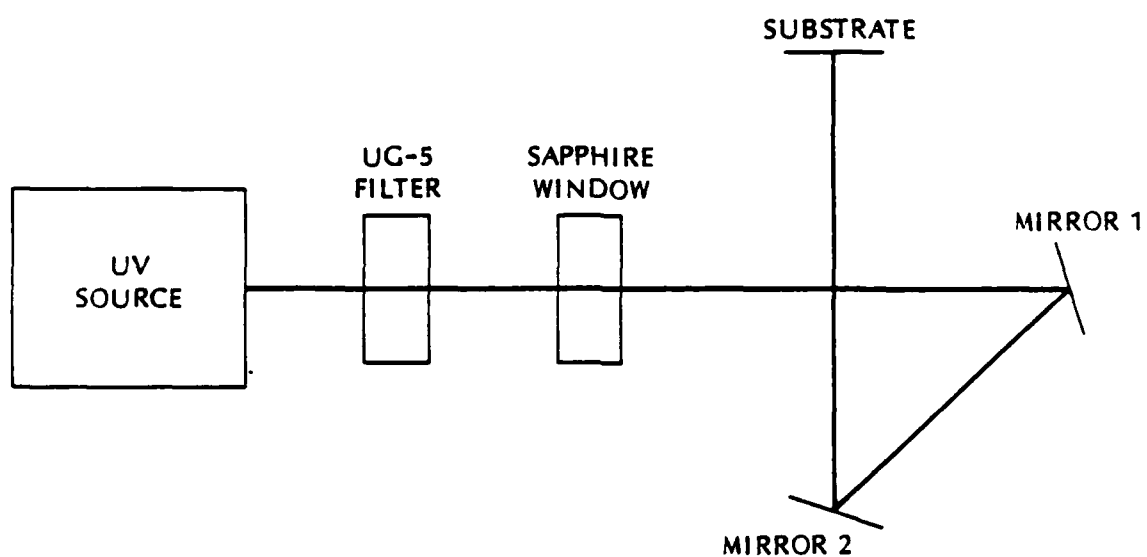


Figure 3-14. Schematic of UV system.

The rate at which source material arrives at the substrate depends on the deposition rate selected for that material. As a representative number, a quarter wave of SiO_2 takes 1 minute to deposit. At a monitoring wavelength of 500 nm, a quarter wave has a thickness of 1.25×10^{-7} m. Multiplying Avogadro's number by an SiO_2 density of 5.9×10^6 g/m³, there are 6.34×10^{28} molecules/m³. For a sample size of 2.25×10^{-4} m², a volume of 2.81×10^{-11} m³ is deposited in 60 seconds; this yields a material arrival rate of 2.97×10^{16} molecules per second. Comparing the two rates just calculated, there should be 25 photons per arriving molecule, a more than adequate ratio.

As an additional UV source, a 160-W mercury lamp (General Electric HSB160/PS30/M) can be mounted inside the vacuum chamber. The outer glass bulb was removed, and four electrical wires were connected to the lamp. Two of the wires were connected to the high voltage lead-throughs normally used for an ion gun. These lead-throughs were in turn connected to the 120-V line voltage in the laboratory. The remaining two lead-throughs were connected to two of the pins of a seven-pin lead-through mounted on the side of the vacuum chamber, and used to start the lamp. No ballast was required for this lamp. In this paper, the lamp is referred to as the interior UV source.

Ion Source

A water-cooled inverted magnetron ion gun (Figure 3-15) is used as an ion source. The ion gun is so called from its discharge



Figure 3-15. Inverted magnetron ion gun.

G = ion gun

geometry, and is capable of producing a well focused intense beam of ions. It is a cold-cathode, magnetically enhanced discharge source, in which ions are extracted through an aperture in the cathode wall. After extraction, the ion beam is collimated and focused by a system of electrodes. A single extraction aperture of 3 mm diameter is used. The voltage applied between anode and cathode is called the discharge voltage, and the voltage applied to the electrodes for extraction and focusing is called the beam voltage. Both argon and oxygen ions were used for this research. Calibration values for different discharge voltages and beam voltages are given in Table 3-1. A more detailed description of the geometry and operation of the ion gun is given in Appendix C.

Substrate Preparation

The substrates used for this research were either 1- x 3-inch glass microscope slides or 1- x 1-inch fused quartz samples. In both cases, the substrates were cleaned following the same procedure. First, the substrates were immersed in warm chromic acid for about 30 minutes. They were then drained, rinsed, and scrubbed by cotton using liquinox soap and deionized water. They were then rinsed using deionized water, and placed in an ultrasonic bath of deionized water and liquinox for about 20 minutes. After this they were placed in an intermediate ultrasonic rinse of deionized water, followed by a final ultrasonic rinse at a different frequency in deionized water. Finally, they were blown dry with nitrogen from an electrostatic nozzle gun. The cleaning procedure is designed to remove surface contamination

Table 3-1. Calibration of Ion Gun

Discharge current (mA)	Discharge voltage (V)	Beam current (mA)	Beam voltage (V)	Measured output (μ A)
<u>Argon ions</u>				
12	400	2.3	1200	24
12	400	2.5	1200	28
12	400	*	1800	*
14	400	0.2	2200	60
16	400	0.4	1500	51.9
<u>Oxygen ions</u>				
10	400	0.2	1500	30.2
10	400	0.2	2000	45.5
10	400	0.2	2500	43.0
15	400	0.35	1500	35.6
15	400	0.2	2000	77.7
20	400	0.5	1000	16.6
20	400	0.4	1500	42.6
20	400	0.25	1800	73.1
20	400	0.2	2000	95.6
20	400	0.2	2500	103.5

Note: All readings taken with a pressure of 1×10^{-5} mbar.

*Discharge breaks down.

since such contamination decidedly influences thin film growth and adhesion. The final cleaning process is glow discharge cleaning and is accomplished in situ immediately prior to thin film deposition. A detailed description of substrate cleaning, including glow discharge cleaning, is given by Maissel and Glang (1970) and will not be included here.

Source Materials

Two materials with high index of refraction were used for this research: titanium oxide (Ti_2O_3) in the form of 1/4-in. to 1/8-in. pieces of 99.9% chemical purity from Cerac, and zirconium oxide (ZrO_2) tablets from E. Merck Chemicals. Silicon oxide (SiO_2), in the form of 1/2-in. to 1/8-in. fused pieces of 99.99% chemical purity from Cerac, was used as a low index material. The materials chosen for examination are the most commonly used dielectric materials in thin film work, and improvements in their deposition would be of the greatest interest.

The Ti_2O_3 is a better source material for the production of TiO_2 than just simply using TiO_2 . TiO_2 loses oxygen on heating, and this is the reason for requiring reactive evaporation. In addition, the TiO_2 within the crucible gradually changes in composition toward lower oxides as film layers are being deposited. Thus, to ensure stability of the composition of the source material, it is preferable to use Ti_2O_3 (Pulker, Paesold, and Ritter, 1976). Even with this material, higher oxygen pressures are required in the vacuum chamber than are required for ZrO_2 . Also, it has been found that powdered forms of

CHAPTER 4

METHODS OF ANALYSIS

To detect any macroscopic or microscopic changes in films that have been irradiated with UV and/or bombarded with ions, a number of methods of analysis are used. Each method is described in its own section below.

Dektak Profilometer

For measurements of physical thickness, a Sloan Dektak Surface Profile Measuring System is used. It is capable of measuring surface profiles from less than 2.5 nm to a maximum of 100,000 nm. In operation, a sample is placed on a stage located beneath a sensing head. The sensing head contains a diamond stylus with a tracking force of about 50 mg. As the sensing head moves relative to the sample, height information is recorded on a strip chart. For measurements of film thickness, a mask should be used during the preparation of the film so that an uncoated portion of the substrate can be used as a reference height.

Spectrophotometer Analysis

Since thin films are used to modify the optical properties of surfaces, optical techniques are useful in analyzing thin films. A spectrophotometer is a device that measures either reflectance from or transmittance through a sample as a function of wavelength over a

wide spectral range. This information can then be used to compute the optical constants of the film(s).

The Cary Model 14 spectrophotometer measures reflectance and transmittance by comparing the relative intensities of two different beams from the same optical source. The two beams are generated by a rotating semicircular mirror that chops the beam at 30 Hz, alternately sending half of the beam to the sample and using the other half as a reference. An optical diagram of the system is given in Figure 4-1. A tungsten lamp acts as a source for the portion of the visible spectrum between 300 and 650 nm; a deuterium lamp is the source for the portion of the UV spectrum from 200 to 300 nm. The wavelength of the incident light is scanned using a 30° fused silica prism in series with a 600-line/mm grating, each with its own collimating mirrors and slit system. Because the pulses of light of the reference beam and sample beam are out of phase with each other, a single photomultiplier tube is used to detect the light. To correct for variations between the output of the source and the responsivity of the photomultiplier tube, a bank of compensating resistors is used.

Before reflectance or transmittance data are taken, a 100% line is established by comparing the reference and sample beams with no sample present. The balance between the two beams must be re-adjusted each time the instrument is changed from reflectance to transmittance and vice versa. In addition, the balance must be adjusted when a new sample holder is used. After the beams have been balanced so as to give a reading of 100%, the sample is positioned in

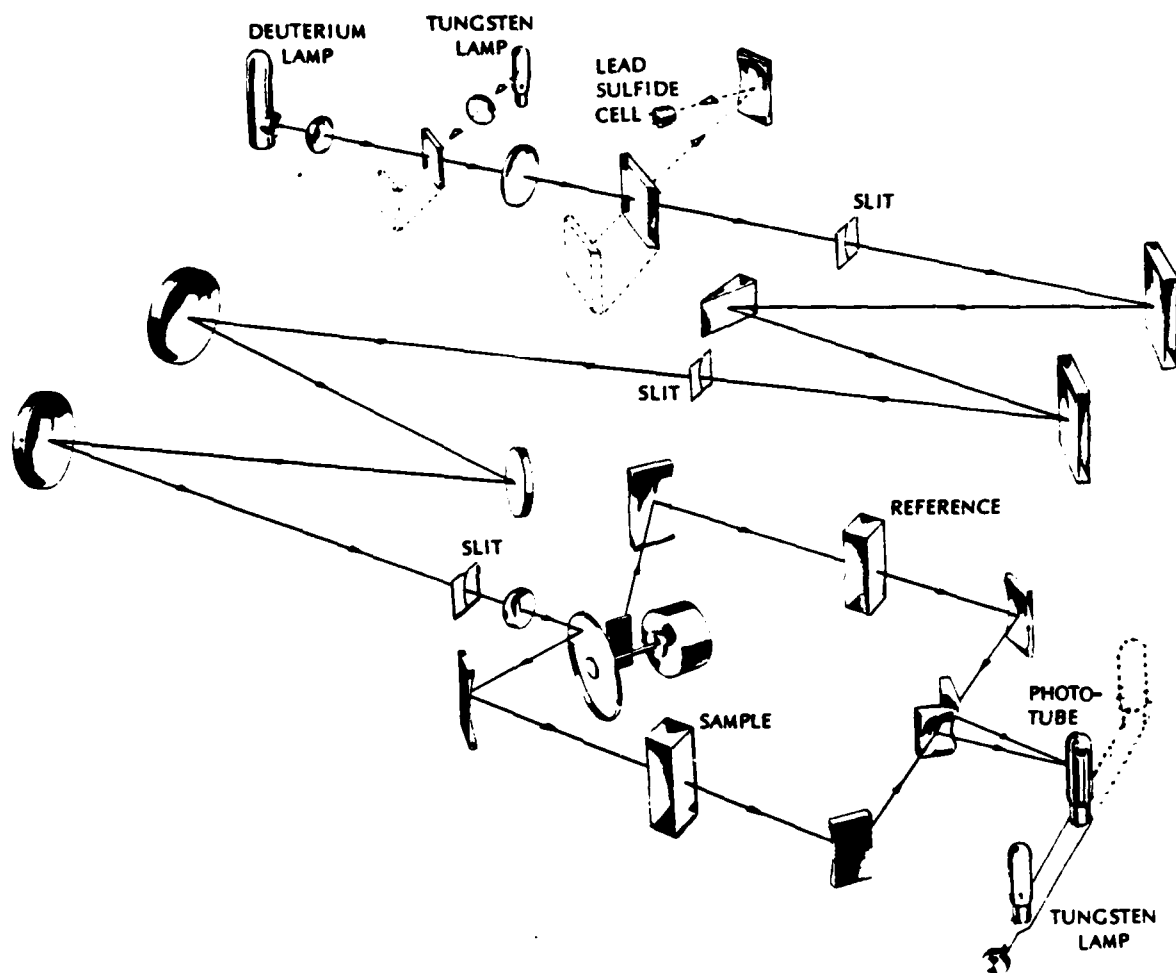


Figure 4-1. Optical diagram of Cary 14 spectrophotometer.

$$\begin{bmatrix} 0 & \pm \frac{i}{n_m} \\ \pm i n_m & 0 \end{bmatrix}$$

for an odd number of quarter waves, and

$$\begin{bmatrix} \pm 1 & 0 \\ 0 & \pm 1 \end{bmatrix}$$

for an even number of quarter waves. The result is that the effective admittance for an odd number of quarter waves is given by the simple relationship

$$n_f = \frac{n_m^2}{n_s}$$

and for an even number of quarter waves, i.e., half waves, the layer acts as though it were not there.

The reflectance from a surface is given by a form of the Fresnel equations, and for a substrate/film assembly whose effective index is n_f the relationship is

$$R = \frac{(1 - n_f)^2}{(1 + n_f)^2}$$

Since any odd number of quarter waves can be treated as one quarter wave plus a number of absentee layers, the reflectance of a substrate/film assembly will cycle between the reflectance from the bare substrate to the reflectance of one quarter wave deposited upon the substrate. Figure 4-2 is a plot of transmittance versus thickness, and if the deposition rate is held constant, a plot of transmittance versus time will look the same.

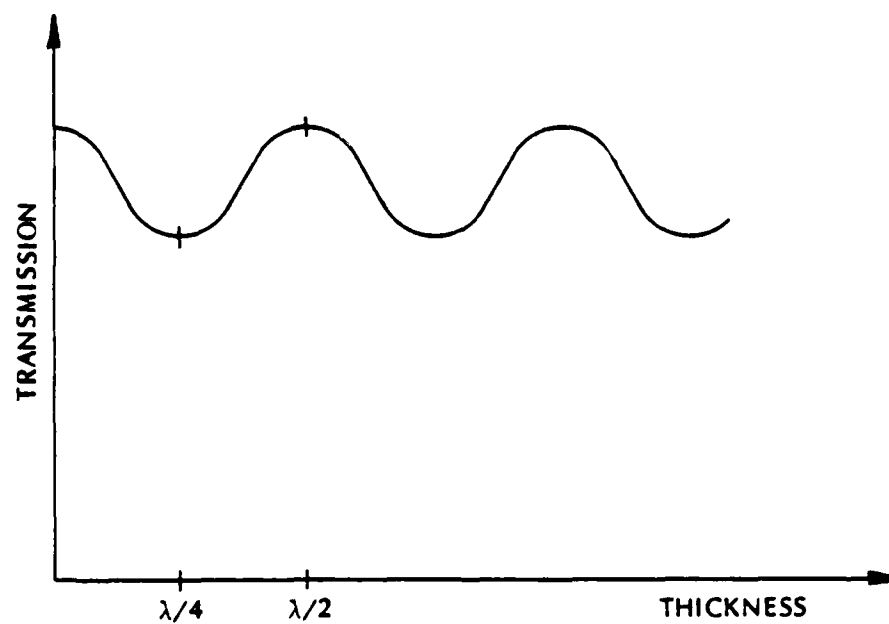


Figure 4-2. Plot of transmittance versus thickness of thin film.

The preceding discussion was in terms of a single monitoring wavelength. However, there will be multiple wavelengths for which a film layer looks like either a quarter wave or a half wave. Using Figure 4-3, it can be seen that the equation for the index of refraction of a film is

$$n_f = \frac{m \frac{\lambda}{2}}{d} ,$$

where d is the physical thickness and λ is the wavelength at which transmittance is an extremum. For a film whose index of refraction is higher than the substrate index, this will be a minimum; for a film with a lower index than the index of the substrate, it will be a maximum. A single measure of transmittance at one wavelength will not yield both thickness and index information. Either a physical measurement of thickness must be made, or multiple measurements of transmittance must be taken at various wavelengths.

To this point, the absorption is assumed to be zero and reflectance and transmittance will sum to 1. However, if absorption is present, then the sum of reflectance and transmittance will be less than 1; the difference between unity and this sum represents the absorption or film losses. This is a rough approximation since it does not take into account losses from the substrate itself. However, it gives a quantitative measure of absorption and is an improvement of the qualitative measure found by holding the film up to the light and seeing how "dark" it is.

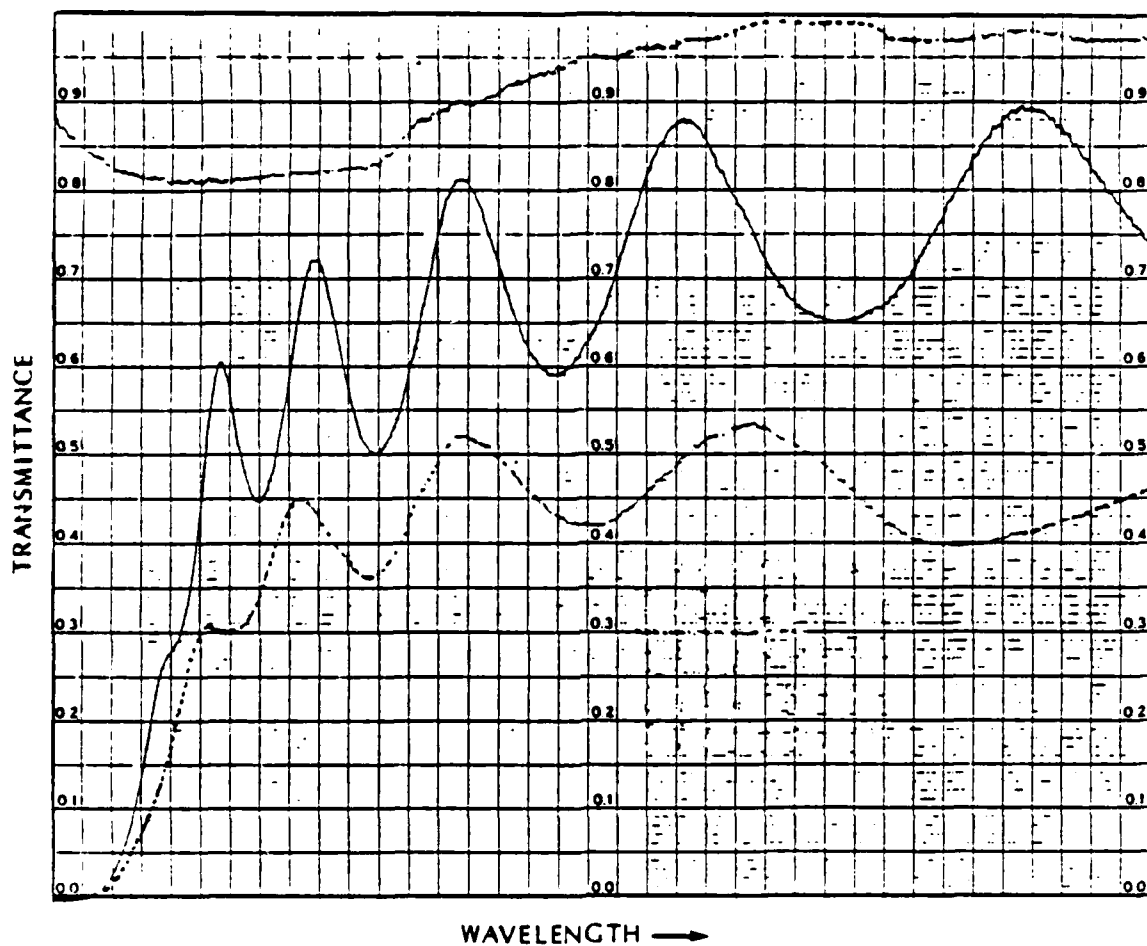


Figure 4-3. Plot of transmittance versus wavelength of thin film.

Upper curve, the reference curve, represents 100% transmittance. Lower two curves are samples.

Since there are many combinations of film thickness and film index that yield the same phase thickness for a film, a computer program can be used to sort out which values are correct. Such a computer program has been written by Dr. Bill Case of the Vought Corporation, Dallas, Texas. The inputs are transmittance, front surface reflectance, and rear surface reflectance for a single wavelength. It is assumed that the index of refraction of the substrate is known. The output gives combinations of physical thickness and optical constants, using a merit function to indicate the closest values.

Narrowband filters can also be examined using the reflectance and transmittance curves from a spectrophotometer. The simplest narrowband filter is a Fabry-Perot etalon, that is, two reflecting surfaces located a distance d apart. The phase thickness of the etalon is given by

$$\delta = 2\pi n d \frac{\cos \theta}{\lambda}$$

where n is the index of the spacer and θ is the tilt angle. For the case of equally reflecting surfaces and phase shifts upon reflection of 0° or 180° , the transmittance of the filter is given by

$$T_F = \left(\frac{T}{(1 - R)^2} \right) \left(\frac{1}{1 + F \sin^2 \delta} \right)$$

where

$$F = \frac{4R}{(1 - R)^2},$$

which produces a set of narrow transmission bands centered where the

phase is an integer number times π . The width of the pass band measured at half the peak transmittance is given by

$$\Delta\lambda_H = \frac{1 - R}{m\pi\sqrt{R}} * \lambda_p$$

where λ_p is the peak wavelength. The resolving power of the etalon is the product of the order number and the finesse, where the finesse is given by

$$\mathcal{F} = \frac{\pi\sqrt{R}}{1 - R} .$$

The all-dielectric equivalent of the etalon consists of a spacer layer whose thickness is a multiple number of half waves with a quarter-wave stack on each side to act as the reflectors. With an all-dielectric narrowband filter it is possible to achieve halfwidths in the visible of 0.5 nm with peak transmittance exceeding 50%. Since the peak transmission wavelength depends on the index of refraction of the spacer layer, narrowband filters are a sensitive measure of a shift in the index.

FECO Interferometer

Two problems were encountered with the use of the spectrophotometer during the course of this research. First is the amount of time it takes to run a trace of a narrowband filter. Because of the rapid penetration of moisture into thin films, the peak wavelength of the filter shifts during the course of a measurement. Second, a number of narrowband filters have been bombarded with ions, and the bombarded region is circular with a diameter of only a centimeter.

Because the region is so small, it is difficult to close down the height of the slits of the spectrophotometer to match the sample area.

For this research, a FECO interferometer was modified in order to quickly examine the peak wavelength of a very small region of a narrowband filter. The normal use of this type of interferometer is to examine surface topology by looking at bright fringes of equal chromatic order (FECO). For this research, a silvered mirror that would normally be present was removed and the narrowband filter was illuminated with a white-light source. The reflected spectrum from the filter was then examined using the remainder of the FECO apparatus. Since a narrowband filter is made to transmit a very narrow band of light, the reflectance spectrum will look like the output of the white-light source minus a very narrow band. In fact, if the area under examination has regions with different peak wavelengths, then the dark fringe will follow a line corresponding to the same optical thickness. As a result of this, it is possible to watch the adsorption of moisture into a filter as the progression of a "spike" growing in the dark fringe, the peak of the "spike" corresponding to the maximum change of effective index of refraction as the moisture penetrates. In addition, if there is birefringence in the narrowband filter, then a polarizer can be placed over the illuminating white light source and the peak wavelength for both transverse-electric and transverse-magnetic polarizations can be examined. It should be emphasized that although the term FECO interferometer is used in this paper for this

experimental setup, the device is not operated as a true FECO interferometer.

Adhesion, Hardness, and Durability

On a macroscopic level, the physical properties of interest for a thin film are the adhesion of the film to the substrate, the hardness of the film, and the durability of the film, in particular the resistance to moisture adsorption. A few simple tests of these properties were performed on samples that had been UV irradiated and ion bombarded. More sophisticated devices exist for the measurement of surface hardness, but none were available.

The test used to measure adhesion between a film and substrate is called the "Scotch tape" test. As the name suggests, a piece of household cellophane tape is applied to the film and then pulled off. The degree to which the film is removed from the substrate is an indication of adhesion. Every attempt was made to apply the cellophane tape with the same amount of force each time.

To measure surface hardness, an equally simple "eraser" test was performed on the samples. For this test, a pencil eraser is rubbed repeatedly over a spot on the sample to see how susceptible the film is to scratching. The amount of damage to the film is an indication of how well the film holds together. Again, every attempt was made to apply the same number of eraser strokes with the same amount of force to all samples.

A Blue M Company Model VP 100AT-1 humidity chamber was used to measure the resistance of films to moisture penetration. Samples

placed in the humidity chamber were subjected to a high humidity for more than 48 hours. The relative humidity was held constant and determined by the readings of both wet and dry bulb thermometers. A relative humidity of 97% was calculated for a dry bulb temperature of 40° C and a wet bulb reading of 39.5° C. It should be mentioned that, during the course of the research of Lee (1983), he and the author made a number of narrowband filters, some of which were irradiated with UV. Lee performed a series of calibrated exposures to different relative humidities but noted no differences for irradiated and non-irradiated samples.

X-Ray Diffraction

On the microscopic level, x-ray diffraction techniques are used to determine the crystalline structure of materials. This is true whether the material is in bulk form or in thin film form. The theory of x-ray diffraction began in 1913 when W. L. Bragg found that crystalline substances gave characteristic patterns of reflected x-radiation. For certain sharply defined wavelengths and directions of incidence, intense peaks of scattered radiation are observed. These peaks are now called Bragg peaks. The theory of x-ray diffraction is covered by many authors, among them Cullity (1956) and Ashcroft and Mermin (1976), and only a brief summary is included here. The x-ray diffraction techniques have been used before to determine the preferential orientation of evaporated thin films (Coleman, Turner, and Ullrich, 1947).

A Norelco Type 12045 x-ray diffraction unit was used to generate x-rays, and a Hewlett-Packard 7047A X-Y recorder was used to record the x-ray diffraction pattern of the samples. This device produces Cu-K γ x-rays from a copper source tube; the wavelength of this radiation is 0.154178 nm. The voltage of the source is set to 30.5 kV. A beam of x-rays is defined by a narrow 1° slit, and strikes the sample at some incident angle θ . Although the samples scatter x-rays in all directions, the detector is positioned so as to receive only those x-rays scattered at the same angle θ relative to the sample. This is an angle of 2θ relative to the incident beam. A filter within the detector is used to block secondary x-ray emissions at longer wavelengths. Figure 4-4 is a diagram of this process.

The diffraction process begins with the scattering of x-rays in all directions from each atom of the sample material. For a crystalline structure, the atoms form a regular periodic structure and the scattered x-rays interfere with each other to form a pattern. For the rays to interfere constructively, the well known Bragg condition must be met. This is given by the equation

$$m\lambda = 2d \sin\theta$$

where m is an integer, λ is the wavelength, θ is the angle of incidence, and d is the spacing between parallel planes within the lattice. The strongly scattered Bragg peak is scattered at the same angle as the incident beam. Thin films can be composed of many planes of crystalline structure, and whenever the x-rays strike a particular set of lattice planes at the Bragg angle, a strong diffraction

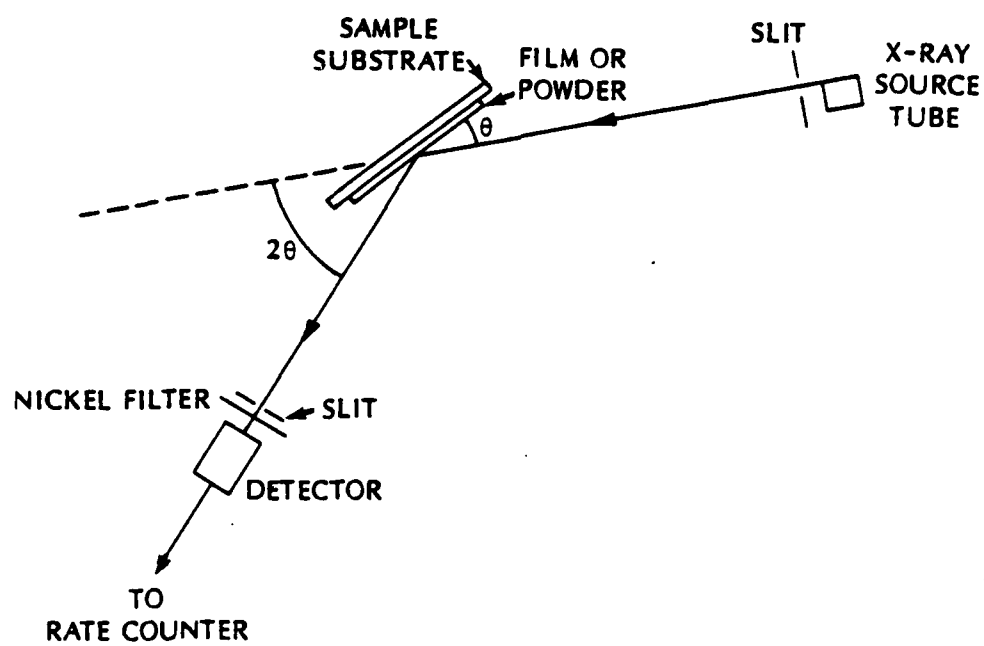


Figure 4-4. X-ray diffractometer diagram.

peak is noted. Each peak in the x-ray diffraction pattern corresponds to a particular set of lattice planes. If the x-ray wavelength is known, then the plane spacing d can be computed for a given angle θ . A table of interplanar spacing has been compiled by Fang and Bloss (1966) and is given as a function of 2θ for a variety of x-ray sources. Tables are available that list the lattice spacings and relative strengths of the diffraction peaks for a number of materials. Also given in the tables are the Miller indices, which describe how the atoms within a crystalline structure are arranged in a unit cell.

For materials that do not have a crystalline structure, i.e., amorphous materials, the x-ray diffraction profile will show no obvious peaks and will consist largely of noise. For a multilayer thin film assembly, the layers of amorphous material will not show up on the x-ray diffraction trace, but an x-ray diffraction analysis can be made of the remaining layers. Also, x-ray diffraction profiles have been run on the source materials as they exist before deposition. To prepare these samples, the source materials are first reduced to powder, then attached to a substrate by means of double-sided cellophane tape.

Transmission Electron Microscope

While x-ray diffraction data show the internal crystalline structure of films, they cannot reveal the columnar structure normally related to thin film growth. However, Pearson (1970) and Guenther and Pulker (1976) have shown that carbon replicas of thin film structures can be examined using a transmission electron

microscope. The carbon replicas are prepared following the procedure described by Pearson.

First, a diamond tip is used to score the coated side of a substrate. If firm pressure is applied to the opposite side of the substrate, it will break along a clean line that begins at the inscribed scratch. A cross-sectional view of the substrate and thin film coating is then exposed. The sample is then placed in a small vacuum chamber, with the edge exposed to two source materials. The edge is first coated with a platinum-carbon preshadow at an angle of about 70° ; it is then coated with a layer of pure carbon deposited at an angle of about 45° .

After the sample is removed from the vacuum chamber, the carbon film is divided into small sections by scoring with a diamond tip. The sample is then dipped into a 5% solution of hydrofluoric acid, and the carbon film floats free. During this procedure care must be taken to ensure that the carbon film does not break apart along the corner of the edge formed by the top of the film and its cross section. To dissolve away any traces of the original film material, the sample is left in the acid solution for a period of about 12 hours. The acid solution is then replaced by deionized water and the carbon film is broken up into the small sections previously scribed. The sections are removed by lifting them out of the deionized water with 300-mesh copper grids. These grids serve as a support structure for viewing the replicas in a transmission electron microscope.

CHAPTER 5

RESULTS

A number of narrowband filters of either 17 or 21 layers and a number of single-layer coatings were made for this research. A list of these thin film coatings and the deposition conditions under which they were made is included in Appendix D. The analysis of these samples, which includes both UV irradiation experiments and ion bombardment experiments, will be discussed by method of analysis.

X-Ray Diffraction

As a reference point, the source materials used in this research were ground into powder and examined using the x-ray diffraction apparatus. A sample of the substrate used to hold these powders was also examined to ensure that the substrate itself would not contribute to the diffraction peaks. The SiO_2 source material is itself amorphous, as shown in Figure 5-1. The ZrO_2 source material (Figure 5-2) has strong diffraction peaks, in agreement with the peaks identified by Sanders, Farabaugh, and Haller (1982). The Ti_2O_3 source material (Figure 5-3) also has strong diffraction peaks, which correctly identify it as Ti_2O_3 .

An analysis of single-layer samples indicated that SiO_2 remains in amorphous form when deposited. This is in agreement with the results of others (Browning, 1983). The application of both UV

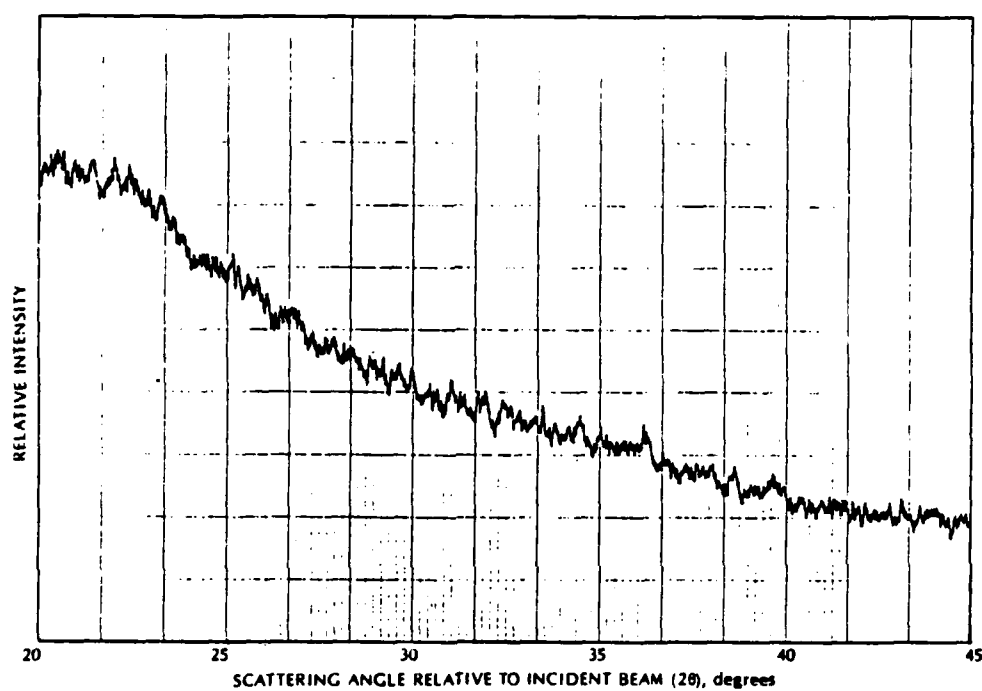


Figure 5-1. X-ray diffraction pattern of powdered SiO_2 source material.

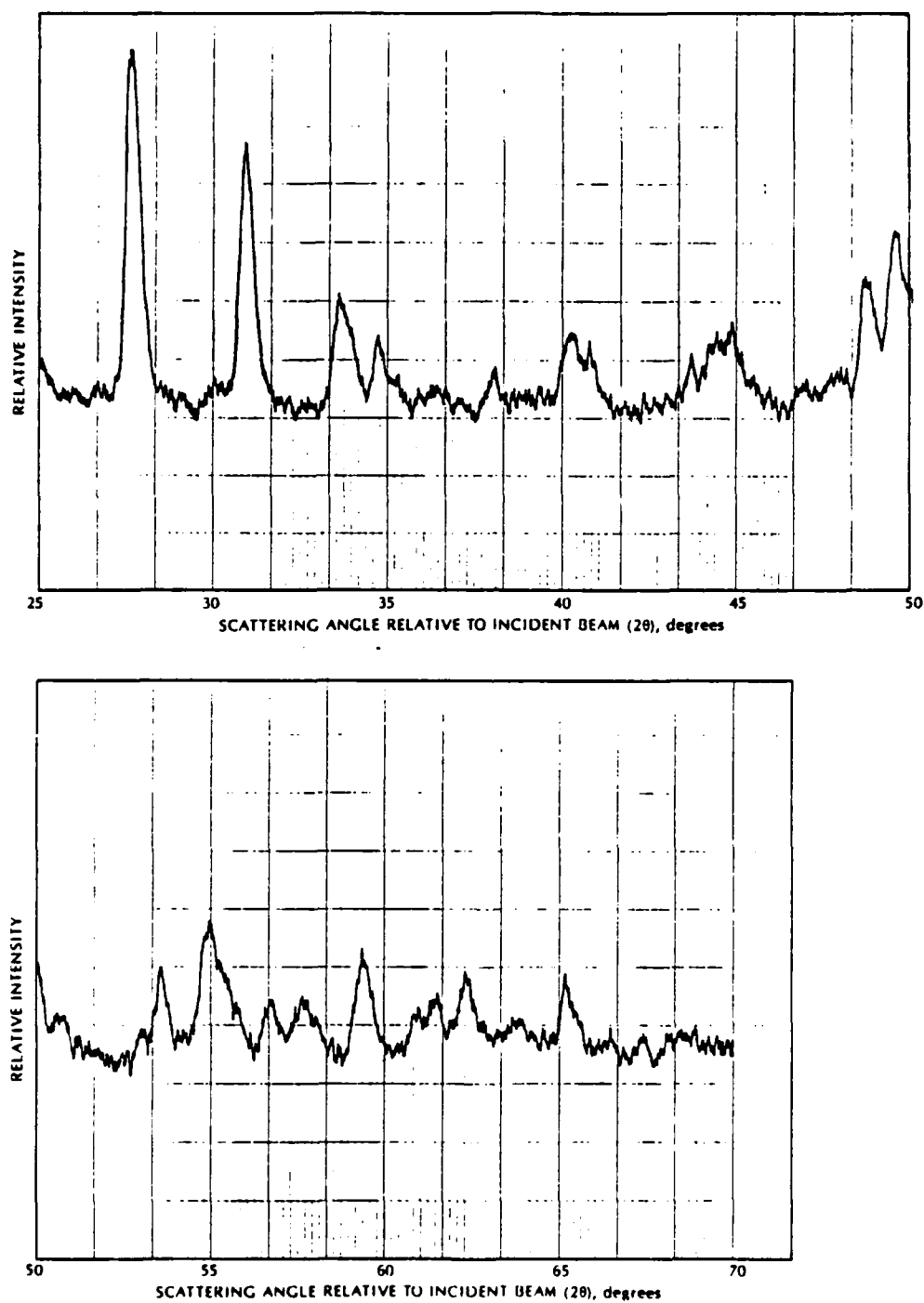


Figure 5-2. X-ray diffraction pattern of powdered ZrO_2 source material.

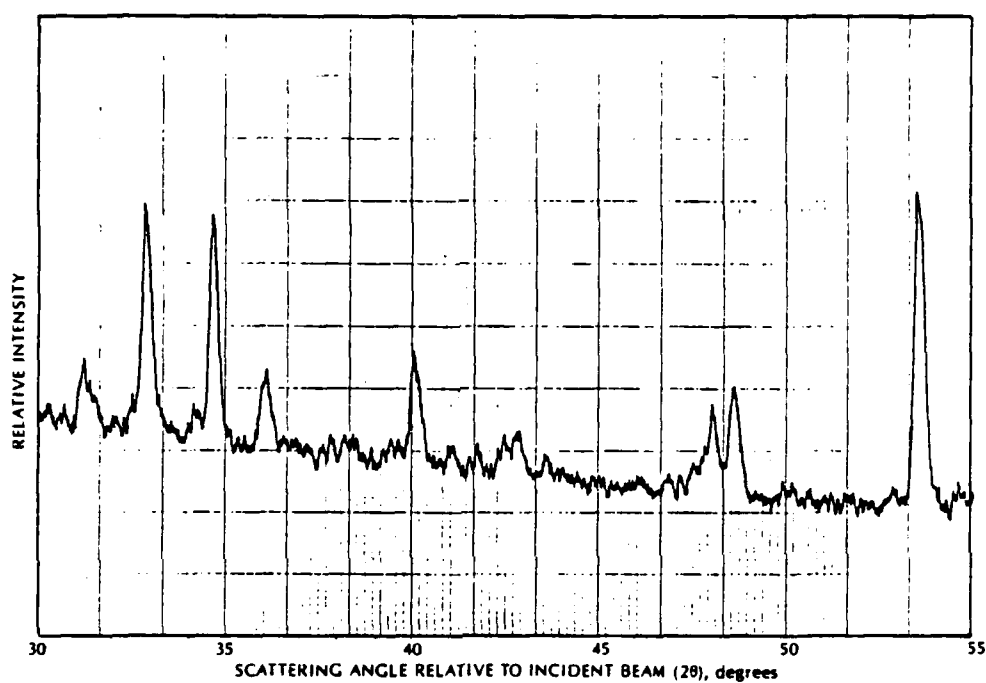


Figure 5-3. X-ray diffraction pattern of powdered Ti_2O_3 source material.

and ion bombardment does not change this amorphous structure; that is, it remains amorphous.

For single-layer samples of ZrO_2 , a sample deposited with neither UV irradiation nor ion bombardment has shown that this material has a strong tendency to remain polycrystalline; although low temperature monoclinic peaks disappear, a single tetragonal peak (111) remains at about 30° . This is in agreement with the findings of Sanders et al. (1982), who have studied the effect of substrate temperature on evaporated ZrO_2 . As shown in Figure 5-4, the addition of UV irradiation has little effect on this structure. The effect of ion bombardment (Figure 5-5) is to enhance the tetragonal peak, indicating that the ion bombardment process has increased the crystalline order of the sample.

In the case of TiO_2 films, all single-layer samples seem to indicate an amorphous structure since there are no apparent peaks in the diffraction patterns. However, another reason for the absence of diffraction peaks could be that the single-layer samples are too thin for x-ray diffraction purposes. Pawlewicz, Exarhos, and Conaway (1983) have stated that it is difficult to characterize TiO_2 films that are thinner than 150 nm or that are amorphous. They have successfully used Raman spectroscopy to characterize such films, but such equipment was not available for this research. However, since it has been found that SiO_2 films are amorphous, it is possible to use narrowband filters made of SiO_2 and TiO_2 to determine the crystalline structure of the TiO_2 .

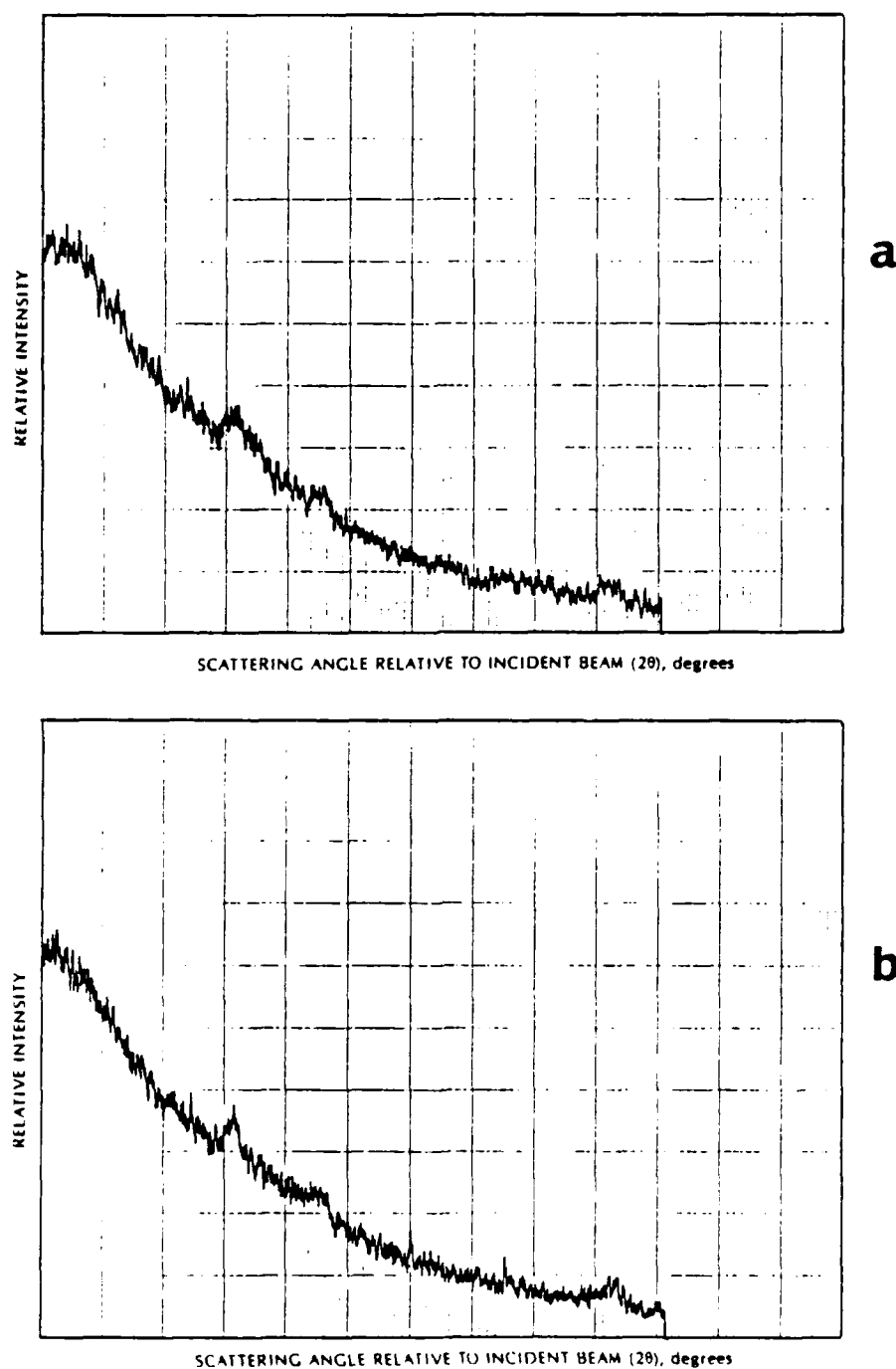


Figure 5-4. X-ray diffraction pattern of single-layer ZrO_2 sample: effect of UV irradiation.

(a) Nonirradiated. (b) UV irradiated.

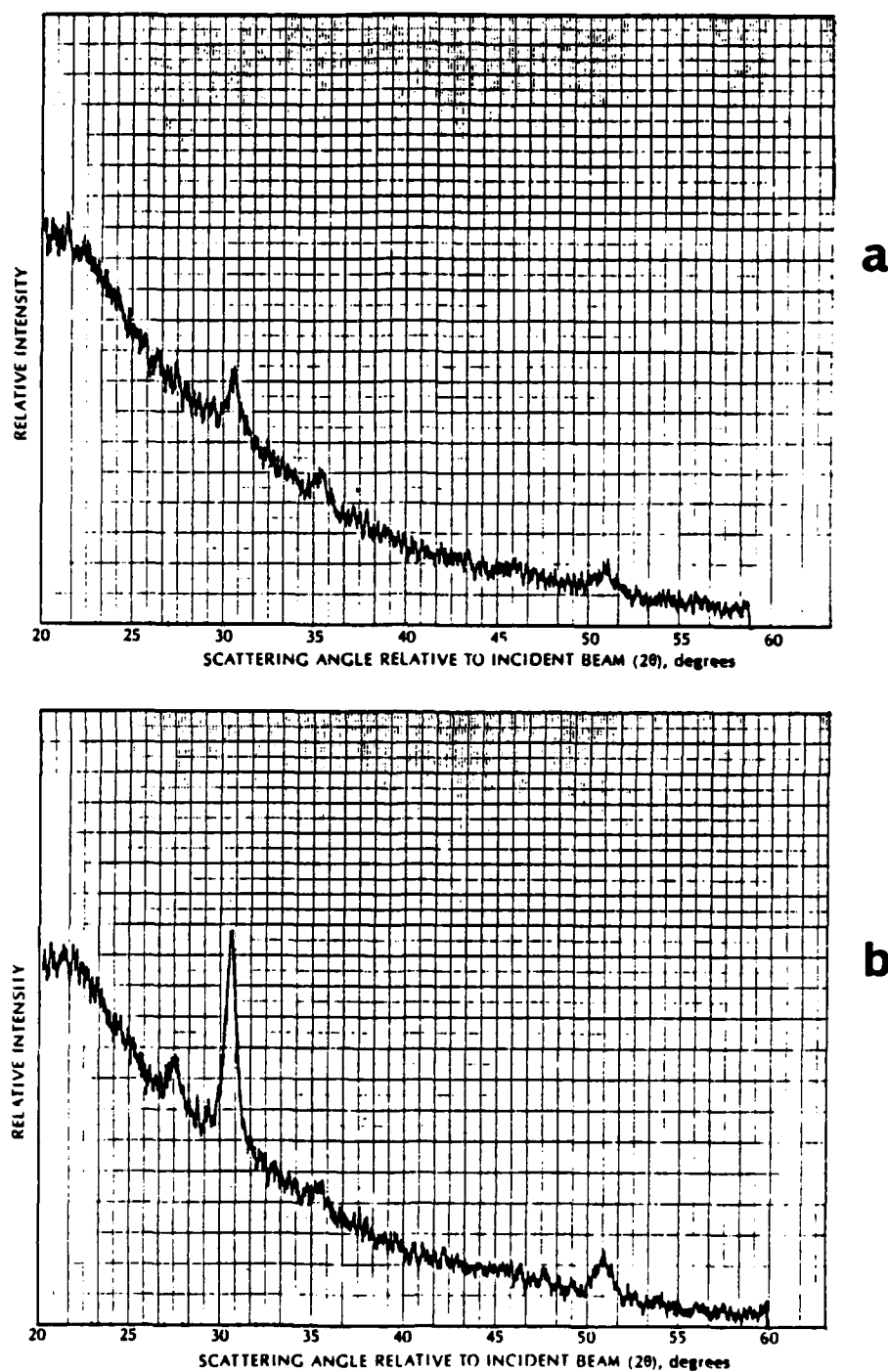


Figure 5-5. X-ray diffraction pattern of single-layer ZrO_2 sample: effect of ion bombardment.

(a) Nonbombarded. (b) Ion bombarded.

An analysis of UV irradiated $\text{SiO}_2/\text{TiO}_2$ filters reveals diffraction peaks for the region of the filter not irradiated with UV (Figure 5-6a). There is a strong diffraction peak at a 2θ value of 25.3° , with additional peaks at 38° and 48° . These diffraction peaks are characteristic of the anatase form of TiO_2 , and this is in agreement with the results of Pawlewicz et al., whose Raman techniques have also revealed the anatase form. For the region of the filter irradiated with UV, the strength of these peaks is reduced (Figure 5-6b). This result is significant because it indicates that the UV is capable of reducing the crystalline order of this material, tending toward amorphous structures.

If the samples just mentioned are rotated 90° in the x-ray diffraction sample holder, the results are as shown in Figures 5-6c and 5-6d. For the sample that was not irradiated with UV, the strength of the diffraction peaks is reduced in much the same way as it is reduced if irradiated with UV. For the sample that was irradiated with UV, the effect of rotation of the samples is to reduce the peaks even more until the sample appears almost amorphous. There are two possible explanations for this anisotropy.

The first explanation involves the columnar structure with which thin films grow as a result of limited mobility and self-shadowing. The maximum degree of shadowing is in a plane defined by the vapor incidence and the normal to the substrate. In a second plane perpendicular to the first, the shadowing is less. This is illustrated in Figure 5-7. The result is that oblique incidence

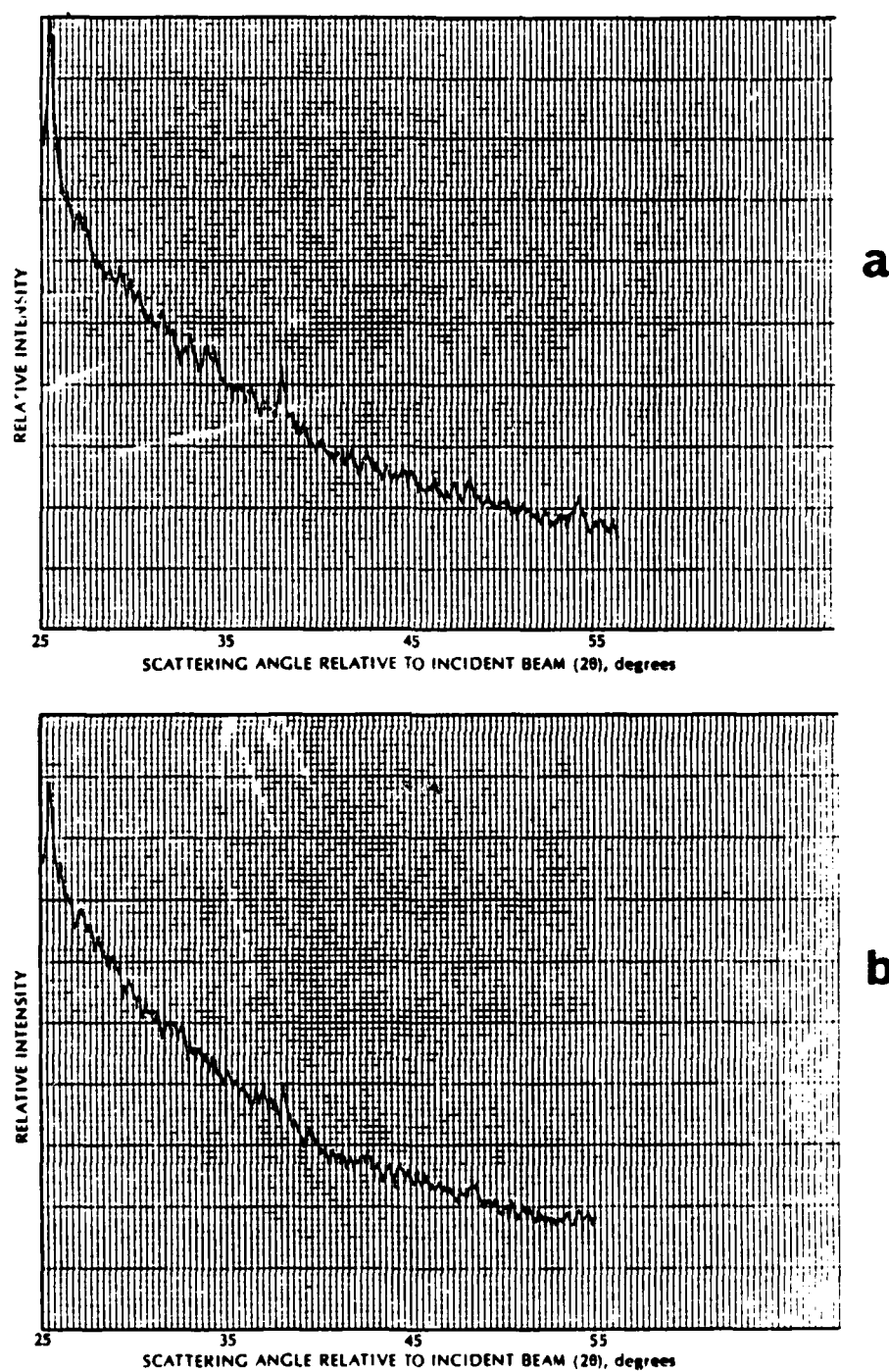


Figure 5-6. X-ray diffraction pattern of $\text{Ti}_2\text{O}_3/\text{SiO}_2$ narrowband filter: effects of UV irradiation and rotation.

(a) Nonirradiated. (b) UV irradiated.

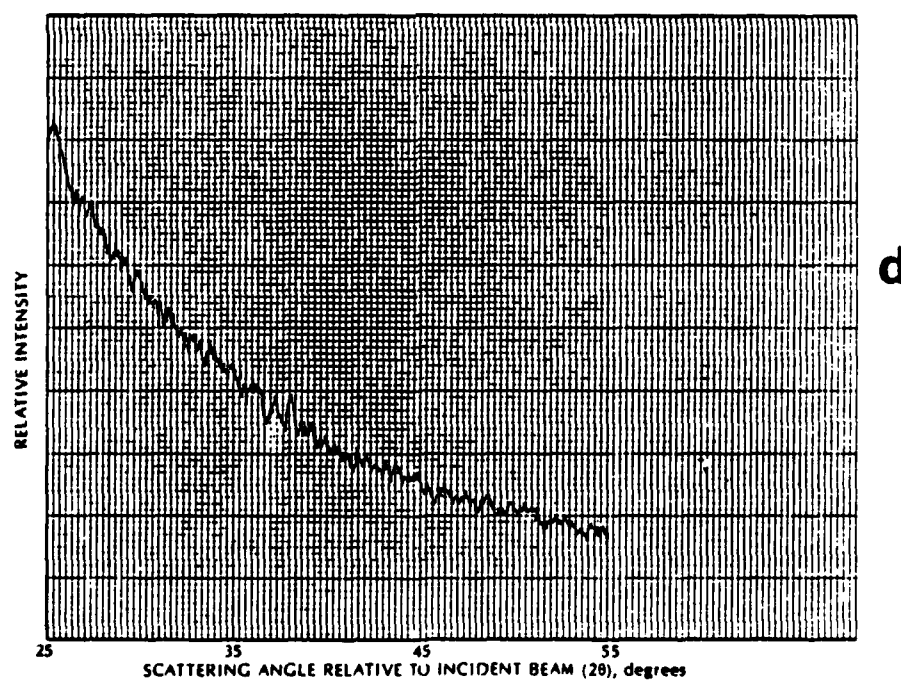
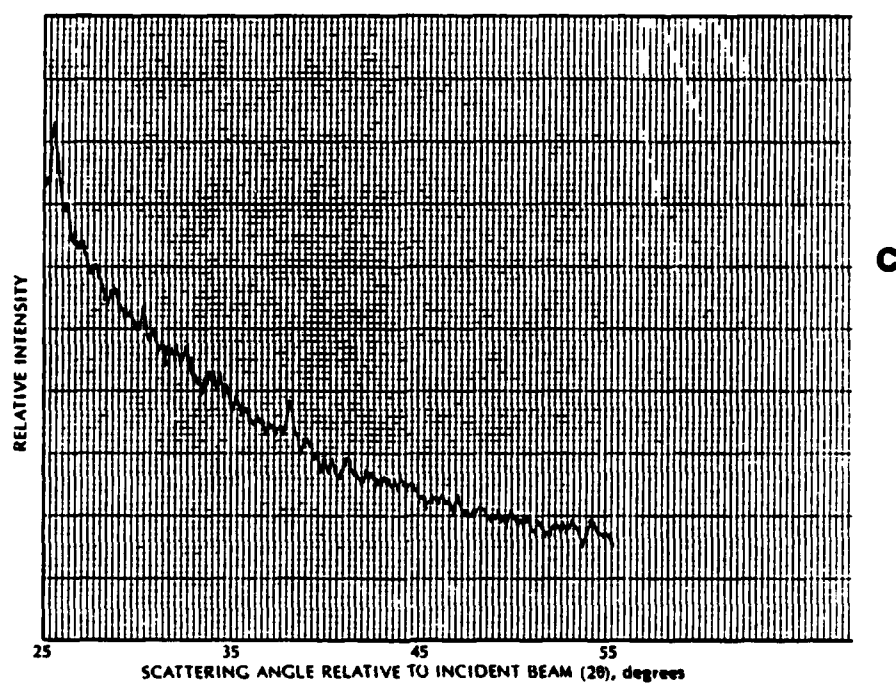


Figure 5-6--Continued

- (c) Nonirradiated, rotated 90°.
- (d) UV irradiated, rotated 90°.

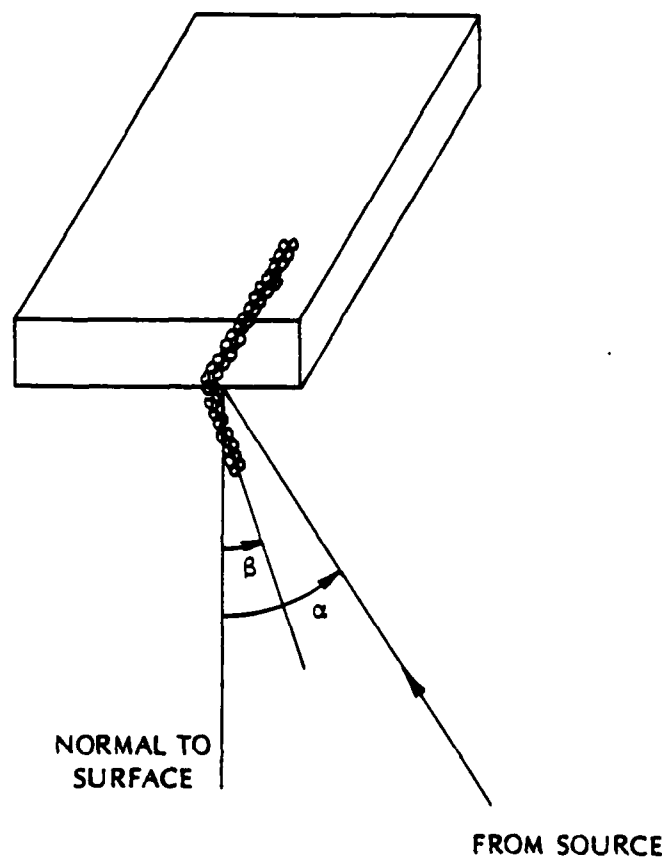


Figure 5-7. Anisotropy of growing films.

deposition often results in a change in column shape. If a cross section is taken of a column that has been normally deposited, it appears circular. However, a cross section of films that are deposited at oblique incidence yields columns that are elongated in the direction perpendicular to the vapor incidence and the normal to the substrate. This result has been verified by micrographs made by Leamy et al. (1980), who have noted that the resulting voids are also elliptical.

For x-rays striking the film/substrate assembly in a plane along the longest axis of the ellipse, the crystalline order extends over a greater length, and hence there is a stronger diffraction peak. When the sample is rotated 90° , the x-rays strike the sample along the shorter axis of the ellipse. For the UV irradiated portion of the sample, the crystalline order is very low and the corresponding diffraction peaks are small. When the sample is rotated 90° , the crystalline order along this direction is so low that diffraction peaks are difficult to detect.

A second possible explanation depends upon the nature of Bragg reflection. Although it has been stated that Bragg reflection occurs for planes parallel to the substrate, the actual reflection occurs for planes that are parallel or almost parallel to the substrate. This is one reason that x-ray diffraction peaks are lines that have some spread to them. In fact, one method of obtaining better diffraction peaks is to "rock" the sample while it is being examined with x-rays. Such an attachment was not available for the x-ray diffractometer

used for this research. Thus, there is a possibility that the planes responsible for the diffraction peaks are nearly parallel to the substrate and produce strong peaks in one direction and weaker peaks in the other direction.

For ion bombarded samples of $\text{SiO}_2/\text{TiO}_2$ filters, no diffraction peaks were seen (Figure 5-8). This was true for any region of the filter examined, and appears to indicate that even small amounts of ion bombardment are capable of reducing the crystalline order of TiO_2 . Pawlewicz (1983) has found that TiO_2 is amorphous when deposited by RF sputtering on substrates that have a bias voltage of just 300 V, indicating that relatively small increases in mobility cause this material to become amorphous when deposited.

Spectrophotometer Analysis for Narrowband Filters

As indicated in Chapter 4, narrowband filters are a sensitive diagnostic tool since the peak wavelength of the filter is very sensitive to changes in refractive index. Additional information, such as the amount of absorption in the film, can also be found in the spectrophotometer traces of these filters. The fact that this is indeed a sensitive tool can be seen by examining Figures 5-9, 5-10, and 5-11.

Each of these traces is of a $\text{ZrO}_2/\text{SiO}_2$ filter deposited with the interior UV source irradiating part of the filter. Looking at the peak of the filter for both the irradiated and nonirradiated regions in Figure 5-9, it can be seen that the absorption is the same for both regions. The shift of peak wavelength to the right indicates that the spacer layer is either thicker or has a higher index of refraction. In

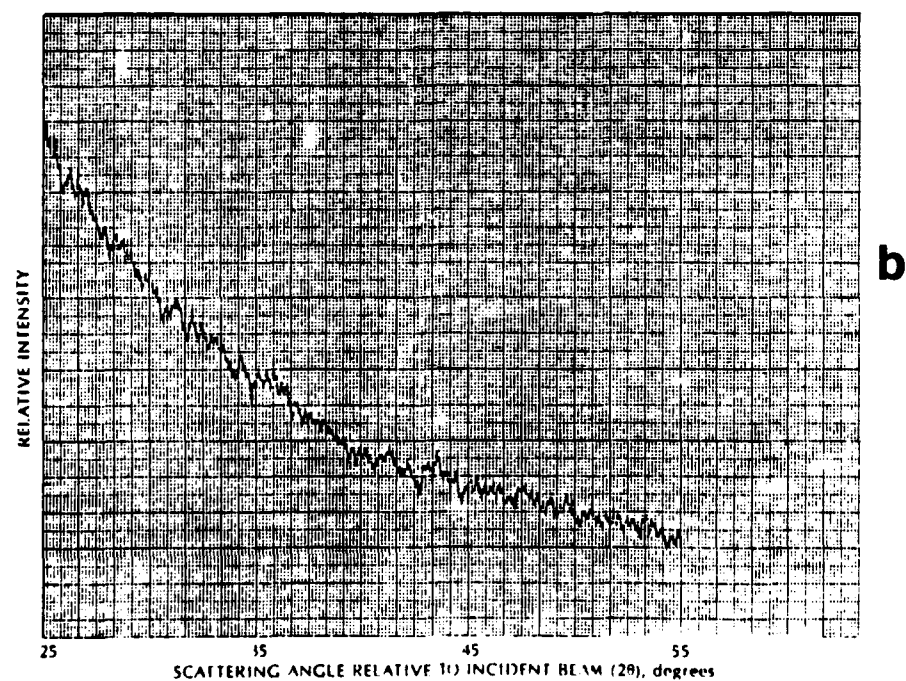
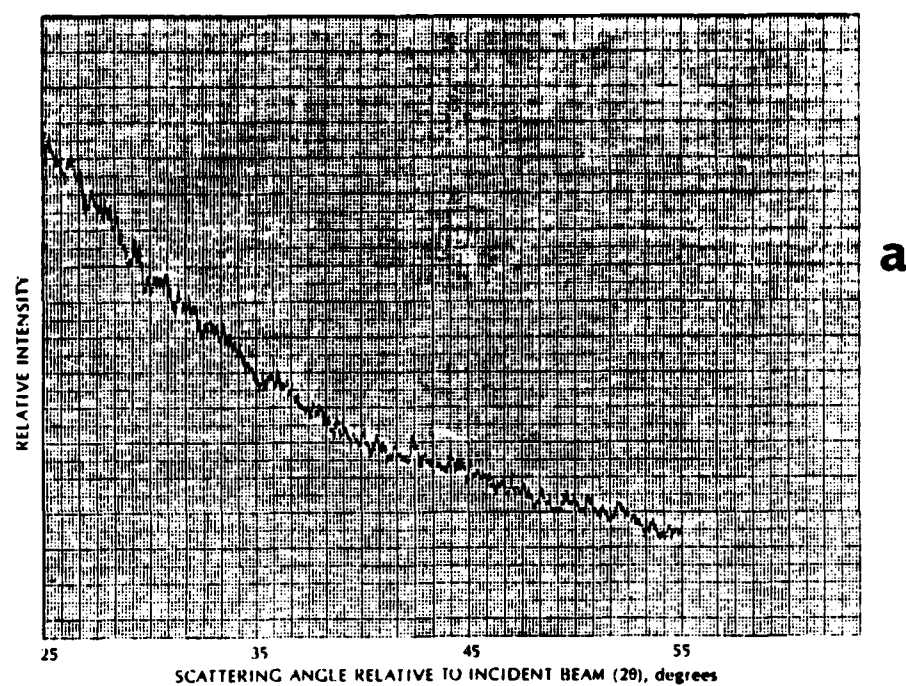


Figure 5-8. X-ray diffraction pattern of $\text{Ti}_2\text{O}_3/\text{SiO}_2$ narrowband filter: effect of ion bombardment.

(a) Nonbombarded. (b) Ion bombarded.

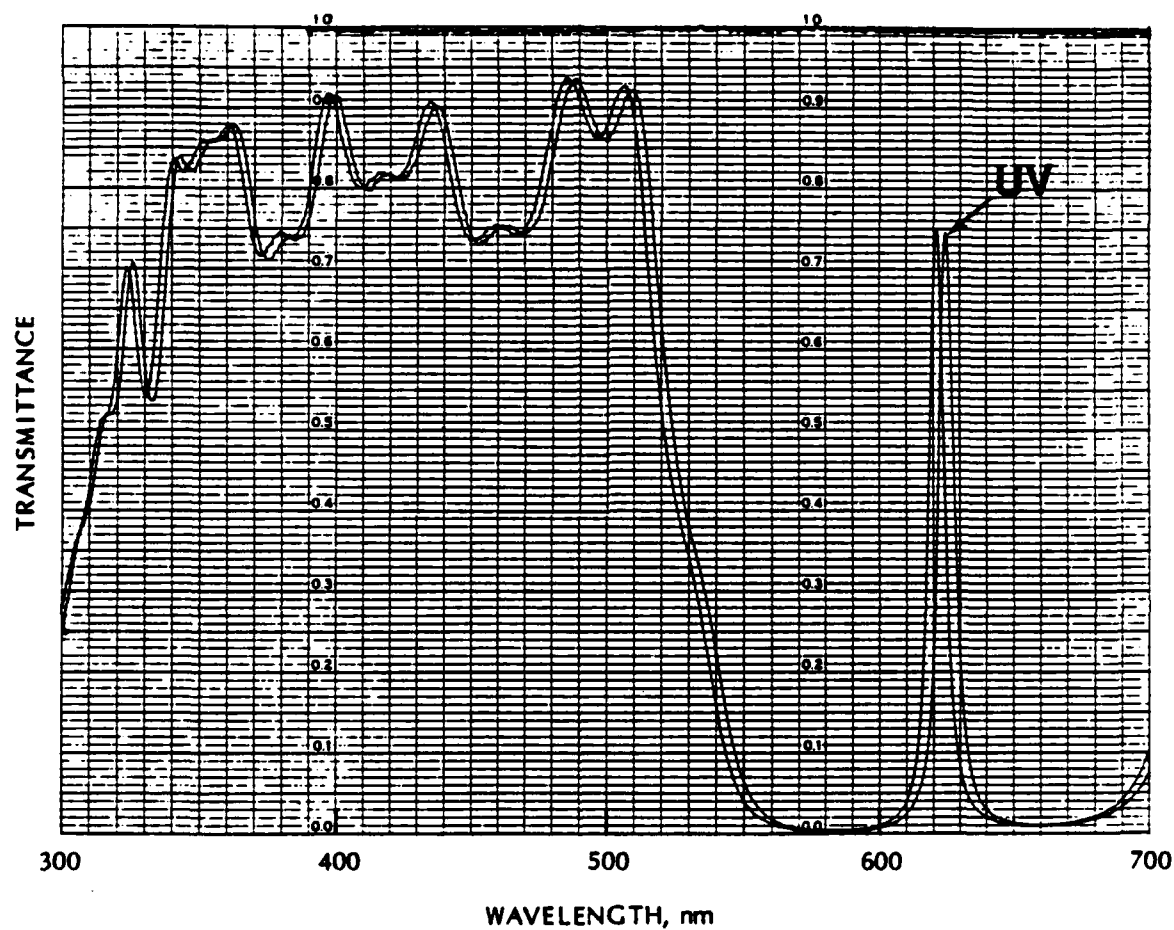


Figure 5-9. Spectrophotometer trace, sample 105.

Upper curve, the reference curve, represents 100% transmittance. The two lower curves represent different locations on the sample, one UV-irradiated (UV) and the other nonirradiated.

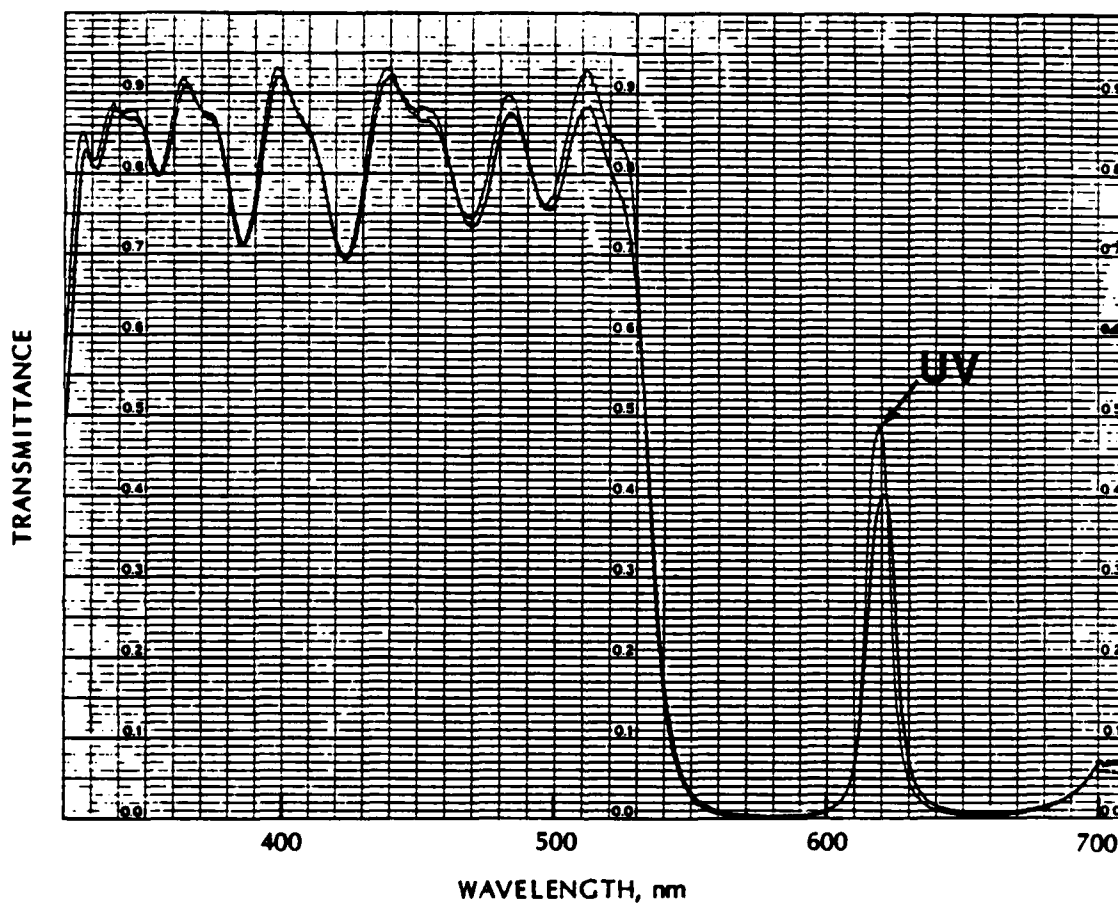


Figure 5-10. Spectrophotometer trace, sample 106.

The two curves represent different locations on the sample, one UV-irradiated (UV) and the other nonirradiated.

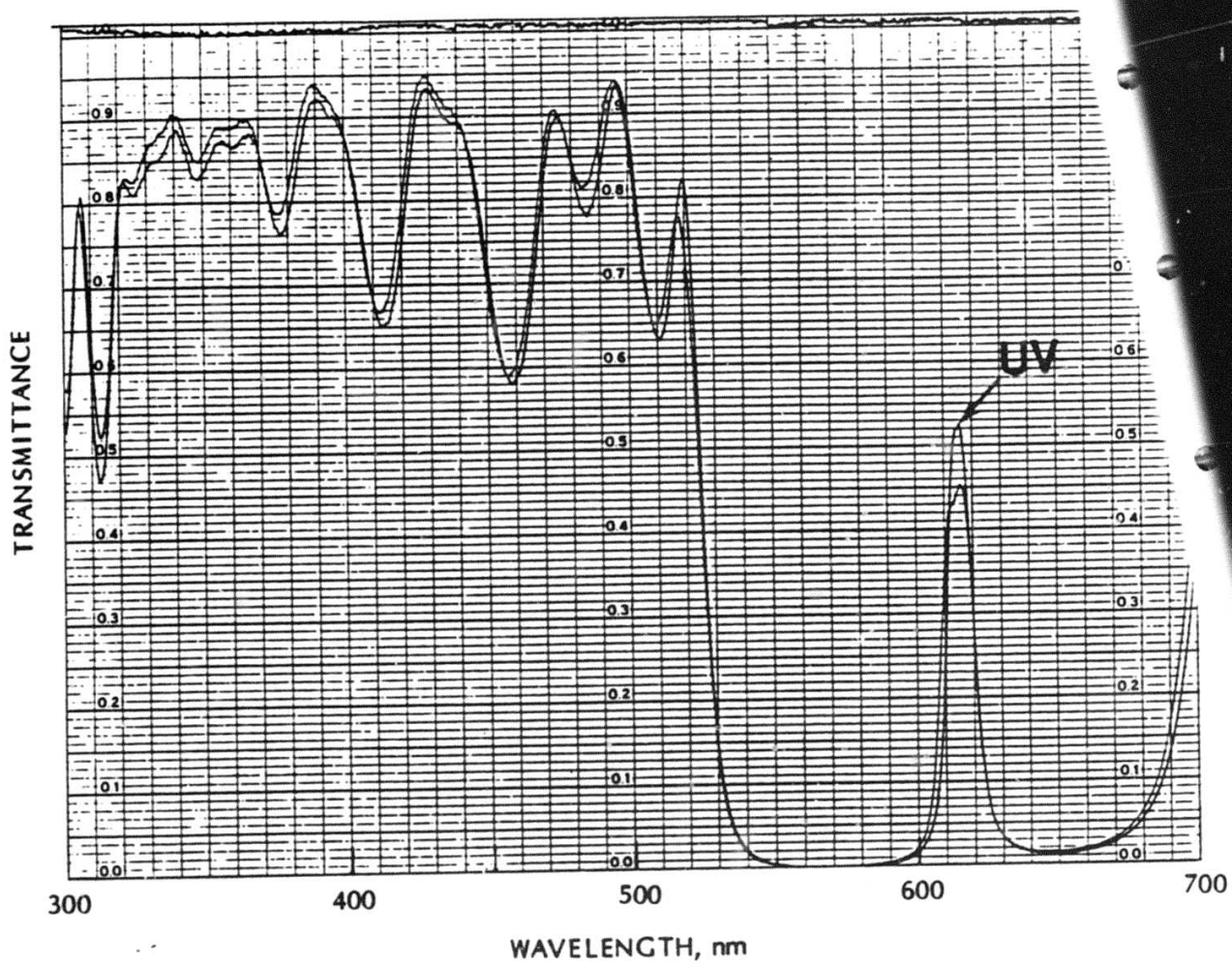


Figure 5-11. Spectrophotometer trace, sample 108.

Upper curve, the reference curve, represents 100% transmittance. The two lower curves represent different locations on the sample, one UV-irradiated (UV) and the other nonirradiated.

both Figures 5-10 and 5-11, the nonirradiated region shows more absorption. Thus in two out of three cases, the UV irradiation improves the transmittance of the peak wavelength, and in no case is it worse.

The effect of UV irradiation upon the absorption within $\text{TiO}_2/\text{SiO}_2$ filters is not clear. Although some samples indicated an improvement in absorption, others indicated increased absorption. However, it has been noted that there is an improvement in stability of the UV irradiated portions of these filters. Figure 5-12 shows the effect of baking a $\text{TiO}_2/\text{SiO}_2$ filter at 125°C for more than 72 hours, then watching the behavior of the filter as moisture repenetrates. The UV irradiated portion of the filter is stable in time; the portion that had not been irradiated during deposition showed a marked shift in optical performance.

The effect of ion bombardment on both $\text{ZrO}_2/\text{SiO}_2$ and $\text{TiO}_2/\text{SiO}_2$ filters is an increase in the absorption of the filters. This is due to the preferential removal of oxygen in the films as they are being deposited, and a subsequent decrease in the oxidation of the film material. The result is an increase in absorption. These results have been for argon ion bombardment. In an attempt to improve the oxidation of the films, oxygen ions were used. The results, however, still show that there is more absorption for the ion bombarded regions than for the regions not bombarded with oxygen ions.

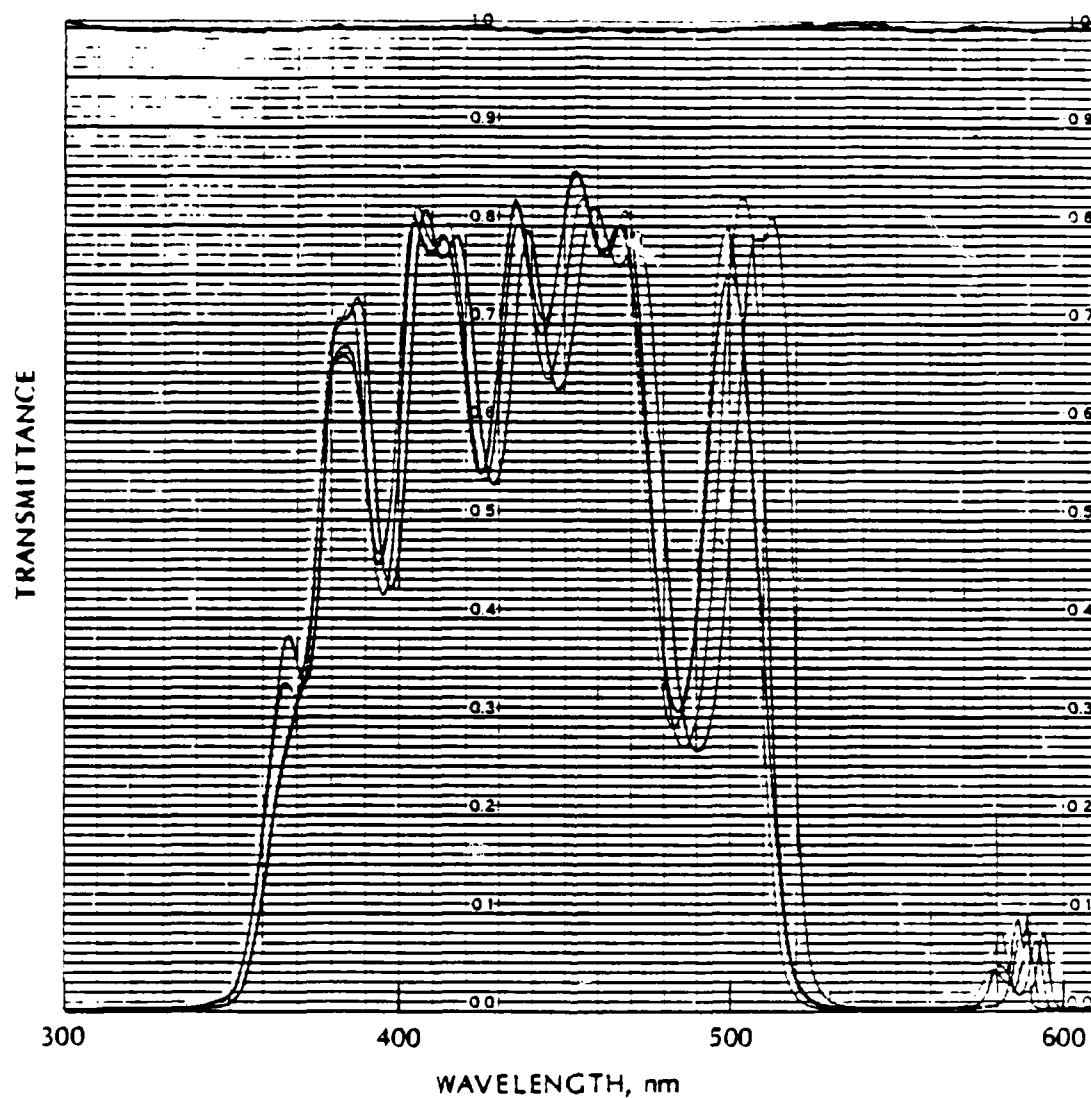


Figure 5-12. Spectrophotometer trace, baked sample.

Upper curve, the reference curve, represents 100% transmittance. The four lower curves are measurements on the sample.

Optical Analysis of Single-Layer Samples

The spectrophotometer traces of single-layer samples of both TiO_2 and ZrO_2 are in agreement with the results previously discussed. However, to this point no information concerning indices of refraction has been discussed. Additional information on single-layer films is available from the optical monitor traces that had been made during the deposition of the single layers. As discussed in Chapter 4, if no absorption is present in a thin film, then the index of refraction of a film/substrate assembly can be determined if the index of the film and the index of the substrate are known. The reflection from the assembly and hence the transmission can then be calculated.

It is also possible to use this procedure in reverse order. That is, if there is no absorption, then the reflection from the film surface can be determined by subtracting the transmission from unity, taking into account the reflection from the back surface of the substrate. Knowing the reflection enables one to calculate the effective index of the assembly, and if the index of the substrate is known, then the index of the film can be calculated.

If absorption is present in the films, the calculations become more complex. Although attempts have been made to calculate optical constants using computer routines, they have not been useful for analyzing the data obtained from spectrophotometer traces of the single-layer samples made for this research. The largest problem is that the reflectivity from both the front and rear surfaces as well as transmission through the sample must be known for a given wavelength.

Because of the construction of the Cary spectrophotometer, it is difficult to obtain these data for the same spot on the film. After transmission values are recorded, the sample must be removed from a holder and placed in a separate holder for reflection measurements. In addition, the balance of the system must be adjusted, and it is difficult to achieve a 100% line for reflection.

An approximation method has been used to obtain optical constants (Manifacier, Gasiot, and Fillard, 1976). Figure 5-13 shows a typical transmission spectrum for a single thin film. It can be seen that there are two transmission limits that enclose the peaks. Although this curve is a plot of transmission versus wavelength, it could also be a plot of transmission versus wavelength divided by thickness of the film. Using the values of T_{\max} and T_{\min} for a given thickness, t , the absorption coefficient can be calculated using the equation

$$\alpha = \frac{C_1[1 - (T_{\max}/T_{\min})^{1/2}]}{C_2[1 + (T_{\max}/T_{\min})^{1/2}]}$$

where

$$C_1 = (n + n_0)(n_1 + n)$$

$$C_2 = (n - n_0)(n_1 - n)$$

where n is the index of the film, n_0 is the index of the incident medium, and n_1 is the index of the substrate. The absorption coefficient, α , is related to the imaginary part of the index of refraction, k , by the equation

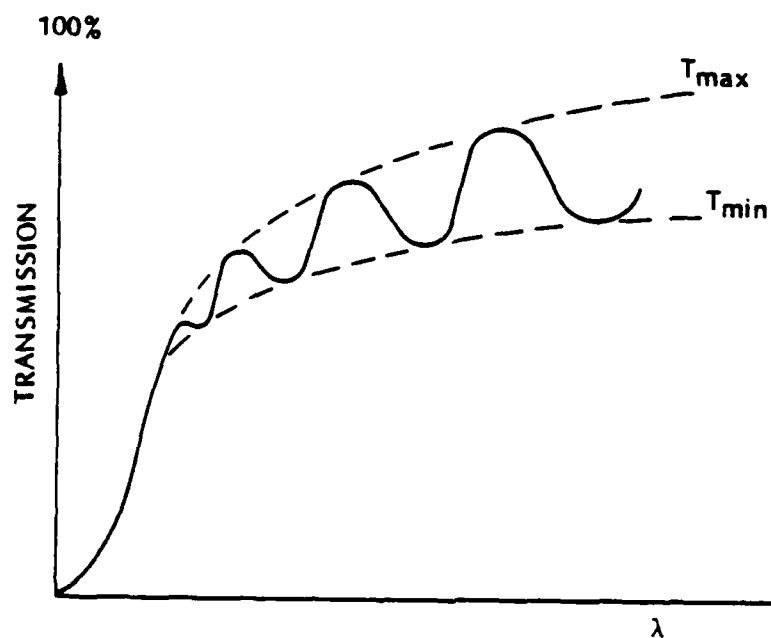


Figure 5-13. Transmission spectrum of single layer film.

$$\alpha = \exp \left(- \frac{4\pi k t}{\lambda} \right) .$$

The real part of the index of refraction is given by

$$n = \sqrt{N + (N^2 - n_0^2 n_1^2)^{1/2}}$$

where

$$N = \frac{n_0^2 + n_1^2}{2} + 2n_0 n_1 \left(\frac{T_{\max} - T_{\min}}{T_{\max} T_{\min}} \right) .$$

Using these equations, optical constants were calculated for the single-layer samples. The results are shown in Table 5-1. Two samples were prepared with neither UV irradiation nor ion bombardment. The index of refraction for ZrO_2 was found to be 1.905; a table of materials lists the index as 2.05. For TiO_2 the calculation yields 2.193; the table gives 2.2. The effect of UV irradiation is to increase the index of refraction of the ZrO_2 to 1.955. The TiO_2 sample showed a slightly lower index but had much lower absorption. For films that have high absorption, a broadening effect often causes the index to increase, and this is the case for the TiO_2 sample that had not been UV irradiated or ion bombarded.

The effect of ion bombardment was always to increase the index of refraction. For ZrO_2 , taking into account the effect of absorption, the index increased with increasing ion powers; the highest index was 2.068. Martin et al. (1983) measured an index of 2.07 with relatively the same amount of absorption. For TiO_2 , the highest index was 2.35, but for this sample the absorption was rather high owing to argon ion bombardment. For oxygen ion bombardment, the absorption was improved by about an order of magnitude and the index was 2.22.

Table 5-1. Calculated Optical Constants for Single-Layer Samples

Thick- ness:		$\lambda/4$	$\lambda/2$	$3\lambda/4$	λ	$5\lambda/4$	$3\lambda/2$	$7\lambda/4$
Sample								
094	n	2.049	1.988	1.927	1.928	1.921	1.911	1.911
	k	0	0	0	1.6×10^{-4}	6.8×10^{-4}	1.0×10^{-3}	0.9×10^{-3}
096	n	2.215	2.138	2.069	2.044	2.014	1.985	1.960
	k	8.4×10^{-3}	8.3×10^{-3}	7.1×10^{-3}	6.5×10^{-3}	6.5×10^{-3}	6.4×10^{-3}	6.2×10^{-3}
097	n	2.221	2.200	2.159	2.133	2.115	2.090	2.068
	k	2.4×10^{-3}	2.3×10^{-3}	4.7×10^{-3}	5.8×10^{-3}	5.8×10^{-3}	5.8×10^{-3}	5.6×10^{-3}
101	n	2.226	2.130	1.961	2.043	2.046	2.030	2.013
	k	6.7×10^{-3}	6.6×10^{-3}	1.3×10^{-2}	5.7×10^{-3}	5.7×10^{-3}	5.7×10^{-3}	5.7×10^{-3}
104	n	2.455	2.416	2.425	2.377	2.398	2.350	2.348
	k	0.0685	0.0726	0.0690	0.0682	0.0645	0.0618	0.0588
107	n	2.014	1.977	1.957	1.958	1.956	1.956	1.955
	k	6.7×10^{-3}	6.7×10^{-3}	4.8×10^{-3}	4.0×10^{-3}	3.5×10^{-3}	3.17×10^{-3}	2.95×10^{-3}
110	n	2.158	2.120	2.127	2.111	2.101	2.110	2.117
	k	0.0201	0.0203	0.0153	0.0128	0.0108	0.0096	0.0088
112	n	2.317	2.279	2.273	2.259	2.244	2.234	2.217
	k	0.0212	0.0214	0.0172	0.0151	0.0139	0.0132	0.0129
113	n	2.208	2.183	2.209	2.189	2.193	2.188	2.193
	k	0.0312	0.0319	0.0267	0.0240	0.0208	0.0186	0.0167
114	n	1.941	1.919	1.913	1.915	1.913	1.909	1.905
	k	6.26×10^{-3}	6.24×10^{-3}	4.68×10^{-3}	3.90×10^{-3}	3.64×10^{-3}	3.45×10^{-3}	3.28×10^{-3}

Note: Each index given is mean index for entire film up to specified thickness.

Optical Birefringence

Early narrowband filters made for this research showed a double peak (Figure 5-14) rather than the single peak transmission line expected for the filter. Through the use of a matched pair of polarizers that could be placed in the Cary spectrophotometer and rotated, it was determined that the filters display birefringence. That is, there are two indices of refraction depending on whether the transverse-electric (TE) or transverse-magnetic (TM) field is analyzed. The amount of birefringence can be determined by measuring the maximum shift in peak wavelength while rotating a polarizer.

The origin of the birefringence is due to the columnar nature of the deposited films, and the principal axes of the dielectric tensor are along the columnar direction (n_3) and normal to the columns both in the plane of incidence of the vapor (n_1) and normal to this plane (n_2). For films deposited normal to the substrate, the birefringence should be uniaxial with an optical axis normal to the substrate surface. It is therefore difficult to detect this birefringence by the use of normal incidence measurements. For films deposited at an oblique angle of incidence, the birefringence should be biaxial with the optic axes in the plane of incidence of the vapor during the film growth.

Several measurements were made to determine the amount of birefringence. The only measurements made while the films were still under vacuum were done by removing the monitoring filter from the optical monitoring system of the Balzers 760 and inserting a mirror.

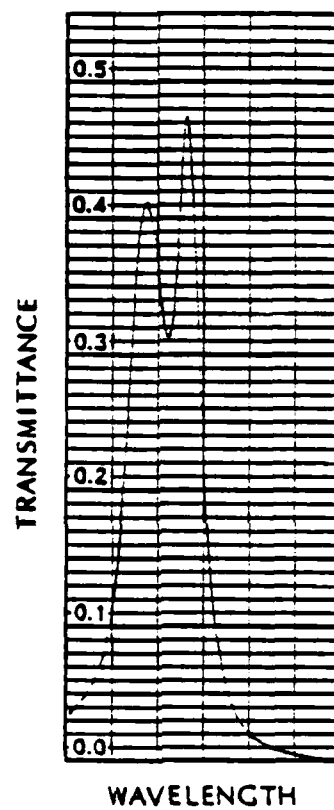


Figure 5-14. Double peak in narrowband filter.

The light from the optical source that travels through the completed narrowband filter within the vacuum chamber and onto this mirror was then put through a small monochromator. By rotating a polarizer in the output of the monochromator and watching with the unaided eye, the extremums of peak wavelength were recorded. Because of the rough method with which this was done, a number of measurements were made by two observers, and the results averaged. No statistical analysis was made on these observations. Two narrowband filters made of TiO_2 and SiO_2 were analyzed in this way. Before air was admitted to the vacuum chamber, the separation of the transmission peaks was 45 Å. After air was admitted to the chamber, the separation was 25 Å. This measurement is in agreement with the theory of columnar growth discussed thus far. That is, the voids are originally empty and the index of refraction of the material/void combination is a maximum. When moisture penetrates into these voids, the effective index is reduced.

Another means of measuring the amount of birefringence is with the modified FECO apparatus discussed in the previous chapter. Using this method, the separation of peak wavelengths for TE and TM modes was also found to be 22%. In fact, even this reduction is consistent with the model since moisture has had a chance to further penetrate the sample. Additional measurements made with the FECO have shown that there is greater birefringence in the irradiated than in the nonirradiated regions of the filter. If a narrowband filter is heated in an oven at 125° C for more than 48 hours, the initial

birefringence of the irradiated region is 35 Å versus 20 Å for the nonirradiated regions. For samples that had been ion bombarded, the results were a bit ambiguous. The penetration of moisture with time changes the amount of birefringence with time. Also, the peak wavelength of a filter in a bombarded region is different from the peak wavelength in regions that had been only mildly bombarded. It is not clear if a smaller separation of peak wavelengths for TE and TM modes in a bombarded region can be compared with a slightly larger separation of peak wavelengths in a nonbombarded region that has a higher peak transmission wavelength. Measurements must be taken in vacuum to interpret these results.

Transmission Electron Microscope

A limited number of samples were examined using the carbon replication procedure discussed in Chapter 4. The purpose of using the transmission electron microscope (TEM) is to see if either UV irradiation or ion bombardment changes the columnar structure of films. For a deposition angle of 27.1° , the tangent law predicts that the angle measured between the substrate and the columns of a film should be 14.4° , as illustrated in Figure 5-15. Although several of the TEM photographs clearly show the multilayers of a thin film assembly, it is difficult to see the exact columnar shape. In Figure 5-16, two separate magnifications show a $\text{ZrO}_2/\text{SiO}_2$ narrowband filter that has been neither irradiated with UV nor bombarded with ions. The broad plateaus seen in the photographs are the amorphous SiO_2 layers,

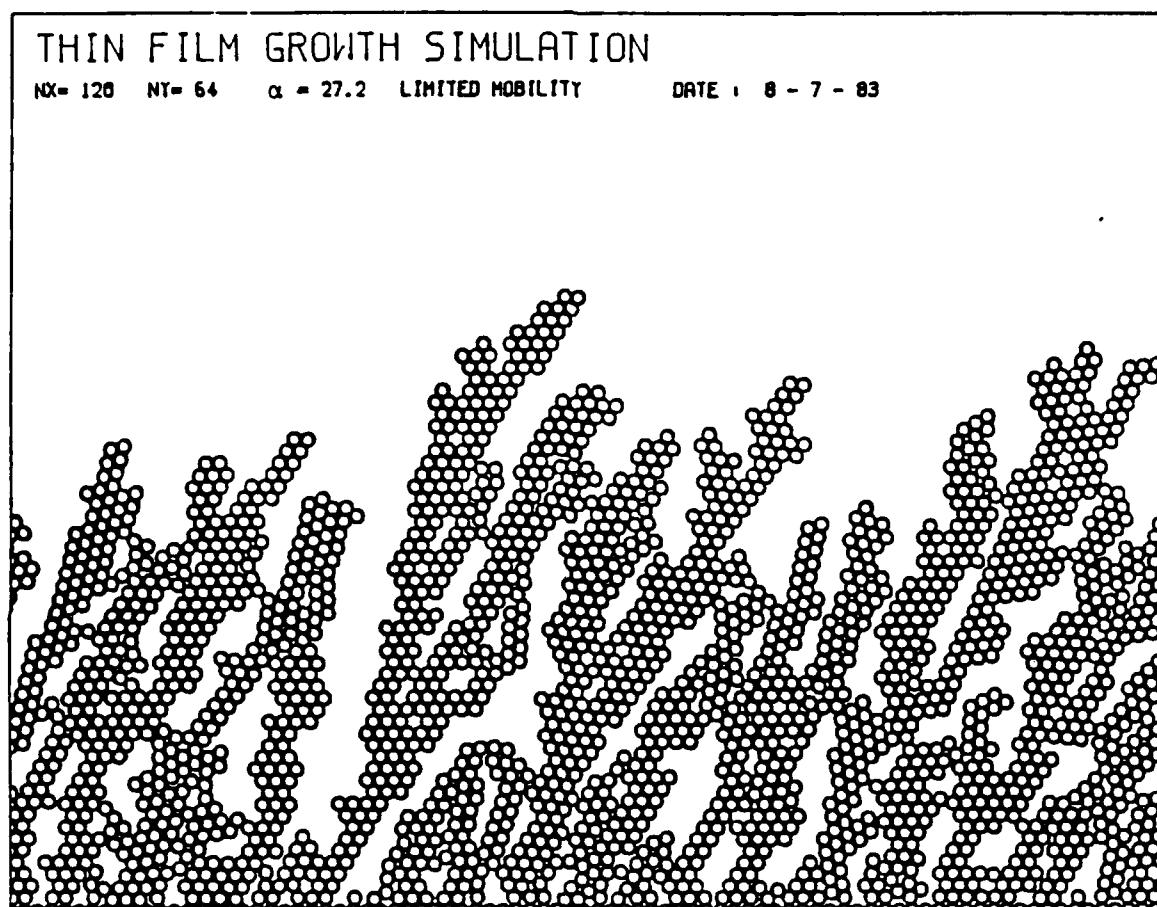
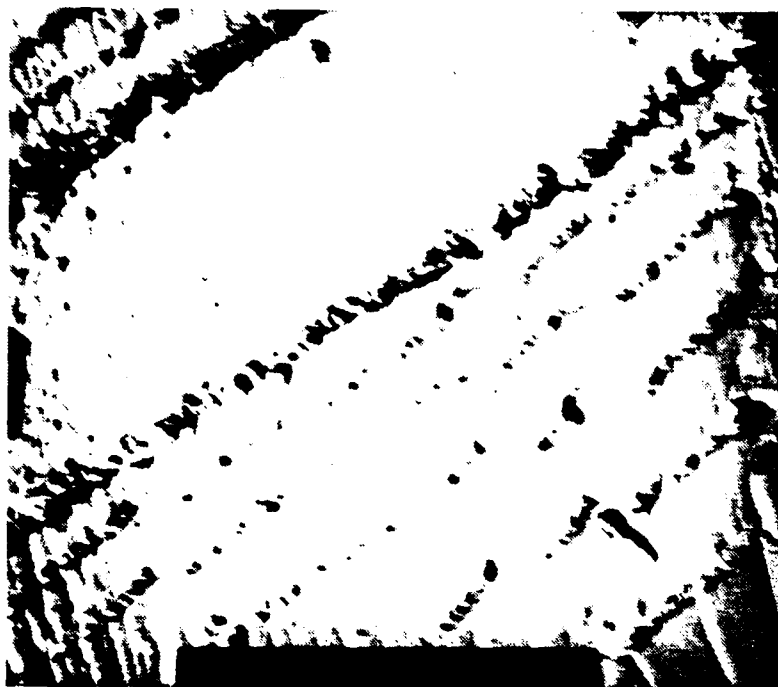


Figure 5-15. Thin film growth simulation for deposition angle of 27.1° .



a



b

Figure 5-16. TEM photographs of $\text{ZrO}_2/\text{SiO}_2$ narrowband filter.

- (a) Microscope magnification factor 15×10^3
(b) Microscope magnification factor 48×10^3

which often break in this characteristic pattern. Figure 5-17 shows a $\text{ZrO}_2/\text{SiO}_2$ narrowband filter that has been ion bombarded. Figure 5-18 shows a $\text{ZrO}_2/\text{SiO}_2$ narrowband filter that has been irradiated with UV. Note that in this case the entire cross section of the filter can be seen without the presence of plateaus.

Adhesion, Hardness, and Durability

One purpose of this research was to investigate not only improvements of the optical characteristics of thin films, but their physical characteristics as well. On the macroscopic level, these physical characteristics are adhesion, hardness, and durability. To look for improvement in adhesion, the "Scotch tape test" was used. However, all films showed good adhesion based upon this test. To look for improvements in hardness, the "eraser test" was used. Again, all film samples showed resistance to abrasion based upon this test. Finally, in the area of durability, a number of samples were subjected to high humidities for a period exceeding 72 hours. In addition, a number of samples were heated in an oven for 72 hours. In both cases, no degradation of samples was observed. Although these tests were unable to show any improvement in macroscopic physical characteristics due to either UV irradiation or ion bombardment, they do point out one reason for the popularity of the refractory oxide materials used for this research: They adhere well to the substrate and to each other.

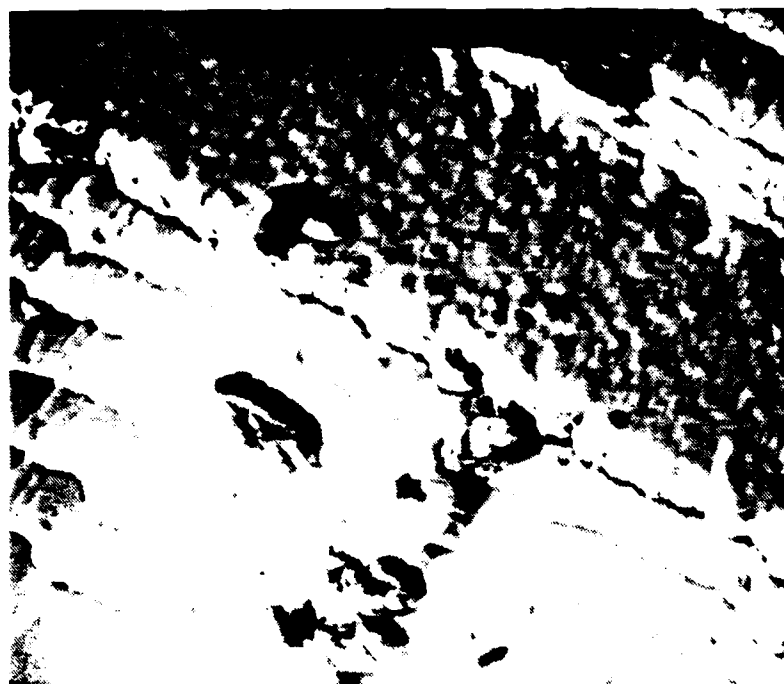
**a****b**

Figure 5-17. TEM photographs of $\text{ZrO}_2/\text{SiO}_2$ narrowband filter, ion bombarded.

- (a) Microscope magnification factor 18×10^3
(b) Microscope magnification factor 70×10^3

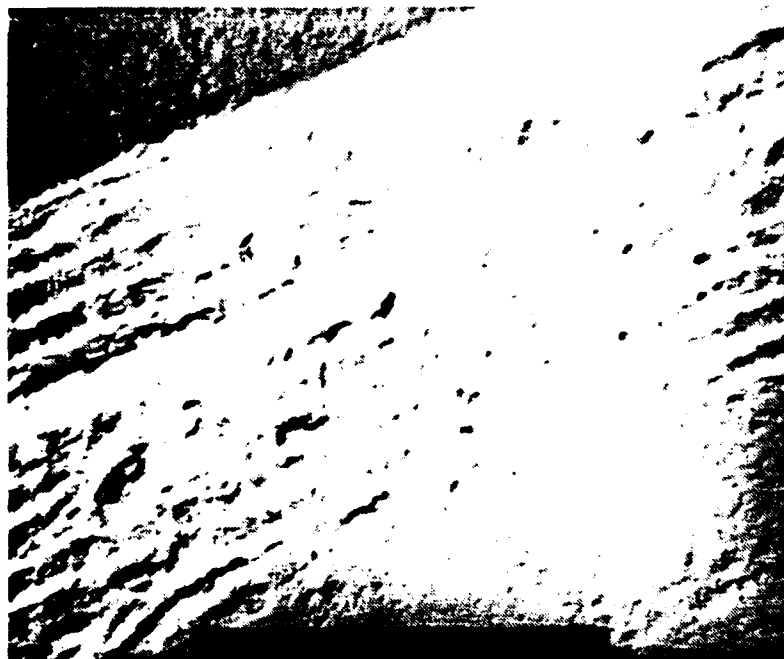


Figure 5-18. TEM photograph of $\text{ZrO}_2/\text{SiO}_2$ narrowband filter, UV irradiated.

Microscope magnification factor 18×10^3

CHAPTER 6

CONCLUSIONS AND RECOMMENDATIONS

Many parameters affect the vapor deposition of thin films. The most important of these are substrate temperature, gas pressure, and the geometry of the substrate in relation to the source materials. Thin film growth models have demonstrated that these parameters can be described in terms of the limited mobility of the condensing vapor material and a shadowing effect due to the molecules already deposited. As a result, thin films grow in columns, with voids between the columns. Atmospheric moisture readily penetrates these voids and changes both the physical and optical properties of the films. Any attempt to improve the performance of the films must be based upon either changing the mobility of the condensing atoms or modifying the self-shadowing. Two possible methods of increasing mobility are UV irradiation and ion bombardment during the film growth.

The impact of UV irradiation is small; however, several effects have been noted. X-ray diffraction analysis indicates that UV irradiation has little effect on ZrO_2 , but it causes TiO_2 films to become more amorphous. Spectrophotometer results indicate that UV irradiation reduces the amount of absorption in ZrO_2 films and slightly increases their index of refraction. For TiO_2 films, there is little reduction in absorption, but they do show a greater stability in time.

The impact of ion bombardment on ZrO_2 films is to increase the crystalline order, as evidenced by an increase in the tetragonal (111) peak. However, TiO_2 films quickly become amorphous with even slight ion bombardment. Optical measurements indicate that ion bombardment increases the absorption in both ZrO_2 and TiO_2 films. This is due to the removal of oxygen from the growing films. The use of oxygen ions in place of argon ions decreases this effect. Ion bombardment does increase the index of refraction of both ZrO_2 and TiO_2 , indicating an increase in the packing density of these films.

A number of recommendations can be made to follow up on this research:

(1) Because of the rapidity with which moisture begins to be adsorbed within a film after it is removed from the vacuum chamber, only optical measurements made while the thin film is still under vacuum will be reliable in determining film structure. It had been anticipated that a scanning monochromator would be constructed for use during this research, but the device was not completed. When it has been integrated into the Balzers BAK 760 vacuum plant, both quartz crystal information and optical transmittances at multiple wavelengths will be available as the thin films grow. This information will aid in determining the impact of both UV irradiation and ion bombardment during film growth.

(2) The present UV irradiation system should be improved by focusing a more intense spot upon the substrate. Although techniques of measurement upon a small spot are more difficult, experience with ion bombarded samples indicates the problem is not insurmountable.

(3) The use of a small UV laser should be considered as an alternative to the mercury-xenon lamp in order to increase the UV irradiation on the substrates. Since ion bombardment increases the crystalline structure of ZrO_2 , this material should be examined carefully under conditions of increased UV irradiation.

(4) Attempts should be made to improve the oxidation during deposition of TiO_2 when ion bombardment is used. This could be accomplished by increasing the background oxygen pressure, although this will cause added wear on the electron beam gun filaments. Higher oxygen pressures within the ion gun itself should be attempted, while at the same time the extraction voltage should be reduced to minimize etching of the growing films.

(5) An ion source should be obtained that provides a more uniform ion flux over the area monitored with the scanning monochromator. This will eliminate the averaging that occurs when only a small region is modified by ion bombardment.

(6) Additional materials should be examined. These should include metals as well as dielectric materials.

(7) Since this research has confirmed that even small perturbations of the deposition conditions can modify growing films, other techniques should be attempted. For example, other researchers have suggested using a piezoelectric crystal to "vibrate" the substrate during deposition. Small movements may be able to disrupt columnar growth and improve the packing density.

APPENDIX A

OPERATIONS CHECKLIST FOR BALZERS BAK 760 AND RELATED EQUIPMENT

Prior to operation, accomplish the following:

- (a) Clean interior of vacuum chamber with vacuum cleaner and replace foil on walls if necessary.
- (b) Replace/replenish source materials.
- (c) Load substrate(s).
- (d) Change quartz crystal if necessary. (Quartz crystal should be replaced when reading on digital control is 150000 or higher.)
- (e) Change optical monitor plate(s). If it is anticipated that several monitor plates will be needed, ensure that there are a sufficient number loaded into the monitor plate changer assembly.
- (f) Close door of vacuum chamber and hold in place using two handles.

A. INITIAL PUMPDOWN

- 1. Obtain 160-liter tank of liquid nitrogen from cryogenics lab; attach liquid nitrogen line to tank. Open valve 3/4 of a turn (this is to prevent wasting the liquid nitrogen by splashing in the cryo-pump).
- 2. Push PUMP button on pumping station control system (PC 101).

The roughing pump will first pump down the cryo-pump until set point A is reached, as indicated by an illuminated indicator on TPG 070. When this is reached, the roughing pump will begin pumping down the vacuum chamber and liquid nitrogen will fill into the cryo-pump.

Set point B determines when a sufficient vacuum has been reached for the cryo-pump to take over for the roughing pump. Set point C determines when the roughing pump has reached a sufficient vacuum for any valve to open. The pressures for the set points are determined by the odd-numbered knob settings; the actual set points are determined by the small set screws in conjunction with the even-numbered knob settings.

3. Open hot water output line; open hot water supply line; push PUMP/HEAT on pumping control system.
Hot water will circulate through coils on vacuum chamber and promote outgassing of contaminants.
4. When cryo-pump is cooled to 16 K, as indicated on gauge above cryo-pump, the valve between the cryo-pump and the vacuum chamber will open. The best procedure is to let pumping continue overnight; when the plant was commissioned, the minimum pressures reached were 1×10^{-7} mbar on the pump gauge and 5.5×10^{-6} mbar on the chamber ionization gauge (IMG 060B). (The ionization gauge can be set to read either linearly or logarithmically; LOG(BLUE) is normally selected. For more accurate

readings, set the switch to LIN(BLUE) and select the proper range on the LIN. RANGE switch.)

B. PRIOR TO COATING RUN

1. Push PUMP button on pumping station control.

This turns off the hot water to the vacuum chamber. Turn off hot water inlet valve; turn off hot water outlet valve.

2. Turn on chilled water supply.

Turn on chilled water outlet valve; turn on chilled water inlet valve; push PUMP/COOL button on pumping station control; turn on outlet valve to ion gun (if installed); turn on inlet valve to ion gun; check that chilled water pressure gauge in chase (marked A) reads 90 to 95 psi. (If it does not, open bypass valve marked B until it does.)

CAUTION: Pressure should not exceed 100 psi.

3. Turn on cold water supply.

Turn on cold water outlet valve; turn on cold water inlet valve.

4. Turn MAIN SWITCH on first rack to ON (1). (This supplies power to the substrate heaters and to the electron guns.)

5. Push HEATER MAINS button on second rack. Select substrate heater temperature by means of thumb switches to left of button.

Temperature is indicated on digital display (ETD 101) in rack 1.

This promotes any remaining outgassing of contaminants.

CAUTION: Ensure that substrate holder is rotating in order to protect it from warping.

6. When ionization gauge shows desired pressure, coating run can begin.

C. COATING OPERATION

1. Accomplish glow discharge in chamber.

This should be done immediately prior to beginning coating run.

It is easiest to accomplish this procedure automatically, as follows:

- a. Program L1/T1 to 600 (seconds) on KB 101. All control entries are made by selecting one of the four blue buttons (L1, L2, L3, L4) and one of the yellow buttons. (See p. 5 of Balzers manual BG 800 089 BE for a description of each.) Numbers are entered in keypad and displayed on bottom digital display; when the correct value has been entered, push ENT button to enter into memory. Any mistakes can be erased by pushing CLR button.
- b. Program L1/T2 to 999999. (This is treated as infinity by the electronics.)
- c. Program L1/N to 100000. (This tells the computer that parameters for source 1 (i.e., L1) are to be used first.)

- d. Set to automatic operation by turning lower toggle switch on BL 101 to up and triggering upper toggle switch once. CONT light should illuminate.
 - e. Push RUN button. (Valve will open, allowing air to enter vacuum chamber until a pressure of about 4×10^{-2} mbar is reached. Throttling control under IBM Personal Computer should be on, with switch set to AUT.)
2. Allow chamber to return to proper vacuum upon completion of glow discharge. Push RUN button to stop execution of program; substrate rotation will continue.

While chamber is returning to vacuum, warm up optical monitor source, UV source, etc. Optical monitor lamp is turned on by first depressing POWER switch, then depressing LAMP ON switch. Program desired values into digital controller if using automatic operation. Typical values for SiO_2 , ZrO_2 , and TiO_2 are given in Appendix B.

3. After proper vacuum pressure is reached, bleed in oxygen to desired pressure.

Turn on oxygen bottle valve and regulator. Turn on valve control unit RVG 040. Turn SET POINT to desired value; valve will open when valve voltage reading is 8. Adjust pressure to desired value by turning SET POINT and watching chamber pressure on ionization gauge.

4. If the IBM Personal Computer is to be used for either quartz crystal or optical monitor information, turn it on. Turn on the toggle switches for the quartz crystal and the optical monitor, located below the IBM unit.
5. Begin coating using either automatic or manual operation.

D. AUTOMATIC OPERATION

NOTE: For automatic operation, toggle switch on both electron gun controls must be set to CONST. RATE.

NOTE: Electron guns will not operate if the six lights at the top of rack 1 are not illuminated. TUBE WATER light out indicates cold water is not on. DOOR light out indicates back door of rack 1 is open. KEY LOCK light out indicates back door is not properly latched. In addition, GUN WATER light on each electron gun control must be illuminated; if they are not on, either the chilled water is turned off or it is not turned to a high enough pressure.

1. If using large crucibles, push ROTATION button on both crucible controls (ETS 110).
2. If using the four-pocket crucibles, rotate proper source material into position by pushing SOURCE 1 (or 2, 3, or 4 as appropriate).
3. If using the crescent-shaped portion of the oscillating crucible, depress OSCILLATE button and select proper speed of oscillation.
4. Reprogram L1/T1 to 0 and L1/T2 to 0. This will prevent glow discharge from starting.

5. Set reflectance reading on optical monitor to 92% (if using glass substrate) using FINE ADJUST.
6. Begin program operation by pushing RUN button.
7. Monitor program execution.

CAUTION: Look at source through front sight windows to ensure that electron beam is striking source material. To reposition beam, use BEAM POS. knob on remote controller. The top gun control is for source 1 and the bottom control is for source 2. The spread of the beam can be controlled by AMPL. LONG. and AMPL. LAT. knobs on electron gun control unit; the frequency of the sweep is controlled using FREQ. LONG. knob.

NOTE: The amount of time elapsed or remaining is indicated on the top digital display of rack 2 by depressing the green T button. Prior to a shutter opening, the time display indicates the amount of time remaining for $T_1+T_2+T_3+T_4$. After the shutter opens, the time display indicates how long the shutter has been open. Time is in seconds.

NOTE: Quartz crystal information is displayed on the top digital display by depressing one of the remaining green buttons. XT gives the difference between 5 MHz and the actual quartz frequency. R gives the deposition rate in angstroms per second. TH gives the thickness in angstroms. The left-hand digit is the source being used.

NOTE: If the layer thickness is incorrect as indicated on the optical monitor, the value can be reentered during program operation. Be sure to select the proper blue layer button along with the yellow button marked TH. Values are entered using the procedure described in step 6a.

8. Upon completion of automatic operation, rotate substrate holder stops. To prevent warping the substrate holder, return toggle switch to manual position and trigger toggle 1 on OU 101 control to rotate substrate holder.

E. MANUAL OPERATION

NOTE: Quartz crystal information is not available during manual operation.

CAUTION: If it becomes necessary to quickly stop the evaporation because of a lack of material, etc., the EMISSION OFF button on the remote control serves as an emergency off switch.

1. Turn bottom toggle switch on digital controller to down. MAN light should illuminate.
2. Turn on substrate rotation using toggle switch 0.
3. Toggle switches 0 thru 11 on OU101 are used as follows:
 - 0 Rotation of substrate holder
 - 1 Glow discharge
 - 2 Source 3 (left-hand thermal source)
 - 3 Source 4 (right-hand thermal source)
 - 4 Shutter 1 (left, rear)
 - 5 Shutter 2 (right, rear)
 - 6 Rotation of crucible for source 1
 - 7 Rotation of crucible for source 2
 - 8 Shutter 3 (left, front)
 - 9 Shutter 4 (right, front)
 - 10 Source 1 (left-hand electron gun source)
 - 11 Source 2 (right-hand electron gun source)

An illuminated light indicates that shutter is open or power is on.

4. Thermal sources are operated by toggling switch 2 or 3, as appropriate, to turn power on, then toggling either CHANNEL 3 (for left-hand thermal source) or CHANNEL 4 (for right-hand thermal source) to select proper power level. Toggling the switch up increases the power by about 1%; toggling it down decreases power by about 1%. The small LEDs indicate the amount of power

selected. They go up in steps of about 10%; i.e., if the third LED from the bottom is illuminated, the power is about 30% of maximum value. The appropriate shutter is opened when the source material has melted into the tungsten coil.

5. Electron gun sources are best controlled manually by selecting CONST. EMIS. position of toggle switch on electron gun control. Top electron gun control panel is for left-hand electron gun; bottom electron gun control panel is for right-hand electron gun. Electron gun sources are used as follows:

- a. Depress green ON button on top drawer of rack 1 to turn off high voltage.
- b. Depress green ON button of electron gun control to turn on filament.
- c. Use EMISSION knob on hand-held remote control to turn up power for selected source; monitor condition of beam and source by watching through sight ports.
- d. To melt a particular area of source material, stop rotation by depressing ROTATION button on crucible control. The two buttons at the top of the remote control rotate the crucible either clockwise or counterclockwise.

NOTE: If a particular source of the four-pocket crucible has been selected, the crucible control unit may rotate the crucible automatically to try to position the correct source back into position. To override this, depress the ROTATION button twice, then use the remote control unit as needed.

- e. Open the appropriate shutter (toggle switch 4 or 5).

- f. Monitor the deposition using the optical monitor and noting quarter-wave points.
6. Upon completion of coating, rotate emission controls on both remote units fully counterclockwise. This will prevent accidentally turning on power to the electron guns when starting a new coating.
7. Turn off power to filaments by depressing OFF button on each gun control unit. Turn off high voltage by depressing OFF button on top panel.

F. AFTER COATING RUN

CAUTION: Chilled water should remain on until chamber has cooled.

1. Turn off substrate heaters by depressing HEATER MAINS button; light will go out.
2. Ensure that substrate holder continues to rotate until chamber has cooled.
3. Turn off oxygen bleed valve by turning SET POINT to 0. Do not turn off toggle switch until valve voltage has reached zero.
4. Turn off regulator and main valve on oxygen bottle.
5. Turn off optical monitor by depressing LAMP OFF and POWER buttons.

6. Turn off rotation or oscillation of crucibles.
7. Turn MAIN SWITCH on rack 1 to off (0).
8. Turn off cold water supply line; turn off cold water output line.
9. When the vacuum chamber has cooled to at least 70° C, shut down the chilled water supply as follows:
 - a. Turn off inlet valve to ion gun.
 - b. Turn off outlet valve to ion gun.
 - c. Depress PUMP switch on pumping station control.
 - d. Turn off chilled water inlet valve.
 - e. Turn off chilled water outlet valve.
 - f. Reduce chilled water system pressure to about 80 psi by turning bypass valve B counterclockwise; monitor using gauge A.
10. To remove samples from chamber, depress VENT button on pumping station control. If chamber will be open for awhile, circulate hot water through chamber walls by opening hot water inlet valve and hot water outlet valve, and depressing VENT/HEAT (white) button.
11. After vacuum chamber has reached atmospheric pressure, depress either STBY button or STBY/HEAT (green) button. This will close the inlet valve to the chamber but keep the cryo-pump operating properly.

12. After removing samples, push PUMP button to pump down system.
13. If more than 18 hours will elapse before the next coating run, shut down the system by pressing OFF after the vacuum chamber has reached a pressure of at least 5×10^{-2} mbar. (The 18 hours represents a tradeoff between the amount of liquid nitrogen it takes to initially cool down the cryo-pump and the amount of liquid nitrogen it takes to keep the cryo-pump cooled down.)

NOTE: After the system has been shut down, depress the REG button to regenerate the cryo-pump. The ballast valve on the roughing pump should be engaged during regeneration, which should last several hours. When regeneration is complete, again depress the REG button.

G. KRATOS UV POWER SUPPLY

CAUTION: To protect from a build-up of ozone, turn on the fan under the vent hood.

1. Set current adjust to position M. Ensure that the proper patch plug (white for mercury-xenon lamp) is installed on the back of the power supply.
2. Turn power on.
3. Ignite lamp by depressing LAMP START button; do not hold down for more than 2 seconds.
4. After lamp comes on, adjust current to 27 A.
5. After voltage reaches 36 V, turn on cooling fan.

H. ION GUN

1. Connect proper gas supply to inlet valve; open main valve and regulator valve on bottle.
2. Supply gas to ion gun by opening valve under the vacuum chamber.
If the vacuum plant has reached a sufficient vacuum and air is not being bled into the chamber, the ionization gauge can be used to estimate the ion gun gas pressure.
3. Turn on both power switches on power supply unit.
4. Turn up discharge voltage until current registers; turn voltage knob until desired current is reached.
5. Turn up beam voltage to desired value.

APPENDIX B

TYPICAL AUTOMATIC DEPOSITION PARAMETERS

Three dielectric materials were used for this research. The input values for the digital controller for automatic deposition are as follows:

Input	Units	SiO ₂	ZrO ₂	TiO ₂
TH	Å	970	772	700
R	Å/sec	10	4	3
M		2.3	4.6	3.3
T1	sec	0	0	0
T2	sec	0	0	0
T3	sec	20	20	40
T4	sec	40	40	20
VP		0.2	0.8	0.8
TN		0.5	0.5	0.5
TV		0	0.3	0.3
P1		15	20	20
P2		20	25	30
P3		30	50	35
P4		15	10	23

NOTES: Layer thickness depends on substrate temperature and is calibrated by using optical monitor to watch for turning points.

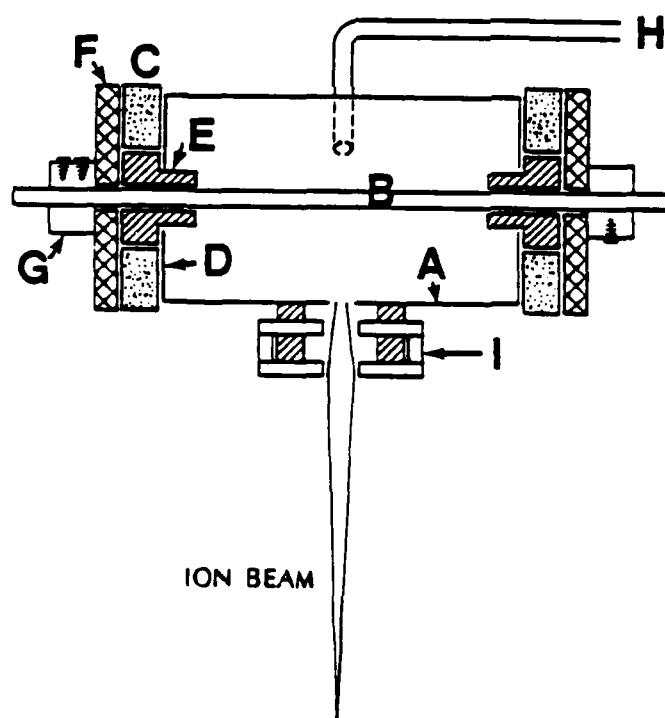
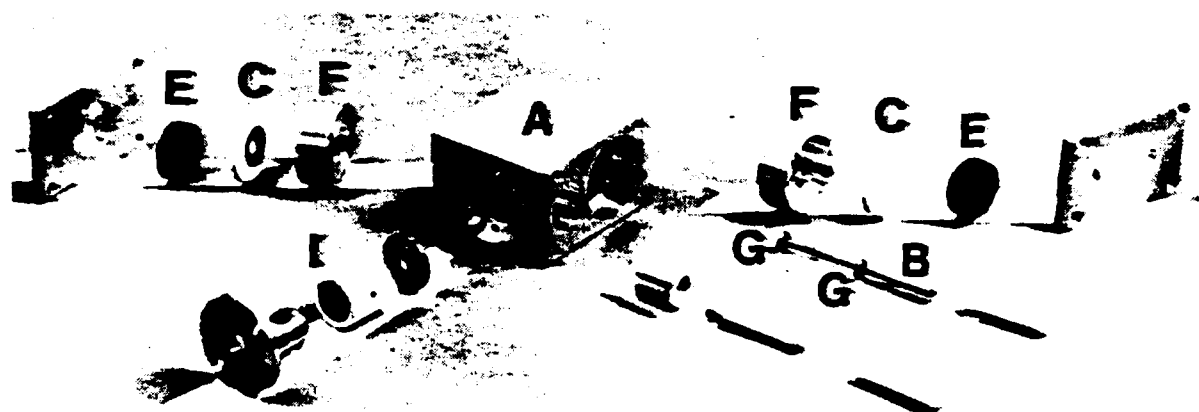
Depending on which material is deposited first, the value for T1 for that material is set to 600 and the value for T2 is set to 999999. After glow discharge is complete, these values are reset to 0 so the glow discharge will not be repeated.

APPENDIX C

THE INVERTED MAGNETRON ION SOURCE

The ion source used in this research is a cold-cathode, magnetically enhanced discharge source, in which ions are extracted through an aperture in the cathode wall. After extraction, the ion beam is collimated and focused by a system of electrodes. Although only argon and oxygen were used for this research, the source is capable of producing a beam of ions of a variety of materials that are in a gaseous form at room temperature.

The ion gun, designed by B. Singh and D. Boyarsky of Denton Vacuum, Inc., is referred to as an inverted magnetron ion source because of the geometry of the discharge. A description of the construction of the ion gun is aided by a view of the disassembled device and the cross-sectional view shown in Figure C-1. The device consists of a cylindrical stainless steel cathode (A), 25 mm in diameter and 30 mm long, in which a coaxial stainless steel anode (B) of 3-mm diameter is mounted. The anode is insulated from the cathode with ceramic insulating bushings (C). These bushings fit into apertures in the cathode end plates (D). Also mounted onto the bushings are two ring magnets (E). These magnets are made of cobalt-samarium and have pole-face magnetic field strengths of about 2 kG; one pole face is in contact with the end plates (D) of the cathode. The magnetic field produced inside the cathode is coaxial with the ion source and has a



- A Stainless steel cathode
- B Stainless steel anode
- C Insulating bushing
- D End plate
- E Ring magnet
- F Ceramic spacer
- G Block
- H Gas pipe
- I Extraction electrode

Figure C-1. Inverted magnetron ion source.

value of about 300 G in the center. Two ceramic spacers (F) used in conjunction with two threaded stainless steel blocks (G) serve to clamp the whole assembly together and make it gas-tight. The gas to be ionized is introduced into the cathode through a stainless steel pipe (H) of inner diameter 2 mm and outer diameter 4 mm, which is soldered into the cathode wall. Although the ion gun can be used in the "self-extraction" mode, a more intense and focused ion beam is obtained by the aid of an additional extraction electrode (I).

The cross-sectional view of the ion gun, Figure C-1, also shows the electrical connections and target location. Also shown in the figure is the magnetic field, which is perpendicular to the plane of the paper. This field is co-axial with the ion source and is perpendicular to the applied radial electric field. A stabilized DC power supply of 0 to 5 kV and 0 to 100 mA is connected between the cathode and anode. A second stabilized DC power supply is used to extract the ion beam, and does so by means of a bias on the first extraction electrode, which is negative with respect to the cathode. The cathode, second extraction electrode, and target are all grounded.

Gas is introduced into the cathode, and owing to thermal ionization both electrons and ions are present. The positive ions are accelerated across the discharge gap and strike the cathode surface with enough energy to liberate electrons by means of secondary electron emission. These emitted electrons accelerate toward the anode and ionize more neutral gas atoms enroute, thus creating more electron-ion pairs that are accelerated in the discharge volume.

An ionization avalanche takes place, and subsequently a steady electric discharge is established between the electrodes. This discharge is characterized by three distinct regions. At the electrodes, charged particle concentration regions called "sheaths" are formed, and quasi-neutral plasma fills the main inter-electrode volume. In this plasma region the electron and ion densities are equal, and the variation of the electric field is quite small. Almost all of the applied voltage falls across the cathode, or Langmuir sheath, which is usually a few millimeters wide, and conditions of this sheath are very critical for discharge stability. The third region is the anode sheath, and it also determines the stability of the discharge; however, it is not well understood and continues to be examined (Singh, 1978).

The discharge of this ion source is very efficient, as it produces a stable ion beam at relatively low chamber pressures. This is best explained by considering the motion of the electrons in the discharge. Once liberated from the cathode surface, the electrons are accelerated across the cathode sheath and enter the plasma with virtually the same energy. The electron motion is divided into essentially four components:

1. Helical Motion Along B Field Lines. Here, the emitted electrons are tied to magnetic field lines and gyrate around them. Since they also travel along these lines, the resultant path is helical.
2. Reflection from Cathode End Plates. Because of the negative potential of the cathode and the gradient in the magnetic field, the electrons are reflected back and forth between points where the lines enter the cathode surface.

3. E and B Drift. Throughout the discharge volume, both the electric and magnetic fields are mutually perpendicular. Thus a Lorentz force is exerted on the electrons, causing them to move in an azimuthal direction.

4. Anode Drift. Here the electrons "jump" from one magnetic field line to the next in the direction of the anode. Since they collide with neutral gas molecules and are affected by the electric field, the electrons eventually reach the anode.

Essentially, the electrons are trapped in the discharge volume, oscillating back and forth along field lines, traveling in azimuthal paths, thus greatly increasing their path length and lifetime in the system. In an efficient electron trap, the electrons that reach the anode are incapable of further ionizing; that is, their energies are degraded by successive collisions to below the ionization threshold energy of the neutral gas.

The positive ions also experience the same forces, but owing to their much greater mass and slower speeds their motion is quite different than that just described. Essentially the ions accelerate to the cathode in paths that are only slightly curved. Some of the ions that are incident on the cathode surface are extracted through a small aperture drilled into the cathode wall. The negatively biased electrode serves to accelerate and focus the ions. Because the extraction voltage and ion beam current are independently variable, the ion source is extremely versatile.

To obtain values of ion current at the substrate for various values of ion beam current and extraction voltage, a stainless steel target was positioned in front of the ion gun at about the same distance as the bombarded substrates. By means of two pins of an

electrical feedthrough, one lead of an ammeter was attached to the target and the remaining lead attached to the grounded substrate holder assembly. The currents measured for both argon ions and oxygen ions are included in Table 3-1.

APPENDIX D

SAMPLES AND DEPOSITION CONDITIONS

Run	Source	Treat- ment	Sub- strate temp, °C	Oxygen pressure, torr x 10 ⁻⁴	Ion gun settings, kV/mA	
					Discharge	Beam
Narrowband filters:						
760-70	Ti ₂ O ₃ /SiO ₂	UV	250	2.5		
760-76	Ti ₂ O ₃ /SiO ₂	UV	100	3.0		
760-77	Ti ₂ O ₃ /SiO ₂	UV	100	3.0		
760-78	Ti ₂ O ₃ /SiO ₂		240	3.0		
760-79	Ti ₂ O ₃ /SiO ₂	UV	240	1.5		
760-80	Ti ₂ O ₃ /SiO ₂	UV	240	2.5		
760-81	Ti ₂ O ₃ /SiO ₂	UV	250	3.0		
760-82	Ti ₂ O ₃ /SiO ₂	UV*	250	3.0		
760-83	Ti ₂ O ₃ /SiO ₂	UV	250	3.0		
760-84	Ti ₂ O ₃ /SiO ₂	ion*	140	0.9		
760-85	Ti ₂ O ₃ /SiO ₂	ion	140	3.0	0.3/20	0.6/0.45
760-86	Ti ₂ O ₃ /SiO ₂	ion	140	3.0	0.3/20	0.6/0.45
760-87	Ti ₂ O ₃ /SiO ₂	ion	140	3.0	0.3/20	0.8/0.6
760-88	ZrO ₂ /SiO ₂	ion	140	3.0	2.3/15	4.0/0.4
760-92	ZrO ₂ /SiO ₂	ion	150	1.0	0.4/12	1.2/0.2
760-98	ZrO ₂ /SiO ₂	ion	150	1.0	0.35/14	1.5/0.2
760-99	ZrO ₂ /SiO ₂		150	1.0		
760-100	ZrO ₂ /SiO ₂	UV/ion	150	1.0	0.3/14	1.5/0.3
760-105	ZrO ₂ /SiO ₂	UV**	150	1.0		
760-106	ZrO ₂ /SiO ₂	UV**	150	1.0		
760-108	ZrO ₂ /SiO ₂	UV**	150	1.0		
760-111	Ti ₂ O ₃ /SiO ₂	ion(O)	150	3.0	0.4/20	1.5/0.4

Run	Source	Treat- ment	Sub- strate temp, °C	Oxygen pressure, torr x 10 ⁻⁴	Ion gun settings, kV/mA	
					Discharge	Beam
Single layers:						
760-93	ZrO ₂	ion	150	1.0	0.4/12	1.2/0.2
760-94	ZrO ₂	ion	150	1.0	0.4/12	1.2/0.2
760-95	ZrO ₂	ion	150	1.0	0.4/12	1.2/0.2
760-96	ZrO ₂	ion	150	1.0	0.4/12	1.5/0.2
760-97	ZrO ₂	ion	150	1.0	0.4/12	1.5/0.2
760-101	ZrO ₂	UV/ion	150	1.0	0.3/14	1.5/0.3
760-102	SiO ₂	UV/ion	150	1.0	0.3/14	1.5/0.3
760-103	Ti ₂ O ₃	UV/ion	150	3.0	0.3/14	1.5/0.15
760-104	Ti ₂ O ₃	UV/ion	150	3.0	0.3/12	1.2/0.15
760-107	ZrO ₂	UV**	150	1.0		
760-109	SiO ₂	UV**	150	1.0		
760-110	Ti ₂ O ₃	UV**	150	3.0		
760-112	Ti ₂ O ₃	ion(0)	150	3.0	0.4/20	2.0/0.2
760-113	Ti ₂ O ₃		150	3.0		
760-114	ZrO ₂		150	3.0		

*Spacer only

**Interior

APPENDIX E

TURNING POINT DATA FOR SINGLE MATERIAL COATINGS

Run	Matl, treat- ment	Percent reflectance at given wavelength*							
		$\lambda/4$	$\lambda/2$	$3\lambda/4$	λ	$5\lambda/4$	$3\lambda/2$	$7\lambda/4$	2λ
094	ZrO ₂ (ion)	75	92.1 1000	79.2 1910	91.9 2857	79 3600	91 4509	79	91
095	ZrO ₂ (ion)	(Erratic optical monitor)							
096	ZrO ₂ (ion)	68.7	89.5 1000	72.2 1965	88	72.8 3800	86.1	73.2	84.5 6400
097	ZrO ₂ (ion)	69	91.3 1080	70	88.5	70	86.8 4495	70.5	85.5
101	ZrO ₂ (ion)	68.5	90 930	73.5 1860	88.5	72.2	86.8	72	85 7080
104	TiO ₂ (ion)	57.5	73.5 900	50 1600	60.5 2530	44.2	52.1 4160	40.2	46 6560
107	ZrO ₂ (UV)	75.5	89.9 850	76.5 1670	89.5 2470	76.2 3300	89 4050	75.9 4920	88.5 6521
109	SiO ₂ (UV)	(Too difficult to read optical monitor)							
110	TiO ₂ (UV)	69.5	86 760	68.1 1420	84.5	68.1	83.6	67	82.5 5840
112	TiO ₂ (ion)	64.5	85.9 830	63.5 1640	83.5	62.9 3135	81 3950	62 4700	78 6260
113	TiO ₂	67	82.9 800	63	78.7	61.5 3110	76.7 3880	60.5	75.5 6170
114	ZrO ₂	78	90 860	78	89.5	77.5 3370	88.7 5056	77.2 5937	88 6710

*Where two values are given, second value is thickness of coating, in A. All runs made starting at a reflectance of 92%.

REFERENCES

- Allen, T. H. (1982), "Properties of ion assisted deposited silica and titania films," Proc. SPIE 325, 93.
- Ashcroft, N. W., and N. D. Mermin (1976), "Determination of crystal structures by x-ray diffraction," Chapter 6 of Solid State Physics, Holt, Rinehart and Winston, Philadelphia.
- Bradford, A. P., G. Hass, M. McFarland, and E. Ritter (1965), "Effect of ultraviolet irradiation on the optical properties of silicon oxide films," Appl. Opt. 4(8), 971-976.
- Browning, S. D. (1983), "Electron bombardment of certain thin films during deposition," PhD Dissertation, Optical Sciences Center, University of Arizona.
- Coleman, H. S., A. F. Turner, and O. A. Ullrich (1947), "Crystal orientation and refractive index of thick evaporated MgF_2 films" (abstr.), J. Opt. Soc. Am. 37(6), 521.
- Cullity, B. D. (1956), Elements of X-Ray Diffraction, Addison-Wesley Publishing Company, Reading, Mass.
- Cuomo, J. J., J. M. E. Harper, C. R. Guarnieri, D. S. Yee, L. J. Attanasio, J. Angilello, and C. T. Wu (1982), "Modification of niobium film stress by low-energy ion bombardment during deposition," J. Vac. Sci. Technol. 20(3), 349-354.
- Dirks, A. G., and H. J. Leamy (1977), "Columnar microstructure in vapor-deposited thin films," Thin Solid Films 47, 219-233.
- Dobrowolski, J. A., and D. Lowe (1978), "Optical thin film synthesis program based on the use of Fourier transforms," Appl. Opt. 17(19), 3039-3050.
- Ebert, J. (1982), "Activated reactive evaporation," Proc. SPIE 325, 29.
- Fang, J. H., and F. D. Bloss (1966), X-Ray Diffraction Tables, Southern Illinois University Press, Carbondale.
- Gautherin, G., and C. Weissmantel (1978), "Some trends in preparing film structures by ion beam methods," Thin Solid Films 50, 135-144.

- Guenther, K. H., and H. K. Pulker (1976), "Electron microscopic investigations of cross sections of optical thin films," Appl. Opt. 15(12), 2992-2997.
- Harris, M., H. A. Macleod, S. Ogura, E. Pelletier, and B. Vidal (1979), "The relationship between optical inhomogeneity and film structure," Thin Solid Films 57, 173-178.
- Hass, G., J. B. Heaney, W. R. Hunter, and D. W. Angel (1980), "Effect of UV irradiation on evaporated ZnS films," Appl. Opt. 19(15), 2480-2481.
- Henderson, D., M. H. Brodsky, and P. Chaudhari (1974), "Simulation of structural anisotropy and void formation in amorphous thin films," Appl. Phys. Lett. 25(11), 641-643.
- Hirsch, E. H., and I. K. Varga (1980), "Thin film annealing by ion bombardment," Thin Solid Films 69, 99-105.
- Hodgkinson, I. J., F. Horowitz, H. A. Macleod, M. Sikkens, and J. J. Wharton (1983), "Birefringence in optical coatings" (abstr.), J. Opt. Soc. Am. 73(12): 1871.
- Hodgkinson, I. J., and A. R. Walker (1973), "Stress relief induced in silicon oxide films by ultraviolet radiation," Thin Solid Films 17, 185-197.
- Koch, H. (1965), "Optische Untersuchungen zur Wasserdampfsorption in Aufdampfschichten (insbesondere in MgF₂-Schichten)," Phys. Status Solidi 12, 533-543.
- Leamy, H. J., G. H. Gilmer, and A. G. Dirks (1980), "The microstructure of vapor deposited thin films," Current Topics in Material Science, Vol. 6, North-Holland Publishing Company, Amsterdam.
- Lee, C. C. (1983), "Moisture adsorption and optical instability in thin film coatings," PhD Dissertation, Optical Sciences Center, University of Arizona.
- Lissberger, P. H., and J. M. Pearson (1976), "The performance and structural properties of multilayer optical filters," Thin Solid Films 34, 349-355.
- Macleod, H. A. (1969), Thin-Film Optical Filters, American Elsevier Publishing Company, New York.
- Macleod, H. A. (1982), "Microstructure of optical thin films," Proc. SPIE 325, 21.

- Maissel, L. I., and R. Glang, eds. (1970), Handbook of Thin Film Technology, McGraw-Hill Book Company, New York.
- Manifacier, J. C., J. Gasiot, and J. P. Fillard (1976), "A simple method for the determination of the optical constants n , k and the thickness of a weakly absorbing thin film," J. Phys. E 9(11), 1002-1004.
- Martin, P. J., H. A. Macleod, R. P. Netterfield, C. G. Pacey, and W. G. Sainty (1983), "Ion-beam-assisted deposition of thin films," Appl. Opt. 22(1), 178-184.
- Messier, R. (1982), Private communication, Materials Research Laboratory, The Pennsylvania State University, University Park, PA 16802.
- Mickelsen, R. A. (1968), "Effects of ultraviolet irradiation on the properties of evaporated silicon oxide films," J. Appl. Phys. 39(10), 4594-4600.
- Movchan, B. A., and A. V. Demchishin (1969), "Study of the structure and properties of thick vacuum condensates of nickel, titanium, tungsten, aluminium oxide and zirconium dioxide," Phys. Met. Metallogr. 28(4), 83-90.
- Nakhodkin, N. G., and A. I. Shaldervan (1972), "Effect of vapour incidence angles on profile and properties of condensed films," Thin Solid Films 10, 109-122.
- Nieuwenhuizen, J. M., and H. B. Haanstra (1966), cited by Dirks and Leamy (1977).
- Ogura, S. (1975), "Some features on the behavior of optical thin films," PhD Thesis, Newcastle Upon Tyne Polytechnic, U.K.
- Pawlewicz, W. T. (1983), Private communication, Battelle Pacific Northwest Laboratories, P.O. Box 999, Richland, WA 99352.
- Pawlewicz, W. T., G. J. Exarhos, and W. E. Conaway (1983), "Structural characterization of TiO_2 optical coatings by Raman spectroscopy," Appl. Opt. 22(6), 1837-1840.
- Pawlewicz, W. T., P. M. Martin, D. D. Hays, and I. B. Mann (1982), "Recent Developments in reactively sputtered optical thin films," Proc. SPIE 325, 105.
- Pearson, J. M. (1970), "Electron microscopy of multilayer thin films," Thin Solid Films 6, 349-358.

- Pulker, H. K., G. Paesold, and E. Ritter (1976), "Refractive indices of TiO_2 films produced by reactive evaporation of various titanium-oxygen phases," Appl. Opt. 15(12), 2986-2991.
- Sanders, D. M., E. N. Farabaugh, and W. K. Haller (1982), "Glassy optical coatings by multisource evaporation," Proc. SPIE 346, 31.
- Singh, B. (1978), PhD Thesis, University of Aston, England.
- Thornton, J. A. (1974), "Influence of apparatus geometry and deposition conditions on the structure and topography of thick sputtered coatings," J. Vac. Sci. Technol. 11(4), 666-670.
- Vook, R. W. (1982), "Theories of nucleation and growth of thin films," Proc. SPIE 346, 2.
- Walker, T. W. (1980), "Laser-induced damage to thin film dielectric coatings," PhD Dissertation, Air Force Institute of Technology.
- Weissmantel, C., G. Reisse, H.-J. Erler, F. Henny, K. Bewilogua, U. Ebersbach, and C. Schürer (1979), "Preparation of hard coatings by ion beam methods," Thin Solid Films 63, 315-325.

APPENDIX G
ELECTRON BOMBARDMENT OF CERTAIN THIN FILMS
DURING DEPOSITION

PhD Dissertation by Steve Browning

TABLE OF CONTENTS

	Page
LIST OF ILLUSTRATIONS	vii
LIST OF TABLES	x
ABSTRACT	xi
1. INTRODUCTION	1
2. ELECTRON SOURCE	4
3. SAMPLE PREPARATION	13
Antimony Trioxide (Sb_2O_3)	14
Potassium Hexafluorozirconate ($2\text{KF} \cdot \text{ZrF}_4$)	15
Silicon Monoxide (SiO)	16
Zinc Sulfide (ZnS)	16
Magnesium Fluoride (MgF_2)	17
4. ANALYSIS METHODS	19
X-Ray Diffraction- Diffractometer	19
Transmission Electron Microscopy- Carbon Replication	24
Transmission Electron Microscopy- Direct Film Observation	27
Guided Wave Analysis- Prism Coupler	28
Surface Plasma Wave Analysis- Induced Absorption	36
Spectrophotometer Analysis	42
Adhesion, Hardness, and Moisture Resistance	47
5. RESULTS	50
Antimony Trioxide (Sb_2O_3)	50
Potassium Hexafluorozirconate ($2\text{KF} \cdot \text{ZrF}_4$)	70
Silicon Monoxide (SiO)	83
Zinc Sulfide (ZnS)	91
Magnesium Fluoride (MgF_2)	108
6. REMARKS ON FILM FORMATION AND ELECTRON INTERACTION	119
7. CONCLUSIONS	123
APPENDIX 1: MOLECULE FLUX CALCULATIONS	133

TABLE OF CONTENTS--Continued

	Page
APPENDIX 2: LIST OF COATING RUNS	135
APPENDIX 3: REPRESENTATIVE SPW GRAPHS	140
APPENDIX 4: DURABILITY TESTS RESULTS	144
APPENDIX 5: CONTROLLED HUMIDITY TEST RESULTS.	146

LIST OF ILLUSTRATIONS

Figure	Page
1.1. Coating Plant Diagram	5
2.2. Electron Bombardment Source Calibration Graphs	8
4.1. X-ray Diffractometer Diagram	20
4.2. X-ray Diffractometer Trace of Adhesive for Powders	23
4.3. Carbon replica film application geometry	25
4.4. Prism coupler configuration	32
4.5. Zig zag ray model of guided light	33
4.6. Induced absorption sample (SPW)	37
4.7. Surface Plasma Wave (Induced Absorption) Measurement Configuration	39
4.8. Spectrophotometer Transmittance curve	44
4.9. FECO sample configuration	46
4.10. FECO measurement configuration	48
5.1. X-ray diffractometer traces of antimony trioxide powder	51
5.2. X-ray diffractometer traces of antimony trioxide films	53
5.3. Cross section fractographs of antimony trioxide films	56
5.4. TEM photographs of antimony trioxide films	60
5.5. Electron diffraction patterns of antimony trioxide films	62
5.6. Representative TEM high magnification photographs	63
5.7. Spectrophotometer R and T curves for antimony trioxide films	66

LIST OF ILLUSTRATIONS--Continued

Figure	Page
5.8. X-ray diffractometer traces of potassium hexafluoro- zirconate powder	71
5.9. X-ray diffractometer traces of potassium hexafluoro- zirconate films on heated substrates	72
5.10. X-ray diffractometer traces of potassium hexafluoro- zirconate films on unheated substrates	76
5.11. Cross-section fractographs of potassium hexafluoro- zirconate films	79
5.12. Spectrophotometer R and T curves for potassium hexa- fluorozirconate	80
5.13. X-ray diffractometer traces of silicon oxide films	84
5.14. Cross-section fractographs of silicon oxide films	87
5.15. Spectrophotometer R and T curves for silicon oxide films	88
5.16. X-ray diffractometer traces of zinc sulfide powder (Irtran)	92
5.17. X-ray diffractometer traces of zinc sulfide films on unheated substrates	93
5.18. Cross-section fractographs of zinc sulfide films	97
5.19. X-ray diffractometer traces of zinc sulfide powder (Atomergic)	98
5.20. X-ray diffractometer traces of zinc sulfide films on heated substrates	100
5.21. Expanded X-ray diffractometer traces of zinc sul- fide films	102
5.22. Spectrophotometer R and T curves for zinc sulfide films	106

LIST OF ILLUSTRATIONS--Continued

Figure	Page
5.23. X-ray diffractometer traces of magnesium fluoride powder	109
5.24. X-ray diffractometer traces of magnesium fluoride films	111
5.25. Cross-section fractographs of magnesium fluoride films	114
5.26. Spectrophotometer R and T curves for magnesium fluoride films	115
A3.1 SPW graphs for silver films	141
A3.2 SPW graphs for zinc sulfide (EB-68)	143

LIST OF TABLES

Table	Page
1. X-ray diffractometer peaks for antimony trioxide films	57
2. Electron diffraction measurements on antimony trioxide films .	59
3. High magnification TEM measurements on antimony trioxide films	61
4. Refractive index of antimony trioxide films as measured with the prism coupler	64
5. Half-wave position from spectrophotometer transmittance curves of antimony trioxide films	68
6. Spectrophotometer measurements and calculated index values for bombarded and non-bombarded antimony trioxide films	69
7. X-ray diffractometer peaks for potassium hexafluorozir- conate films	74
8. Surface plasma wave analysis of potassium hexafluoro- zirconate films	81
9. Spectrophotometer measurements and calculated index values for bombarded and non-bombarded potassium hexafluoro- zirconate films	82
10. Surface plasma wave analysis of silicon monoxide films	89
11. Spectrophotometer measurements and calculated index values for bombarded and non-bombarded silicon monoxide films .	90
12. X-ray diffractometer peaks for zinc sulfide powder.	95
13. Refractive index of zinc sulfide films as measured with the prism coupler	105
14. Surface plasma wave analysis of zinc sulfide films	105
15. Spectrophotometer measurements and calculated index values for bombarded and non-bombarded zinc sulfide films . . .	107
16. X-ray diffractometer peaks for magnesium fluoride powder . . .	110

LIST OF TABLES--Continued

Figure	Page
17. Surface plasma wave analysis of magnesium fluoride films . . .	116
18. Spectrophotometer measurements and calculated index values for bombarded and non-bombarded magnesium fluoride films	117
19. Bonding character of studied materials	130
A1. Refractive index, density for the bulk form, and molecular weight of the materials used in this study	136
A2. Coating runs and conditions	137
A3. Check runs on silvered prisms used in the SPW experiments . .	142
A4. Hardness and adhesion tests.	145
A5. Controlled humidity test results	147

CHAPTER 1

INTRODUCTION

Vacuum deposited thin film multilayers are widely used to control the spectral character of radiation in optical systems. Individual films are ideally modeled as continuous, homogeneous slabs of material. In reality, they may be porous, composed of aggregate crystallites, have a nonuniform distribution of closely packed columns, or any of several other possible configurations. Both the optical and physical properties of these films depend directly on the actual film microstructure, or how the material is arranged on the substrate. In turn, the layer microstructure is largely dependent on the conditions inside the coating plant during deposition. Several models have been presented to portray the variation in this structure. Movchan and Demsheshin (1969) introduced one such model showing the effects of substrate temperature on several different film materials. This model was supplemented by Thornton (1974) to include pressure inside the chamber. By controlling these and other conditions and introducing additional process parameters, important film properties can be dramatically improved. For example, Martin et al. (1983) demonstrated that the packing density of material in a film could be increased by bombarding the substrates with argon ions during film deposition. Allen (1982) showed how a similar bombardment with oxygen ions could be used to alter the stoichiometry or oxygen content of several different oxide

films. Both of these instances of ion assisted deposition made the films less susceptible to moisture adsorption and damage. In addition, changing a film's crystallite size with substrate temperature has been shown by Martin and Turner (1966) to affect its optical characteristics. These are just a few examples of a wide range of evaporation conditions which can be manipulated to produce films to exacting specifications.

The idea of bombarding the substrate with electrons during evaporation of a film is not new. R.M. Rice (1947) of the Bausch and Lomb Optical Company patented and used this process for years, referring to it as "beaming". It has demonstrated a marked effect on the physical and optical properties of some films. Layers of zinc sulfide have long been known to be particularly improved in their adhesion to the substrate and resistance to moisture. Bangert and Pfefferkorn (1980) showed this to be due to a change in microstructure of the films brought about by an electron assisted phase transition. In other words, the bombarding electrons cause a change in the film crystal structure from one form to another. Also, epitaxial processes have been improved by electron bombardment. Chambers and Prutton (1967) demonstrated that electrons bombarding alkali halide substrates create F centers, which leads to increased nucleation densities for the condensing metal films. Aluminum oxide films deposited from an electron beam evaporation source often show anomalous absorption, shown by Hoffman and Leibowitz (1971) to be caused by electrons bombarding the substrate and affecting film stoichiometry.

A thorough understanding of the effects of electron bombardment on film microstructure and the subsequent effects on,

macroscopic properties has yet to be attained. A systematic variation of the parameters associated with the electron bombardment technique and analysis of the resulting films should provide new insight into the dynamics of thin film formation. In this paper, I will first describe the implementation of a source of variable electron energies and fluxes, along with some theoretical calculations of expected electron flux densities at the substrates. Next follows a calibration of this source as a function of the various parameters associated with it, for example, filament power and substrate potential. Preparations of single layer thin films of several widely used materials will then be described, some of which will be electron bombarded during deposition and others not. These films will then be analyzed by several different micro- and macrostructural methods. Specifically, any changes brought about in the physical and optical properties of the films by electron bombardment will be sought. If found, an attempt will be made to correlate the degree of change to the electron bombardment parameters. Finally, I will try to explain these effects in the light of current thinking on thin film vapor deposition.

CHAPTER 2

ELECTRON SOURCE

The coating chamber used for the preparation of the thin film samples was an Edwards EC-18, pumped by rotary and oil diffusion pumps. The modification of this plant for electron bombardment closely resembles that of the original patent by Rice (1947), with one important difference to be explained later.

Figure 2.1 schematically shows the coating chamber as modified for electron bombardment. A seven inch length of 0.010 inch diameter tungsten wire, wound in a coil and mounted in a crucible, forms the electron source filament. A larger loop filament originally was placed around the circumference of the chamber at the level of the glow discharge aluminum anode. It was felt that this configuration would provide a more uniform distribution of electron flux over the substrates. However, this large amount of tungsten wire required more current to reach appreciable electron emission temperature than the available feed through could accomodate. Thus a shorter, smaller diameter filament wire was utilized. It is mounted just above the baseplate, at the same level as the evaporation material sources, about 38 centimeters from the substrates. The secondary of a 45 volt transformer set provides heating power for the filament, and it is held at DC ground potential. Also grounded are all the fixtures inside the plant, with the exception of the rotating substrate holder. The

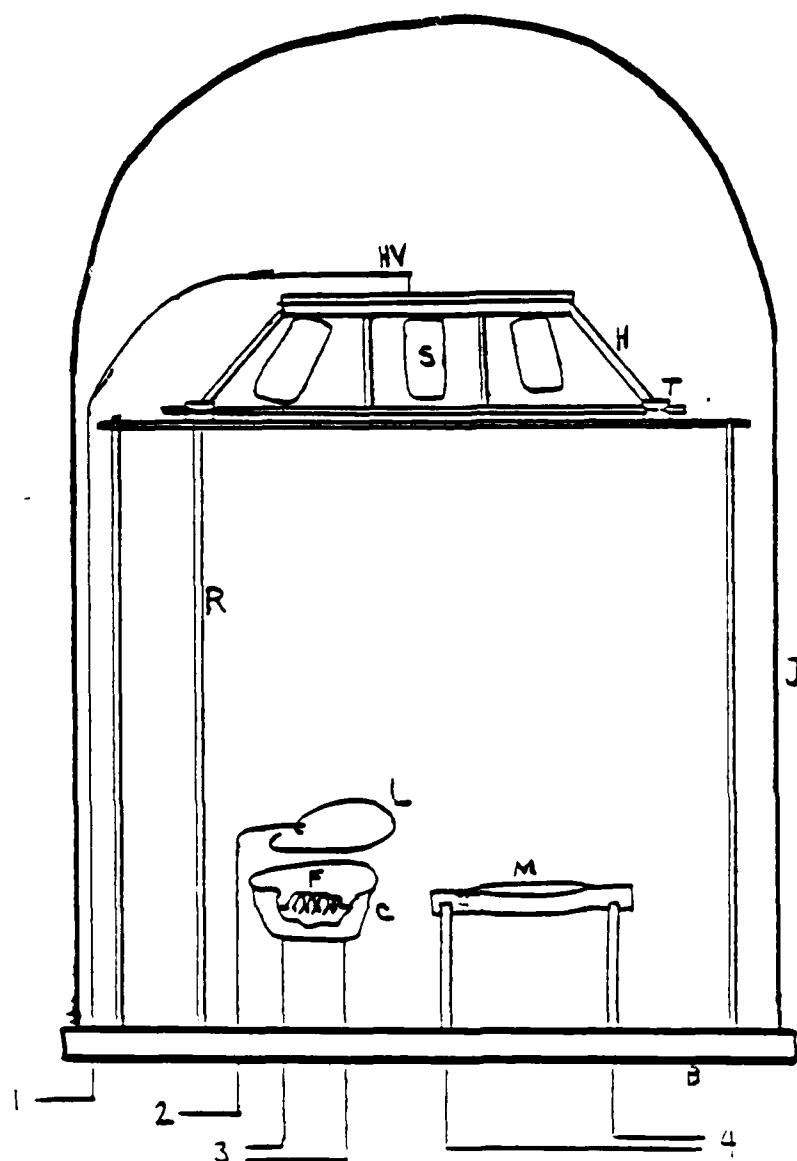


Figure 2.1. Coating plant diagram.

F - filament, C - crucible (cutaway view), L - accelerating loop, M - evaporant material source, B - base plate, J - bell jar, R - rotary drive rod, HV - high voltage lead, S - substrate, H - substrate holder, T - teflon roller, 1 - to high voltage supply, 2 - to another high voltage supply, 3 - to grounded secondary of filament transformer, 4 - to source transformer secondary.

substrate holder is electrically isolated by teflon rollers and its potential is controlled by a modified glow discharge power supply. The supply can provide a positive voltage of up to five kilovolts for electron bombardment, or alternately a high negative voltage to a glow discharge ring. The power supply is essentially a step-up transformer followed by a full wave bridge rectifier, so a straightforward arrangement of relay switches accomplishes the reversal of polarity.

The above configuration is almost identical to that originally proposed. However, preliminary measurements indicated extremely low electron flux levels and efficiency. To alleviate this problem, a nichrome (NiCr) wire loop was placed about one inch above the electron source filament and held at a positive potential of a few hundred volts with respect to it. This dramatically increased the flux on the substrate holder, so this important modification was made to the original design. The loop effectively aids the high substrate cage voltage in drawing off the cloud of thermal electrons from around the filament, thus increasing its efficiency.

During actual evaporations, the bombardment filament and loop are shielded from the materials sources with aluminum foil to avoid contamination. The rate of electrons falling on the substrate holder was measured by placing a galvanometer directly in the circuit connecting the high voltage supply to the feed through for the substrate holder. The holder was glass beaded clean prior to making these measurements. Figure 2.2 shows graphs of current on the substrate holder as a function of the various parameters associated with electron bombardment. Graph 2.2a shows a collected current

plateau for increasing filament voltage with constant potentials on the substrate holder and accelerating loop. This plateau could be due to either increased filament resistance with temperature or the accumulation of a cloud of thermal electrons surrounding the filament and preventing further emission. Graph 2.2b illustrates the effect of the accelerating loop on collected current for several high voltage settings on the substrate holder. The effect is linear for the most part. Some slight plateaus are evident at the higher settings as the filament efficiency is increased. Graphs 2.2c, 2.2d, and 2.2e show the effect of increasing the substrate holder voltage at a given filament setting for several loop voltages at three different chamber pressures. The most striking feature of these plots is the obvious plateau in collected current at pressures of 5.0×10^{-5} and 1.0×10^{-4} torr. This means that for these pressures, an increase in the electron energy on the substrates is accomplished without changing the flux very much. Also, the increase of current with pressure, due to secondary emission from gas molecules, is quite noticeable. Indeed, if calibrated, this could serve as a vacuum ion gauge for the system.

A fairly good idea of filament efficiency can be deduced from the graphs of Figure 2.2. For example, the temperature of the filament for a variac setting of 35 volts was measured with a Pyro optical pyrometer and found to be 1977°K (3100°F). Higher filament temperatures were very difficult to measure accurately with the pyrometer. Using this value for T in Dushman's equation for emitted current density from Eastman's book (1949), along with the appropriate constants for tungsten;

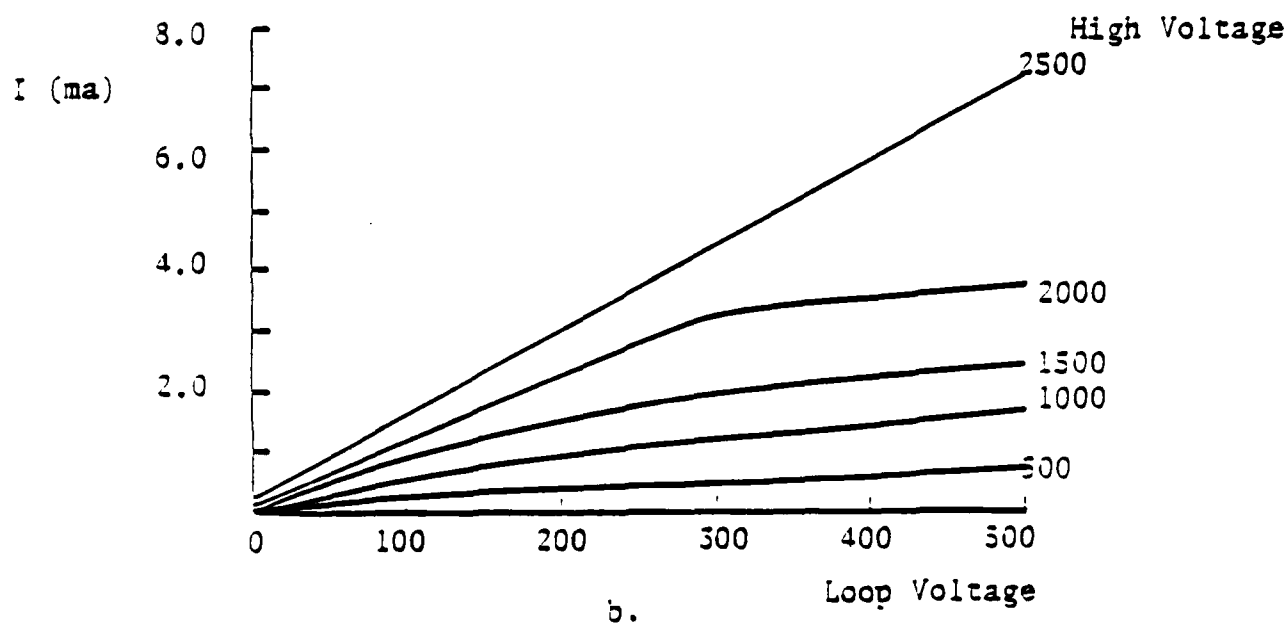
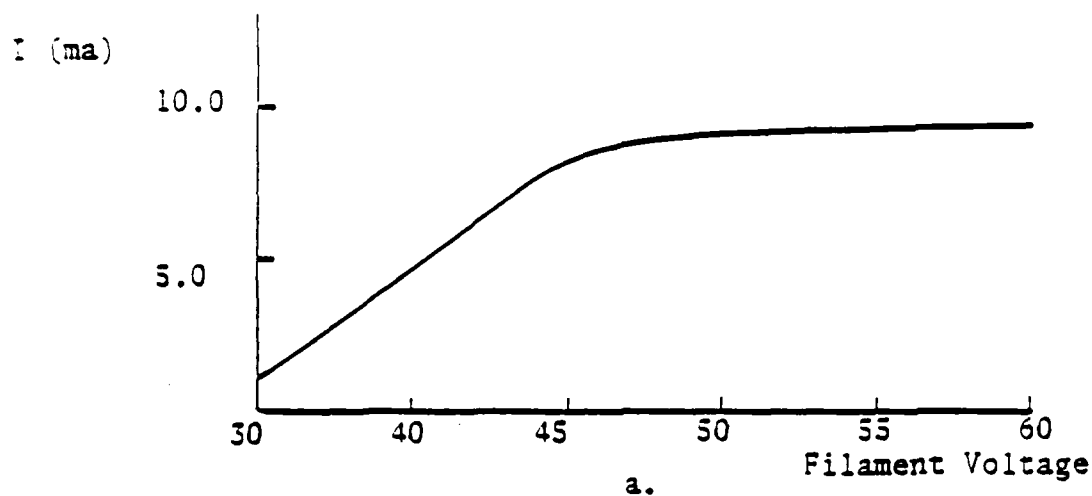


Figure 2.2. Electron bombardment source calibration graphs.

- a. Pressure - 0.7×10^{-5} torr, substrate holder potential - 2500 volts, loop voltage - 500 volts
- b. Pressure - 0.7×10^{-5} torr, filament setting - 50
- c. Pressure - 0.7×10^{-5} torr, filament setting - 50
- d. Pressure - 5.0×10^{-5} torr, filament setting - 50
- e. Pressure - 1.0×10^{-4} torr, filament setting - 50

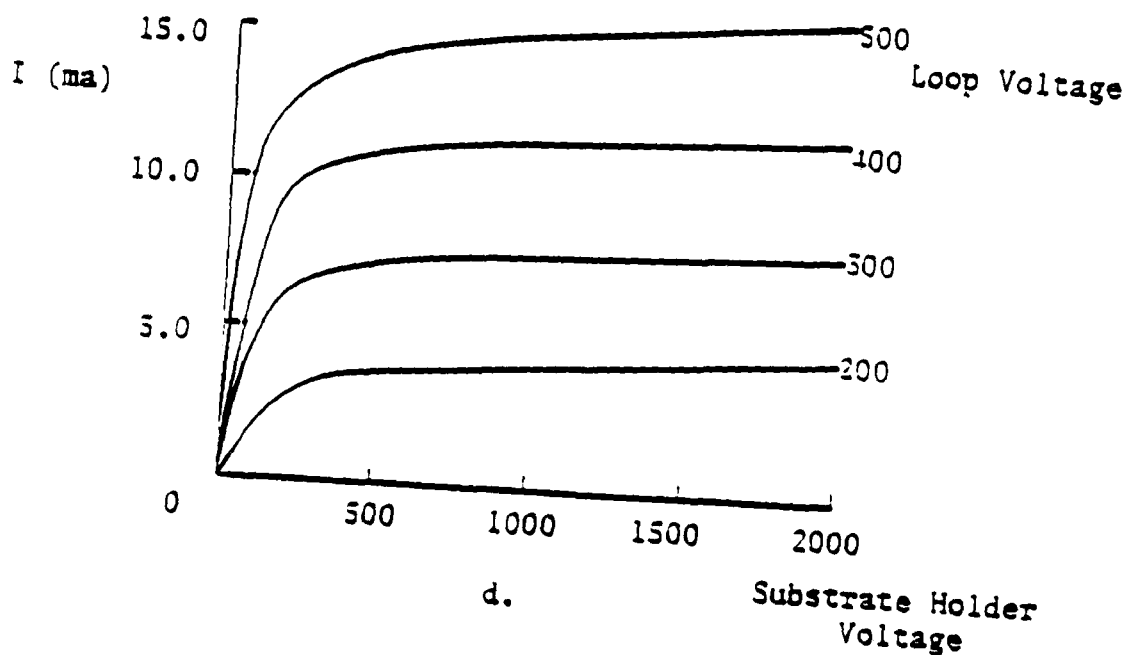
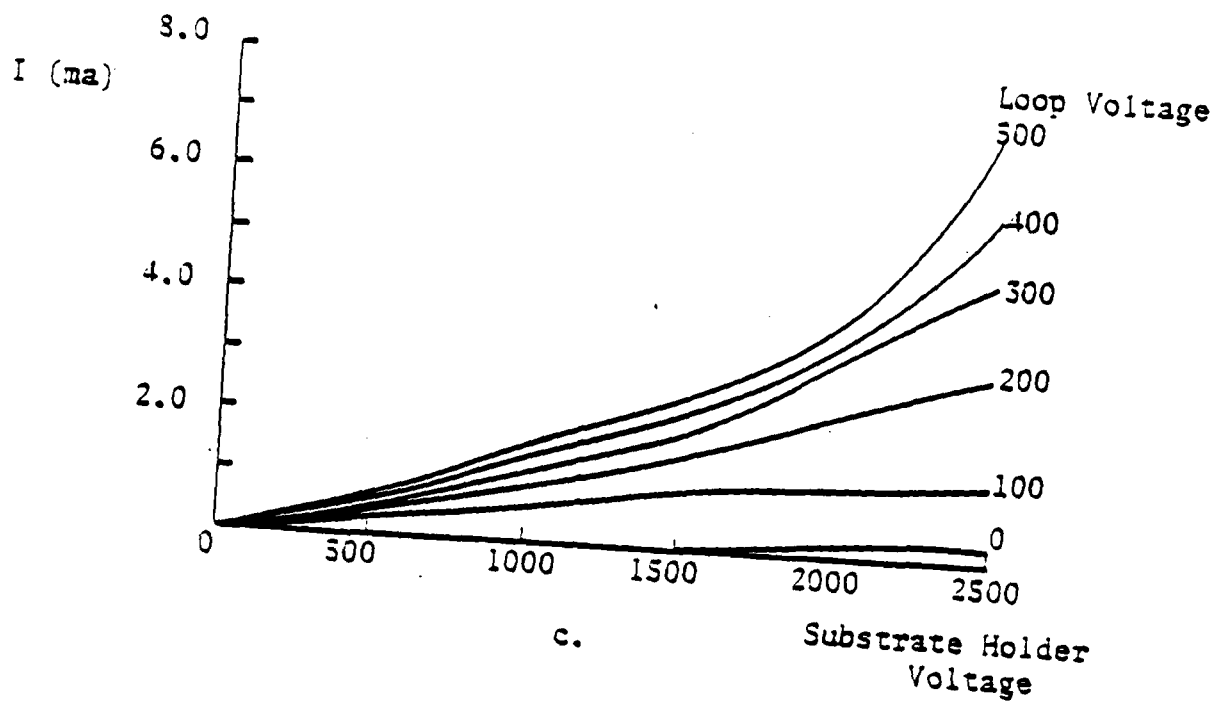


Figure 2.2. cont. Electron bombardment source calibration graphs

c. Pressure- 0.7×10^{-5} torr
 d. Pressure- 5.0×10^{-5} torr

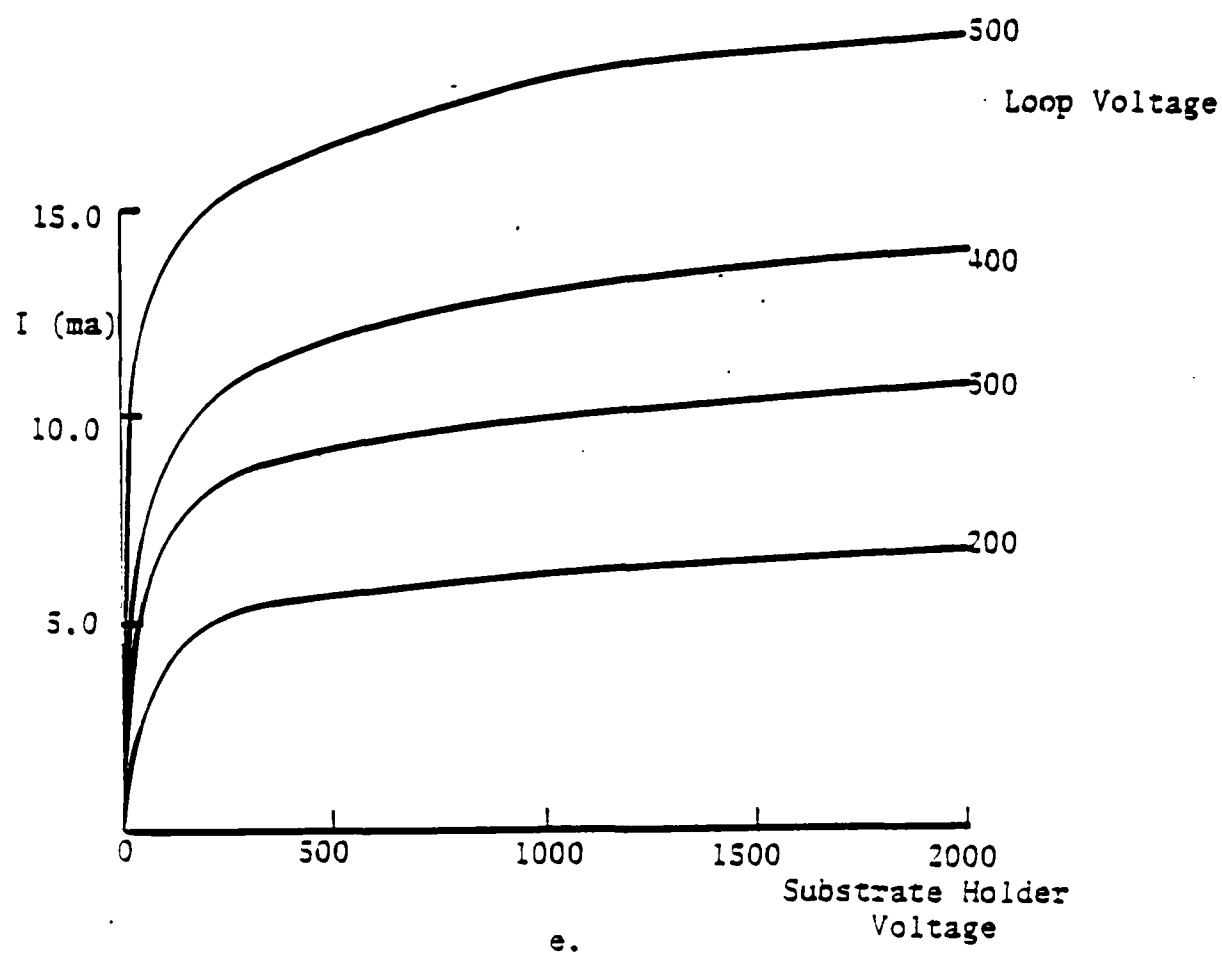


Figure 2.2.cont. Electron bombardment source calibration graphs.

Pressure- 1.0×10^{-4} torr

$$J = AT^2 \exp(-b_0/T)$$

where $b_0 = 52,400$ and $A = 60.2 \times 10^{-4}$ amps per square meter, we calculate $J = 7.26$ amps per square meter or emitted current $I = 1.03$ milliamps. Actual measured current on the substrate holder was 420 microamps, for an efficiency of about 40 percent. Of course, efficiency will vary for different substrate and loop voltages, as well as different filament temperatures.

One point of this study will be to ascertain the effect of varying electron flux on the film for different samples. As a numerical example, the molecule arrival rate at the substrates for an antimony trioxide film can be compared to the electron arrival rate. A typical deposition rate for the antimony trioxide is 1.6 angstroms per second. This has a corresponding molecule arrival rate of 1.72×10^{14} molecules per square centimeter per second. This was calculated using the bulk density of antimony trioxide and assuming a packing density of 1.0 in the film.

The electron flux corresponding to 40 milliamps over the 150 square centimeter substrate holder turns out to be 4.27×10^{15} electrons per square centimeter per second. Thus it is easy to obtain an electron arrival to molecule arrival ratio of anywhere from zero to ten by adjusting the electron source parameters. Alternately, the deposition rate could be changed, but it was felt best to leave as many conditions as constant as possible and only vary the electron bombardment. Molecule flux calculation parameters for all materials

are shown in Appendix 1, along with a sample computation for antimony trioxide.

In calculating the electron to molecule arrival ratios, it was assumed that the electron flux was uniform over the entire substrate holder. No difference was assumed between the flux on the substrates and the flux on the metal holders. Thus any reduction in flux on the substrates due to charging effects was ignored. Sabirov (1982) showed that for zirconium oxide films, charge build-up from an electron stream similar to ours resulted in up to -55 volts potential on an insulator substrate. At the applied high voltages, this would have a negligible effect on repelling the arriving electrons.

Only materials which could be thermally evaporated were investigated. This was done because the available plant was not equipped with an electron beam evaporation gun. Moreover, the electron flux could be more effectively controlled using the installed source. Stray electrons from an electron beam gun would show a spread in energy due to numerous collisions with plant fixtures and be difficult to calibrate, while those from the electron source filament would all be directed to the substrates with the same energy.

CHAPTER 3

SAMPLE PREPARATION

Appendix 2 contains a complete listing of all the coating runs performed in this study with the evaporation conditions.

Thin films of the materials of interest were evaporated onto glass microscope slides along with, in some cases, sodium chloride plates (used for TEM sample preparation, described later). The glass slides were first cleaned by immersing in warm chromic acid for about 20 minutes, then drained, rinsed, and scrubbed with cotton and Liquinox soap under tap water. An ultrasonic bath of Liquinox in deionized water and two ultrasonic rinses in deionized water followed. Finally, the substrates were blown dry with nitrogen from an electrostatic nozzle gun. This elaborate procedure is necessary to prevent contamination at the film-substrate interface, a common cause of film degradation. The slides were two different sizes, either 1x3 inch or 2x2 inch. The 2x2's were coated on only half of one side by placing a mask in front. These were to be used for FECO measurements, explained in the next chapter. The sodium chloride plates were not cleaned prior to film deposition because of their hygroscopic nature.

For each individual thin film material, conditions inside the coating chamber were kept as nearly identical as possible for each run, apart from the electron bombardment. The only exception to this was substrate temperature, which was either raised to a certain elevated

value with quartz infrared lamps or kept at room temperature. A dial surface thermometer placed on the back side of one of the substrates indicated the run temperature. For the optical constants measurement samples, a system of moveable shutters was fitted into the plant. The system allowed two sets of substrates to be coated in the same pump down cycle. One set was electron bombarded and the other not. It was felt that any difference in optical constants brought about by electron bombardment would be small, thus differences due to other evaporation conditions would be minimized this way. Because of space limitations on the substrate holder, only two sets of samples could be produced in each run that the shutters were utilized. Prior to all depositions, the chamber was glow discharged for ten minutes at about 1500 volts and 150 milliamps at 50 millitorr pressure of air to remove any oil vapor contamination backstreaming from the pumps. The evaporation conditions for each material are summarized in the following sections.

Antimony Trioxide (Sb_2O_3)

This material has proven useful as a high index layer in guided wave structures, as reported by Turner and Browning (1980) and Al-Jumaily, Browning, and Turner (1982). Since scattering losses in these structures can severely limit performance, the proper deposition conditions are important. Fine mesh powdered antimony trioxide from Cerac was first calcined at atmospheric pressure in a quartz dish at 500°C for one hour. This process rendered the fine white powder into slightly yellowed, more compact form. This material was evaporated from a platinum boat. Its outgassing during deposition raised the

pressure inside the chamber to values of $1.0-2.0 \times 10^{-4}$ torr, a much lower pressure than for non-calcined material. Substrates were heated to around 150°C or left at room temperature. Film thickness was monitored in reflection on a separate glass witness plate to a value of four quarterwaves at $\lambda=550$ nanometers for X-ray diffraction and TEM carbon replication samples, or alternately to a value of about 800 angstroms using a quartz crystal monitor for samples used in TEM direct film and electron diffraction analysis. The quartz crystal oscillator is useful for films whose thickness is insufficient to bring the optical monitor to a quarterwave turning point. In order to maintain a constant deposition rate of about 1.6 angstroms per second, it was necessary to steadily increase power to the source during the run. This fairly slow rate was the highest possible without blowing the evaporation material out of the boat with too much applied power.

Potassium Hexafluorozirconate ($2\text{KF} \cdot \text{ZrF}_4$)

This material has a short wavelength absorption cutoff well into the ultraviolet, around 120 nanometers, but is highly soluble in water. Bartle and Turner (1962) suggested that it could find use as a low index layer in multilayer filter structures, much as cryolite and chiolite have. The fine, white, crystalline powder from Alpha Products was evaporated from a molybdenum boat without prior treatment. These films were also monitored to four quarterwaves thickness at $\lambda=550$ nanometers. Since this material is so soluble in water, it was not practical to prepare thinner films for direct film TEM observations. Substrate temperature was either at ambient or near 100°C , while

pressure was $2.0-6.0 \times 10^{-5}$ torr during deposition. The material outgassed slightly when preheating, but the pressure soon returned to the value it had at the beginning of the procedure. The evaporation rate was very stable for the utilized source power level, being nearly 30 angstroms per second.

Silicon Monoxide (SiO)

The reflecting aluminum surfaces of astronomical telescopes have long been protected with a layer of silicon oxide. The films are usually referred to as SiO_x , since the exact stoichiometry depends greatly on the residual oxygen pressure and evaporation rate. Si_2O_3 and even SiO_2 films are possible for certain conditions, as shown by Allen (1982). Bradford et al. (1965) demonstrated an interesting increase in oxygen content for a silicon oxide film irradiated with ultraviolet light at atmospheric pressure. Chunks of silicon monoxide from E. Merck Company were evaporated from a tantalum boat. In order to maintain a film composition as close as possible to the original material, rapid evaporations of 20 angstroms per second at pressures near 3.0×10^{-5} torr were carried out. Substrate temperature was either near 150°C or room temperature. Film thickness was optically monitored to four quarterwaves at $\lambda = 550$ nanometers. A drop in pressure during evaporation and its subsequent rise thereafter indicated a certain amount of reaction of evaporant material with residual gases.

Zinc Sulfide (ZnS)

This widely used material has shown perhaps the most dramatic and useful improvement with electron bombardment. Although previously

scrutinized by Bangert and Pfefferkorn (1980), film samples were prepared for analysis to characterize the consistency of the electron bombardment process in the systems used in this study. Small chunks of zinc sulfide from Irtran were evaporated from a molybdenum boat. This material did not adhere well to heated substrates in the coating chamber, so they were left at room temperature. The evaporation rate was around nine angstroms per second at pressures of $0.5-1.0 \times 10^{-4}$ torr.

Magnesium Fluoride (MgF_2)

So-called "mag" fluoride is probably the most commonly used material for single layer antireflection coatings in the industry today. Its durability and adhesion when deposited on a hot (300°C) substrate make it very useful for widespread applications. Films were evaporated from a tungsten boat at a rate of 20 angstroms per second on a substrate heated to around 160°C . Pressure was $6.0-9.0 \times 10^{-5}$ torr.

Several bare substrates were electron bombarded without film deposition to check for anomalous effects and oil vapor contamination, as suggested by Holland (1963). If oil contamination were present, the electrons would cause a reaction with the residual gases, leading to brownish deposits. No discoloration was observed on the front surface, but a small amount of metallic deposit was seen on the back of the substrate, near one end. This was attributed to a small amount of sputtering of aluminum substrate holder material due to its high potential. The holder fluoresced with a blue glow at the edges of the substrates and at several tiny points as it came near a grounded, sharply pointed heater shield during its rotation under electron

bombardment. This was not perceived as a problem which would affect the deposited films, so no steps were taken to correct it.

CHAPTER 4

ANALYSIS METHODS

Several techniques were used to analyze the films, each described in its own section below.

X-Ray Diffraction- Diffractometer

X-ray diffraction has long been known to be an effective, non-destructive method of obtaining precise quantitative information about not only thin films, but a wide variety of other material forms as well. Turner and Ullrich (1947) used this analysis to effectively explain birefringence in magnesium fluoride films. The theory is marvelously described by Cullity (1978), so no attempt will be made to detail it here.

The specific X-ray technique used in this study involves the diffractometer (GE model XRD-5), shown in Figure 4.1. Cu K α_1 X-rays from a copper source tube are defined into a beam by a narrow slit of 3° angular width. This impinges on the sample at a particular angle 2θ , which in this case was scanned from 20° to 80° at 4° per minute. The sample scatters the X-rays in all directions, but the detector is situated so that it sees only those X-rays leaving the sample at the same angle that the incident rays strike it. The detector sits behind a 0.2° angular slit and a nickel filter, the slit defining the beam

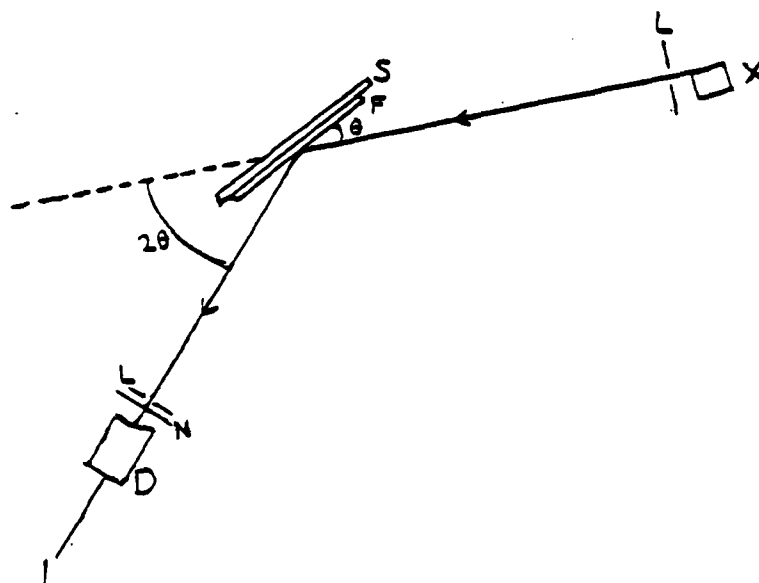


Figure 4.1. X-Ray diffractometer diagram.

X - x-ray source tube, L - slit, S - sample substrate, F - film or powder, N - nickel filter, D - detector, I - to rate counter.

and the filter blocking unwanted secondary X-ray emission of longer wavelengths.

Actually, each atom in the sample scatters the X-rays in all directions. Since a crystal is composed of a regular, repeated arrangement of atoms, the scattered X-rays overlap and interfere in a definite pattern. The sample scatters X-rays strongly when the incident angle and wavelength satisfy the Bragg relation

$$n\lambda = 2d\sin\theta,$$

where n is an integer, λ is the X-ray wavelength, θ is the incident angle, and d is a particular lattice plane spacing in the sample. The strongly scattered beam, called Bragg diffraction, leaves the sample at the same angle that the original beam was incident on it. Thus when a film crystallite is oriented such that a particular set of its lattice planes is parallel to the substrate and the incident angle satisfies the Bragg relation, a peak occurs in the diffractometer trace of X-ray counts versus angle of incidence. Therefore, each peak in such a trace corresponds to its own set of lattice planes. Knowing the X-ray wavelength, one can compute the lattice spacing, or vice versa. Fang and Bloss (1966) have compiled a table of lattice spacings as a function of diffractometer angle for several different X-ray sources. Smith (1945) has assembled an index of lattice spacings for an astounding number of materials in powder form, along with the corresponding Miller indices. The Miller indices define the particular group of atoms within a crystal structure, the spacing between the

planes of which is the d of the Bragg formula. More exactly, if one considers a crystal to be composed of a repeated assembly of unit cells composed of only a few atoms, the Miller indices give the number of units in three different directions from a point which must be traversed to reach the corresponding point in the next unit cell. The lattice spacings of different sets of Miller indices for a material thus indicate the separations of various specific points in the lattice from each other. For many materials, not only the Miller indices and lattice spacings are given, but also the relative strengths of the diffraction peaks are listed for powder samples.

Not only the films but also the evaporation material itself can be analyzed with the X-ray diffractometer. This can give an idea of how the evaporation affects the crystal structure. To prepare such a powder sample, a glass slide is smeared with petroleum jelly as an amorphous adhesive. Then a small amount of the powder to be analyzed is spread out over the slide. This sample then goes through the same procedure of X-ray analysis as the thin film samples. As a check, a diffractometer trace was made of a slide with the adhesive only. Figure 4.2 shows this trace to have no peaks, so the background of the adhesive does not alter the powder traces.

For materials exhibiting no crystal structure, or amorphous materials, the X-ray diffractometer trace will have no discernable peaks. Also, it should be pointed out that the X-ray diffractometer analyzes the basic internal molecular arrangement of the film material. Overall film microstructure, i.e., the well known characteristic columnar growth, will not be straightforwardly deducible from the

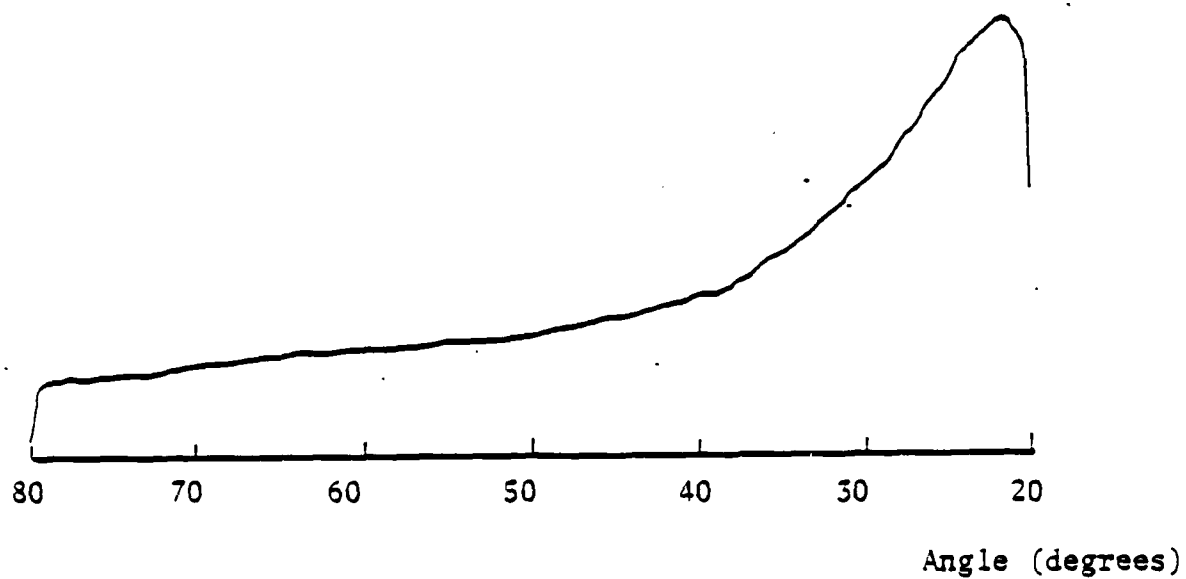


Figure 4.2. X-Ray diffractometer trace of adhesive for powders.

X-ray data. The diffractometer used in this study did not have a rocking mechanism on the sample mount, so only lattice planes parallel to the substrate could be detected.

Transmission Electron Microscopy- Carbon Replication

Whereas the X-ray diffractometer gives a view of molecular arrangements within the thin film, a carbon replica of a film cross section viewed in a transmission electron microscope (TEM) provides interesting information about overall thin film microstructure, as shown by Guenther and Pulker (1976). This technique is an excellent means of ascertaining the effects of varying process parameters on film properties.

Carbon replicas of thin film cross sections are prepared by employing the same basic procedure as given by Pearson (1970). A substrate is scored on its filmed side with a diamond tip, making a one millimeter scratch at one edge. Pressure exerted from the opposite side of the substrate causes it to break along a fairly straight line, starting at the scratch mark. This exposes a cross sectional edge of the substrate-film combination. The piece with this edge is placed in a vacuum chamber, where it is first coated with a platinum-carbon pre-shadow at an angle of about 70° . Next, a support film of pure carbon is deposited, forming a continuous layer over the cross section and top of the sample. Figure 4.3 diagrams the carbon evaporating configuration. The carbon coated sample is then removed from the vacuum chamber. After scoring the carbon film into several sections, the sample is slowly dipped into a five percent hydrofluoric acid (HF)

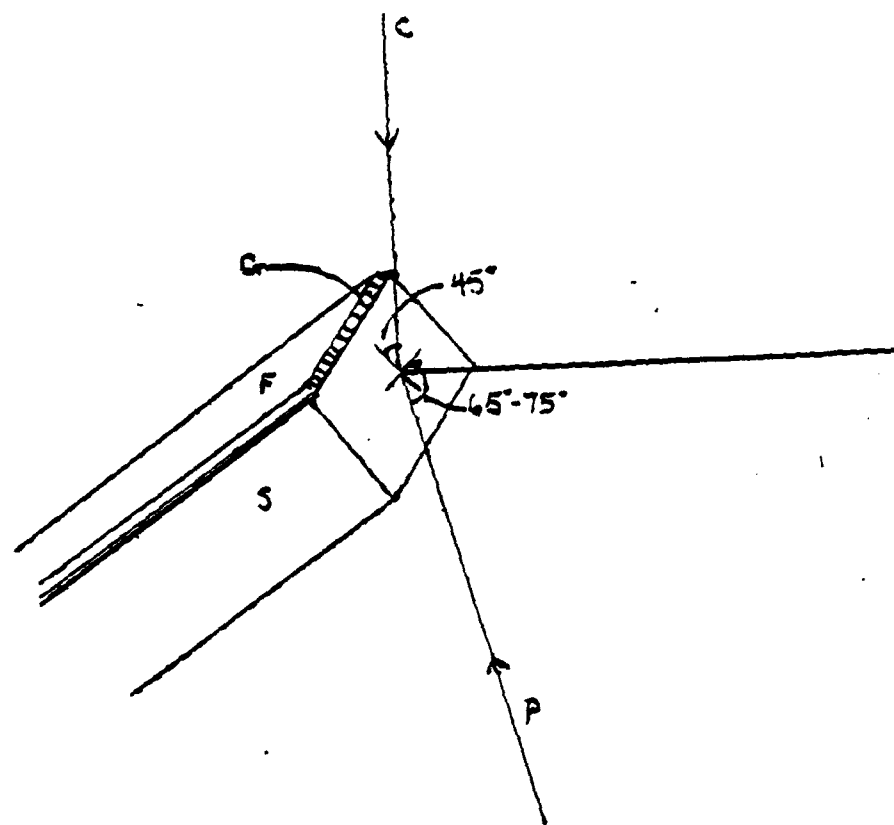


Figure 4.3. Carbon replica film application geometry.

F - film, S - substrate, G - columnar growth artifacts,
P - direction of incidence of platinum-carbon vapor,
C - direction of incidence of carbon vapor.

planes of which is the d of the Bragg formula. More exactly, if one considers a crystal to be composed of a repeated assembly of unit cells composed of only a few atoms, the Miller indices give the number of units in three different directions from a point which must be traversed to reach the corresponding point in the next unit cell. The lattice spacings of different sets of Miller indices for a material thus indicate the separations of various specific points in the lattice from each other. For many materials, not only the Miller indices and lattice spacings are given, but also the relative strengths of the diffraction peaks are listed for powder samples.

Not only the films but also the evaporation material itself can be analyzed with the X-ray diffractometer. This can give an idea of how the evaporation affects the crystal structure. To prepare such a powder sample, a glass slide is smeared with petroleum jelly as an amorphous adhesive. Then a small amount of the powder to be analyzed is spread out over the slide. This sample then goes through the same procedure of X-ray analysis as the thin film samples. As a check, a diffractometer trace was made of a slide with the adhesive only. Figure 4.2 shows this trace to have no peaks, so the background of the adhesive does not alter the powder traces.

For materials exhibiting no crystal structure, or amorphous materials, the X-ray diffractometer trace will have no discernable peaks. Also, it should be pointed out that the X-ray diffractometer analyzes the basic internal molecular arrangement of the film material. Overall film microstructure, i.e., the well known characteristic columnar growth, will not be straightforwardly deducible from the

X-ray data. The diffractometer used in this study did not have a rocking mechanism on the sample mount, so only lattice planes parallel to the substrate could be detected.

Transmission Electron Microscopy- Carbon Replication

Whereas the X-ray diffractometer gives a view of molecular arrangements within the thin film, a carbon replica of a film cross section viewed in a transmission electron microscope (TEM) provides interesting information about overall thin film microstructure, as shown by Guenther and Pulker (1976). This technique is an excellent means of ascertaining the effects of varying process parameters on film properties.

Carbon replicas of thin film cross sections are prepared by employing the same basic procedure as given by Pearson (1970). A substrate is scored on its filmed side with a diamond tip, making a one millimeter scratch at one edge. Pressure exerted from the opposite side of the substrate causes it to break along a fairly straight line, starting at the scratch mark. This exposes a cross sectional edge of the substrate-film combination. The piece with this edge is placed in a vacuum chamber, where it is first coated with a platinum-carbon pre-shadow at an angle of about 70° . Next, a support film of pure carbon is deposited, forming a continuous layer over the cross section and top of the sample. Figure 4.3 diagrams the carbon evaporating configuration. The carbon coated sample is then removed from the vacuum chamber. After scoring the carbon film into several sections, the sample is slowly dipped into a five percent hydrofluoric acid (HF)

solution, allowing the carbon film to float free. Extreme caution must be exercised during the dipping to prevent the support film from tearing along the corner formed by the top and cross sectional edge of the sample. The carbon must be allowed to soak in the HF overnight to dissolve away any traces of sample material still adhering to it. This insures that only the skeletal shadow of sample film features formed by the evaporated platinum remains on the carbon support film. Deionized water replaces the HF solution using a slow flush. After this, the carbon film is carefully broken along the scored lines and the resulting pieces scooped up onto the dull sides of 300 mesh copper grids. The carbon replica is then viewed in a Phillips model EM 200 TEM at an 80 keV energy level and the results photographed.

It is of interest to note that some apprehension has been expressed by Heavens (1965) about the carbon replica being somehow deformed by the concentrated beam of the TEM, possibly leading to erroneous interpretations of the photographs. This did not seem to be a problem in this study, since the images showed no noticeable change while under observation in the TEM.

Transmission Electron Microscopy- Direct Film Observation

While the carbon replicas discussed in the preceding section give a view of cross sectional film microstructure, TEM observations of the actual films themselves provide additional information about not only microstructural crystallite size, but internal crystal structure as well. It should be pointed out here that artifacts such as columnar growth are not observable with direct film TEM, and scanning electron

microscopy (SEM) of actual film cross sections shows low contrast and generally poor results, also pointed out by Guenther and Pulker (1976).

The procedure for preparing samples for direct film TEM observation is extremely simple, except for making the grids on which the films are to be mounted. Fortunately, these "holey" grids were fabricated and made available by the operators of the TEM, so only the reference for their preparation technique by Fukami and Adachi (1965) will be given here. Basically, a film of the material of interest is deposited in the usual manner, except that the substrate must be water soluble. This is the reason for using sodium chloride plates in these runs. Also, film thickness must be less than 1000 angstroms to allow electron penetration in the TEM. After deposition, the sample is removed from the vacuum chamber and the film is scored into many small sections. The substrate is then slowly dipped into deionized water and the film floats free. After several minutes, the film is broken into pieces which are scooped up onto the holey grids. These grids are then observed in a Jeol model JEM 100B TEM at 100 keV electron energy level.

By a manipulation of the electron optics controls of the TEM, one can produce electron diffraction patterns of the film as well as high magnification images. Electron diffraction is essentially the same type of effect as X-ray diffraction, the main difference being wavelength of the incident radiation. A constructive interference of the electron waves leads to concentrations of intensity at certain angles corresponding to the lattice spacings of the material. The concentric rings of the resulting patterns not only can be analyzed for

lattice spacings, as with X-ray diffraction results, but also relative crystallite sizes can be inferred from the grainy appearance of the rings, well explained by Thun and Hass (1958).

Lattice spacings can be computed from the formula

$$d = n\lambda / (2\sin\theta),$$

where λ is the electron wavelength, θ is the measured angle of a line, and n is an integer. This is the exact Bragg diffraction formula for X-rays as well.

At extremely high magnification, the electron microscope reveals interference fringes of the electrons from the lattice planes. The spacing of these fringes can be measured and compared to those of a graphitized carbon reference sample, which are known to be 3.4 angstroms apart. The fringe spacings were measured from photographs using a stereo viewer with a 0.7x objective and a 10x ruled filar eyepiece.

Guided Wave Analysis (Prism Coupler)

The methods of the previous sections reveal the physical structure of thin films on a microscopic level. Such high resolution techniques are necessary to detect the minute changes brought about by electron bombardment. Changes in the optical properties are equally subtle, requiring precise measurement capabilities.

One such measurement involves coupling monochromatic light with a prism into the film to be analyzed, described by Tien et al. (1969). Figure 4.4 diagrams the set-up. The light, here a collimated laser beam, enters one face of the coupling prism and is refracted toward another face, the hypotenuse. The prism angle between these two faces is such that the incident angle of the light on the hypotenuse is greater than critical, so the light is totally internally reflected. The film to be studied is brought very close to the prism hypotenuse, so that the air gap between them measures only a few wavelengths. The coupling prism assembly sits on a turntable, separated from the laser. The angle of the light entering the prism is now varied by manually rotating the turntable. Films of sufficient thickness can "capture" some of the light from the prism hypotenuse when the proper angles are reached, "frustrating" the total internal reflection. When this occurs, a dark band called a mode line is evident in the totally reflected beam, and often a streak of guided light appears across the film. By measuring these coupling angles and knowing the prism and substrate properties, the film's refractive index and thickness can be calculated.

The basic electromagnetic theory of guided waves has been described by Kapany and Burke (1972), as well as other authors. One can assume a zig-zag ray model for the guided light, as suggested by Figure 4.5. Starting at point A, we assume a phase of zero. In propagating to point B, the phase becomes $(n_f d \cos \alpha) / \lambda$. On total internal reflection, an additional phase of $-\pi_{12}$ occurs. In going to point C, again a phase of $(n_f d \cos \alpha) / \lambda$ is added. Finally, another total internal reflection phase of $-\pi_{10}$ occurs. When the total phase change in going from point

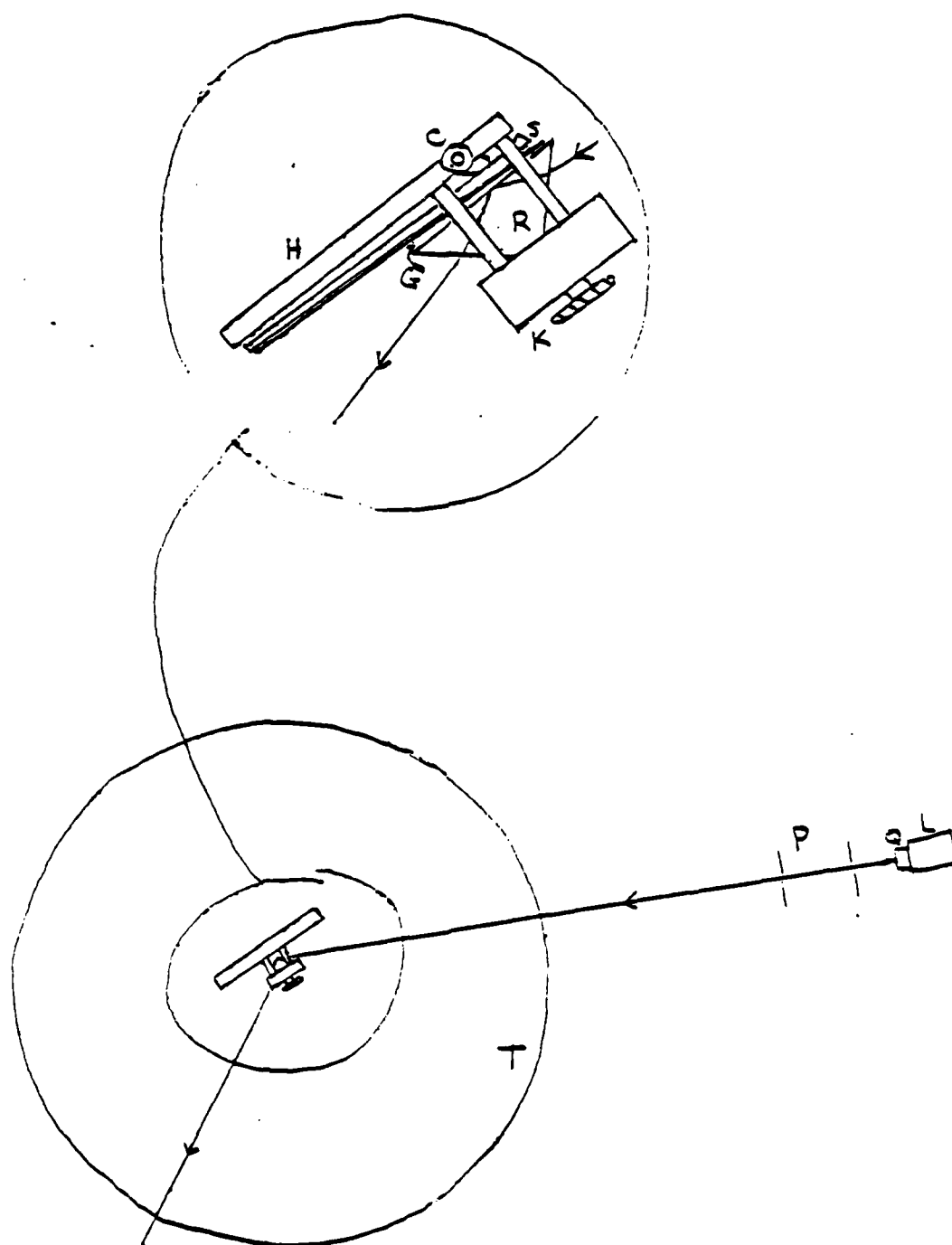


Figure 4.4. Prism coupler configuration.

L - laser, Q - half wave plate, P - pinholes,
 T - turntable, K - screw clamp, C - cam shaft,
 S - sample, R - coupling prism, G - air gap.

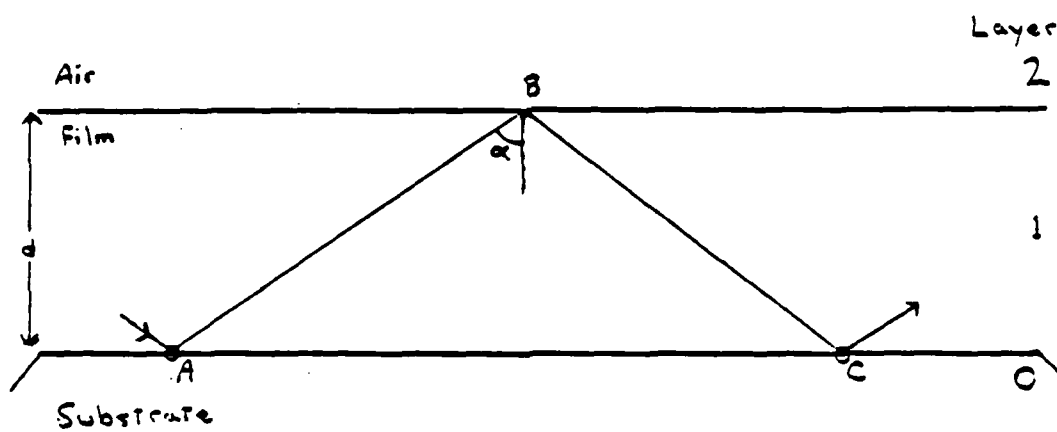


Figure 4.5. Zig zag ray model of guided light.

A to point C is an integral multiple of 2π , the waves can constructively interfere and reinforce each other, allowing propagation to continue. This is a simplified explanation of the dispersion relation

$$2n_f d \cos \alpha / \lambda - \phi_{12} - \phi_{10} = 2m\pi,$$

where the integer m is called the mode order. ϕ_{12} and ϕ_{10} vary with polarization, so the dispersion relation requires that for a given film, s and p polarizations propagate at different angles α . The dispersion equation is straightforwardly deducible from Maxwell's equations, as taught by Burke (1980).

Two programs exist in our laboratory to perform waveguide index calculations. The first, CUPIO, was written as partial requirement for a Master's degree by Bruce Reinbolt (1975). The required inputs are wavelength of light, prism refractive index and angle, substrate index, and two coupling angles for either s (TE) or p (TM) polarization. To use this program, the film must be thick enough to support at least two modes of either polarization. A subsequent program based on the same procedure was written by myself to allow calculations for thinner films, where only one s and one p mode are present. Basically, the programs start with an assumed film refractive index. Substituting this value into the dispersion equation for guided modes and the expressions for the phase shifts at the air-film and film-substrate boundaries leads to an error. This error establishes a refinement of the originally assumed value. This iteration continues until the error is negligible. Having thus computed film index, the

thickness is immediately derived from the dispersion relation. Both programs assume homogeneous, isotropic single layers.

The equipment used in this study has been in use in the laboratory for several years to measure the optical properties of many different thin films. A helium-neon laser (Spectra Physics model 120, 5 milliwatt) is fitted with a rotatable half wave plate polarizer. This enables either s or p polarized light to be used. The coupling prism was strontium titanate (SrTiO_2) with an index of 2.391 and prism angle of 43.335, or alternately flint glass, with index 1.8418 and angle 43.374. Because of the prism clamp arrangement, only a certain range of coupling angles was possible. Thus it was sometimes necessary to use two different prisms to cover the entire range of possible mode indices. When this was called for, a simple calculation allowed conversion of coupling angles for input into the computer programs. A screw clamp on a teflon holder held the prism against the filmed side of the substrate, while an adjustable cam shaft pressed on the opposite side to improve the coupling efficiency. The assembly rested on an XYZ stage set on a Societe Genevoise turntable. This enabled angle measurements to the nearest second of arc, although for each observed mode the uncertainty in measured coupling angle amounted to a few minutes.

The precision of this method derives from the ability to measure the coupling angles so exactly. Uncertainty in the position of the coupling can be minimized by not pressing the prism too tightly against the film, and this also diminishes the effect of the prism on the modal behavior of the film, a problem pointed out by King and Talim

(1981). Of course, only films with refractive index higher than the substrate can be analyzed this way, and the films must be thick enough to support at least two modes to be able to calculate both refractive index and thickness.

Surface Plasma Wave Analysis

Another extremely sensitive technique for determining film refractive index involves coupling radiation into a surface plasma wave (SPW) on a thin metal film, detailed by Raether (1977) and used by Abeles (1976). This is essentially an induced absorption situation, described from an admittance point of view by Turner and Berning (1955). As they explain, a single absorbing film can absorb all the incident light if it is backed by a perfect reflector and this combination antireflected. The perfect reflection arises from total internal reflection from a prism hypotenuse, seen in Figure 4.6. The antireflection comes about by tailoring the thickness of the absorbing layer to match the admittance at the air-absorber interface to that at the absorber-prism interface. More directly, at angles of incidence on the hypotenuse greater than critical, the admittance in the air becomes purely imaginary, thus total reflection occurs. The absorber has a complex index, so the admittance through this layer assumes complex values. After passing through a certain thickness of absorber material, the admittance has become purely real. For the right absorber thickness and incident angle, This real admittance matches that inside the glass. Turner and Berning matched admittances by adding a dielectric phase layer between the glass and absorber. This phase

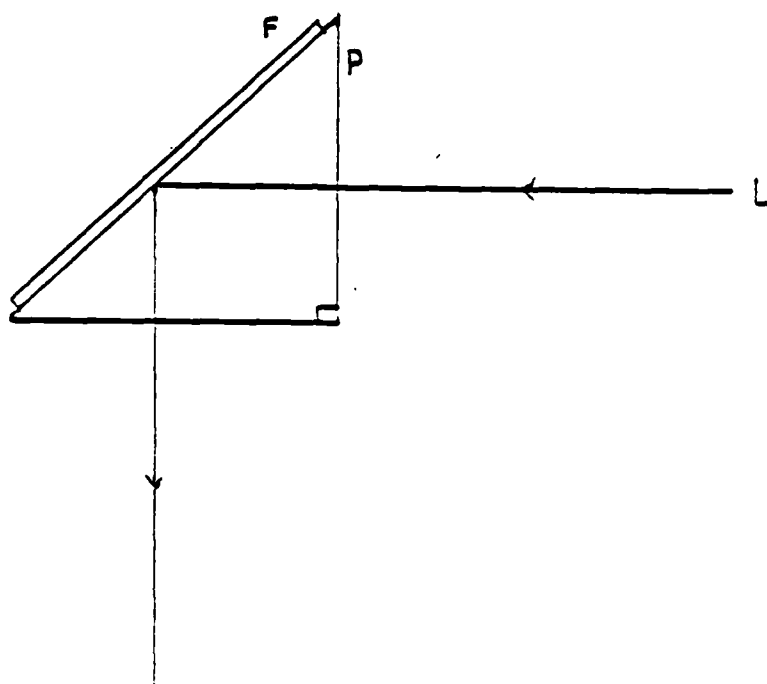


Figure 4.6. Induced absorption sample (SPW).

layer and its effects on absorption merit closer attention in the light of the study by Otto and Sohler (1971). These authors suggest the excitation of guided modes in a dielectric film on the other side of the absorber, in particular the lowest order p mode behaving as a surface plasma wave. It seems reasonable that induced absorption and surface plasma waves are really two different views of the same phenomenon in this configuration, but as stated, further inquiry is in order.

The hypotenuse of a right angle prism is coated with a thin silver film in the evaporation plant. The prism is then placed on a spectrometer table and illuminated through one face with a laser beam. The assembly is shown in Figure 4.7. The beam totally internally reflects off the hypotenuse, exits through the other prism face and into a detector-telescope combination. The reflectivity is measured as a function of incident angle and plotted. At a particular angle, the reflectivity dips to a minimum due to the excitation of a SPW at the air-silver interface. This attenuated total reflection technique is known as the Kretschmann configuration. Knowing the thickness of the silver film, its optical constants can be computed from the profile of the reflectance dip. Once these constants are established, the prism is again placed in the coating chamber. A dielectric film is then deposited, and the measurement process repeated. Dielectric film thickness must be monitored to an effective half wave at the incident angle for which the reflectivity was minimum. Now the refractive index and thickness of the dielectric layer can be computed from its reflectance dip profile. The computations assume uniform layers and no absorption in the dielectric layer. The angle as measured on the

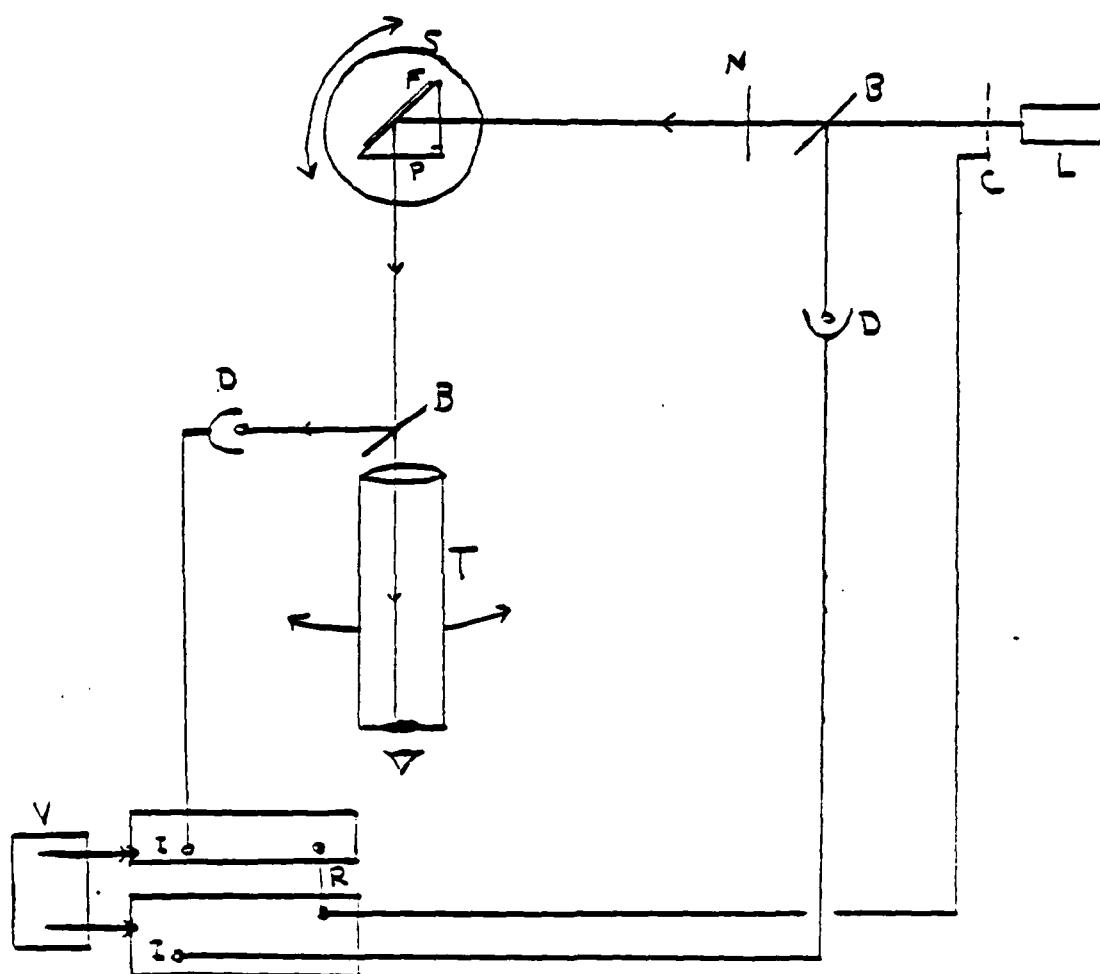


Figure 4.7. Surface plasma wave (Induced absorption) measurement configuration.

L - laser, C - chopper, B - beam splitter, N - neutral density filter, P - prism, F - film, D - detector, T - spectrometer telescope, I - lock-in amplifier signal input, R - lock-in amplifier reference input, S - spectrometer table, V - divider.

spectrometer had to be converted into incident angle on the hypotenuse using Snell's law and the prism angle. Also, the reflectivity values had to be corrected for the four percent reflection loss at each of the other two faces. This was accomplished by simply dividing the measured value by 0.92. The 100 percent reading was established by removing the prism from the table and rotating the detector arm until the incident laser beam shone directly into it. As with the guided wave technique discussed in the previous section, the sensitivity of this method owes itself to the high degree of angle measurement precision. Also, dielectric films of any refractive index can be analyzed.

Highly precise right angle prisms of borosilicate glass ($n=1.516$) were obtained from Melles-Griot. They were subjected to the same cleaning procedure as the microscope slides previously discussed. Four prisms at a time were coated in the plant with silver evaporated from a molybdenum boat. Thickness was monitored with the quartz crystal monitor to a value near 50 nanometers.

Each prism was measured on a Wild number 79 spectrometer and its silver film constants computed. As a check, two prisms were returned to the chamber. One was electron bombarded at 1000 volts for six minutes, the flux level being 1.3×10^{15} electrons per square centimeter per second. The other was shuttered during this bombardment. These two prisms were then taken out and remeasured, and one of the other prisms which had been left out of the chamber was also remeasured. Table A3 lists the measurement results for these prisms for the before and after cases. The slight change in optical constants brought on by electron bombardment is not significant when

compared to the change due to oxidation of the silver surface layer or variations in the measurement conditions.

After measuring the bare silver films of all four prisms, two were placed in the coating chamber. As a check, both were coated simultaneously with the dielectric material. They were then removed and measured on the spectrometer. The two remaining prisms were then placed in the chamber. One was overcoated with the dielectric while being electron bombarded at 2000 volts and a flux level near 1.6×10^{15} electrons per square centimeter per second. The other was shuttered during this deposition. When the first prism had been completed, the shutters were moved to cover it and expose the remaining prism, all without breaking vacuum. This prism was given the same coating but without electron bombardment. The same power level was applied to the evaporation source to try and match the deposition rates, and thickness was controlled with the quartz crystal monitor.

An initial series of runs was made with the optical monitor to establish a rough idea of the quartz monitor behavior, but these samples generally were not close enough to the required thickness to give precise results. Also, the chamber was not glow discharged prior to dielectric deposition because of the catastrophic effect on the silver films. The same four prisms were reused for each material. The old coatings were stripped off in a warm nitric acid solution of about 50 percent. They were then washed under tap water with cotton and Liquinox soap, rinsed thoroughly with deionized water, and blown dry with the nitrogen gun.

The computer programs available for the optical constants calculations from these measurements were written by Dr. J.F. Tang. They are based on a random sampling approach to finding the global extremum of a merit function, used by Tang and Zheng (1982) as the basis for a numerical synthesis technique for designing multilayer interference filters. Basically, initial ranges of values for the optical constants are input, along with the corrected reflectivity measurements at three different angles in the reflectivity dip. The programs initiate a search throughout the ranges for values which will minimize the merit function. This merit function is an expression comparing the reflectivity dip profiles of the initial and refined optical constants. An error factor, representing the size of this merit function, gives a rough idea of the accuracy of the computed values.

In general, the silver film results were accurate to three decimal places, as indicated by the extremely low error factor. Unfortunately, the dielectric films did not always exhibit similar precision. Only two decimal places were reliably determined. Small amounts of absorption, scatter, and film inhomogeneity probably all contributed to the lack of precision in these measurements.

Appendix 3 shows a few representative graphs of measured reflectivity as a function of corrected angle for bare silver films and subsequent dielectric deposits.

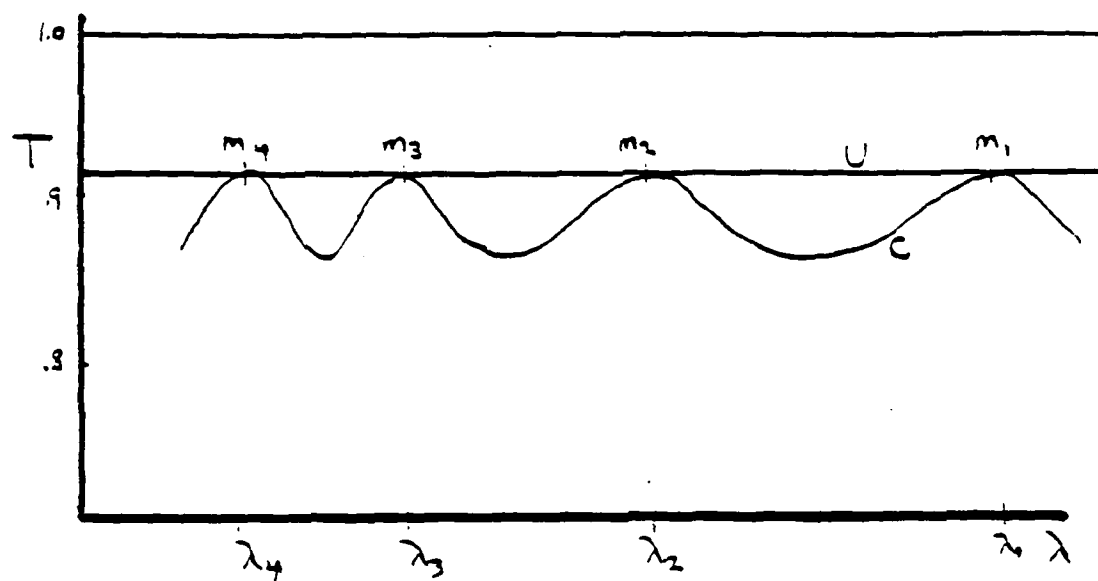
Spectrophotometer Analysis

A spectrophotometer can provide reflectance or transmittance of a sample as a function of wavelength over a wide spectral range.

From this, the optical constants can be computed. The method enjoys widespread use and has been explained quite elegantly by Berning (1963) and summarized by Turner (1976), but the precision is not as great as the two preceding methods. However, it was employed in this study to obtain an easily understood presentation of the effects, if any, of electron bombardment on film optical properties.

Basically, the double beam spectrophotometer (Cary 14) measures relative transmittance or reflectance by comparing the intensities of two different beams from the same source. Wavelength of the incident light is scanned using a dispersing prism in tandem with a ruled diffraction grating. A bank of compensating resistors corrects for variations in source output and detector response with wavelength. The beams are first compared with no sample present to establish a 100 percent line. Then the sample is inserted into the path of one of the beams and the wavelength scan is repeated. The visible spectrum between the wavelengths 330 and 650 nanometers was investigated. Using some simple relations between refractive index, physical thickness, and reflectance or transmittance, the film's refractive index can be calculated. To improve the accuracy and eliminate material dispersion effects, film physical thickness was measured separately using a Hilger-Watts FECO interferometer, and this value was used in the equations. Using Figure 4.8, we see the expression for film index becomes;

$$n_f = (m\lambda/2)/h_f,$$



$$n_f h_f = m_i \lambda / 2$$

$$m_{i+1} = m_i + 1$$

Figure 4.8. Spectrophotometer transmittance curve.

where h_f is the physical thickness value from the FECO, m is an integer, and λ is the wavelength at which the transmittance is an extremum. This is a maximum for a film with index higher than that of the substrate, and a minimum for a film with lower index. Basically, the rays reflected from the air-film interface interfere with those reflected from the film-substrate interface. For certain wavelengths of light, the thickness of the film causes this interference to be constructive, or the rays to be added in amplitude. Other wavelengths suffer destructive interference. Wavelengths for which the thickness causes no addition or subtraction display reflection and transmission equal to that of the bare substrate. At these wavelengths, the optical thickness of the film is one half of the wavelength.

Comparing reflectance and transmittance curves, a rough idea of film absorption loss can be obtained. Any bulk and surface scattering losses will be included in this calculation. For a perfect dielectric film with no loss, reflectance and transmittance at any wavelength will add to unity. The difference in this sum from unity represents film losses.

The FECO (Fringes of Equal Chromatic Order) measures physical thickness of a film by looking at the wavelength shift of interference minima (dark fringes) between the sample and a reference flat surface. The sample consists of a substrate coated with a film patch forming a step, then entirely coated with aluminum, as shown in Figure 4.9. The aluminum provides a highly reflecting surface to improve fringe contrast and eliminate phase shift differences in the reflections from the air-film and air-substrate interfaces. The sample-reference

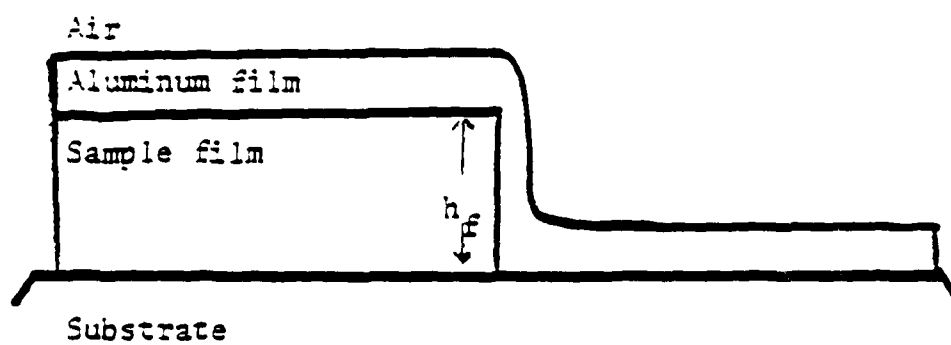


Figure 4.9. FECO sample configuration.

interface is illuminated with white light at the step using a microscope objective. The reflected light is dispersed with a prism and viewed with an eyepiece. The field shows dark fringes at the wavelengths for which the distance between the sample and reference flat is an integral number of half waves. There is a displacement in wavelength of each fringe at the sample step. By measuring this shift for the different fringes (interference orders), the height of the step above the substrate (film thickness) can be calculated. Figure 4.10 diagrams the set up. From this figure, we get the expression for h_f to be

$$h_f = (\Delta\lambda/2)\lambda'/(\lambda' - \lambda),$$

where the quantities are as labeled.

Adhesion, Hardness, and Moisture Resistance

The physical properties of thin films, when considered on a macroscopic level, include film hardness, degree of adhesion to the substrate, and resistance to penetration and damage by water vapor in the atmosphere. Simple, straightforward tests of these properties were performed on bombarded and non-bombarded film samples of all the materials in this study. The first two tests were explained in detail by Macleod (1969).

The well known "Scotch tape" test provides a rough idea of how strongly a film adheres to its substrate. As the name implies, a strip

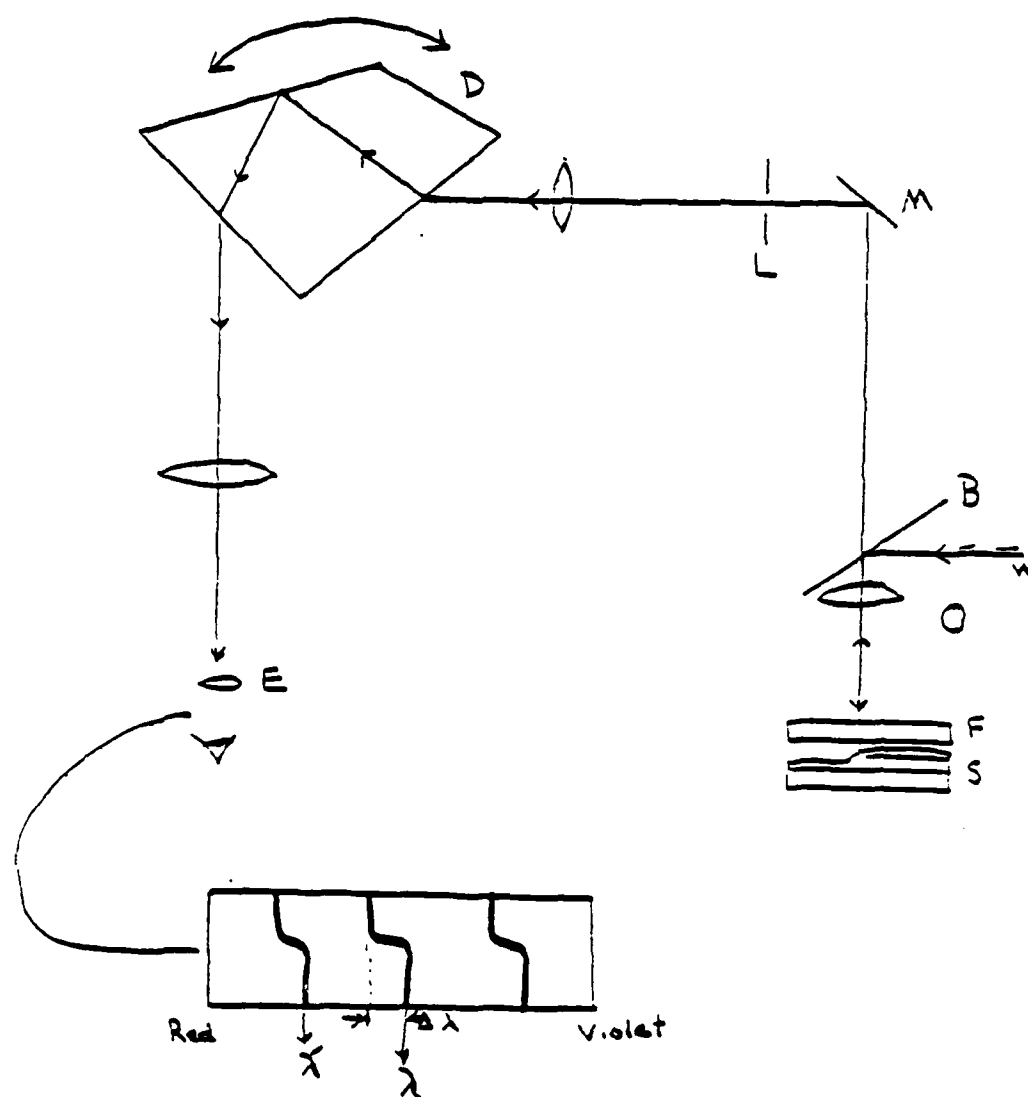


Figure 4.10. FECO measurement configuration.

S - sample, F - reference flat,) - microscope objective, W - white light, B - beam splitter, M - mirror, L - slit, D - dispersing prism, E - eyepiece.

of common cellophane tape is applied to the film and then lifted off. If the film peels off with the tape, it obviously is not adhering well.

Equally crude but just as effective is the "eraser" test of film hardness. The sample is rubbed with a pencil eraser to see if any scratch damage can be inflicted. This gives an idea of how strongly a film can "hold itself together". Different films can be compared by applying the same number of strokes at the same pressure to each sample. In this test, 20 strokes of the eraser at moderately high pressure were applied, about the same conditions as trying to remove a pencil mark from paper. Certain devices exist which allow for little variation in test harshness, but none was available. All samples were subjected to this test at the same time, and every effort was made to keep the same applied pressure on each sample.

In addition, films placed in a controlled humidity chamber can be observed for moisture resistance. By gradually increasing the relative humidity in the chamber, the level at which damage begins can be determined, as well as the extent of penetration and damage. A Blue M model VP 100AT-1 chamber was used for this investigation. Samples were left for at least 24 hours at each of several successively higher relative humidities, and the results of a visual inspection of the samples were collected. Relative humidity was determined by comparing wet and dry bulb thermometer readings and consulting a table provided by the chamber manufacturer.

The durability test results for all materials are gathered in Appendix 4.

CHAPTER 5

RESULTS

The analytical results for each material appear in the following sections.

Antimony Trioxide

According to Remy (1956), the crystalline state of antimony trioxide can exist in two forms. Cubic senarmonite is stable below 570°C while rhombic valentinite is stable above this temperature. X-ray diffraction analysis of the powdered source material reveals a great number of peaks for both structures. The data table has listings for only the cubic form, and the peaks with no corresponding listing were assumed to be due to the presence of rhombic structure. Certain changes accompanied the evaporative heating of the powder. Almost all peaks were still observable after heating, but that at 27.6° corresponding to the (222) lattice plane spacing was greatly enhanced. Also the peak at 32.2° corresponding to the (400) planes was slightly reduced. Figure 5.1 is a graph of X-ray intensity versus incident angle for the two powder samples of antimony trioxide, with some of the peaks identified.

Thin film samples showed only several of the most intense peaks that appeared in the powder samples. The angles, lattice spacings, and corresponding Miller indices are given in Table 1. Only

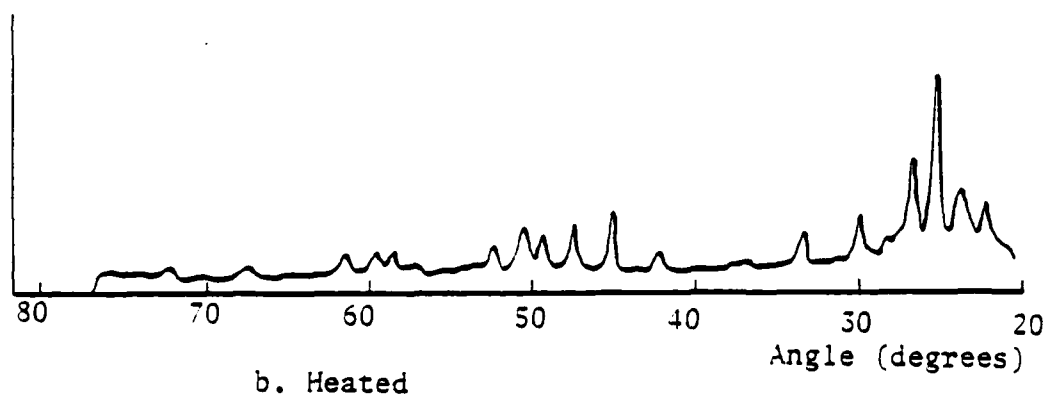
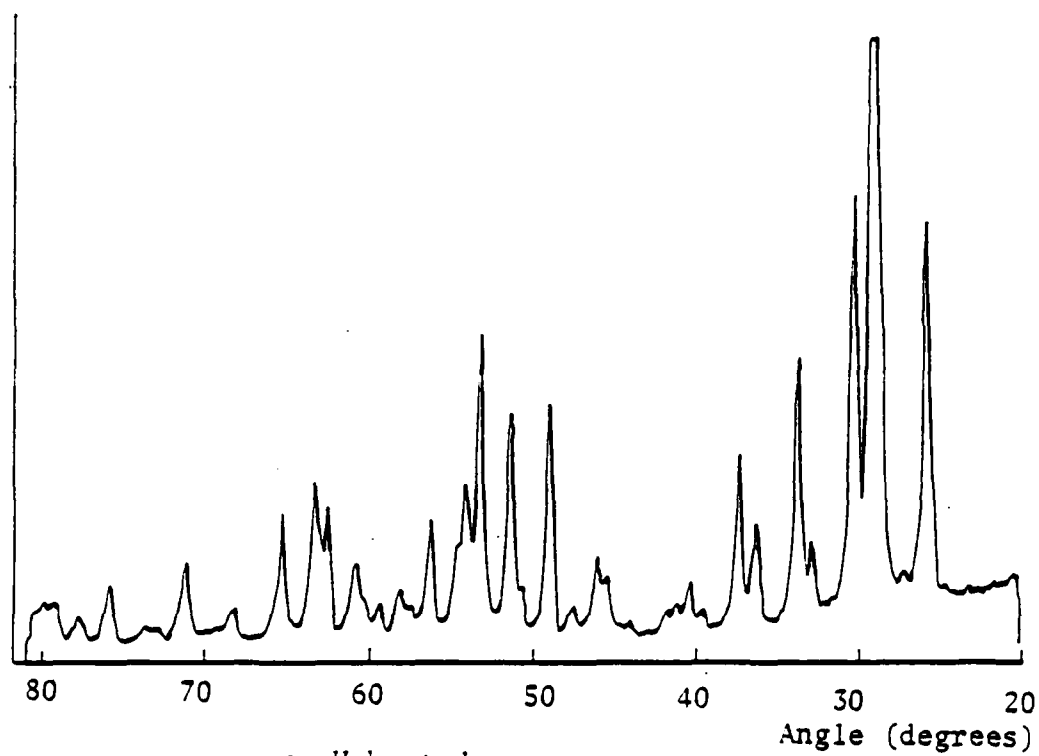


Figure 5.1. X-ray diffractometer traces of antimony trioxide powder.

Note: Top graph has expanded vertical scale.

peaks associated with the cubic form appear, and the same peaks are evident for both heated and unheated substrates. Figure 5.2 shows the traces for thin film samples of antimony trioxide on heated and unheated substrates for several electron bombardment voltages. The electron bombardment conditions for each sample are listed by its graph. These plots show a reduction in the peaks of the (222) and (440) planes, and an enhancement of the (400) peak, with electron bombardment. In other words, there is not a rearrangement of the crystal structure per se, but a different set of lattice planes becomes preferentially oriented parallel to the substrate. The X-ray diffractometer traces provide the most concrete evidence of bombarding electrons affecting the microstructure. As previously shown, the molecule arrival rate typical of the antimony trioxide films was 1.72×10^{15} molecules per square centimeter per second. Electron arrival rates were 1.6×10^{12} to 1.5×10^{15} electrons per square centimeter per second, at energies from 1000 to 2000 electron volts. It is apparent from the traces that these different flux levels and energies did not produce very large differences from each other in the crystal microstructure of the evaporated films.

Apparently an electron to molecule arrival ratio of less than 0.01 was sufficient to nearly saturate the bombardment effect. It is interesting to note Figure 5.2b, the trace of the film bombarded after deposition. The film was bombarded for 10 minutes at a flux of 1.4×10^{15} electrons per square centimeter per second at a potential of 1000 volts. Comparing this trace to the others, we see that the (222) peak suppression is not quite as pronounced as in films where

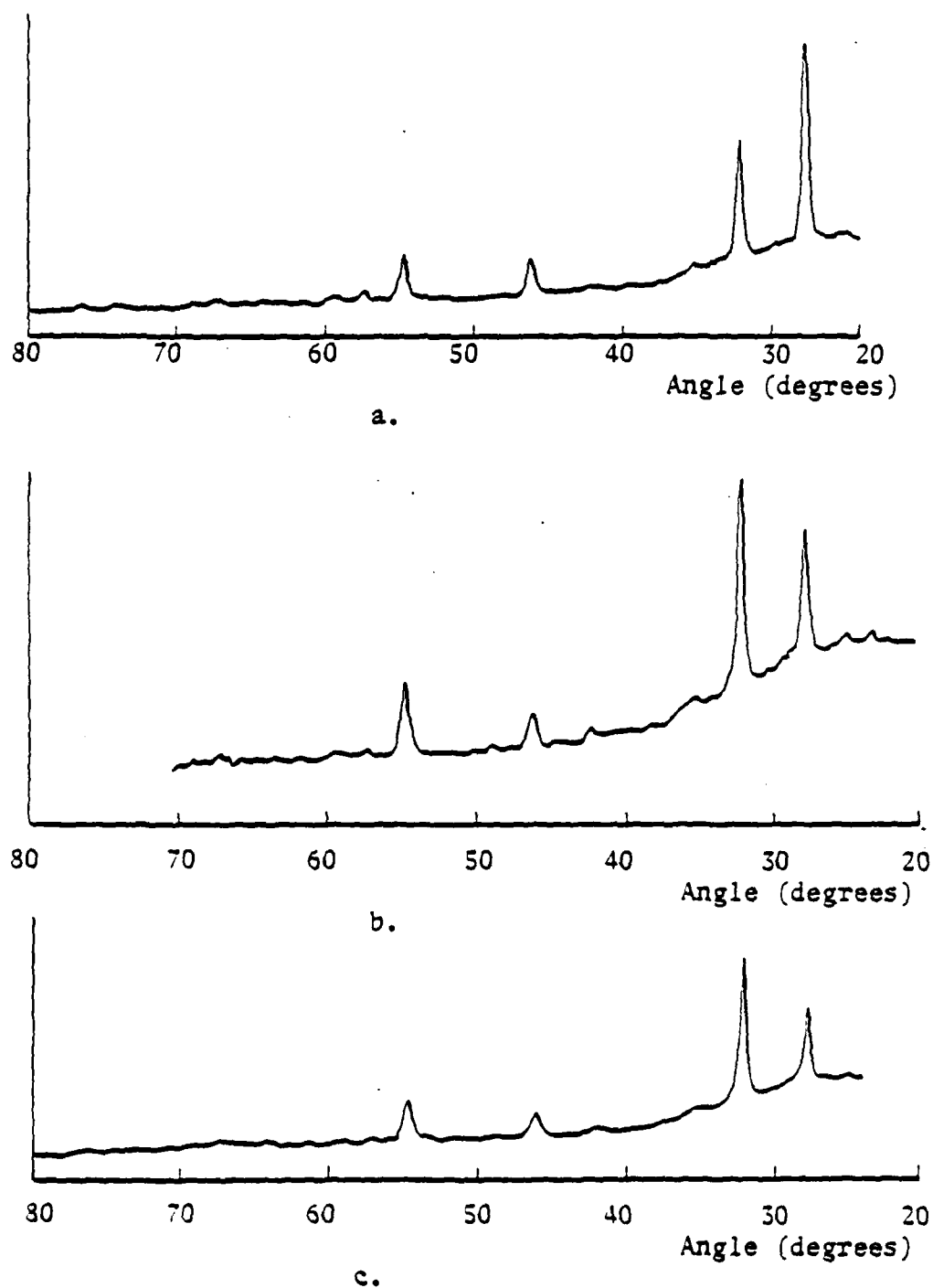
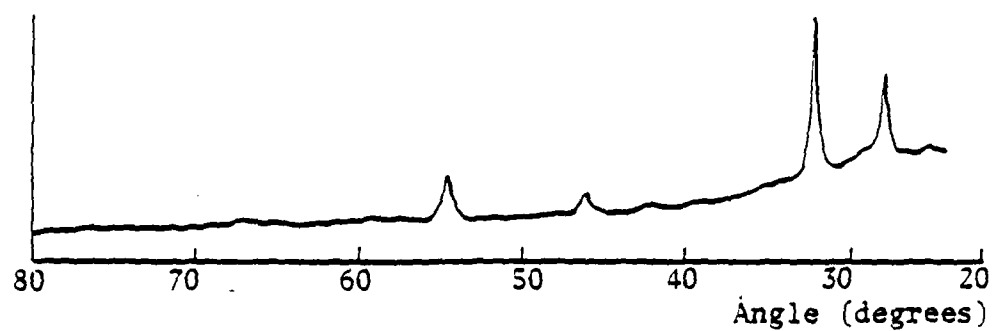
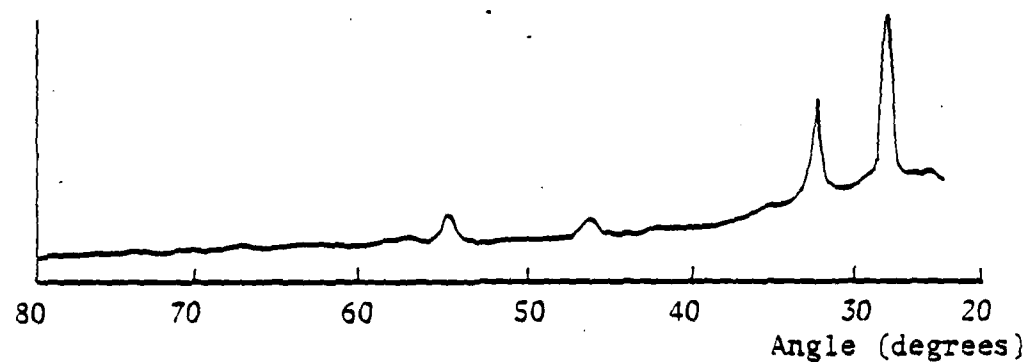


Figure 5.2. X-ray diffractometer traces of antimony trioxide films.

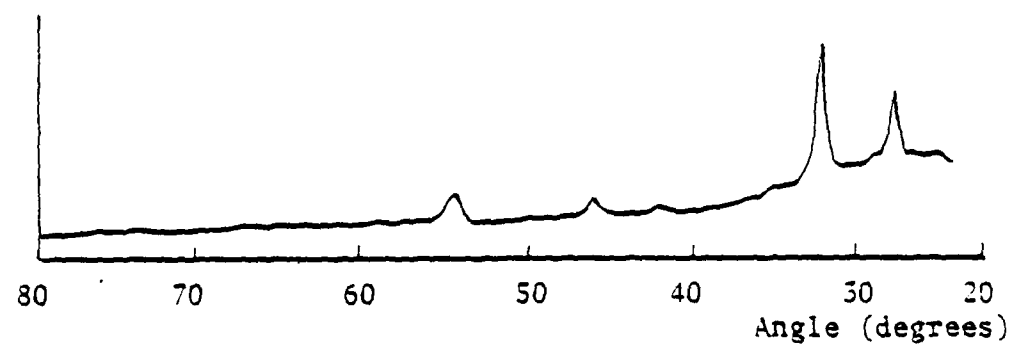
- a. Sample EB-7, heated substrate, no bombardment
- b. Sample EB-23X, heated substrate, bombarded after deposition
- c. Sample EB-8, heated substrate, bombarded at 1000 volts
- d. Sample EB-9, heated substrate, bombarded at 2000 volts
- e. Sample EB-11, unheated substrate, no bombardment
- f. Sample EB-10, unheated substrate, bombarded at 1000 volts



d.



e.



f.

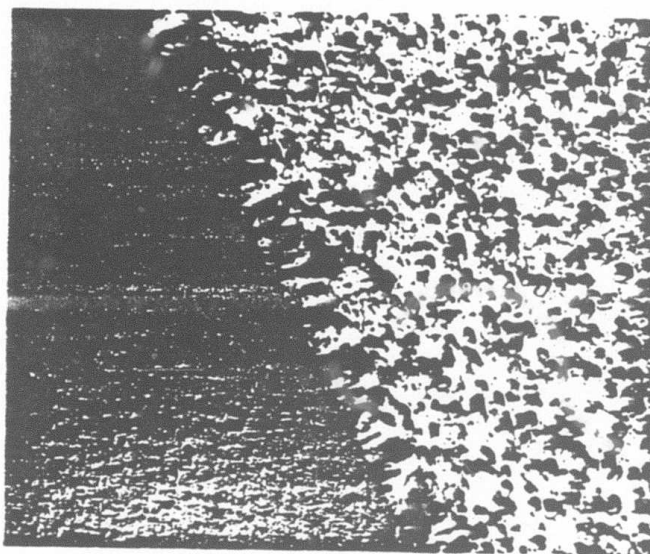
Figure 5.2. cont. X-ray diffractometer traces of antimony trioxide films.

bombardment accompanied deposition. Electron bombardment thus appears more efficient if applied during deposition for antimony trioxide films. Also, its effect seems to be slightly increased with increasing substrate potential. The different electron to molecule arrival ratios indicate that the effect is gradual and no real threshold exists. Also, substrate temperature did not seem to make any difference in the electron bombardment effect.

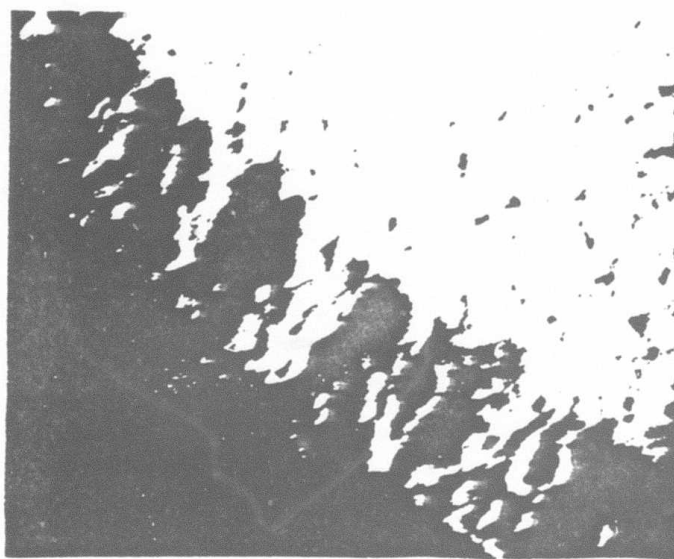
TEM photographs of carbon replicas were not quite as easily interpreted. All the films seem to have some sort of columnar structure, and any changes brought about by electron bombardment are difficult to see. Figure 5.3 shows some of these photographs along with the electron bombardment conditions for antimony trioxide films.

Direct film TEM photographs also are a bit difficult to interpret, but some observations are possible. Figure 5.4 is a collection of photographs of antimony trioxide films for different bombardment conditions, all at a magnification of 87,500. Most obvious is the grainy appearance of all the films, which seem to be composed of closely packed, randomly oriented crystallites. The sample showing the largest crystallite size is EB-14, deposited on a substrate at 190°C and not bombarded. The next largest crystallites seem to be in EB-15, this sample electron bombarded on a 155°C substrate. The remaining samples all contain smaller crystallites and were deposited on cooler substrates.

The electron diffraction patterns for the above samples provide some interesting information. The patterns are shown in Figure 5.5. The concentric circles of each pattern occur at the same radii for all



a. Sample EB-11



b. Sample EB-11

Figure 5.3. Cross section fractographs of antimony trioxide films.

- a. Sample EB-11, unheated substrate, no bombardment
- b. Sample EB-8, unheated substrate, bombarded at 1000 volts.

Table 1. X-Ray diffractometer peaks for antimony trioxide films.

Miller indices are for senarumontite crystal structure.

Angle (Degrees)	Lattice spacing (angstroms)	Miller Indices
27.8	3.22	(222)
32.1	2.79	(400)
35.1	2.56	(331)
46.0	1.97	(440)
54.6	1.68	(622)

samples, indicating the same basic crystal structure exists in all the films and confirming the X-ray diffraction results. However, the large number of rings include several which do not coincide with any of the lattice plane spacings listed in the table. Table 2 is a list of the measured ring radii, their corresponding lattice spacing as computed from the Bragg formula, and the Miller indices where applicable. The ring radius was converted to diffraction angle in radians by dividing it by 40 centimeters, the sample to photograph distance in the TEM.

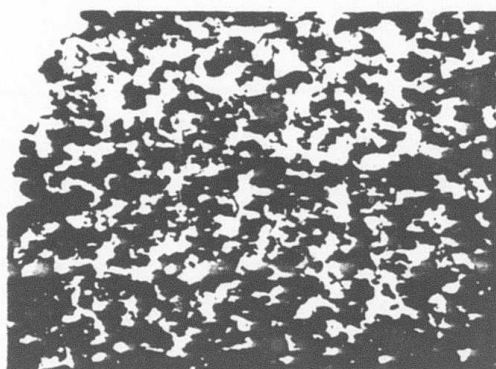
In the samples which show some diffraction rings darker than others, these rings correspond to the (111) and (222) lattice plane spacings for senarumontite. As previously stated, relative crystallite sizes in the films can be inferred from the grainy appearance of the rings. Smooth, continuous circles indicate a large number of tiny crystallites, while large spots result from a few bigger crystallites. Gathering this information from the electron diffraction patterns, a few contradictions are encountered in comparing it to the photographs in Figure 5.4. Samples EB-17 and EB-19 both have largely spotted diffraction patterns, but the photographs seem to show comparatively small crystallites. The photographs of EB-14 and EB-15 indicate larger crystallites, but the diffraction rings are fairly continuous and only slightly grainy. The discrepancy is greater for EB-14 than for EB-15. However, both photographs and diffraction rings for samples EB-18 and EB-20 indicate tiny crystallites.

High magnification images of these films all reveal electron interference fringes. Table 3 is a collection of measured fringe spacing, and Miller indices where applicable. Most samples had a fringe

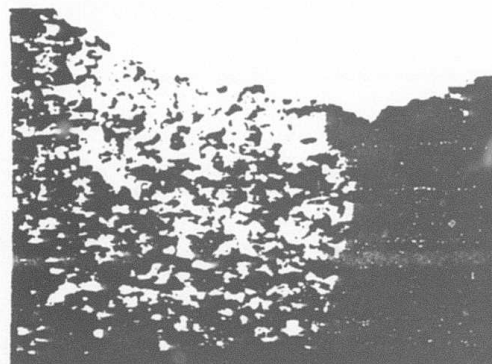
Table 2. Electron diffraction measurements on antimony trioxide films.

Miller indices are for senarumontite crystal structure.

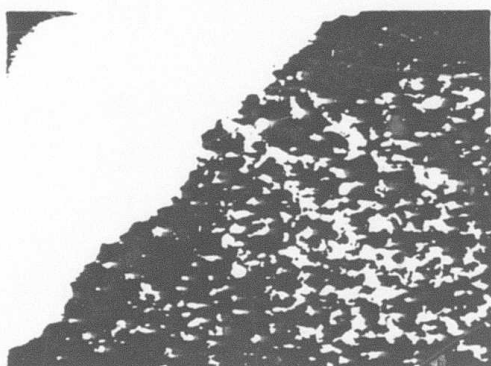
Ring Radius (mm)	Lattice Spacing (angstroms)	Miller Indices
5	24.8	
9	8.27	
10.5	6.44	(111)
14	4.51	
15	4.13	(222)
17.5	3.22	
19	3.10	(400)
21	2.78	(331)
22.5	2.56	(511)
24	2.07	
27.5	2.02	
31.5	1.74	
32	1.71	
36.5	1.48	
40.5	1.29	
42	1.27	(662)
46	1.15	



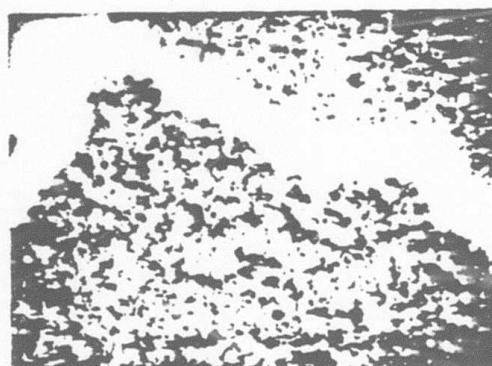
a.



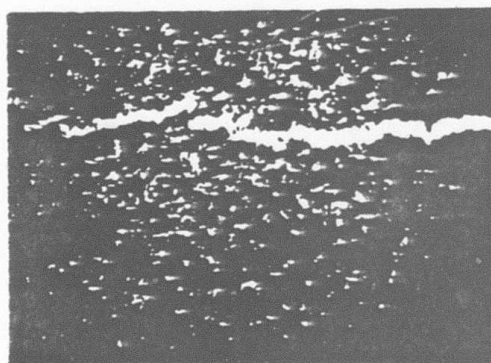
b.



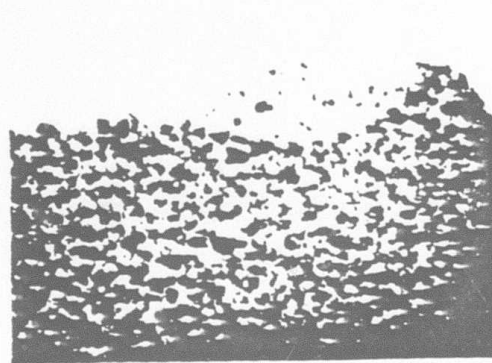
c.



d.



e.



f.

Figure S.4. TEM photographs of antimony trioxide films.

Table 3. High magnification TEM measurements on antimony trioxide films.

Miller indices are for senarumontite crystal structure.

Sample	Bombardment Voltage	Substrate Temperature	Fringe Spacing	Lattice Spacing	Miller Indices
EB-14	none	190C	0.319	6.38	(111)
EB-15	1000	155C	0.321	6.43	(111)
EB-17	none	30C	0.326	6.52	(111)
EB-18	2000	120C	0.429	8.57	
EB-19	400	130C	0.369	7.38	
EB-20	1000	30C	0.322	6.44	(111)
Graphite			0.170	3.40	(002)

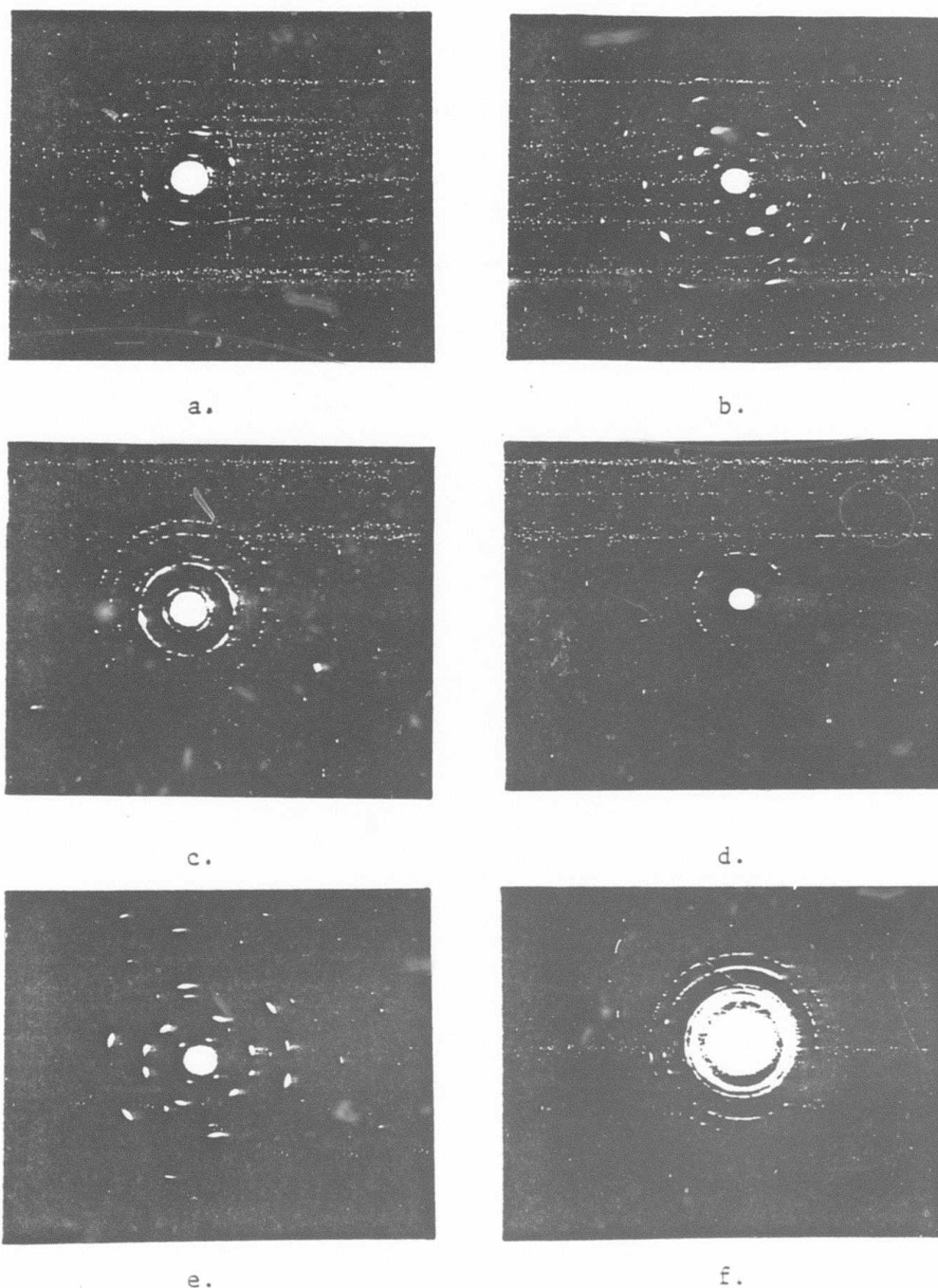
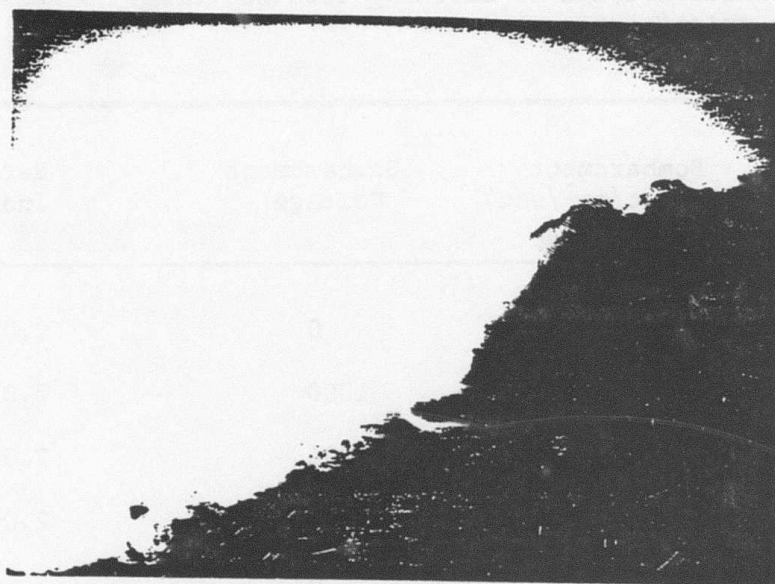
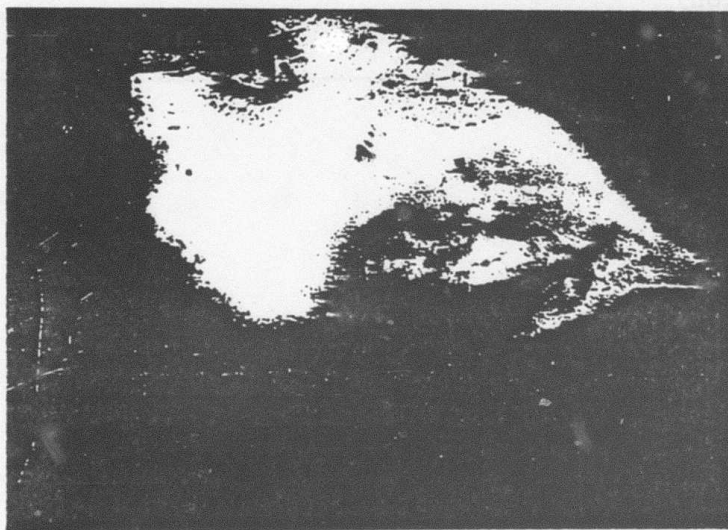


Figure 5.5. Electron diffraction patterns of antimony trioxide films.

- a. Sample EB-14, heated substrate, no bombardment
- b. Sample EE-19, heated substrate, bombarded at 400 volts
- c. Sample EE-15, heated substrate, bombarded at 1000 volts
- d. Sample EE-18, heated substrate, bombarded at 2000 volts
- e. Sample EE-17, unheated substrate, no bombardment
- f. Sample EE-20, unheated substrate, bombarded at 1000 volts.



a. Sample EB-18, antimony trioxide film



b. Graphite reference

Figure 5.6. Representative TEM high magnification photographs.

Table 4. Refractive index of antimony trioxide films as measured with the prism coupler.

Sample	Bombardment Flux ($\text{c}/\text{cm}^2/\text{sec}$)	Bombardment Voltage	Refractive Index
EB-7	none	0	2.093
EB-8	1.6×10^{12}	1000	2.079
EB-9	3.5×10^{12}	2000	2.085
EB-10	1.5×10^{15}	1000	2.068
EB-11	none	0	2.056
EB-23	none	0	2.091
EB-23X (after deposition)	1.4×10^{15}	1000	2.111

spacing corresponding to the (222) lattice planes of senarmontite. Those corresponding to the measured spacings of samples EB-18 and EB-19 are unknown. Figure 5.6 shows a representative high magnification photograph of an antimony trioxide film next to that for the graphite standard. The graphite was provided by the operators of the TEM.

Table 4 lists the refractive indices of several antimony trioxide films, along with the electron bombardment conditions, as measured with the prism waveguide coupler. It is evident that the different conditions of deposition had much greater influence on refractive index than the electron bombardment.

Surface plasma wave analysis was not performed on films of this material.

The spectrophotometer traces for several different antimony trioxide films are shown in Figure 5.7. These traces also contain the curves for the monitor plates used in these runs, and were used to determine the work to monitor ratio. The wavelengths corresponding to the halfwave positions were compared. Table 5 lists these and the resulting work to monitor ratios, which averaged out to 1.1. Table 6 contains the measured optical constants for a bombarded and a non-bombarded film.

All films adhere well to the substrate, evidenced by the Scotch tape test, but all films were completely rubbed off the substrate in the eraser test. The films were completely impervious to moisture damage, even at conditions of very high humidity. Antimony trioxide powder is not water soluble in either crystalline form. Evidently the

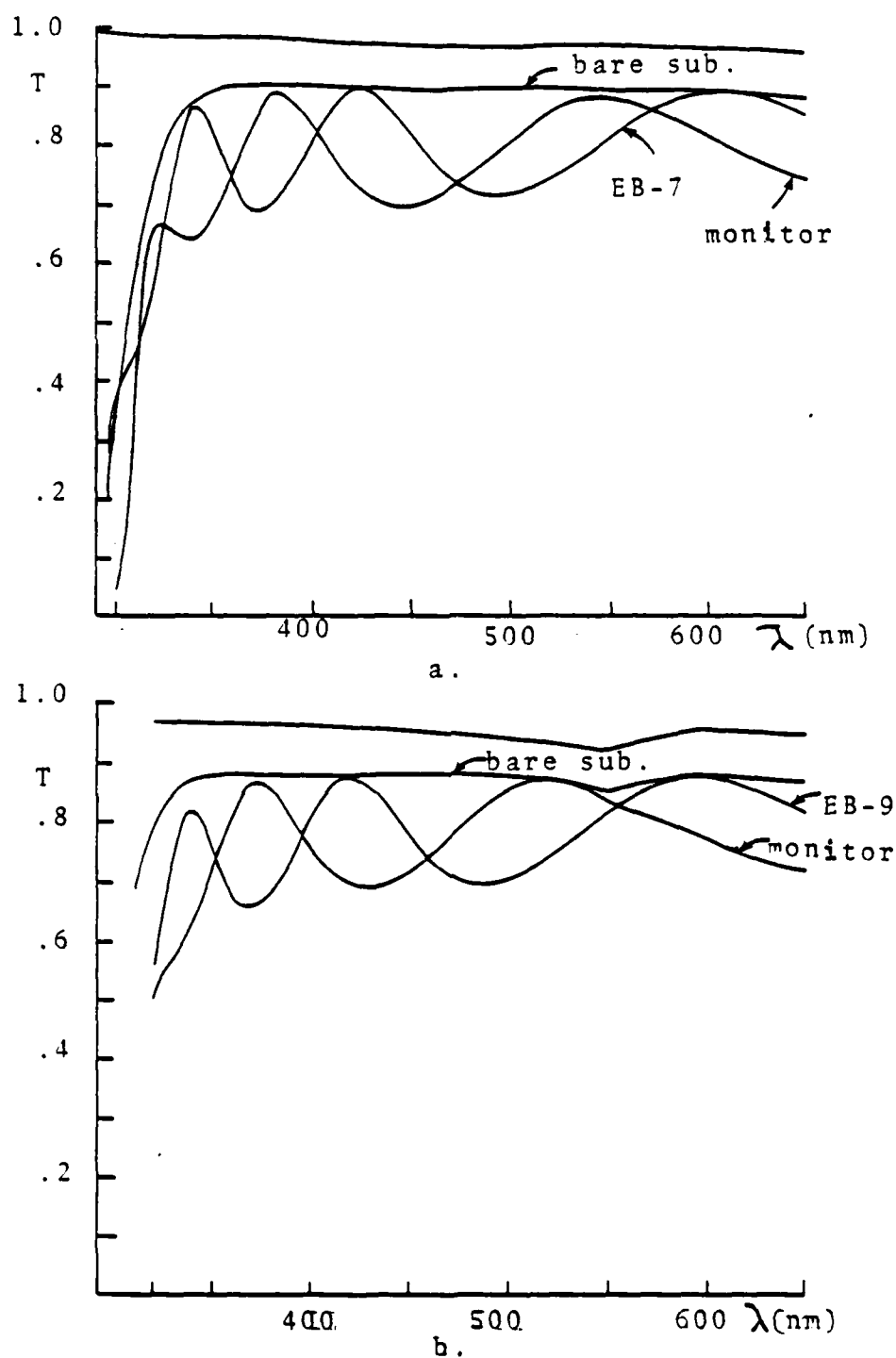
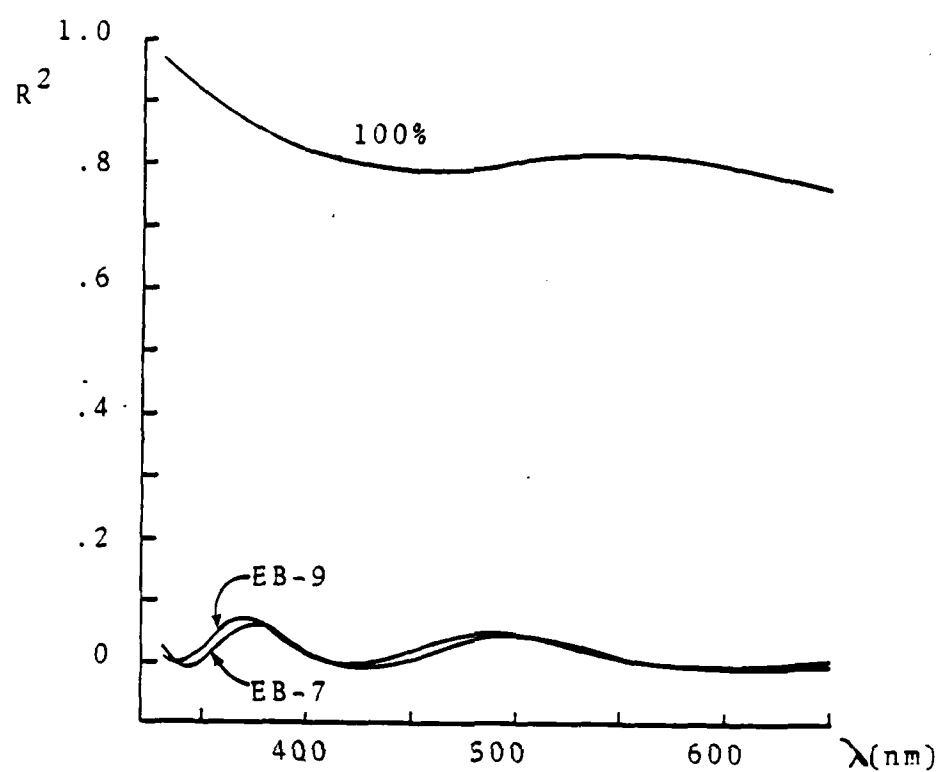


Figure 5.7. Spectrophotometer R and T curves for antimony trioxide films.

- a. Sample EB-7, heated substrate, no bombardment
- b. Sample EB-9, heated substrate, bombarded at 2000 volts



c.

Figure 5.7. cont. Spectrophotometer R and T curves for antimony trioxide films.

c. Samples EB-7 and EB-9

Table 5. Half wave positions from spectrophotometer transmittance curves of antimony trioxide films.

Sample	Work $\lambda/2$ (nm)	Monitor $\lambda/2$ (nm)	Work/Monitor Ratio
EB-7	607	544	1.12
	425	383	1.11
	341	323	1.05
EB-8	639	535	1.19
	445	380	1.17
	356	330	1.08
EB-9	588	521	1.13
	417	373	1.12
EB-10	611	532	1.15
	427	379	1.13
EB-11	617	540	1.14
	429	384	1.12

Table 6. Spectrophotometer measurements and calculated index values for bombarded and non-bombarded antimony trioxide films.

Sample	λ (nm)	R	T	1-R-T	FECO d (nm)	$\lambda/2$	index
EB-7 (no bombardment)	375	.27	.70	.03	295	425	2.16
	496	.25	.74	.01		606	2.05
EB-9 (2000v)	370	.29	.67	.04	290	418	2.16
	486	.25	.73	.02		587	2.02

change in microstructure brought on by electron bombardment had no effect on these macroscopic properties.

Potassium Hexafluorozirconate

References to this material other than that previously mentioned are practically nonexistent in the literature. As stated before, direct film TEM analysis was not performed on thin films of this material. Fortunately, X-ray diffraction and TEM photographs of carbon replicas yielded consistent, easily interpreted results.

Upon heating, the source material crystals melted together to form a liquid, which cooled to a single, solid chunk of matter in the boat after evaporation. This mass had to be broken up and pulverized to make a powder sample for X-ray diffraction analysis. Figure 5.8 shows the X-ray traces for melted and unmelted powder samples of potassium hexafluorozirconate. The principle effect of the melting seems to be a suppression of the peak at 47.7° and the appearance of the peak at 27.8° . The other peaks were not greatly affected.

As with antimony trioxide, thin films of potassium hexafluorozirconate show only a few peaks. However, only the peaks at 47.6° and 49.2° appear strongly in both the film and powder samples. Table 7 lists the angles where the peaks occur, their lattice spacings, and the corresponding crystal structure from the reference tables. No Miller indices were given by the reference. It can be seen that the films exhibit peaks corresponding to both α and β forms of $\text{KF}\cdot\text{ZrF}_4$. The diffractometer traces are seen in Figure 5.9 for films deposited on heated substrates.

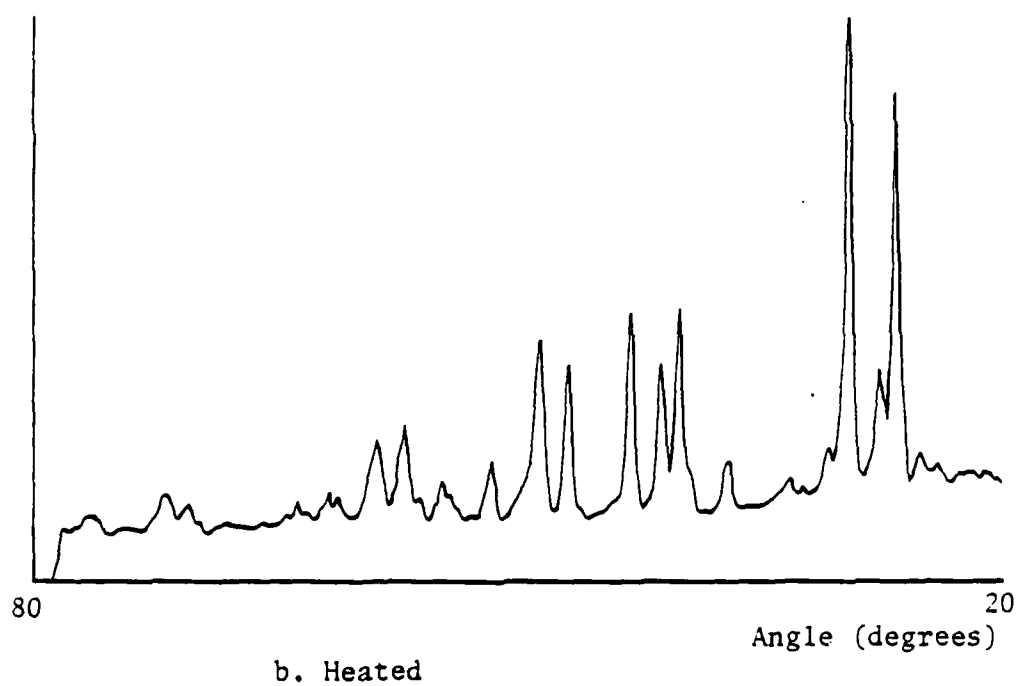
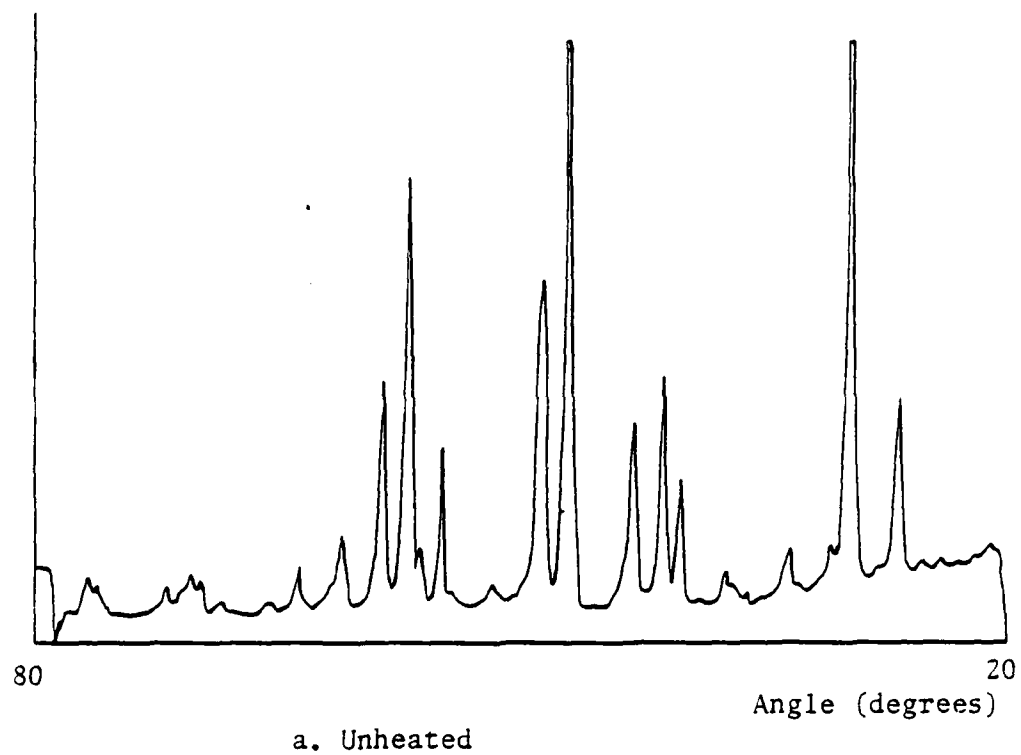
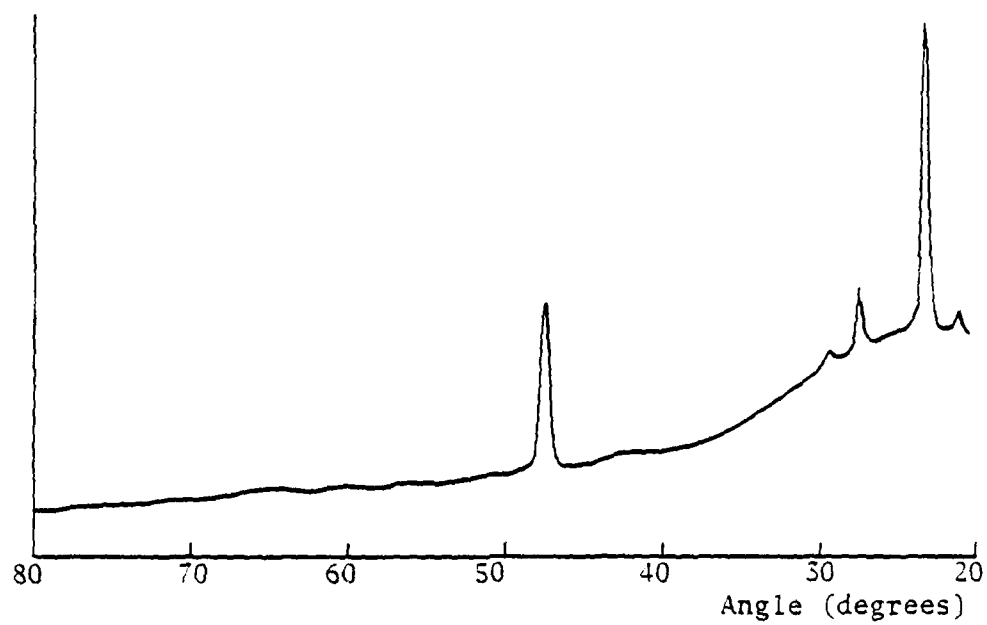
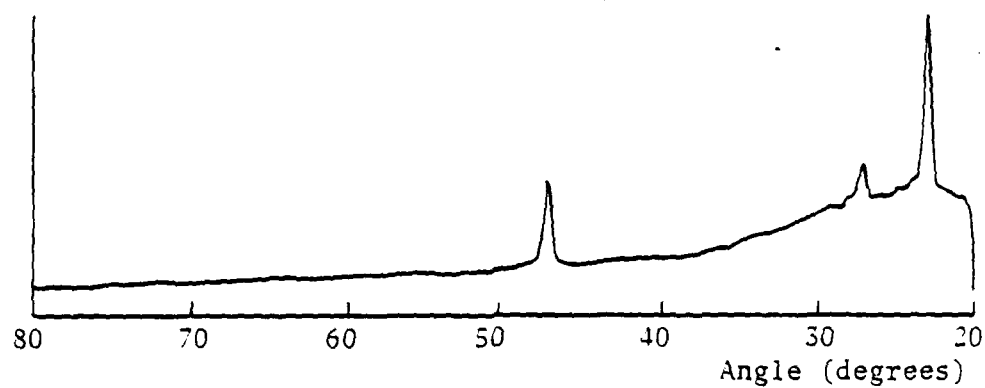


Figure 5.8. X-ray diffractometer traces of potassium hexafluorozirconate powder.



a.



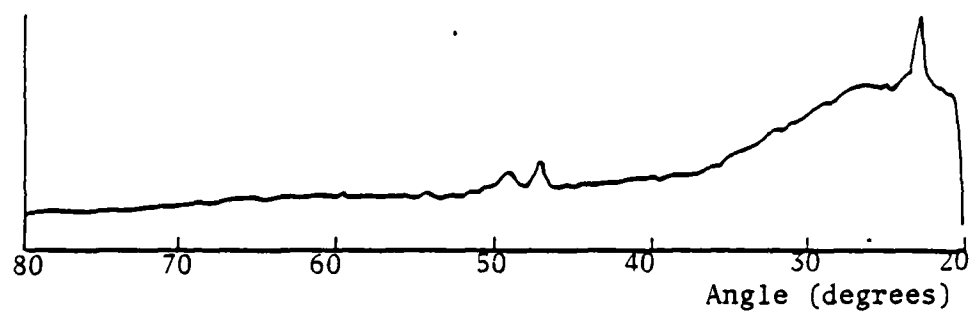
b.

Figure 5.9. X-ray diffractometer traces of potassium hexafluorozirconate films on heated substrates.

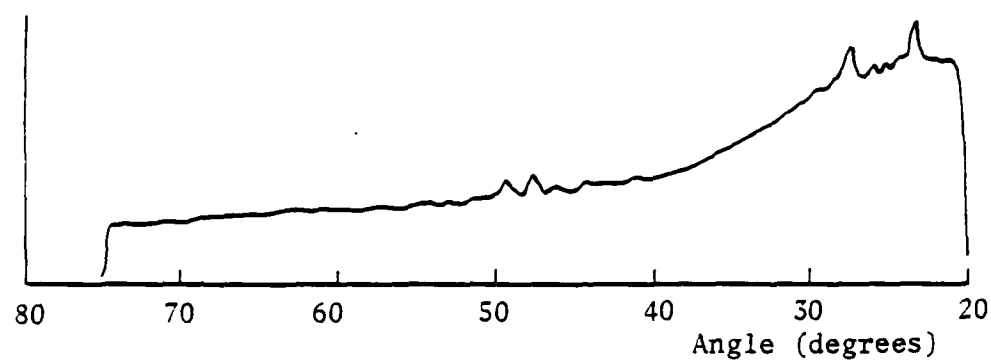
Note: Top graph has expanded vertical scale.

Figure 5.9. X-Ray diffractometer traces of potassium hexafluorozirconate films on heated substrates.

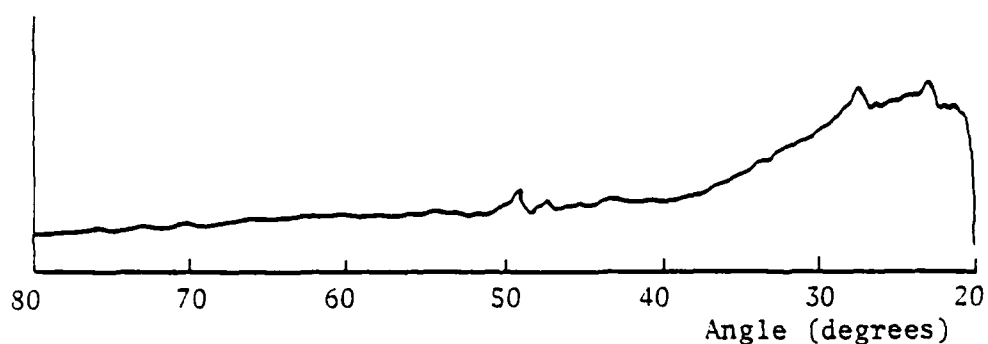
- a. Sample EB-12, no bombardment
- b. Sample EB-12X, bombarded after deposition
- c. Sample EB-37, bombarded at 500 volts
- d. Sample EB-13, bombarded at 1000 volts
- e. Sample EB-36, bombarded at 1500 volts.



c.



d.



e.

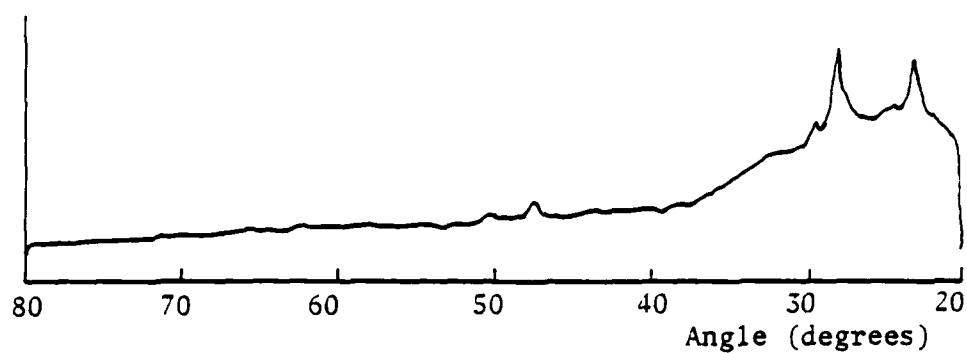
Figure 5.9.cont. X-ray diffractometer traces of potassium hexafluorozirconate films on heated substrates.

Table 7. X-Ray diffractometer peaks for potassium hexafluorozirconate films.

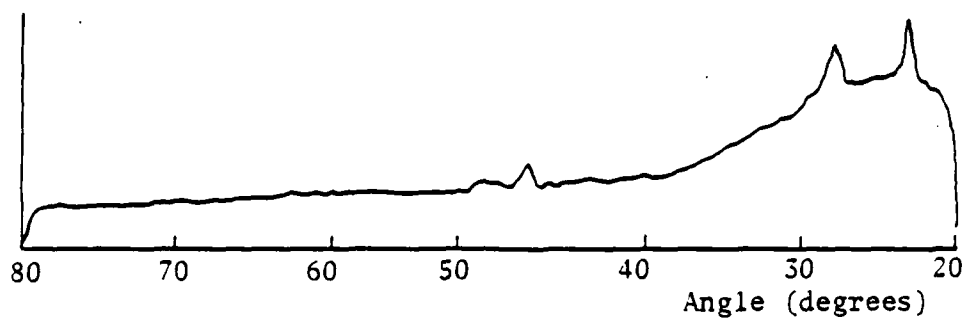
X-Ray Angle (Degrees)	Lattice Spacing (Angstroms)	Crystal Form Kf.ZrF ₄
23.2	3.83	α
27.5	3.21	β
29.7	3.01	α
47.5	1.91	α and β
49.2	1.84	α and β

The film samples on heated substrates show a definite trend. With increasing electron bombardment energy, an extreme reduction in peak intensity occurs for all peaks. Sample EB-36 is practically amorphous. Unlike antimony trioxide, bombarding the film after deposition did not affect the relative peak strengths in the diffractometer traces. The sample was bombarded at a potential of 1000 volts and an electron flux of 1.4×10^{15} electrons per square centimeter per second for 10 minutes. Electron flux levels were 3.4×10^{14} to 1.1×10^{15} electrons per square centimeter per second, and the molecule arrival rate corresponding to the deposition rate of 30 angstroms per second was 2.1×10^{15} molecules per square centimeter per second. The electron to molecule arrival ratios were thus 0.16 to 0.52. Again we see a gradual effect with no apparent threshold for this material bombarded during deposition. The films' tendency to become increasingly amorphous with bombardment energy apparently would eventually saturate at a complete absence of crystal structure. This was not too far away from the conditions produced by the bombardment levels used here.

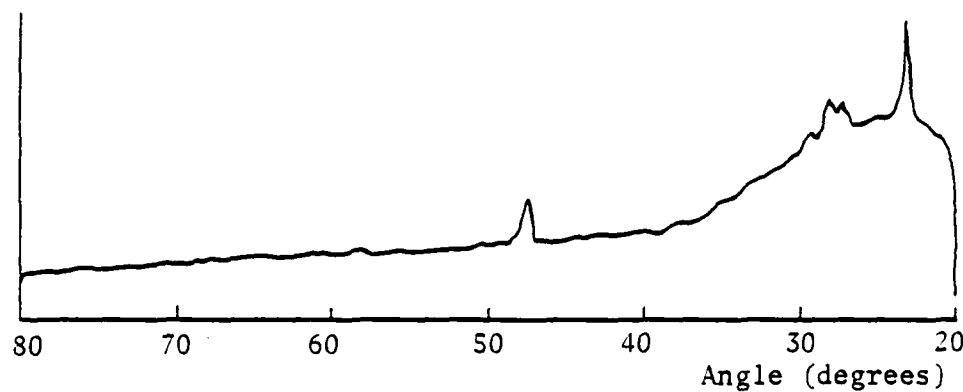
With unheated substrates, the results are a little different. The diffractometer traces are seen in Figure 5.10. Electron bombardment produces a shift in relative peak intensities, even after deposition, along with an overall reduction of crystallinity. However, due to the extreme fogging of these films shortly after removal from the coating chamber, they are of academic interest only. Residual water vapor in the plant was probably incorporated into the films during deposition. The electron flux levels and molecule arrival rate



a.

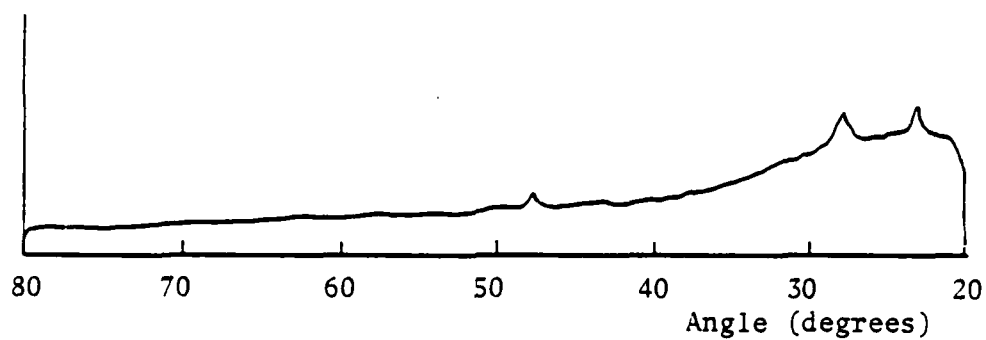


b.

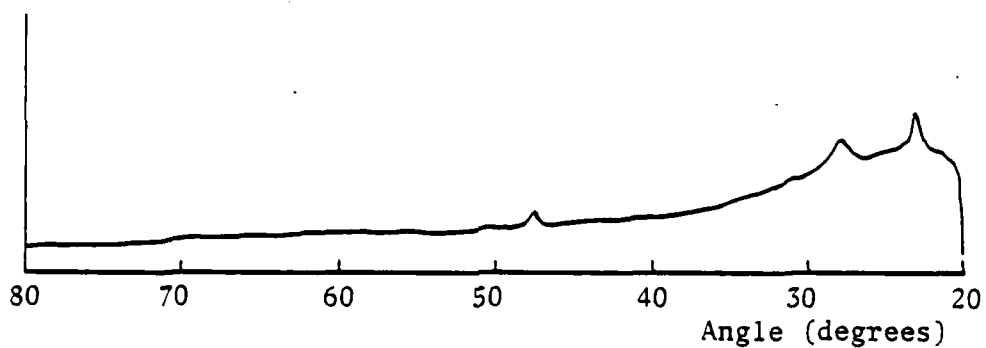


c.

Figure 5.10. X-ray diffractometer traces of potassium hexafluorozirconate films on unheated substrates.



d.



e.

Figure 5.10.cont. X-ray diffractometer traces of potassium hexafluorozirconate films on unheated substrates.

were essentially the same as those for the heated substrates. It is noteworthy that electron bombardment of these films on unheated substrates resulted in diffractometer traces which approach that for a non-bombarded film on a heated substrate (EB-35 and EB-12). This would indicate that electron bombardment of this material has the same effect as substrate heating, to a limited extent, although actual substrate temperature rise during bombardment was negligible.

TEM photographs of carbon replicas show similar results to those of the X-ray diffractometer. In Figure 5.11, the non-bombarded film shows definite columnar structure. In contrast, the bombarded film appears greatly amorphous with no columns or crystallites evident. The replica of the film on an unheated substrate indicates the decomposition of the film by the large spots scattered throughout the image.

Table 8 lists the results of the SPW analysis for films of potassium hexafluorozirconate. It is evident that the difference between the bombarded and non-bombarded film indices is not as great as that for the two non-bombarded films of the same run. Evidently, the uncertainty in the measurement exceeds the effects of electron bombardment at the levels used.

Figure 5.12 shows the spectrophotometer traces of reflectance and transmittance for the various potassium hexafluorozirconate films. Table 9 lists the refractive index, absorption, and FECO thickness. From these results, we see that electron bombardment has a negligible effect on the optical properties of these films. It does seem to increase the absorption a little, especially towards shorter

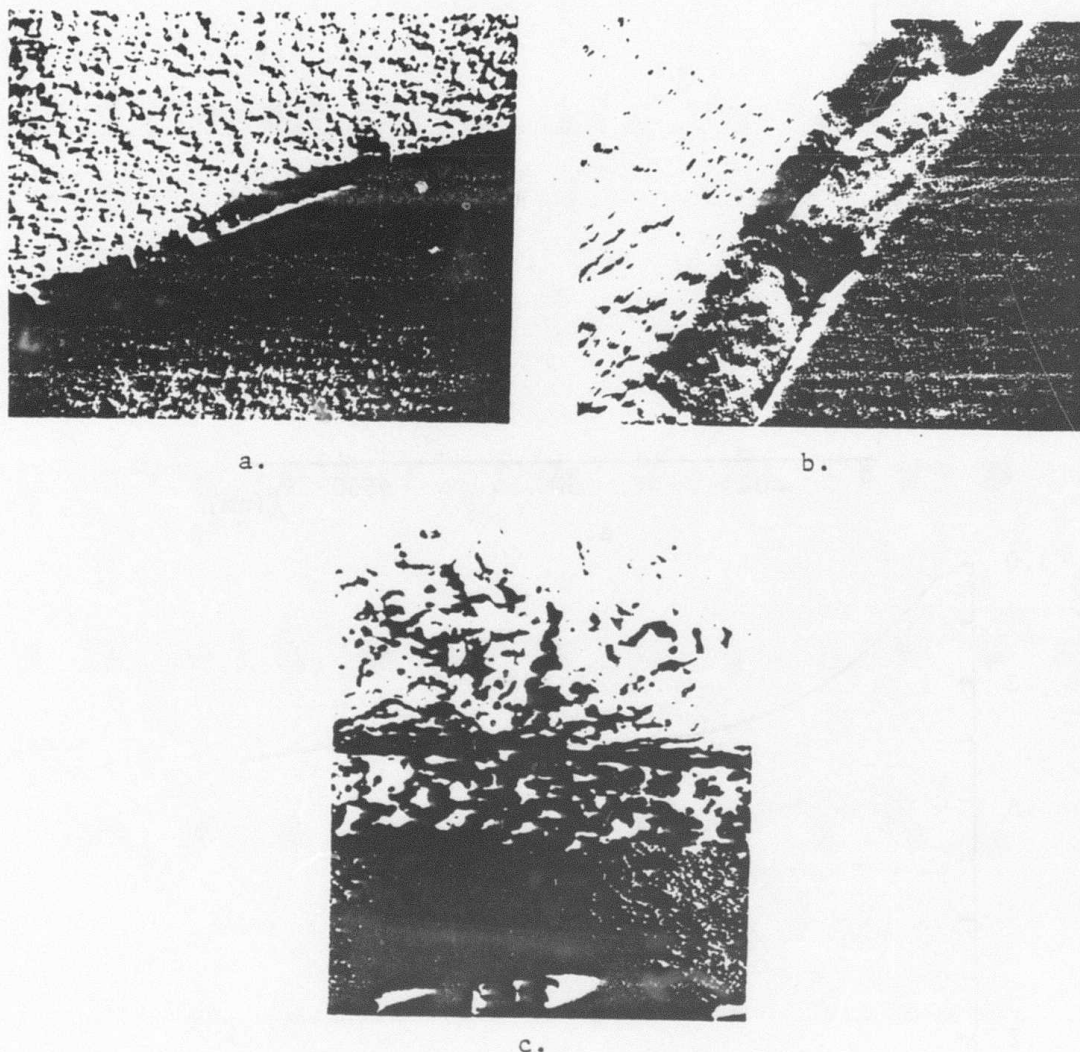


Figure 5.11. Cross section fractographs of potassium hexafluorozirconate films.

- a. Sample EB-12, heated substrate, no bombardment
- b. Sample EB-13, heated substrate, bombarded at 1000 volts
- c. Sample EB-32, unheated substrate.

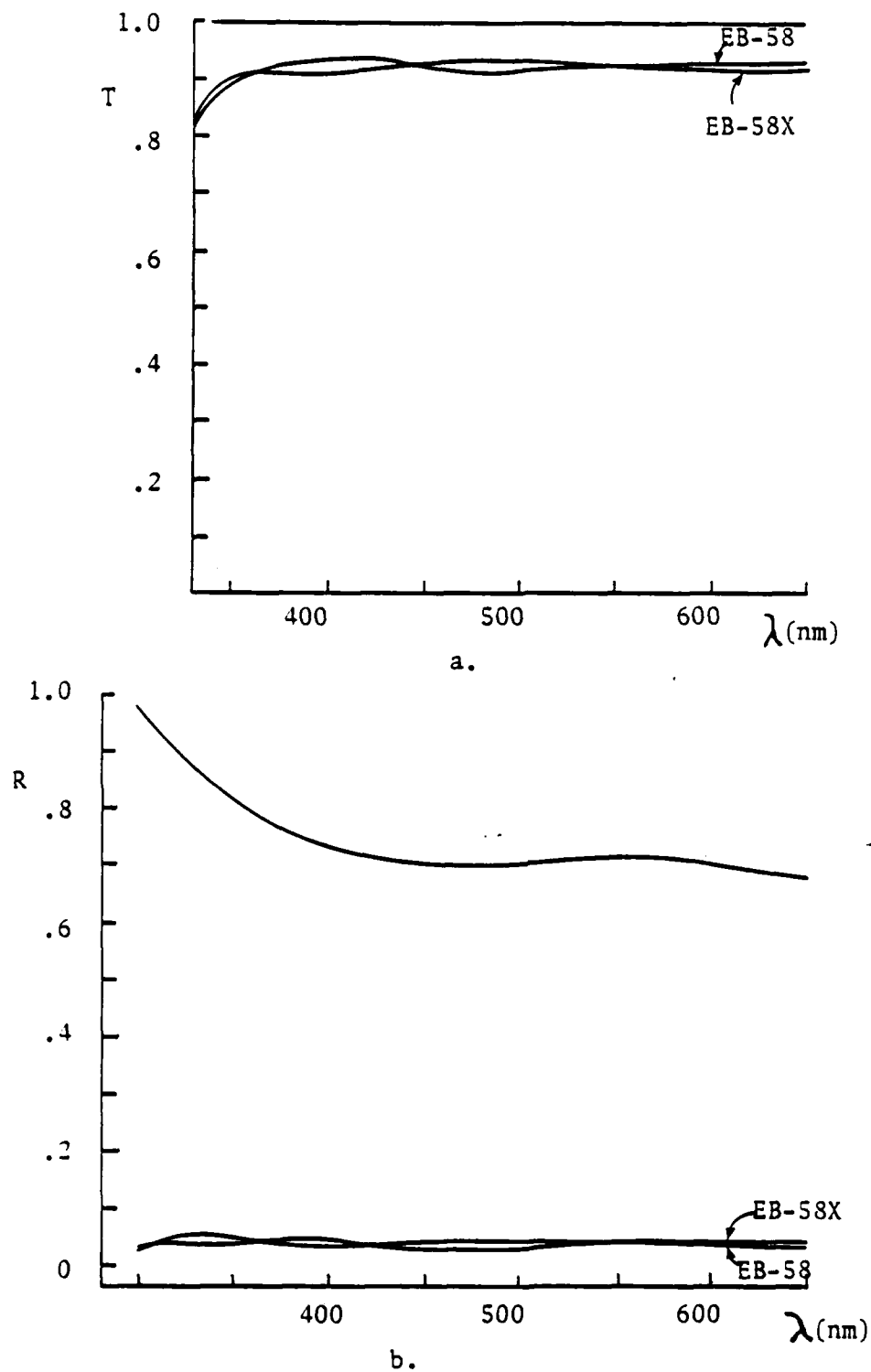


Figure 5.12. Spectrophotometer R and T curves for potassium hexafluorozirconate.

Same pump down cycle.

Table 8. Surface plasma wave analysis of potassium hexafluorozirconate films.

Sample	Bombardment Flux	Bombardment Volts	Index
EB-69	none	0	1.37
EB-69	none	0	1.34
EB-70	none	0	1.35
EB-70X	1.6×10^{15}	2000	1.33
EB-76	none	0	1.40
EB-76	none	0	1.36
EB-77	none	0	1.39
EB-77X	1.6×10^{15}	2000	1.38

Table 9. Spectrophotometer measurements and calculated index values for bombarded and non-bombarded potassium hexafluorozirconate films.

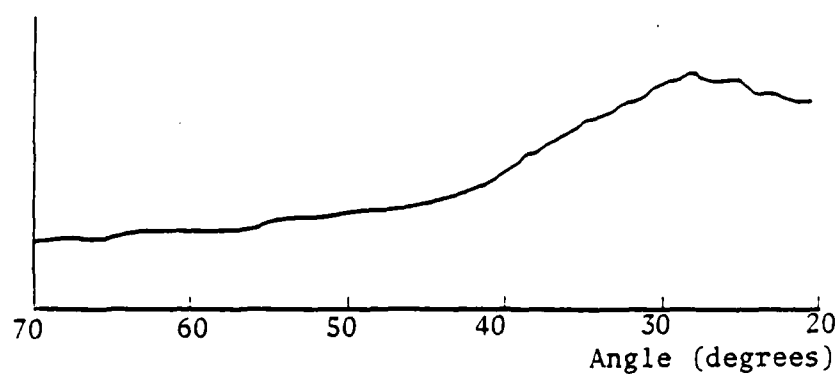
Sample	λ (nm)	R	T	1-R-T	RECO d	$\lambda/2$	index
EB-58 (no bombardment)	409	.05	.93	.02	358	483	1.35
	483	.06	.92	.02			
EB-58X (bombarded at 2000 V)	381	.05	.91	.04	450	608	1.35
	488	.04	.93	.03			
	608	.06	.92	.02			

wavelengths. Both bombarded and non-bombarded films show the absorption cutoff of the substrate. The slight absorption can be seen which probably caused the rather wide variations in the SPW index results.

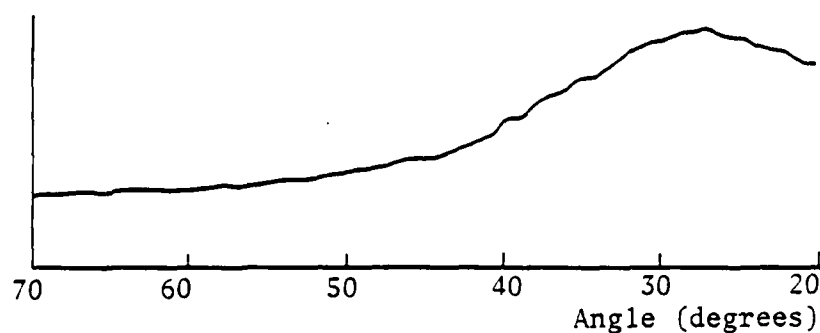
Films deposited on a heated substrate show no damage from the Scotch tape test for both bombarded and non-bombarded conditions. However, bombarded films display slightly less scratch damage from the eraser test. The humidity test results were rather interesting. The film bombarded during deposition began to show spots when the humidity reached 70 percent. The non-bombarded film and that bombarded after deposition showed similar spots at 80 percent relative humidity. One would have expected the film without columnar structure to be more impervious to moisture damage due to the lack of pores between the columns. The milky films deposited on unheated substrates were heavily damaged by the eraser and Scotch tape tests. These films were already very cloudy from moisture damage on exposure to the atmosphere in the laboratory, which has a relative humidity of around 35 percent. Electron bombardment thus does nothing to improve the properties of films on unheated substrates.

Silicon Monoxide

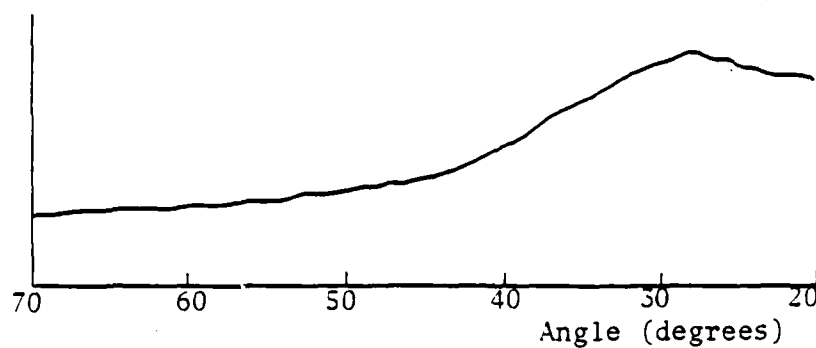
Again, direct film TEM analysis was not performed on these films, and powder samples were not made for X-ray diffraction studies. Figure 5.13 shows the X-ray diffractometer traces for the different films. The molecule arrival rate corresponding to the deposition rate of 20 angstroms per second was 5.7×10^{15} molecules per square



a.



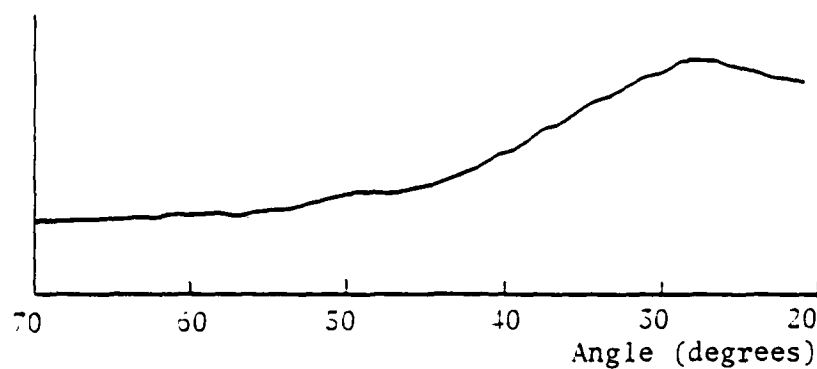
b.



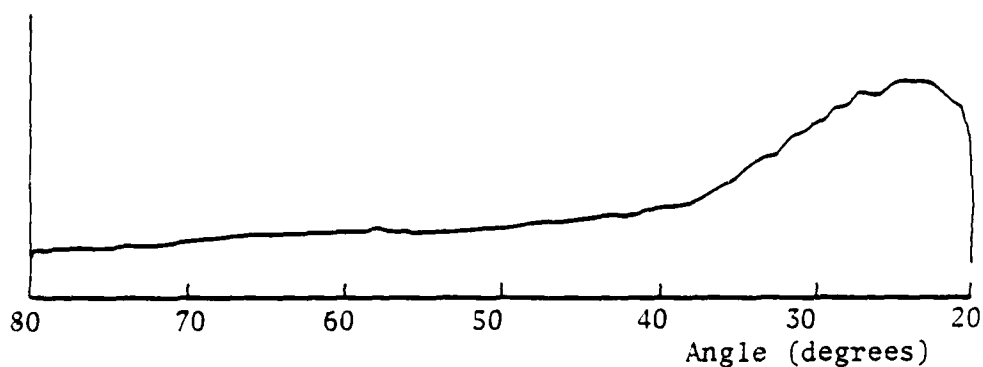
c.

Figure 5.13. X-ray diffractometer traces of silicon monoxide films.

- a. Sample EB-25, no bombardment
- b. Sample EB-25X, bombarded after deposition
- c. Sample EB-24, bombarded at 1000 volts
- d. Sample EB-27, bombarded at 2000 volts
- e. Sample EB-29, unheated substrate, bombarded at 2000 volts.



d.



e.

Figure 5.13. cont. X-ray diffractometer traces of silicon monoxide films.

- a. Sample EB-25, no bombardment
- b. Sample EB-25X, bombarded after deposition
- c. Sample EB-24, bombarded at 1000 volts
- d. Sample EB-27, bombarded at 2000 volts
- e. Sample EB-29, unheated substrate, bombarded at 2000 volts.

centimeter per second. Electron arrival rates of up to 1.5×10^{15} electrons per square centimeter per second were applied. In no case does any sign of a peak appear in any of the traces, indicating completely amorphous film structure. Obviously the electron bombardment has not affected the crystal microstructure of the silicon monoxide films. Just as dramatic are the photographs of the carbon replicas from the TEM shown in Figure 5.14. In fact, the complete absence of structure in the images made the film cross sections difficult to locate when viewing the samples in the TEM.

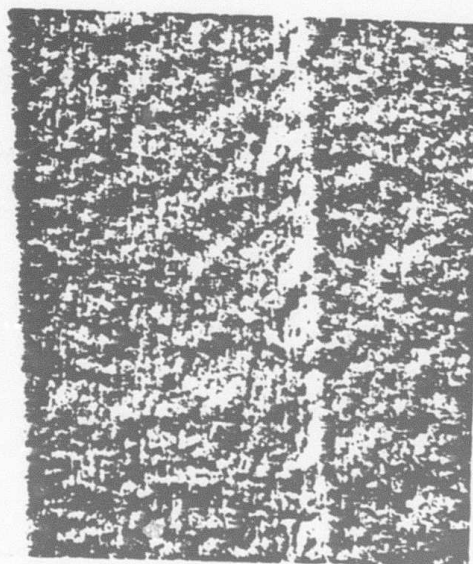
Table 10 contains the SPW analysis results for silicon monoxide films. Not surprisingly, the variation in refractive index of the different samples due to the different run conditions exceeded any measurable difference attributable to electron bombardment. Absorption in the films definitely contributed to the uncertainty in these results.

The presence of absorption is brought out clearly in the spectrophotometer traces of Figure 5.15. Table 11 contains the measurements of index and absorption, along with the FECO thickness and electron bombardment conditions. The index and absorption appear to be extremely sensitive to variations in chamber conditions during evaporation. Both bombarded and non-bombarded film samples show a pronounced absorption cutoff near 420 nanometers towards the shorter wavelengths.

The silicon monoxide films held up extremely well under the durability tests, confirming their usefulness as protective overcoat layers. They were not damaged by either the Scotch tape or eraser tests. Also, no spotting or degradation of any kind occurred at even the



a.



b.

Figure 5.14. Cross section fractographs of silicon monoxide films.

- a. Sample EB-25, heated substrate, no bombardment
- b. Sample EB-24, heated substrate, bombarded at 1000 volts

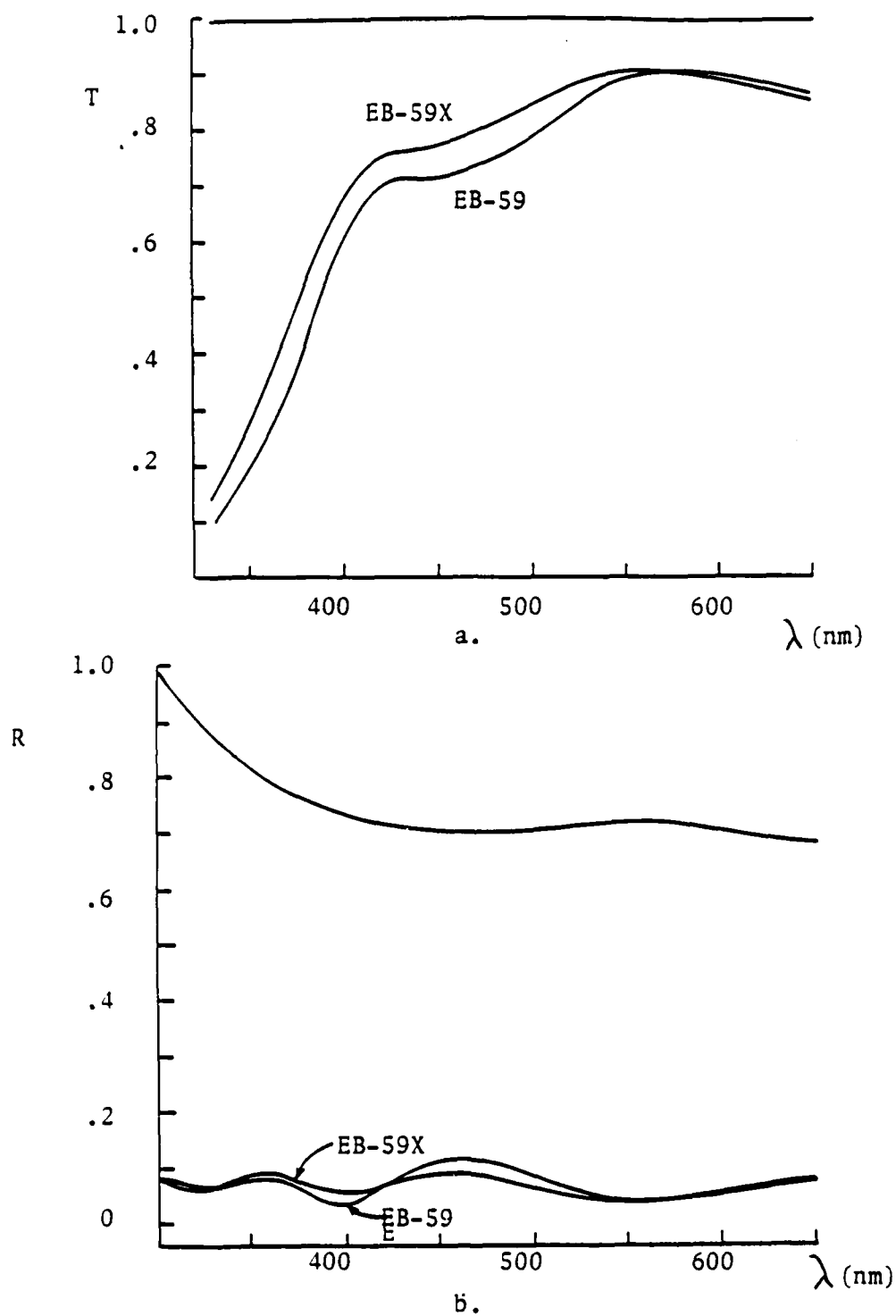


Figure 5.15. Spectrophotometer R and T curves for silicon monoxide films.

Same pump down cycle.

Table 10. Surface plasma wave analysis of silicon monoxide films.

Sample	Bombardment Flux (/cm ² /sec)	Bombardment Potential	Index
EB-62	none	0	1.95
EB-62	none	0	1.98
EB-63	none	0	1.86
EB-63X	1.6×10^{15}	2000	1.85
EB-64	none	0	1.85
EB-64X	none	0	1.87

Table 11. Spectrophotometer measurements and calculated index values for bombarded and non-bombarded silicon monoxide films.

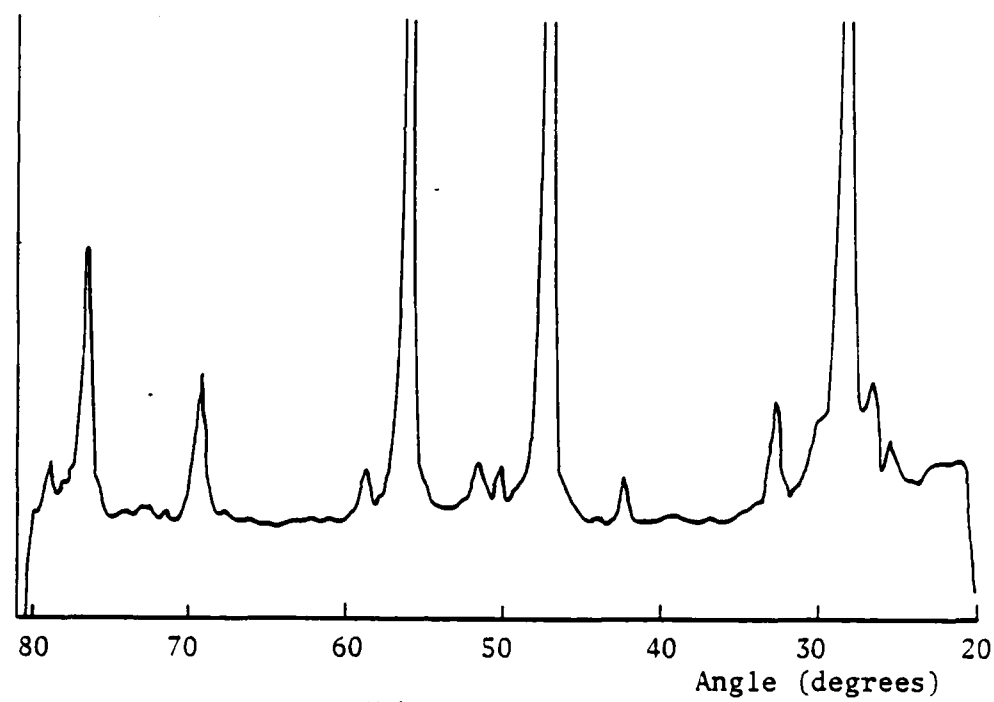
Sample	λ (nm)	R	T	1-R-R	RECO d (nm)	$\lambda/2$	n
EB-59 (no bombardment)	583	.06	.90	.04	324	583	1.80
EB-59X	568	.06	.90	.04	310	568	1.83

highest humidity levels. Again, electron bombardment had no measurable effect on the macroscopic properties of these films.

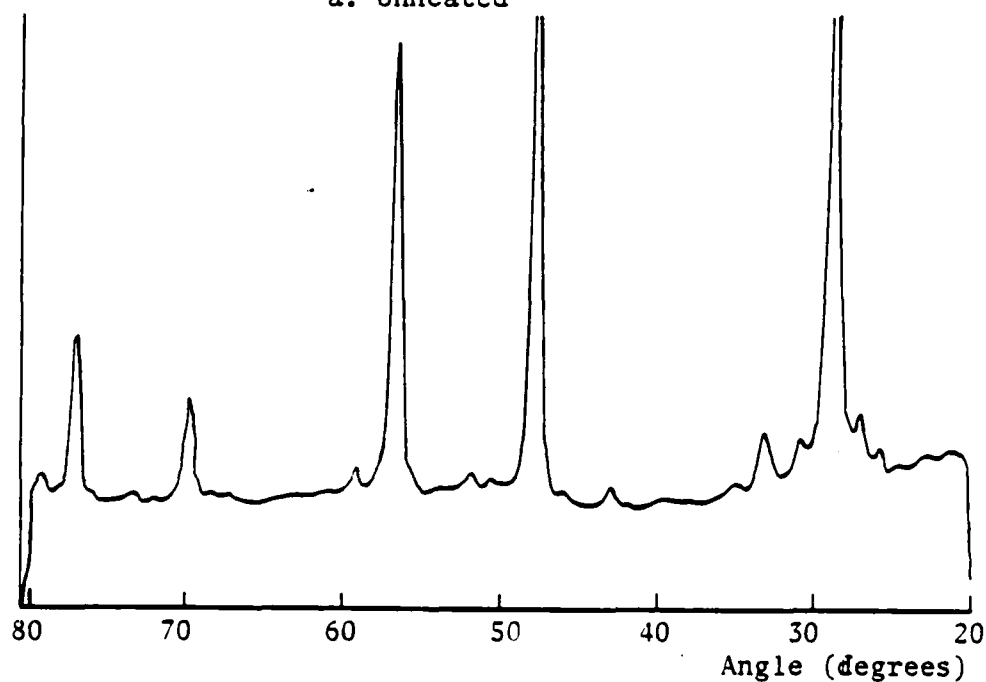
Zinc Sulfide

Zinc sulfide can exist in either a cubic sphalerite structure, stable below 1000°C, or a hexagonal close packed (HCP) wurtzite structure. Figure 5.16 shows the X-ray diffractometer traces for powder samples of heated and unheated zinc sulfide. The two traces are practically identical except in absolute amplitude of the peaks, probably due to a thickness difference of the powders. Unfortunately, many lattice spacings of one structure are equal to those of the other. Peaks from both structures are evident in the powder samples, but those of the cubic form dominate. Table 12 lists the diffractometer angles, their lattice spacings, and the Miller indices for the two different structures.

Figure 5.17 shows the X-ray diffractometer traces of zinc sulfide films. These traces show only two peaks. That at 28.5° has a corresponding lattice spacing of 3.12 angstroms, which is characteristic of both cubic and HCP structures. The peak at 47.8° , with spacing 1.91 angstroms, is also characteristic of both crystal structures. The deposition rate of nine angstroms per second had a corresponding molecule arrival rate of 2.27×10^{15} molecules per square centimeter per second. From the traces, an electron flux of around 1.3×10^{15} electrons per square centimeter per second at energies of 1000 and 2000 electron volts during deposition led to a suppression of the 47.8° peak and an enhancement of the 28.5° peak. Increasing the energy enhanced the

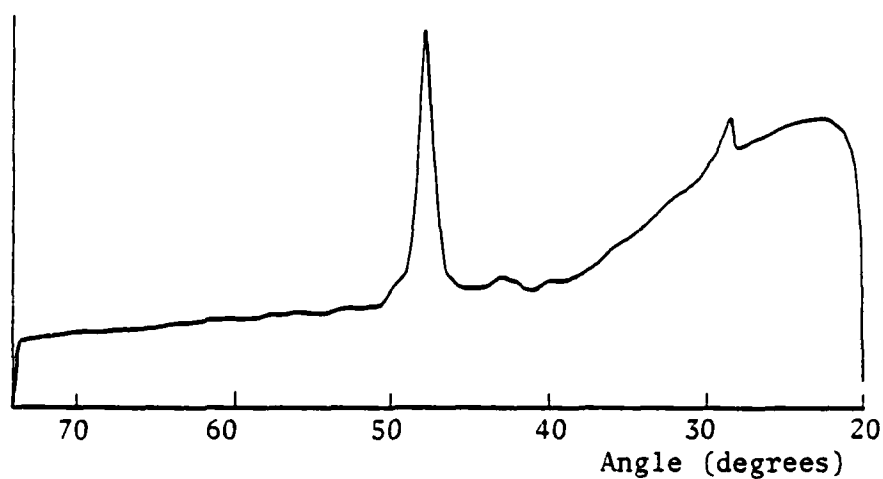


a. Unheated

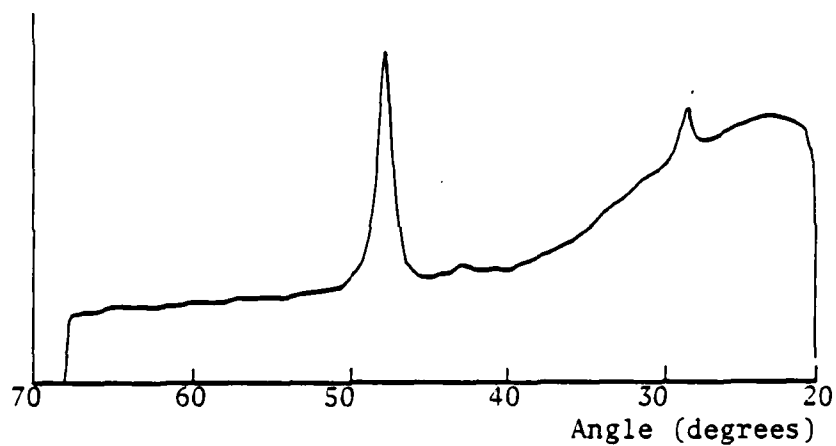


b. Heated

Figure 5.16. X-ray diffractometer traces of zinc sulfide powder (Irtran).



a.



b.

Figure 5.17. X-ray diffractometer traces of zinc sulfide films on unheated substrates.

- a. Sample EB-38, no bombardment
- b. Sample EB-38X, bombardment after deposition
- c. Sample EB-42, bombarded at 1000 volts
- d. Sample EB-40, bombarded at 2000 volts.

Table 12. X-Ray diffractometer peaks for zinc sulfide powder.

Angle (Degrees)	Lattice Spacing (Angstroms)	Miller Indices	
		Cubic	HCP
27.1	3.29		(100)
28.7	3.11	(111)	(002)
30.8	2.90		(101)
33.2	2.70	(200)	
47.6	1.91	(220)	(110)
56.4	1.63	(311)	(112)
59.1	1.56	(222)	(004)
69.6	1.35	(400)	
76.8	1.24	(331)	
78.2	1.22	(420)	(211)

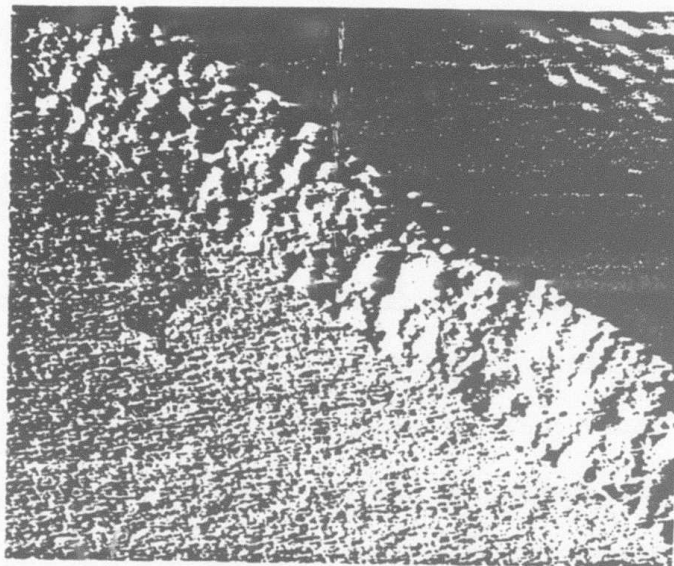
effect. A film bombarded with a similar electron flux for 10 minutes after deposition showed little effect in its X-ray trace.

From these results, several explanations of the effects of electron bombardment can be inferred, none conclusively. A shift from one crystal structure to the other or a rearrangement of lattice planes parallel to the substrate of either particular structure are two possible explanations. The films definitely do not tend to become amorphous with electron bombardment.

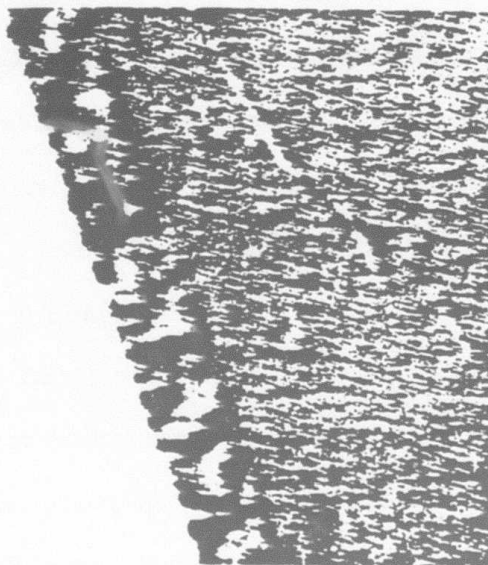
TEM photographs of cross section replicas shed little light on what is actually happening. As seen in Figure 5.18, all films show some columnar structure, with little difference between the samples.

Due to the importance of zinc sulfide as a component in optical filters, as well as its history of being affected by electron bombardment, a subsequent group of films was made and the experiments repeated. This time, the source material was a 300 mesh powder from Atomergic Chemicals, evaporated from a tantalum boat at about seven angstroms per second. Chamber pressure varied between $0.5-1.0 \times 10^{-4}$ torr. The substrates were heated to 100°C and allowed to stabilize for around 20 minutes prior to film deposition to insure good uniformity.

Figure 5.19 shows the diffractometer traces for the heated and unheated powder samples. Again, they are identical except for absolute amplitude, and as before they show peaks for both crystal structures, with those of the cubic form dominating. These traces indicate the source materials from the different suppliers to be practically identical.



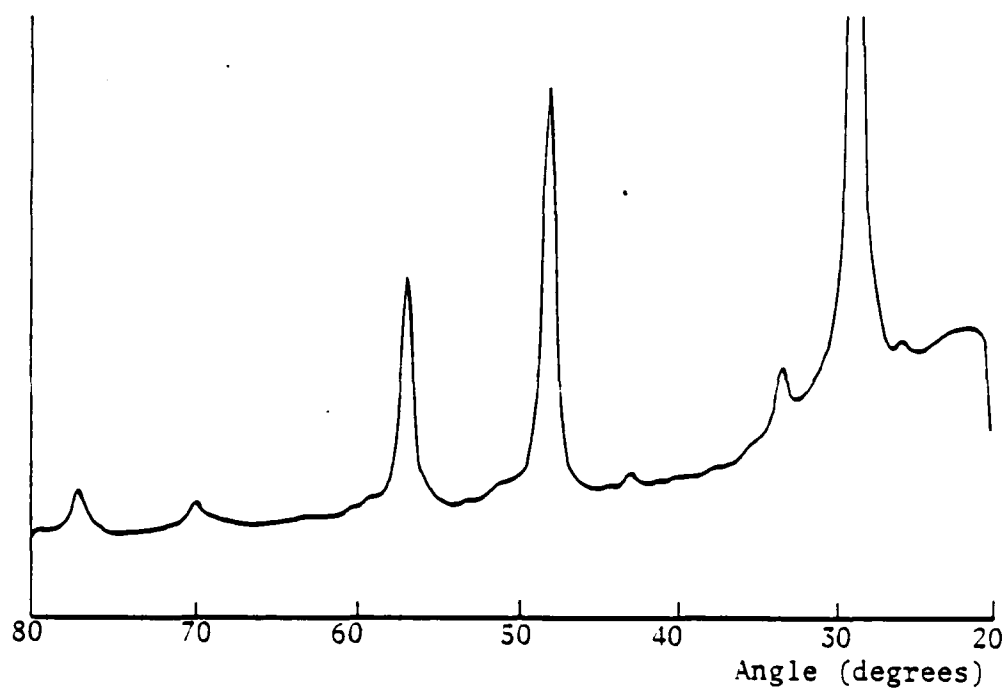
a.



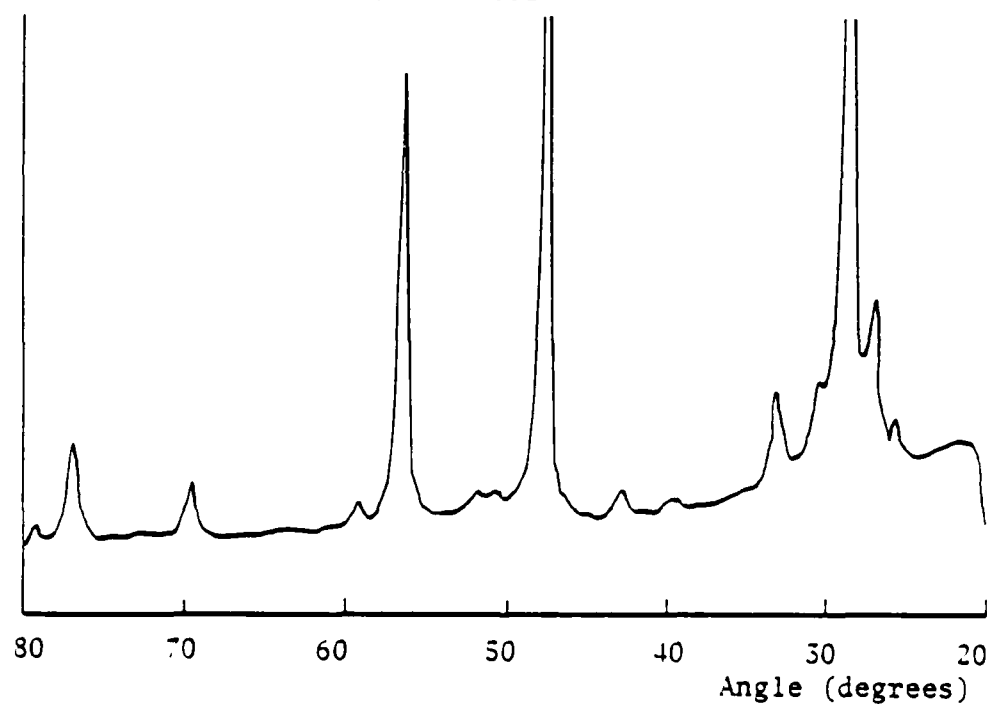
b.

Figure 5.18 Cross section fractographs of zinc sulfide films.

- a. Sample EB-38, unheated substrate, no bombardment
- b. Sample EB-40, unheated substrate, bombarded at 2000 volts.



a. Unheated

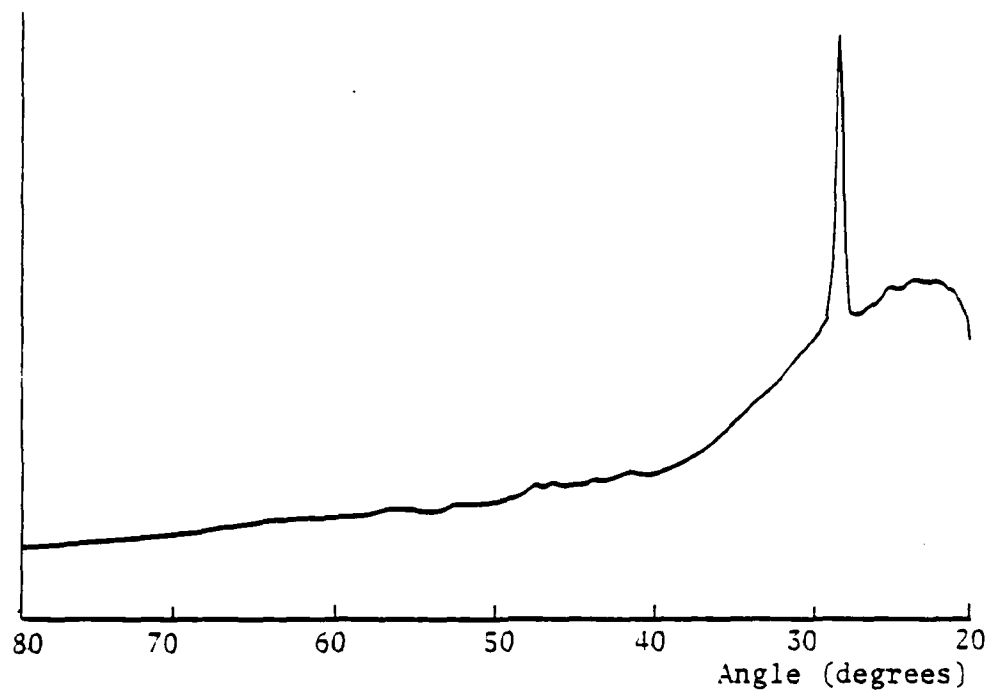


b. Heated

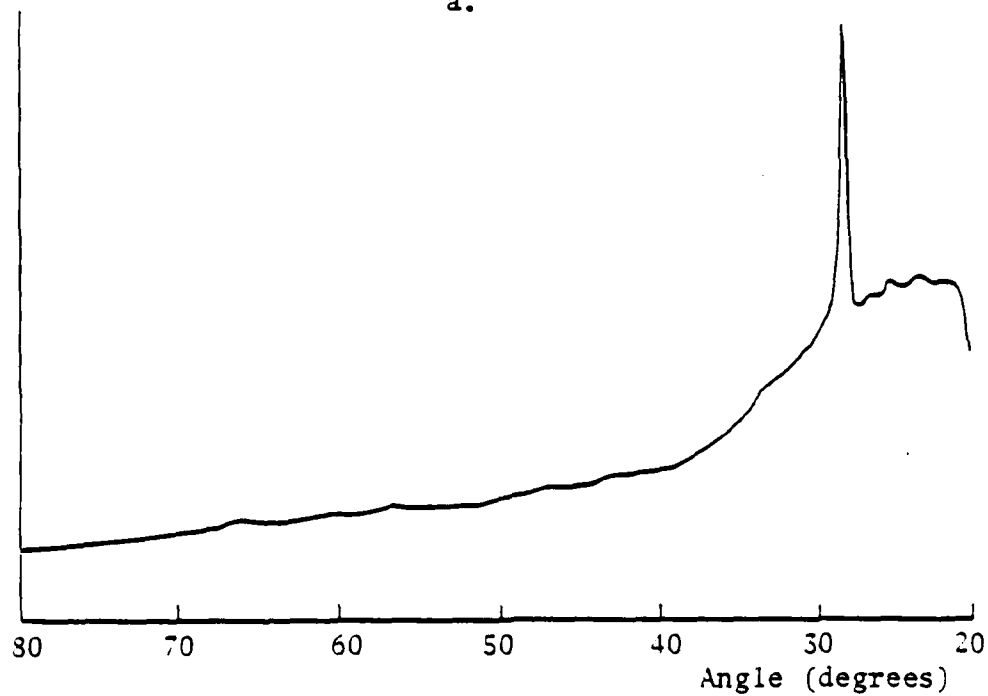
Figure 5.19. X-ray diffractometer traces of zinc sulfide powder, (Atomergic).

Thin films of this material show only the peak at 28.5° in the diffractometer traces. The corresponding lattice spacing is 3.12 angstroms, with Miller indices of (111) in the cubic form and (002) for HCP. Figure 5.20 shows that the peak does not perceptibly shift for bombarded versus non-bombarded films. The diffractometer traces for unheated substrates show the tendency for electron bombardment to eliminate the 47.7° peak. In a result reminiscent of potassium hexafluorozirconate, we see that electron bombardment begins to accomplish the same result as substrate heating.

There is a slight difference in lattice spacing for the two different structures. The HCP spacing of 3.128 angstroms has a corresponding peak angle of 28.51° , while the cubic spacing of 3.123 angstroms has a corresponding peak angle at 28.56° . By decreasing the diffractometer angle scan rate, this difference in angle can be resolved. Figure 5.21 shows the expanded diffractometer trace of the angle range 28.00° to 29.00° for bombarded and non-bombarded films. There is indeed a definite shift of the peak away from 28.51° towards 28.56° , indicating the disappearance of HCP structure zinc sulfide in the film and the appearance of the cubic form with electron bombardment. This confirms the results of Bangert and Pfefferkorn (1980). No flux levels were mentioned by these authors. The bombardment effect increases with both energy and flux. The effect is saturated by the utilized flux level, and the lowest level producing a discernable peak shift was 4.8×10^{13} electrons per square centimeter per second. The electron to molecule arrival ratio was 0.02. Also, comparing Figures 5.21a and 5.21b, we see the shift of the peak from 28.51° to 28.56° for



a.



b.

Figure 5.20. X-ray diffractometer traces of zinc sulfide films on heated substrates.

- a. Sample EB-51, no bombardment
- b. Sample EB-51X, bombarded after deposition
- c. Sample EB-53; bombarded at 2000 volts.

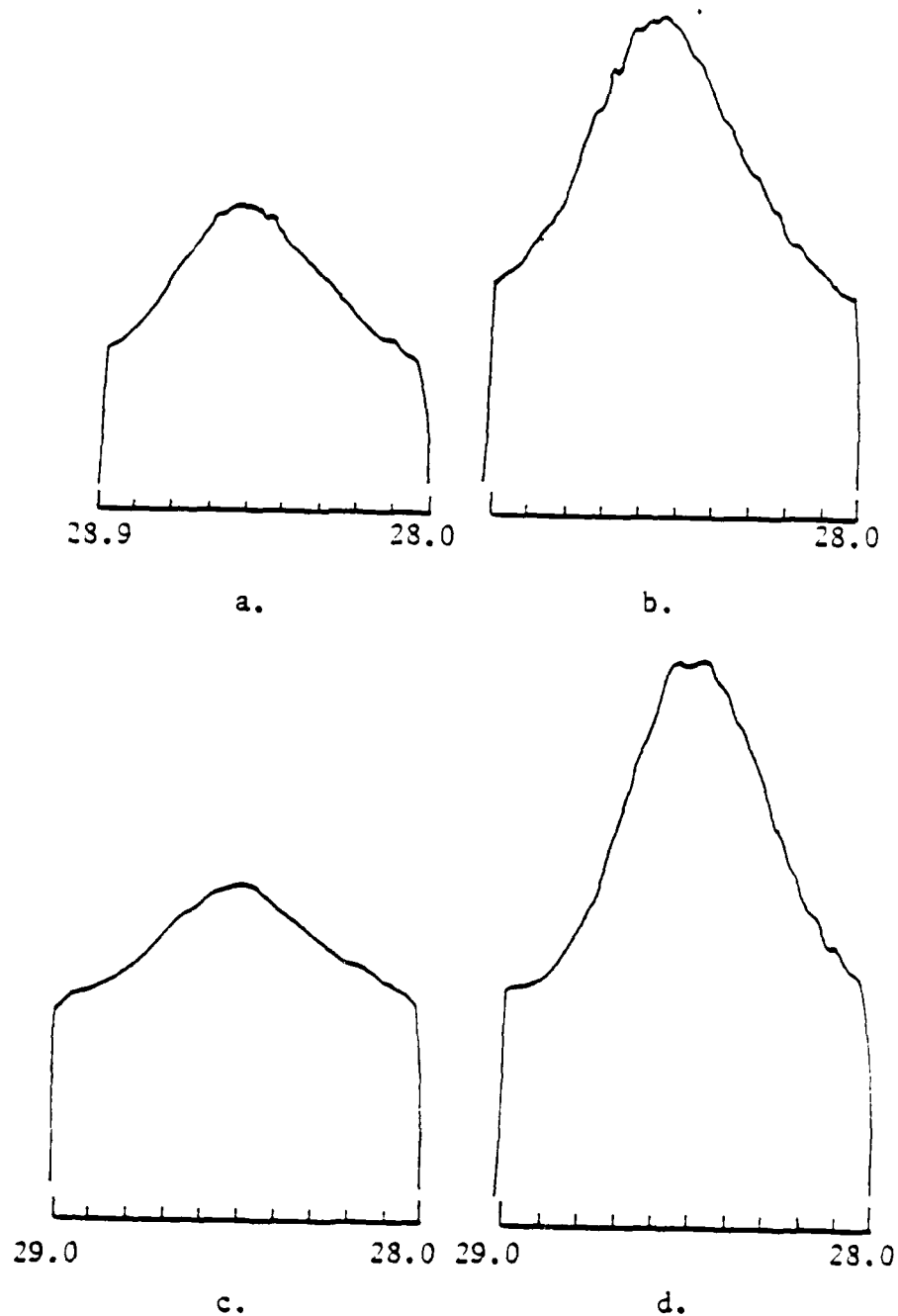


Figure 5.21. Expanded x-ray diffractometer traces of zinc sulfide films.

- a. Sample EB-51, no bombardment, moisture damaged
- b. Sample EB-51, no bombardment
- c. Sample EB-73, bombarded at 1000 volts
- d. Sample EB-75, bombarded at 300 volts.

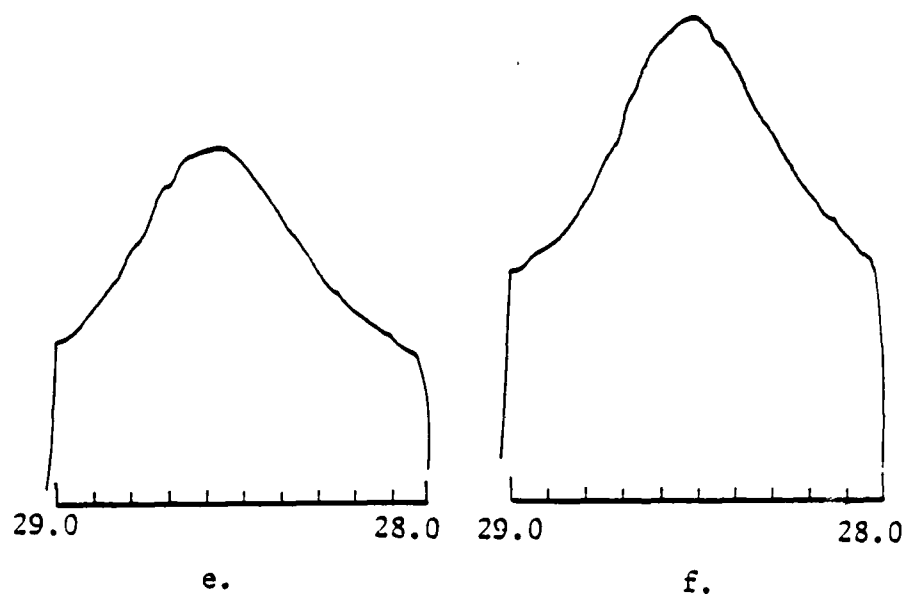


Figure S.2L cont. Expanded x-ray diffractometer traces of zinc sulfide films.

-
- e. Sample EB-53, bombarded at 2000 volts
 - f. Sample EB-74, bombarded at 1000 volts.

the non-bombarded film after it was moisture damaged in the humidity chamber. This further confirms that a shift in crystal structure of zinc sulfide is responsible for moisture damage in thin films.

Table 13 contains the refractive index of bombarded and non-bombarded zinc sulfide films as measured by the prism coupler. The results are fairly consistent, with little variation among the different samples. Apparently the electron bombardment does not affect the refractive index of the films.

The SPW results are listed in Table 14. Again, probably because of absorption, the index values show a fair amount of variation. Any effects due to electron bombardment are overwhelmed.

The spectrophotometer curves of the zinc sulfide films are seen in Figure 5.22. Table 15 contains the calculated optical constants and the respective measured parameters. The refractive index closely matches that measured by SPW, and again we see a small amount of absorption. No appreciable difference exists between bombarded and non-bombarded films. In both instances, a strong absorption cutoff towards the short wavelength end of the spectrum begins near 370 nanometers.

The results of the durability tests are encouraging for applying electron bombardment. The non-bombarded film on an unheated substrate was easily lifted by the Scotch tape test, even when said film was bombarded after deposition. The eraser test heavily damaged the films in both instances. However, the films deposited on unheated substrates with electron bombardment showed no damage from the Scotch tape test and only slight scratch damage from the eraser test. All

Table 13. Refractive index of zinc sulfide films as measured with the prism coupler.

Sample	Bombardment Flux (/cm ² /sec)	Bombardment Voltage	Index
EB-38	none	0	2.351
EB-40		1000	2.348
EB-42		2000	2.356
EB-57	none	0	2.340
EB-57X	1.6×10^{15}	2000	2.343

Table 14. Surface plasma wave analysis of zinc sulfide films.

EB-65	none	0	2.34
EB-65X	none	0	2.31
EB-66	none	0	2.31
EB-66X	1.6×10^{15}	2000	2.30
EB-67	none	0	2.29
EB-67X	1.6×10^{15}	2000	2.29
EB-68	none	0	2.31
EB-68X	none	0	2.31

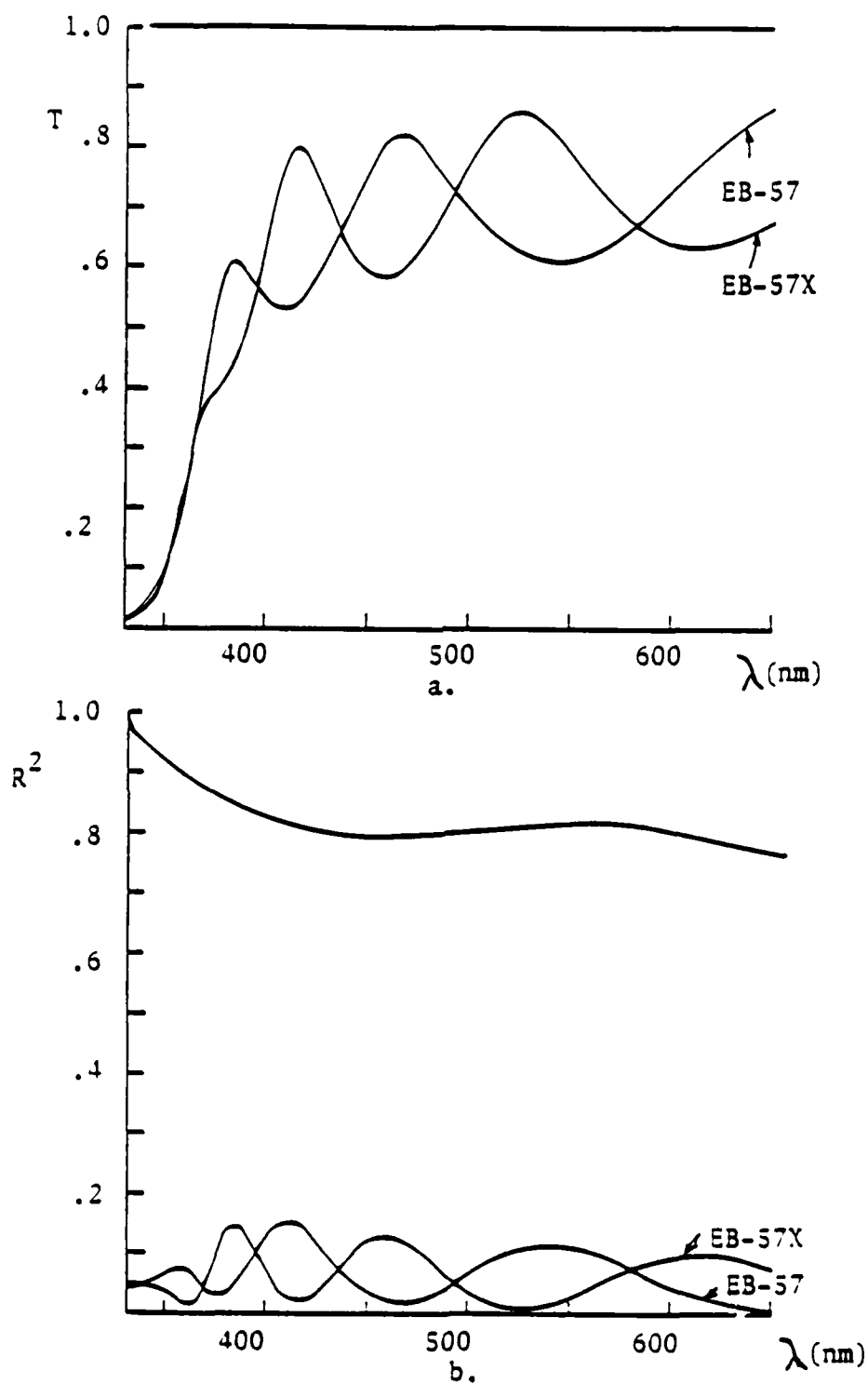


Figure 3.22. Spectrophotometer R and T curves for zinc sulfide films.

Same pump down cycle.

Table 15. Spectrophotometer measurements and calculated index values for bombarded and non-bombarded zinc sulfide films.

Sample	λ (nm)	R	T	1-R-T	FECO d (nm)	$\lambda/2$	n
EB-57	385	.25	.61	.14	200	467	2.34
	409	.44	.53	.03			
	467	.16	.82	.02			
	540	.37	.61	.02			
EB-57X	385	.41	.45	.14	225	526	2.34
	416	.16	.80	.04			
	457	.40	.58	.02			
	526	.11	.86	.03			
	612	.35	.63	.02			

these samples held up well under high humidity conditions. For films deposited on heated substrates, the Scotch tape test did not lift either the bombarded or non-bombarded films. However, the bombarded films showed less scratch damage from the eraser test, even when bombarded after deposition. The non-bombarded films began to show moisture damage when the humidity reached 80 percent, while the bombarded samples did not suffer damage until the humidity was 94 percent. From these results, optimum film durability is achieved for zinc sulfide when deposited on unheated substrates with electron bombardment.

Magnesium Fluoride

Films of this material were the subject of a comprehensive paper quite a few years ago by Turner and Ullrich (1947). Due to its widespread use in the industry, electron bombardment studies were carried out on it.

Figure 5.23 shows X-ray diffractometer traces of heated and unheated powder samples of magnesium fluoride. Table 16 lists the peak angles, lattice spacings, and Miller indices. The powder samples are practically identical except for a slight suppression of the (112) peak with heating.

X-ray traces of the film samples, seen in Figure 5.24, were a bit difficult to interpret. None of the peaks was very prominent, indicating too low a value of film thickness for optimum measurements. Magnesium fluoride films of greater thickness show much more definite peaks. However, it was possible to discern a definite increase in peak height with increasing electron bombardment energy, particularly for

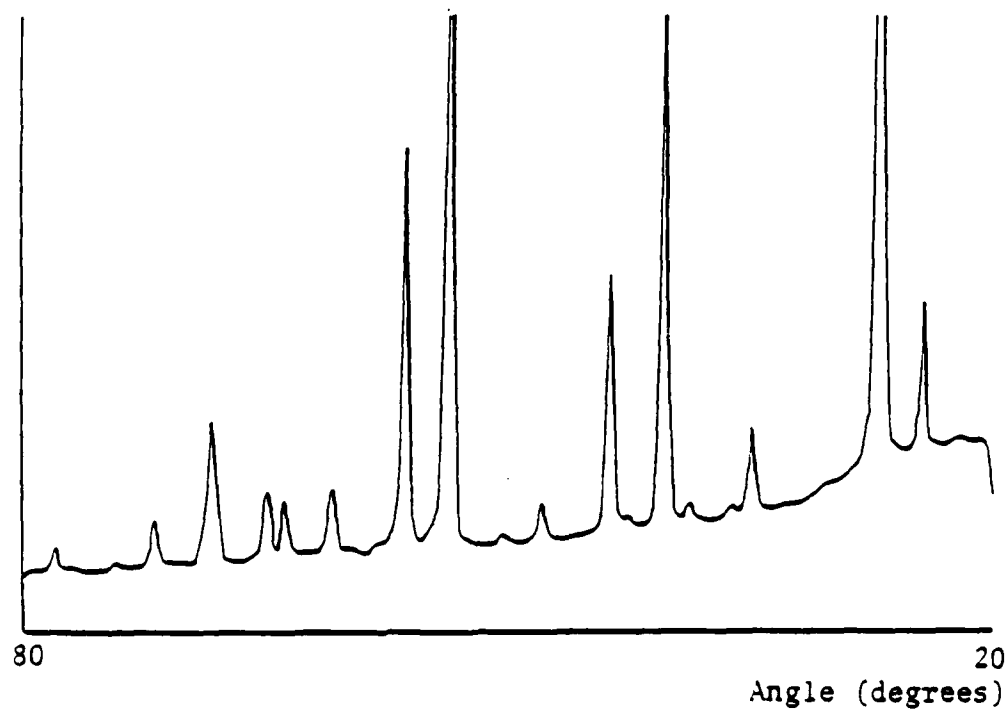
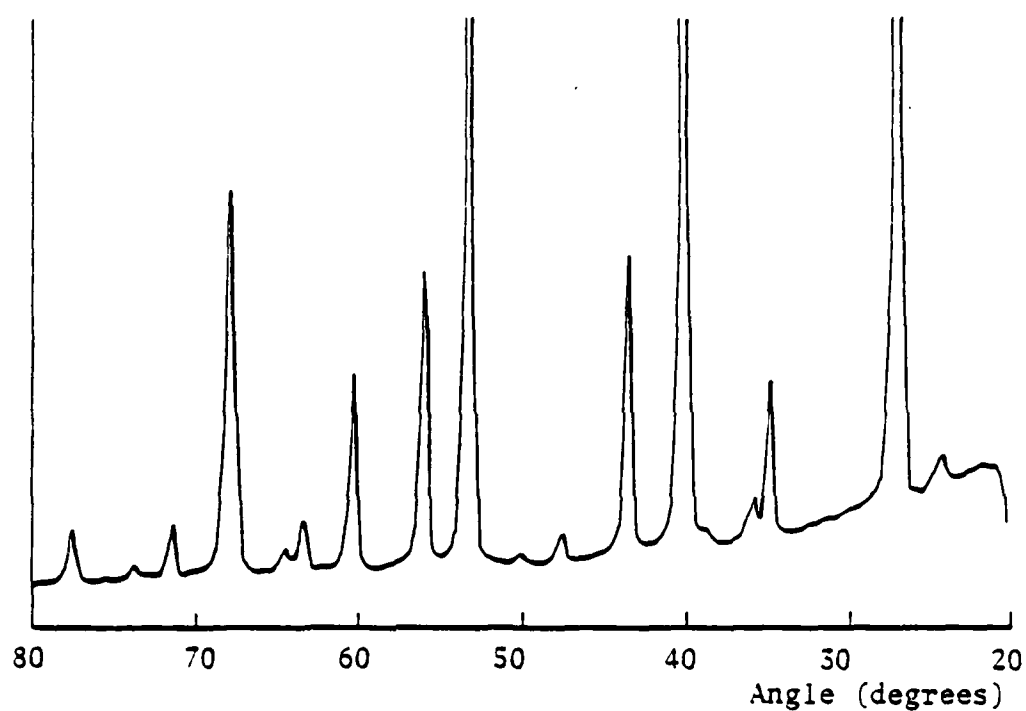
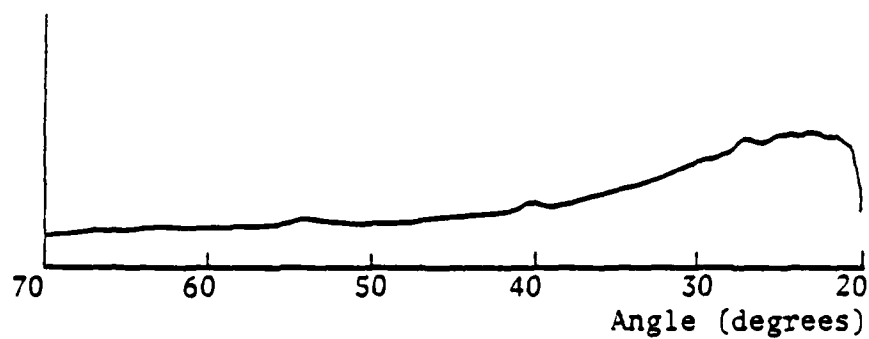


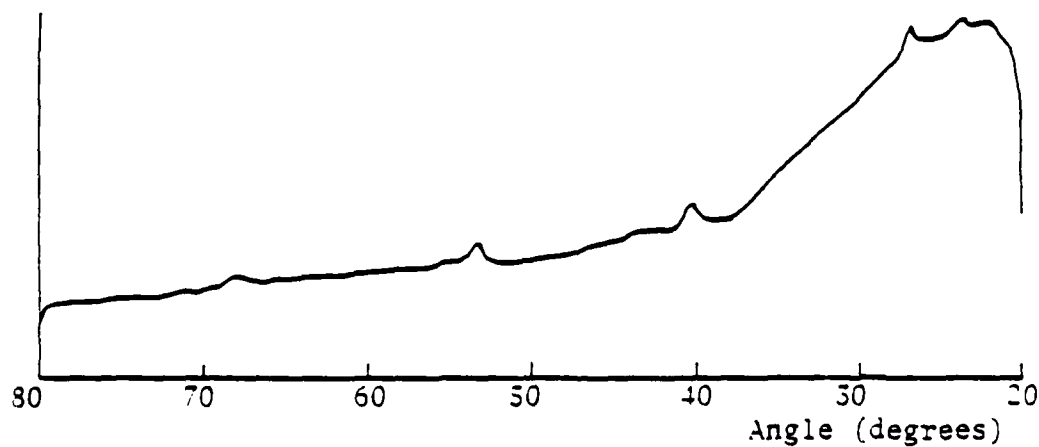
Figure 5.23. X-ray diffractometer traces of magnesium fluoride powder.

Table 16. X-Ray diffractometer peaks for magnesium fluoride powder.

Angle (Degrees)	Lattice Spacing (Angstroms)	Miller Indices
27.1	3.29	(110)
34.8	2.58	(101)
40.0	2.25	(111)
43.4	2.08	(210)
53.1	1.72	(211)
55.9	1.64	(220)
60.2	1.54	(002)
63.3	1.47	(310)
64.4	1.45	(221)
67.8	1.38	(112)
71.4	1.32	(311)
73.6	1.29	(320)
77.4	1.23	(212)



a.



b.

Figure 5.24. X-ray diffractometer traces of magnesium fluoride films.

a. Sample EB-47, no bombardment

b. Sample EB-47X, bombarded after deposition

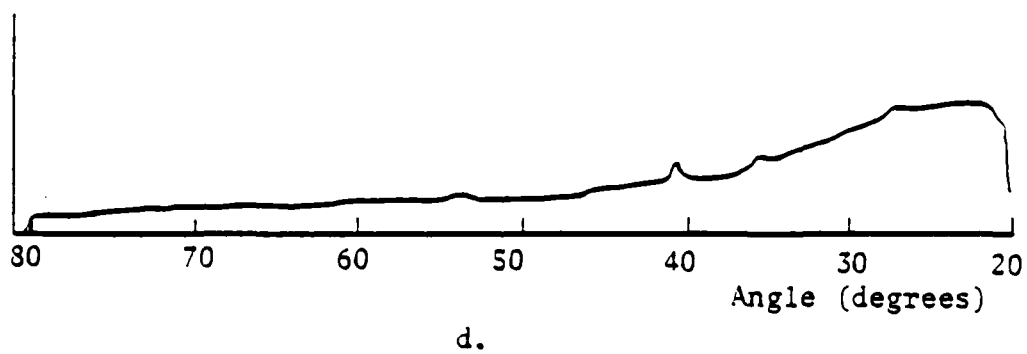
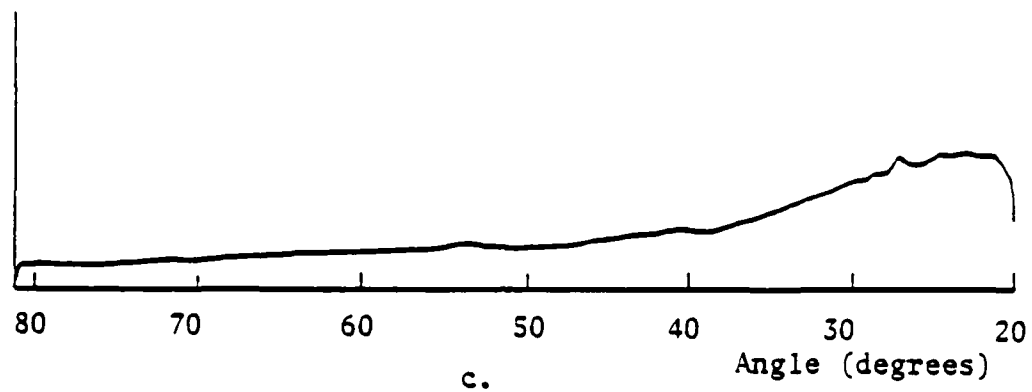


Figure 5.24.cont. X-ray diffractometer traces of magnesium fluoride films.

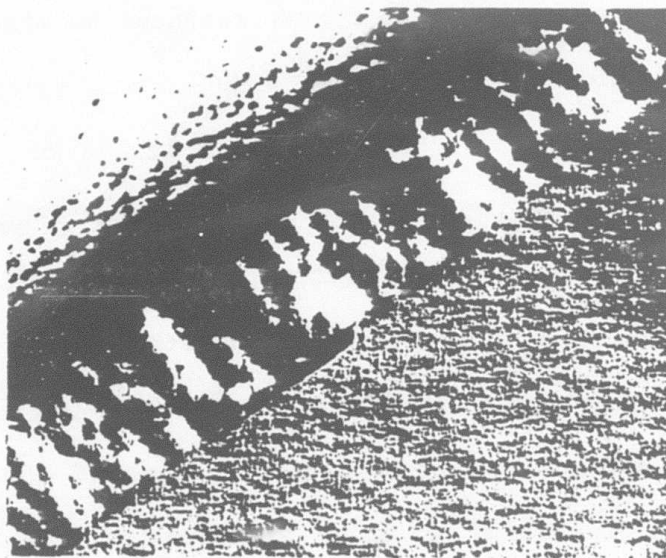
c. Sample EB-46, bombarded at 1500 volts

d. Sample EB-45, bombarded at 2000 volts.

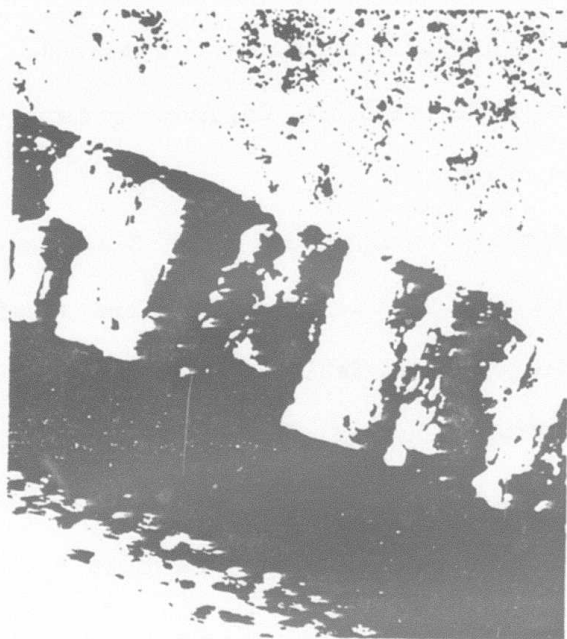
the peak at 40.6° (111). Its corresponding lattice spacing is 2.23 angstroms. Other peaks which appear enhanced by electron bombardment are at 34.8° (101) and 53.8° (211), with lattice spacings 2.58 and 1.71 angstroms, respectively. Electron flux levels of up to 1.3×10^{15} electrons per square centimeter per second were applied. The molecule arrival rate was 5.6×10^{15} molecules per square centimeter per second. Bombarding the film after deposition had the effect of only slightly increasing peak height. The electron flux was 1.1×10^{15} electrons per square centimeter per second at a potential of 1000 volts for 10 minutes. The peak at 27.56° (110), with spacing 3.27 angstroms, did not seem to be changed by electron bombardment.

TEM photographs of cross section replicas reveal little difference in microstructure between bombarded and non-bombarded samples, as seen in Figure 5.25. Columnar growth structure is seen in both types of samples.

Interestingly enough, both the SPW and spectrophotometer results always give magnesium fluoride films a refractive index of 1.38, whether bombarded or not. Table 17 contains the SPW values. In Figure 5.26, the transmittance curves of the bombarded and non-bombarded films coincide almost exactly. However, the reflectance curve for the bombarded film is uniformly lower than that for the non-bombarded, indicating the presence of greater absorption across the entire spectrum of interest. This is brought out in the calculated values of Table 18. Raine (1976) points out that absorption due to the presence of F centers tends to occur mostly in the shorter wavelength region. However, in light of the durability results below, the increase in



a.



b.

Fig. 5.25. Cross section fractographs of magnesium fluoride films.

- a. Sample EB-47, heated substrate, no bombardment
- b. Sample E2-45, heated substrate, bombarded at 2000 volts.

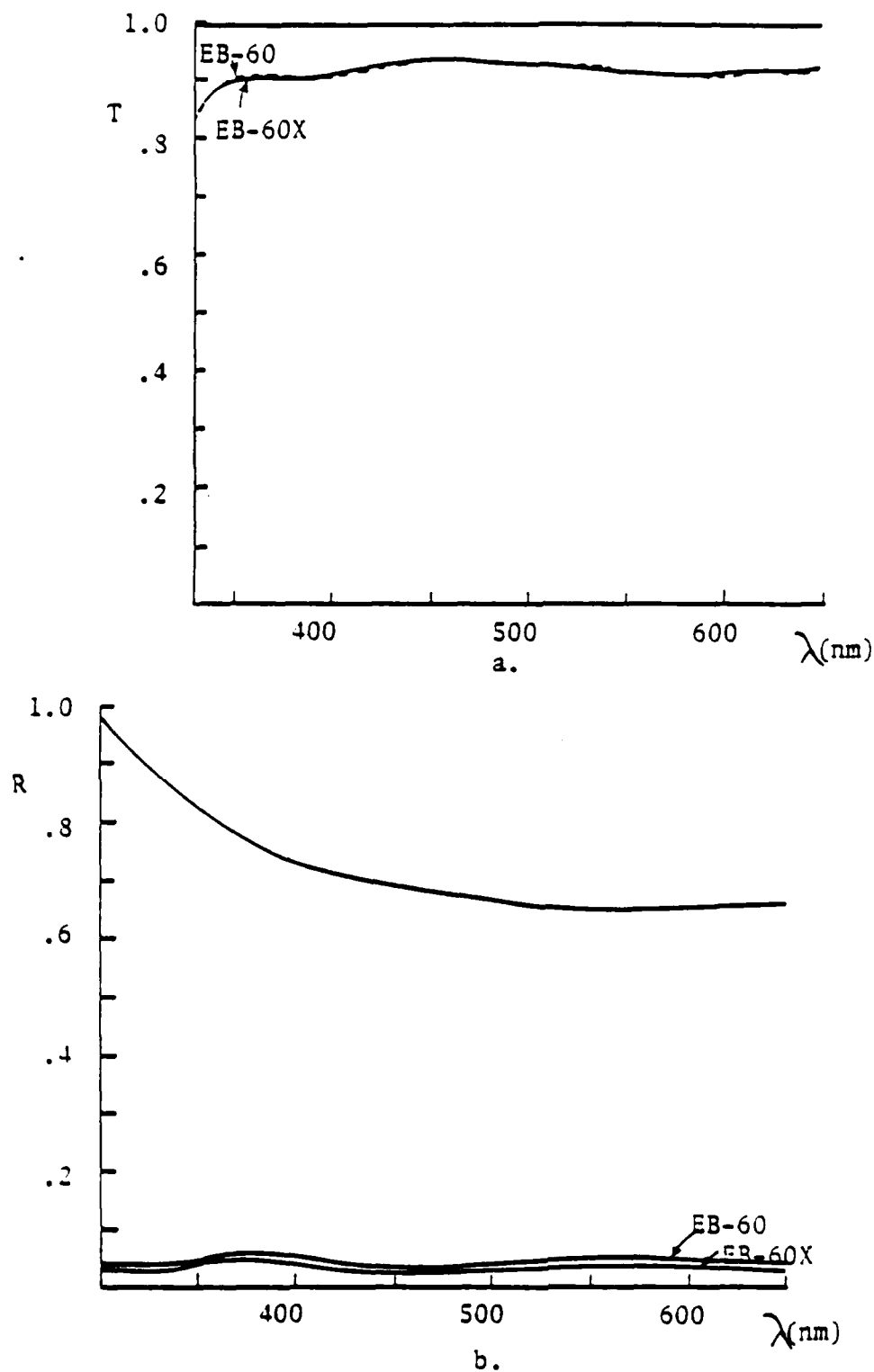


Figure 5.26. Spectrophotometer R and T curves for magnesium fluoride films.

Same pump down cycle.

Table 17. Surface plasma wave analysis of magnesium fluoride films.

Sample	Bombardment Flux (/cm ² /sec)	Bombardment voltage	Index
EB-71	none	0	1.38
EB-71X	none	0	1.38
EB-72	none		1.38
EB-72X	1.6×10^{15}	2000	1.38

Table 18. Spectrophotometer measurements and calculated index values for bombarded and non-bombarded magnesium fluoride films.

Sample	λ (nm)	R	T	1-R-T	FECO d (nm)	$\lambda/2$	n
EB-60	382	.08	.90	.02	424	585	1.38
	465	.05	.93	.02			
	585	.08	.91	.01			
EB-60X	382	.06	.90	.04	424	585	1.38
	465	.04	.93	.03			
	585	.05	.91	.04			

"absorption" is probably due to greater scattering from electrons having disrupted the film.

The durability test results are rather interesting. The non-bombarded magnesium fluoride film was not lifted at all by the Scotch tape test and showed only moderate scratch damage from the eraser test. The film bombarded after deposition also was not lifted, but was more heavily damaged by the eraser test. Finally, the film bombarded during deposition was slightly lifted by the Scotch tape test and moderately damaged by the eraser test. The humidity tests revealed that magnesium fluoride films generally resisted moisture damage extremely well. The only evidence of damage was a small amount of spotting at a humidity of 94 percent on the sample bombarded after deposition. Electron bombardment either during or after deposition had a detrimental effect on overall film mechanical durability. Even though the electron to molecule arrival ratio was appreciable, the electron bombardment effects on magnesium fluoride films do not appear to be very considerable.

CHAPTER 6

REMARKS ON FILM FORMATION AND ELECTRON INTERACTION

To understand more fully the bombarding electron interactions with the thin films, a brief look at the theory of film formation is presented here. Chopra (1969) gives an excellent review in his book, as well as numerous references.

It is generally recognized that a thin film forms in discrete stages. Nucleation, agglomeration, and secondary filling or supplemental growth are the steps common to most materials, although agglomeration is much more pronounced in metal films. As evaporant molecules arrive at the substrate, they are attracted by the quadrupole and dipole moments of the substrate molecules. The arriving molecules, once surface-bound, can continue to move along the substrate surface. They are now called adatoms because they have been adsorbed by the substrate. Their mobility depends on several factors, including the nature of the materials and substrate temperature. Adatoms begin to cluster at specific areas, called nucleation sites. The positions of these sites are determined by factors such as discontinuity defects on the substrate surface and arriving molecule flux. As additional molecules arrive and migrate along the surface, they bond onto these existing nucleation clusters. The clusters grow and expand outward until another is encountered. Depending on the material as well as numerous other parameters, the clusters can coalesce into one

crystallite or simply butt into each other. Metals tend to agglomerate, leaving large voids which give rise to secondary nucleation and filling. In the case of most dielectrics, as more evaporant molecules arrive, they continue to bond onto the existing crystallites, which grow upward to form columns. Pulker and Jung (1971) and Ogura (1975) have given more detailed studies of such columnar growth. The columns are not necessarily composed of a homogeneous crystal structure, but may contain many fibrous constituents. This phenomenon has yet to be satisfactorily explained. We see then that film crystallite size, columnar structure, and void content or packing density depend on nucleation density on the substrate surface and adatom mobility after arrival. Increased nucleation forms smaller crystallites, while higher mobility tends to enlarge crystallite size.

The effects of bombarding the substrate with electrons can now be analyzed. First, Chopra points out that the presence of electrostatic charge can lower the free energy of an adatom, facilitating condensation. This leads to more nucleation sites per unit area. Chambers and Prutton (1967) contend that the increase in nucleation sites is the result of the electrons causing more surface defects on the substrate, but their depositions were formed on cleaved salt plates. Stirland (1966) achieved similar results for gold films evaporated onto cleaved rocksalt plates. By either mechanism, nucleation is enhanced by the electrons, which should lead to a decrease in crystallite size.

Electron collisions with adatoms could increase surface mobility if an elastic collision with the nucleus takes place. As

pointed out later, this type of collision is not common. However, the electrons often inelastically scatter from the bound electrons, which could break up the molecular bond or the lattice bond, breaking up crystallites that have already formed. Thus we expect the principle result of electron bombardment to be an overall decrease in crystallite size, both from increased nucleation density and destruction of existing crystallites.

One point to mention about films bombarded after deposition concerns electron penetration into the film. This is often called scattering range. Beaman and Isasi (1972) give a summary of formulas for this range obtained by different investigators. Basically, four electron-molecule interactions are possible. 1) Elastic scattering with no energy loss is possible from the nucleus or 2) the bound electrons, although the authors claim that the latter is negligible. 3) Inelastic scattering from the nucleus produces Bremsstrahlung radiation, while 4) inelastic scattering from the bound electrons can ionize the molecule or, less frequently, eject an inner core electron. The first and fourth processes mentioned above dominate the scattering interaction. The following expression was presented for the range, although others more explicitly dependent on atomic number were also given;

$$R = 0.064E_0/\rho,$$

where R is the penetration in micrometers, E_0 is the electron potential in kilovolts, and ρ is the material density in grams per cubic centimeter. Using the bulk density values for the materials and E_0

equal to one kilovolt, electron ranges from 120 to 300 angstroms were calculated. These values are typically less than 10 percent of total film thickness, which may explain the general lack of change in X-ray diffractometer traces for films bombarded after deposition. However, antimony trioxide films do not fit into this pattern. The diffractometer traces indicate crystal reorientations for bombardment during or after deposition to be comparable. This could possibly indicate that the films' interaction depth with the X-rays is on the same order as the electron range. It could alternately indicate that the films' lattice bonding energy is less than the amount of energy an electron can transfer to the molecule. This lattice bonding energy is certainly weak, as evidenced by total film removal in the eraser test.

CHAPTER 7

CONCLUSIONS

In the beginning, it was felt that the effects of bombarding thin films with electrons as they were being deposited could best be explained with a transfer of energy or momentum approach. A certain electron flux at a certain energy bombarding a certain number of arriving molecules would produce a definable change in the microstructure. This change could then be correlated to changes in macroscopic quantities. While this approach may indeed apply for some instances, others exist where it clearly does not. Therefore, rather than concentrating on one or two materials, a fairly representative sampling of thermally evaporated materials was investigated. Many others exist, but those selected cover a wide range of applications and include some of the most commonly used in the industry today.

From the results in Chapter 5, electron bombardment shows no clear general trend for all materials in either micro- or macrostructural properties. However, the X-ray diffractometer traces indicate that the bombarding electrons definitely affect the crystal structure, except for silicon monoxide, where no crystal structure existed anyway. The results of electron bombardment of each material will be summarized in the following sections. Specific emphasis will be placed on the X-ray traces in trying to interpret these results.

We have used antimony trioxide extensively as a waveguiding layer in several integrated optics experiments in our laboratory. As previously stated, scattering losses in guided wave structures can be very detrimental to overall performance. The light must propagate through film for up to several centimeters rather than just a few wavelengths, as in typical interference filters. Scattering can arise from surface roughness at the layer boundaries as well as from impurities and discontinuities within the film. Often these internal dislocations are the actual walls and voids of the growth columns discussed earlier. Channin, Hammer, and Duffy (1975) investigated bulk and surface scattering in epitaxially formed zinc oxide waveguides. They found that slowing the deposition rate and annealing the films at high temperatures after deposition decreased bulk scattering. Both of these processes tend to form very large crystallites. Surface scattering was reduced by sophisticated polishing of the substrates prior to deposition.

The above results are probably not applicable to vacuum deposited films because while crystallites in epitaxial films may be large, their common orientation excludes the presence of voids. In other words, the crystallites butt against each other with faces having the same crystallographic orientation, so they fit together very closely. If bulk scattering is assumed to have a Rayleigh form, smaller voids would reduce the scatter. This comes from the dependence of the scattering cross section on the sixth power of the radius of the inclusions. Thus, for vacuum deposited films, the crystallites must be reduced in size. The idea behind electron

bombardment of the antimony trioxide films was to pulverize the growing columns to compact the film and break up the crystallites, eliminating the crystal structure. From the results of all the analyses, particularly the X-ray diffraction and TEM carbon replicas, the original ideas of electron bombardment effects were not entirely applicable to antimony trioxide. The growth columns did not seem greatly affected, and the crystal structure was rearranged, not eliminated entirely.

Reviewing the antimony trioxide results, we see that the X-ray traces indicate a different set of lattice planes becoming preferentially oriented parallel to the substrate, even at electron to molecule arrival ratios as low as 0.01. The rearrangement increases with electron flux to a point, then little further change takes place. The fact that these changes occurred even after deposition suggests a weak lattice bonding for antimony trioxide, further evidenced by the complete removal of the films from the substrate in the eraser test. The TEM cross sections do not look vastly different for bombarded and non-bombarded films, although the non-bombarded film appears more coarse, suggesting a lower packing density. Electron diffraction indicates that the films have smaller crystallites when electron bombarded than when not, perhaps due to the breaking up of forming crystallites. This coincides with the predicted results. Refractive index suffers little change from the bombarding electrons, evidenced by the prism coupler and SPW results. Also, the waveguiding quality as evidenced by the appearance of a nice, clean streak in the prism coupler set-up was not improved by electron bombardment. All samples

guided poorly, indicating that factors other than film crystallite size dominated the scattering process. Spectrophotometer traces reveal that bombarded films have slightly more absorption or scatter. The durability is not affected by electron bombardment. The crystallite changes nearly saturate at electron to molecule arrival ratios of less than unity. All in all, the arriving electrons appear to reduce crystallite size, rearrange the crystallites to preferentially orient the (400) plane parallel to the substrate, and possibly increase the packing density slightly. These changes have only minimal effect on film optical and macrostructural behavior.

In contrast, potassium hexafluorozirconate showed much more dramatic, easily understood behavior. Electron bombardment eliminated crystal structure if applied during deposition. An electron to molecule arrival ratio of almost 0.5 almost completely eliminated crystallinity on a heated substrate. This indicates possible multiple collisions of one electron with several different molecules. The electron bombardment was more efficient when the substrates were heated, indicating that the effect is partly due to elevating the energy level of the condensing molecules. The fact that films bombarded after deposition were not greatly affected points out that once the crystallites become formed, the lattice bonding energy is greater than what the electrons can transfer to the molecules. The only difference in optical properties caused by electron bombardment seems to be a slight increase in absorption towards the ultraviolet, consistent with the idea of electrons ejecting an anion from the molecules and replacing them in the lattice, forming an F center. This is in

agreement with the results obtained by Chambers and Prutton (1967), as well as Hoffman and Leibowitz (1971). Film durability was only slightly affected by electron bombardment induced changes in the microstructure.

Silicon monoxide shows no effects at all from the bombarding electrons. Microstructural and observable properties undergo no alterations. An electron to molecule arrival ratio of up to 0.26 was insufficient to bring about any changes. The silicon and oxygen atoms accumulate without regular repetitions of molecular arrangements because of the variable nature of their covalent bonding. In other words, shared electron pairs can exist between the atoms in any of several configurations. This also explains the lack of an established unique stoichiometry for films of this material. Bombarding electrons which disrupt the bonding do so indiscriminately, so the result is indistinguishable from the original situation. The optical properties of the films showed variations which were more attributable to residual gas pressure differences than to any other parameter.

By studying zinc sulfide, the results of Bangert and Pfeifferkorn (1980) were expanded and clarified. The long observed but little understood improvements in a "beamed" zinc sulfide film can now be seen in a quantitative light. When heated and evaporated, zinc sulfide vapor condenses on the substrates predominantly with HCP crystal structure, the form stable at elevated temperatures. However, the structure shifts to cubic as the film attempts to stabilize, disrupting the film and allowing moisture penetration. Electron bombardment during deposition with an electron to molecule arrival

ratio of 0.02 causes a perceptible change from HCP to cubic structure, and a ratio of 0.9 saturated this change, suggesting multiple electron collisions. Resistance to moisture penetration and damage improved with increasing bombardment flux, but was more pronounced for films deposited on unheated substrates. Adsorption of residual water vapor into the films during deposition is greater in this case. For this reason, as well as the lower temperature, any HCP structure is more likely to be changed to cubic as the film is forming. Conversely, films deposited on heated substrates will have more HCP structure both during and after deposition, which disrupts the film as it changes form and stabilizes. Films bombarded after deposition showed little effect, again suggesting the inability of the electrons to transfer energies to the molecules greater than the lattice bonding energy. Film optical properties were hardly changed at all by electron bombardment.

Magnesium fluoride was a bit more difficult to understand, mainly because the films were too thin to provide good X-ray diffraction peaks. These small peaks were enhanced by electron bombardment, possibly because the crystallites are smaller and more numerous, enhancing X-ray interaction with the film. Electron to molecule arrival ratios of up to 0.23 were applied without saturating this peak enhancement. The increase in optical losses, along with a deterioration in durability, points out that the bombarding electrons weaken overall film structure. The changes in optical absorption are consistent with the findings by Raine (1976), but in his study the absorption was much more pronounced.

In view of the results for these very different film materials, general comments about the trends of electron bombardment are difficult to make. Each material was characterized as to the type of bonding between its constituent elements on the basis of electronegativity. Values from Gordy and Thomas (1956) were used. High electronegativity differences indicate largely ionic bonding, while low differences mean the bond is mainly covalent. Ionic bonds mean lower polarizability, hence lower refractive index. Table 19 lists each material, its electronegativity difference value, refractive index, and bonding character. This bonding character does not seem to play an important role in determining the effects of electron bombardment on a particular material. For instance, potassium hexafluorozirconate and magnesium fluoride both have ionic bonding, but each behaves in its own way under electron bombardment. Apparently, molecular bonding type can not be used to predict the effects of electron bombardment. Lattice bonding seemingly determines whether or not a film will be affected by bombardment after deposition, but does not explicitly affect bombardment results during deposition.

Some generalities are possible, however. The electron bombardment effects for most materials saturated at electron to molecule arrival ratios of less than unity, suggesting multiple electron collisions. Crystallites seem to be made smaller, and eliminated in potassium hexafluorozirconate, by electron bombardment. Also, the effects tend to increase gradually with electron flux and energy. It can not readily be stated that electron bombardment will always produce an improvement in film properties. Zinc sulfide seems

Table 19. Bonding character of studied materials.

Material	Electronegativity Difference	Index	Bond Type
Sb_2O_3	1.7	2.10	moderately covalent
$2\text{KF} \cdot \text{ZrF}_4$	3.1	1.35	very ionic
	2.4		
SiO	1.7	(1.85)	moderately covalent
ZnS	1.0	2.35	very covalent
MgF_2	2.7	1.38	very ionic

to be a special case, involving an actual change in crystal microstructure from one form to another. Magnesium fluoride films show detrimental effects from the bombarding electrons, while silicon oxide shows no effects at all. For the materials studied, many changes in film microstructure induced by electron bombardment have been shown to accompany changes in macrostructural properties.

On the whole, electron bombardment is a process which must be carried out on each individual material to determine its exact behavior. For the materials in this study, several recommendations are possible. Antimony trioxide is a good candidate for electron bombardment if the films are to be used as waveguides. I say this because of the reduction in crystallite size brought about by the bombarding electrons, although the guiding results in this study were inconclusive. Films deposited in different runs under supposedly identical conditions showed wide variations in guide quality. Further investigation is required, perhaps using higher quality polished substrates. Potassium hexafluorozirconate definitely needs to be evaporated onto heated substrates. Electron bombardment makes the films amorphous, a useful effect for guided wave applications. Silicon monoxide is not changed by electron bombardment, so there is no point in applying it here. Zinc sulfide films definitely should be electron bombarded to increase longevity and durability. Magnesium fluoride is not greatly affected by electron bombardment, but the effects are detrimental, so it should not be applied here.

Further investigations into the effects of electron bombardment of thin films during deposition are certainly called for. The behavior

of bombarded multilayer structures, particularly in regard to packing density and moisture adsorption, would be most enlightening. Other materials, particularly those which have widely varying properties for different crystal structures, would also be very interesting to study.

APPENDIX 1

MOLECULE FLUX CALCULATIONS

To get an idea of the arrival rate of molecules at the substrates during a deposition, some simple calculations were carried out. I should actually refer to the sticking rate, since re-evaporation effects are ignored. First, the deposition rate in angstroms per second was calculated by dividing the total film thickness as monitored by total deposition time. It should be pointed out here that the work to monitor ratio was 1.1, as previously shown. In other words, the samples to be analyzed were 10 percent thicker than the monitor indicated, due to the geometry of the plant fixtures. Total film physical thickness was calculated assuming film refractive index equal to that of the bulk material. The deposition rate in angstroms per second was converted to grams per square centimeter per second using the density of the bulk material. This figure was then converted to molecules per square centimeter per second using Avogadro's number and the molecular weight of the material. The above assumptions greatly simplified the calculations. However, film refractive index is generally less than that of the bulk material due to packing densities of less than unity, which also leads to a film density less than bulk density. These two effects tend to cancel each other in the calculations.

A sample computation for antimony trioxide appears below.

Table A1 lists the different materials with their bulk refractive indices, densities, and molecular weights.

Antimony Trioxide

5500 angstroms (monitored optical thickness) \times 1.1 (work to monitor ratio) \times 1/2.1 (bulk refractive index) \times 1/1800 seconds (total deposition time) = 1.6 angstroms per second (deposition rate)

1.6 angstroms per second \times 1 cm/ 10^8 angstroms (conversion factor) \times 1 square centimeter \times 5.2 grams per cubic centimeter (density) \times 6.02×10^{23} molecules (Avogadro's number) \times 1/292 grams (molecular weight) = 1.72×10^{14} molecules per square centimeter per second

APPENDIX 2

LIST OF COATING RUNS

The following table is a complete list of the coating runs performed along with the deposition conditions.

Table A.1. Refractive index, density, and molecular weight for the bulk form of the materials used in this study.

Material	Refractive Index ¹	Density (g/cm ³)	Molecular Weight
Sb ₂ O ₃	2.10	5.2	292
2KF.ZrF ₄	1.35 ²	3.5 ³	283
SiO	(1.85)	2.1	44
ZnS	2.35	4.1	97
MgF ₂	1.36	2.9	62

1. Values from Sloan Handbook (1973-74)

2. From Bartle and Turner (1962)

3. No value was found, so a simple displacement of liquid (acetone) was used.

Table A.2. Coating runs and conditions.

Sample	Material	Substrate Temperature (C)	Pressure (torr)	Bombardment Voltage	Bombardment Flux (/cm ² /sec)
EB-7	1	170	1.1×10^{-4}	0	0 ₁₂
EB-8	1	150	1.6×10^{-4}	1000	1.6×10^{12}
EB-9	1	150	1.0×10^{-4}	2000	3.5×10^{12}
EB-10	1	60	1.3×10^{-4}	1000	1.5×10^{15}
EB-11	1	45	1.2×10^{-4}	0	0
EB-12	2	110	0.6×10^{-4}	0	0 ₁₅
EB-12X	2	110	1.0×10^{-4}	1000	1.4×10^{15}
EB-13	2	105	0.5×10^{-4}	1000	1.1×10^{15}
EB-14	1	190	1.0×10^{-4}	0	0 ₁₄
EB-15	1	155	1.2×10^{-4}	1000	3.0×10^{14}
EB-17	1	30	1.0×10^{-4}	0	0 ₁₄
EB-18	1	120	1.5×10^{-4}	2000	5.0×10^{13}
EB-19	1	130	1.2×10^{-4}	400	6.2×10^{14}
EB-20	1	30	1.1×10^{-4}	1000	3.0×10^{14}
EB-21	1	155	0.8×10^{-4}	0	0
EB-22	1	150	0.9×10^{-4}	0	0
EB-23	1	145	1.0×10^{-4}	0	0
EB-23X	1	145	1.0×10^{-4}	1000	1.4×10^{15}
EB-24	3	175	2.2×10^{-5}	1000	4.8×10^{14}
EB-25	3	175	1.3×10^{-5}	0	0
EB-25X	3	175	1.3×10^{-5}	1000	4.8×10^{14}
EB-26	3	145	1.9×10^{-5}	0	0
EB-26X	3	145	2.0×10^{-5}	2000	1.5×10^{15}
EB-27	3	140	2.9×10^{-5}	2000	1.5×10^{15}
EB-28	3	150	2.1×10^{-5}	1500	1.6×10^{15}
EB-29	3	35	2.8×10^{-5}	200	1.5×10^{15}
EB-30	3	30	2.4×10^{-5}	0	0
EB-30X	3	30	2.8×10^{-5}	2000	1.5×10^{15}
EB-31	2	30	4.0×10^{-5}	1500	1.2×10^{15}
EB-32	2	30	0.5×10^{-4}	0	0
EB-32X	2	30	1.0×10^{-4}	1000	1.4×10^{15}
EB-33	2	50	0.6×10^{-4}	1000	1.2×10^{15}
EB-34	2	30	0.5×10^{-4}	1500	1.3×10^{15}
EB-35	2	30	4.9×10^{-5}	500	5.5×10^{14}
EB-36	2	115	0.7×10^{-4}	1500	1.3×10^{15}
EB-37	2	115	3.5×10^{-5}	500	5.5×10^{14}
EB-38	4	30	0.8×10^{-4}	0	0
EB-39	4	30	1.1×10^{-4}	1500	1.3×10^{15}
EB-40	4	30	1.2×10^{-4}	2000	1.3×10^{15}
EB-41	4	30	0.8×10^{-4}	500	6.0×10^{14}
EB-42	4	30	3.0×10^{-5}	1000	1.2×10^{15}
EB-43	2	30	2.6×10^{-5}	1000	1.2×10^{15}

Table A.2.--continued.

Sample	Material	Substrate Temperature (C)	Pressure (torr)	Bombardment Voltage	Bombardment Flux (/cm ² /sec)
EB-44	2	30	2.6x10 ⁻⁵	2000	1.6x10 ¹⁵
EB-45	5	175	0.9x10 ⁻⁴	2000	1.6x10 ¹⁵
EB-46	5	160	0.8x10 ⁻⁴	1500	1.3x10 ¹⁵
EB-47	5	155	0.9x10 ⁻⁴	0	0
EB-47X	5	155	2.0x10 ⁻⁵	1500	1.2x10 ¹⁵
EB-48	5	165	0.9x10 ⁻⁴	1000	1.4x10 ¹⁵
EB-49	4	30	1.0x10 ⁻⁴	1500	1.3x10 ¹⁵
EB-50	4	135	0.7x10 ⁻⁴	0	0
EB-51	4	100	0.6x10 ⁻⁴	0	0
EB-51X	4	100	2.0x10 ⁻⁵	1500	1.2x10 ¹⁵
EB-52	4	100	5.0x10 ⁻⁵	2000	1.6x10 ¹⁵
EB-53	4	100	4.6x10 ⁻⁵	2000	1.6x10 ¹⁵
EB-54	4	100	0.5x10 ⁻⁴	1500	1.3x10 ¹⁵
EB-55	4	100	0.6x10 ⁻⁴	1000	1.2x10 ¹⁵
EB-56	4	100	5.0x10 ⁻⁵	500	6.0x10 ¹⁵
EB-57X	4	100	0.6x10 ⁻⁴	2000	1.6x10 ¹⁵
EB-57	4	100	0.5x10 ⁻⁴	0	0
EB-58X	2	100	2.2x10 ⁻⁵	2000	1.6x10 ¹⁵
EB-58	2	100	1.4x10 ⁻⁵	0	0
EB-59X	3	100	1.5x10 ⁻⁵	2000	1.6x10 ¹⁵
EB-59	3	100	0.6x10 ⁻⁵	0	0
EB-60X	5	100	2.6x10 ⁻⁵	2000	1.6x10 ¹⁵
EB-60	5	100	1.8x10 ⁻⁵	0	0
EB-61X	3	100	0.7x10 ⁻⁵	2000	1.6x10 ¹⁵
EB-61	3	100	5.0x10 ⁻⁶	0	0
EB-62X	3	115	1.2x10 ⁻⁵	2000	1.6x10 ¹⁵
EB-62	3	115	0.5x10 ⁻⁵	0	0
EB-63X	3	110	1.9x10 ⁻⁵	2000	1.6x10 ¹⁵
EB-63	3	110	0.8x10 ⁻⁵	0	0
EB-64X	3	100	1.4x10 ⁻⁵	2000	1.6x10 ¹⁵
EB-64	3	100	1.0x10 ⁻⁵	0	0
EB-65X	4	30	3.3x10 ⁻⁵	2000	1.6x10 ¹⁵
EB-65	4	30	2.8x10 ⁻⁵	0	0
EB-66X	4	30	1.4x10 ⁻⁵	2000	1.6x10 ¹⁵
EB-66	4	30	0.9x10 ⁻⁵	0	0
EB-67X	4	30	1.8x10 ⁻⁵	2000	1.6x10 ¹⁵
EB-67	4	30	1.1x10 ⁻⁵	0	0
EB-68X	4	30	1.1x10 ⁻⁵	0	0
EB-69	2	30	0.9x10 ⁻⁵	0	0
EB-70X	2	30	2.4x10 ⁻⁵	2000	1.6x10 ¹⁵
EB-70	2	30	1.6x10 ⁻⁵	0	0
EB-71	5	30	1.4x10 ⁻⁵	0	0
EB-72X	5	30	4.3x10 ⁻⁵	2000	1.6x10 ¹⁵
EB-72	5	30	1.8x10 ⁻⁵	0	0
EB-73	4	100	4.5x10 ⁻⁵	1000	3.1x10 ¹²

Table A.2.--continued.

Sample	Material	Substrate Temperature (C)	Pressure (torr)	Bombardment Voltage	Bombardment Flux (/cm ² /sec)
EB-74	4	100	3.4×10^{-5}	1000	1.9×10^{13}
EB-75	4	100	4.5×10^{-5}	300	2.3×10^{13}

1- Sb_2O_3 2- $2\text{KF} \cdot 2\text{rF}_4$ 3- SiO 4- ZnS 5- MgF_2

APPENDIX 3

REPRESENTATIVE SPW PLOTS

This appendix should serve as an illustration of the types of graphs encountered in using the SPW technique. The graphs for each sample were omitted from the text to avoid repetitious figures.

Figure A3.1 shows the results of the check run on the silver films. Table A.3 lists the numerical values as computed from these graphs. Figure A3.2 shows the pair of curves for run EB-68. These curves highlight the difference which can occur between films produced in the same run under identical conditions.

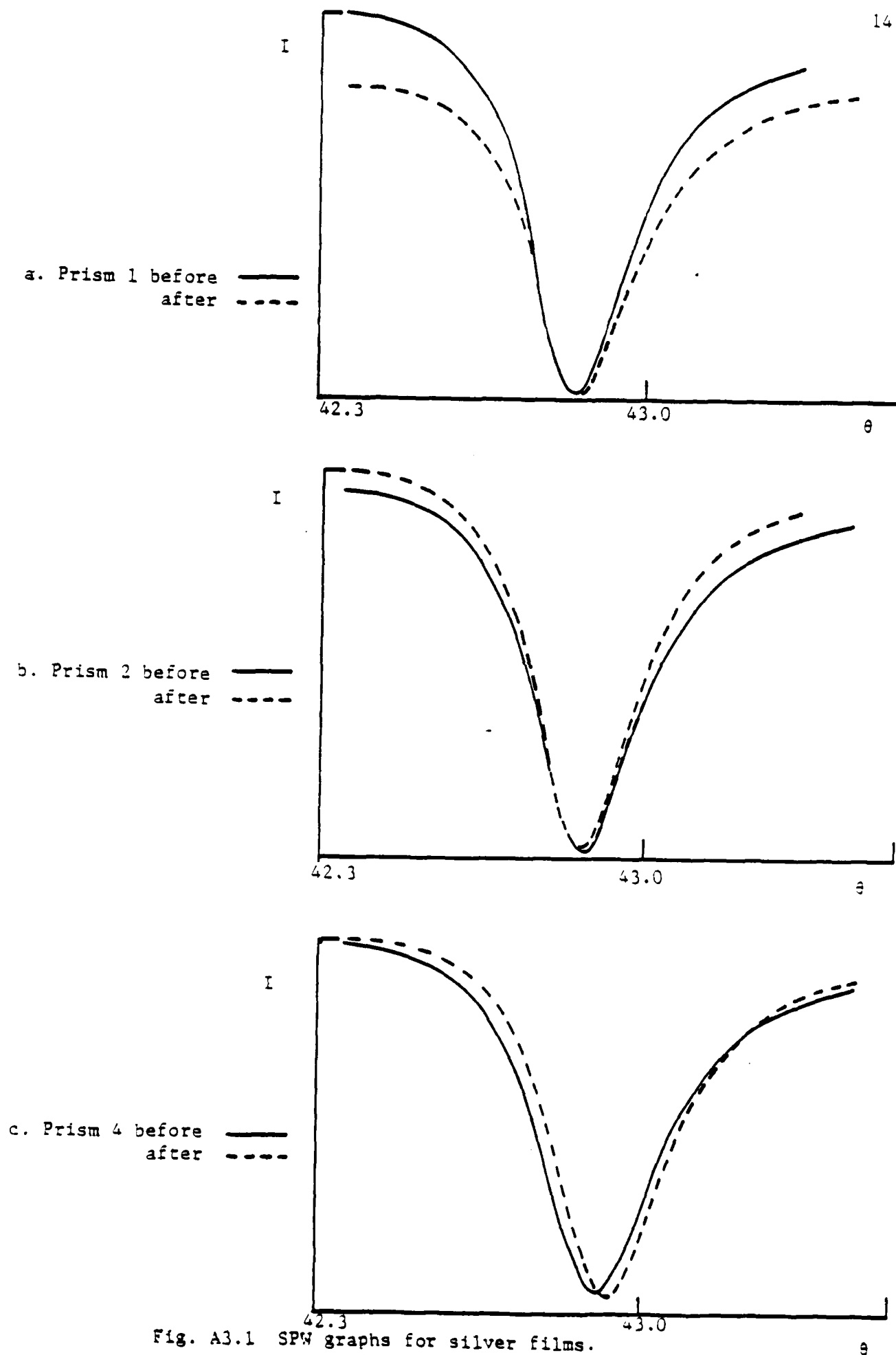


Table A.3. Check runs on silvered prisms used in the SPW experiments.

Sample prism		n	k	d (nm)	Conditions
4	before	.114	4.116	52.0	left in atmosphere in closed jar
	after	.106	4.066	54.0	
2	before	.103	4.132	52.0	shuttered in vacuum chamber
	after	.095	4.146	53.0	
1	before	.072	4.132	49.0	electron bombarded
	after	.109	4.158	51.0	

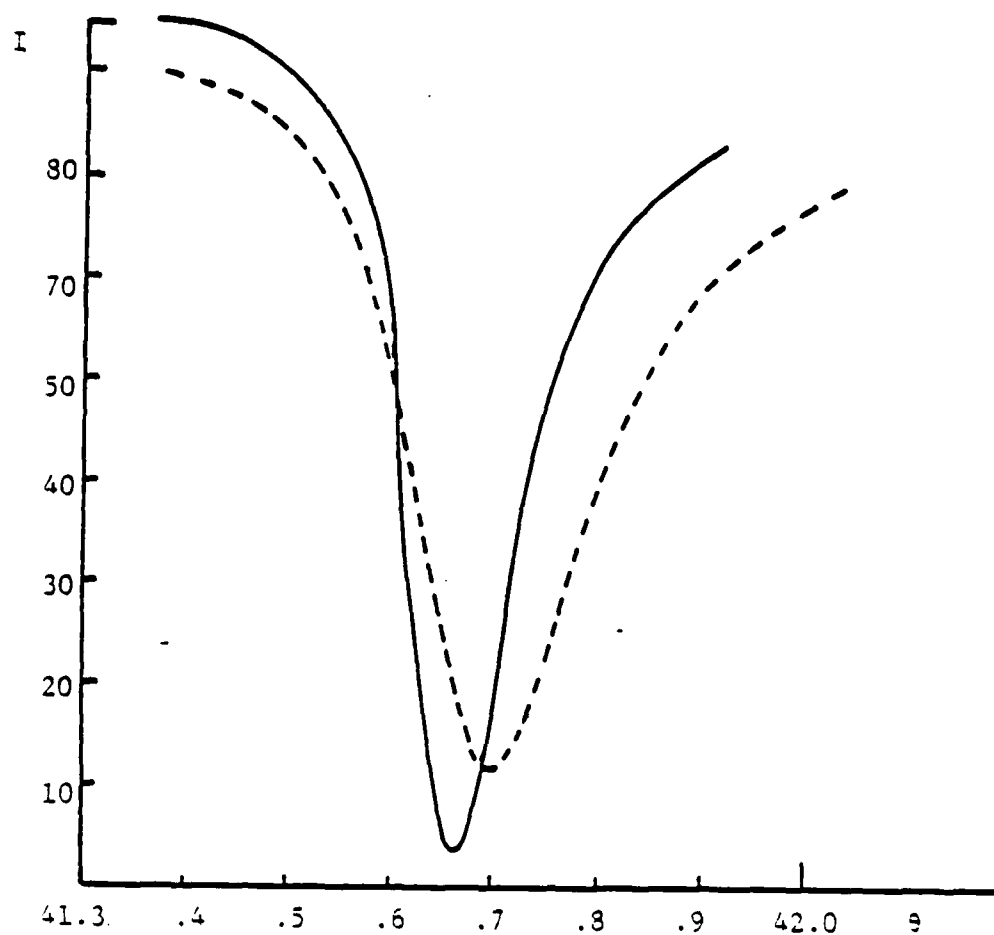


Fig. A3.2 SPW graphs for zinc sulfide (EB-68).

Prism 3 ———
Prism 2 - - - -

APPENDIX 4

DURABILITY TESTS RESULTS

The following two tables contain the results of
all the durability tests performed on the samples.

Table A.4. Hardness and adhesion tests.

Sample	Material	Bombarded ?	Scotch Tape	Eraser
EB-10	1	Y	ND	VH
EB-11	1	N	ND	VH
EB-12	2	N	ND	M
EB-12X	2	AD	ND	S
EB-13	2	Y	ND	S
EB-23	1	N	ND	VH
EB 23X	1	AD	ND	VH
EB 24	3	Y	ND	ND
EB 25	3	N	ND	ND
EB 25X	3	AD	ND	ND
EB-27	3	Y	ND	ND
EB-29	3	Y	ND	ND
EB-30	3	N	ND	ND
EB-30X	3	AD	ND	ND
EB-32	2	N	ND	H
EB-32X	2	AD	ND	H
EB-33	2	Y	M	H
EB-38	4	N	VS	M
EB-38X	4	AD	VH	M
EB-39	4	Y	ND	VS
EB-41	4	Y	ND	S
EB-45	5	Y	VS	M
EB-47	5	N	ND	M
EB-47X	5	AD	ND	H
EB-50	4	N	ND	H
EB-51	4	N	ND	H
EB-51X	4	AD	ND	M
EB-52	4	Y	ND	M

1	Antimony trioxide	Y - Yes	ND - No damage
2	Potassium hexafluorozirconate	N - No	VS - Very slight damage
3	Silicon monoxide	AD - After deposition	S - Slight damage
4	Zi=c sulfide		M - Moderage damage
5	Magnesium fluoride		H - Heavy damage
			VH - Very heavy damage

APPENDIX 5

CONTROLLED HUMIDITY TEST RESULTS.

Table A.5. Controlled humidity test results.

Sample	40%	50%	60%	70%	80%	90%
EB-10	NC	NC	NC	NC	NC	NC
EB-11	NC	NC	NC	NC	NC	NC
EB-12	NC	NC	NC	NC	spots	cloudy
EB-12X	NC	NC	NC	NC	spots	cloudy
EB-13	NC	NC	NC	NC	spots	cloudy
EB-23	NC	NC	NC	NC	NC	NC
EB-23X	NC	NC	NC	NC	NC	NC
EB-24	NC	NC	NC	NC	NC	NC
EB-25	NC	NC	NC	NC	NC	NC
EB-25X	NC	NC	NC	NC	NC	NC
EB-27	NC	NC	NC	NC	NC	NC
EB-29	NC	NC	NC	NC	NC	NC
EB-30	NC	NC	NC	NC	NC	NC
EB-30X	NC	NC	NC	NC	NC	NC
EB-32	NC	NC	NC	NC	spots	cloudy
EB-32X	NC	NC	NC	NC	spots	cloudy
EB-33	NC	NC	NC	NC	NC	cloudy
EB-38	NC	NC	NC	NC	NC	NC
EB-38X	NC	NC	NC	NC	NC	NC
EB-39	NC	NC	NC	NC	NC	NC
EB-41	NC	NC	NC	NC	NC	NC
EB-45	NC	NC	NC	NC	NC	NC
EB-47	NC	NC	NC	NC	NC	NC
EB-47X	NC	NC	NC	NC	NC	small patch
EB-50	NC	NC	NC	NC	tiny spot	large patches
EB-51	NC	NC	NC	tiny spot	spot	large patches
EB-51X	NC	NC	NC	NC	NC	large patches
EB-52	NC	NC	NC	NC	NC	large patches
EB-73	NC	NC	NC	spots	large spots	large patches
EB-74	NC	NC	NC	NC	spots	large patches
EB-75	NC	NC	NC	NC	NC	NC

NC - No changes

ABSTRACT

The performance of multilayer thin film optical filters depends largely on the microstructure of the component layers. This microstructure varies with the deposition parameters inside the coating chamber. By controlling these parameters, optical filters can be produced to exacting specifications.

In 1947, R. M. Rice established the technique of bombarding the substrate with electrons of several kilovolts as the films were being deposited. This process improved the durability of zinc sulfide films dramatically. This study was performed to quantitatively analyze the effects of bombardment on film microstructure and subsequent effects on optical and mechanical properties.

I installed an electron source filament inside the coating chamber and electrically isolated the substrate holder, which was connected to a positive high voltage supply. An accelerating loop placed just above the filament enhanced its efficiency. The source was calibrated by measuring the current through the substrate holder.

Single layer films of five different materials were deposited, each at its own set of electron bombardment parameters. The microstructure was analyzed with an X-ray diffractometer and a transmission electron microscope. Optical properties were measured with guided waves,

induced absorption, and spectrophotometric analysis. Film durability was analyzed with Scotch tape, eraser, and controlled humidity tests.

Antimony trioxide films showed a shift in lattice orientation, but this did not affect columnar structure or macroscopic quantities. Potassium hexafluorozirconate films showed elimination of both crystal structure and columnar growth, resulting in slightly reduced durability and some absorption. Silicon monoxide films suffered no change in structure or properties. Zinc sulfide films demonstrated the change in crystal structure, which was quantified and shown to improve moisture resistance. Optical properties were unaffected. Magnesium fluoride films showed a slight increase in crystallinity with only subtle changes in durability and optical properties.

Generally, electron bombardment reduced or rearranged crystal structure. The effects on macroscopic properties varied with each material, with no clear trend evident.

REFERENCES

- Abeles, F., "Optical Properties of Very Thin Films," *Thin Solid Films* 34, 291 (1978).
- Al-Jumaily, G., S. D. Browning, and A. F. Turner, "Polarization-Insensitive Refracting System for Integrated Optics," Optical Society of America Tucson meeting, October, 1982, paper FM8.
- Allen, T. H., "Properties of Ion-Assisted Deposited Silica and Titania Films," *Proc. SPIE* 325, 93 (1982).
- Bangert, H. and H. Pfefferkorn, "Condensation and Stability of ZnS Thin Films on Glass Substrates," *Appl. Opt.* 19, 3878 (1980).
- Bartle, L. and A. F. Turner, "UV Absorption in Evaporated Films of Double Fluorides," *JOSA* 52, 1310 (1962).
- Beaman, D. R. and J. A. Isazi, Electron Beam Microanalysis, Special Technical Publication 506, American Society for Testing and Materials, Philadelphia, 1972, 8-10.
- Berning, P. H., "Theory and Calculation of Optical Thin Films" in Physics of Thin Films, Volume 1, George Hass, ed., Academic Press, New York, 1963.
- Burke, J. J., "Optical Waveguides and Integrated Optics," Graduate level course in Optical Sciences, University of Arizona, Tucson, 1980.
- Bradford, A. P. et al., "Effect of Ultraviolet Irradiation on the Optical Properties of Silicon Oxide Films," *Appl. Opt.* 4, 971 (1965).
- Chambers, A. and M. Prutton, "Improved Epitaxy of Nickel on Rocksalt Substrates Due to Electron Bombardment," *Thin Solid Films* 1, 235 (1967).
- Channin, D. J., J. M. Hammer, and M. T. Duffy, "Scattering in ZnO-Sapphire Optical Waveguides," *Appl. Opt.* 14, 923, (1975).
- Chopra, K. L., Thin Film Phenomena, McGraw-Hill Book Company, New York, 1968, Chapter 4.
- Coleman, H. S., A. F. Turner, and O. A. Ullrich, "Crystal Orientation and Refractive Index of Thick Evaporated MgF_2 Films," Optical Society of America New York meeting, 21 February 1947, paper 23.

- Cullity, B. D., Elements of X-Ray Diffraction, Addison-Wesley Publishing Company, Reading, Mass., 1978.
- Eastman, A. V., Fundamentals of Vacuum Tubes, McGraw-Hill Book Company, New York, 1949, Chapter 1.
- Fang, J. H. and F. D. Bloss, X-Ray Diffraction Tables, Southern Illinois University Press, 1966.
- Fukami, K. and K. Adachi, "A New Method of Preparation of a Self-Perforated Micro Plastic Grid and its Application (I)," J. Elec. Micr. 14, 112 (1965).
- Gordy, W. and W. J. O. Thomas, "Electronegativities of the Elements," J. Chem. Phys. 24, 440 (1956).
- Guenther, K. H. and H. K. Pulker, "Electron Microscopic Investigations of Cross-Sections of Optical Thin Films," Appl. Opt. 15, 2992 (1976).
- Heavens, O. S., Optical Properties of Thin Solid Films, Dover Publications, New York, 1965, 37.
- Holland, L., Vacuum Deposition of Thin Films, Chapman and Hall, London, 1963.
- Kapany, N. S. and J. J. Burke, Optical Waveguides, Academic Press, New York, 1972.
- King, R. J. and S. P. Talim, "A Comparison of Thin Film Measurements by Guided Waves, Ellipsometry, and Reflectometry," Optica Acta 28, 1107 (1981).
- Macleod, H. A., Thin Film Optical Filters, Adam Hilger Ltd., London, 1969, 252.
- Martin, P. J. et al., "Ion-Beam-Assisted Deposition of Thin Films," Appl. Opt. 22, 178 (1983).
- Martin, T. P. and A. F. Turner, "Effect of Crystallite Size on the Infrared Dispersion of LiF Films," J. Appl. Phys. 37, 1749, (1966).
- Movchan, B. A. and A. V. Demsheshin, "Investigation of the Structure and Properties of Thick Vacuum Deposited Films of Nickel, Titanium, Tungsten, Alumina, and Zirconium Dioxide," Fizika Metall 28, 83 (1969).
- Ogura, S., "Some Features on the Behavior of Optical Thin Films," Ph.D. Thesis, Newcastle-Upon-Thyne Polytechnic, U.K., 1975.
- Otto, A. and W. Sohler, "Modification of the Total Reflection Modes in a Dielectric Film by One Metal Boundary," Opt. Comm. 3, 254, (1971).
- Pearson, J. M., "Electron Microscopy of Multilayer Thin Films," Thin Solid Films 6, 349, (1970).

- Pulker, H. K. and E. Jung, "Correlation Between Film Structure and Sorption Behavior in Vapor Deposited ZnS, Cryolight, and MgF_2 Films," Thin Solid Films 9, 57 (1971).
- Raether, H., "Surface Plasma Oscillations," in Physics of Thin Films, Volume 9, George Hass, ed., Academic Press, New York, 1977.
- Raine, K. W., "Anomalous Optical Absorption in Dielectric Thin Films Deposited by Electron Bombardment," Thin Solid Films 38, 323 (1976).
- Reinbolt, B. J., "Computer Programs for the Optical Analysis and Design of Thin Film Planar Waveguides," M.S. Thesis, University of Arizona, Tucson, Arizona 1975.
- Remy, H., Treatise on Inorganic Chemistry, Volume 1, Elsevier Publishing Company, Amsterdam, 1956, 665.
- Rice, R. M., "Method of Deposition of Films of Material," U.S. Patent 2420724, 1947.
- Sabirov, R. S., "Study of the Charged-Particle Stream During Electron Beam Evaporation," Sov. J. Opt. Tech. 49, 171 (1982).
- Smith, J., ed, Index to Powder Diffraction File, ITS Special Publication 48, American Society for Testing and Materials, Philadelphia, 1945.
- Sloan Technology Corporation, Thin Film Equipment Catalog, Santa Barbara, CA 1973-74.
- Stirling, D. J., "Electron-Bombardment-Induced Changes in the Growth and Epitaxy of Evaporated Gold Films," Appl. Phys. Lett. 8, 326, (1966).
- Tang, Jin-Fa and Q. Aheng, "Automatic Design of Optical Thin Film Systems-Merit Function and Numerical Optimization Method," JOSA 72, 1522, (1982).
- Thornton, J. A. , "Influence of Apparatus Geometry and Deposition Conditions on the Structure and Topography of Thick Sputtered Coatings," J. Vac. Sci. Tech. 11, 666 (1974).
- Thun, R. and G. Hass, "Electron Diffraction Studies of Structure Changes in Vacuum Deposited Films" in 1958 Fifth National Symposium on Vacuum Technology Transactions, Pergamon Press, London, 1958.
- Turner, A. F., "A Brief Compendium of Elementary Computational Methods in Applied Thin Film Optics," Symposia notes, American Vacuum Society Chicago meeting, September, 1976.

Turner, A. F. and P. H. Berning, "Induced Absorption in Thin Films,"
Optical Society of America New York meeting, April, 1955,
paper 45.

Turner, A. F. and S. D. Browning, "Refracting Boundaries in Thin Film
Glass Lightguides," Proc. SPIE 204, 53 (1980).

APPENDIX H
LASER DAMAGE MEASUREMENTS ON
ALL-DIELECTRIC NARROW-BAND FILTERS

MS Thesis by Lew DeSandre

CHAPTER 3

EXPERIMENTAL APPARATUS

Laser Damage Facility

The setup used to perform the laser damage testing consisted of a continuous wave (CW) argon laser, a microscope for focusing the laser beam and viewing the test sample, and a monochromator system. A silicon photodiode detector and lock-in amplifier were also employed to measure relative beam intensities during beam scans. The detector-amplifier system also monitored scatter from the test sample under irradiation. A schematic and photographs of the test facility are shown in Figs. 32 and 33.

To view moisture adsorption patches and other defects in the test samples prior to and just after laser irradiation, the sample was observed microscopically in monochromatic light. The monochromator system was assembled at the Optical Sciences Center for an earlier project and was modified in this laser damage experiment. It consisted of a Bausch-and-Lomb tungsten-halogen light source, a high-intensity monochromator-collimator, and an x-y-z translation stage. When viewed through the microscope, an approximately 1.3-mm-diameter area on the test sample was seen at a focal length of 0.535 cm.

The laser used to perform the damage testing was a Coherent-Innova Model 90-4 argon laser. The laser was vertically polarized and the output power in the TEM₀₀ mode at 514.5 nm was rated at 1.7 W,

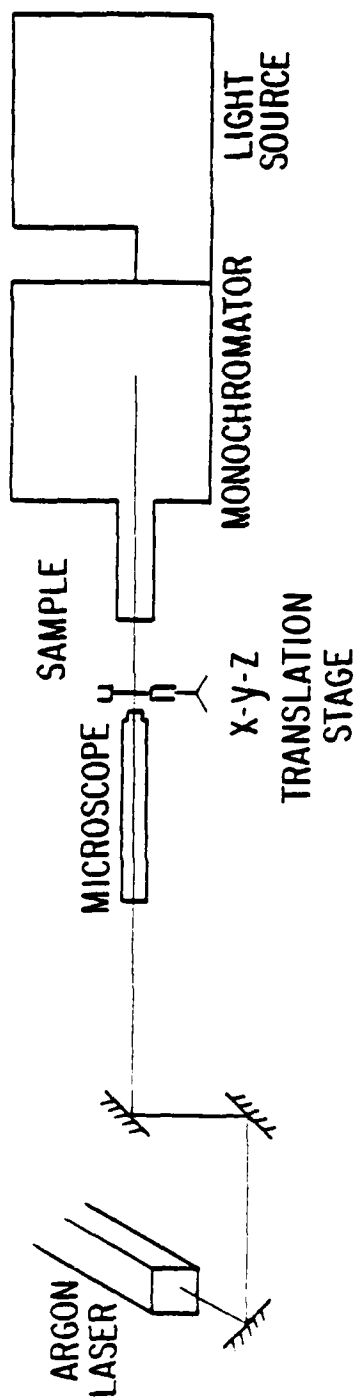


Fig. 32. Laser damage test facility.

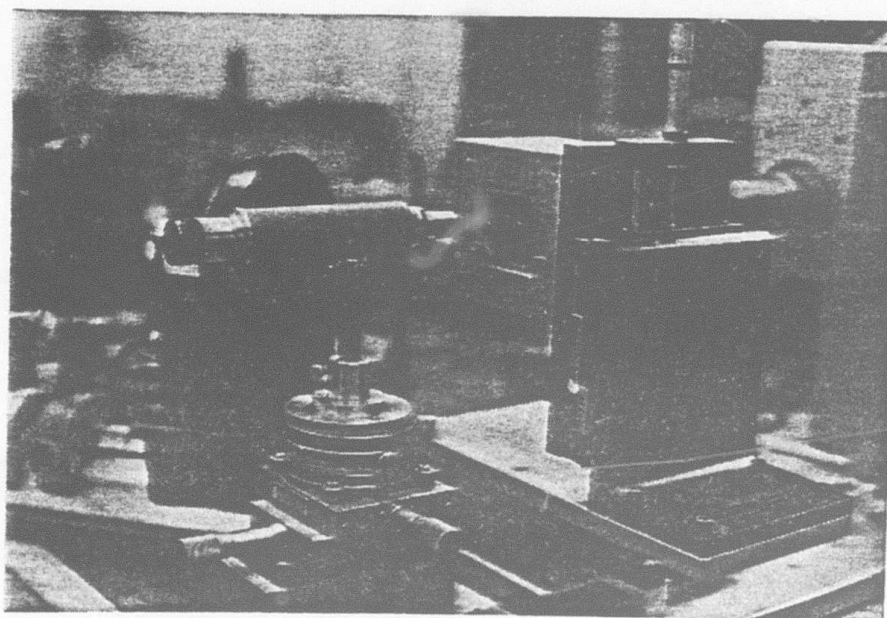
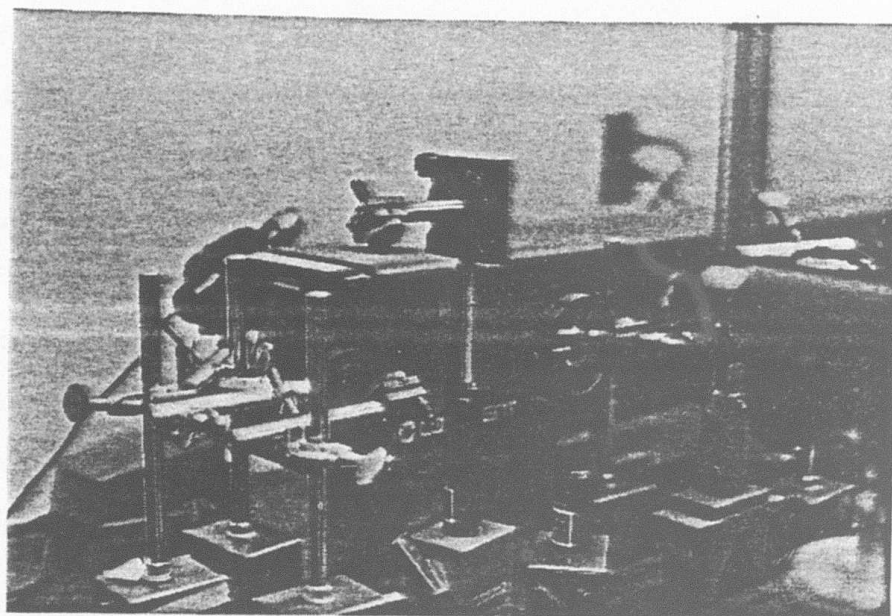


Fig. 33. Laser damage test facility.

although output power as high as 2.5 W was achieved. Long term power stability under optical feedback regulation was rated at $\pm 0.5\%$, however a 2% fluctuation was experienced under 2.0 W and even larger instability at output powers greater than 2.0 W. This was probably due to occasional fluctuation in the cooling water pressure.

The output power was measured internally, within the head assembly. A beamsplitter following the output coupler mirror directed the output beam through a diffuser onto a photocell. The photocell provided the output power signal used to measure and to regulate the output power.

Beam Scans

The laser used to perform the damage testing was an excellent single mode source. Scans at the beam's focal plane were made prior to damage testing.

The setup for the beam scans is shown in Fig. 34. The output beam was attenuated to prevent detector overload, chopped, and directed along the axis of the microscope. Beam scans were made in directions in the focal plane of the microscope using a 25- μm pinhole at 2.0-W output power. The light emerging from the pinhole was collected by a converging lens, focused onto a photodiode detector, and then measured by an EG&G 5205 lock-in amplifier.

The spatial profiles of the focused beam are shown in Figs. 35 and 36. The beam profile at 2.0-W output power was Gaussian with a $1/e^2$ waist diameter of 115 μm . The error bars represent the deviation of two shots at each output power. The measured beam profile represents a

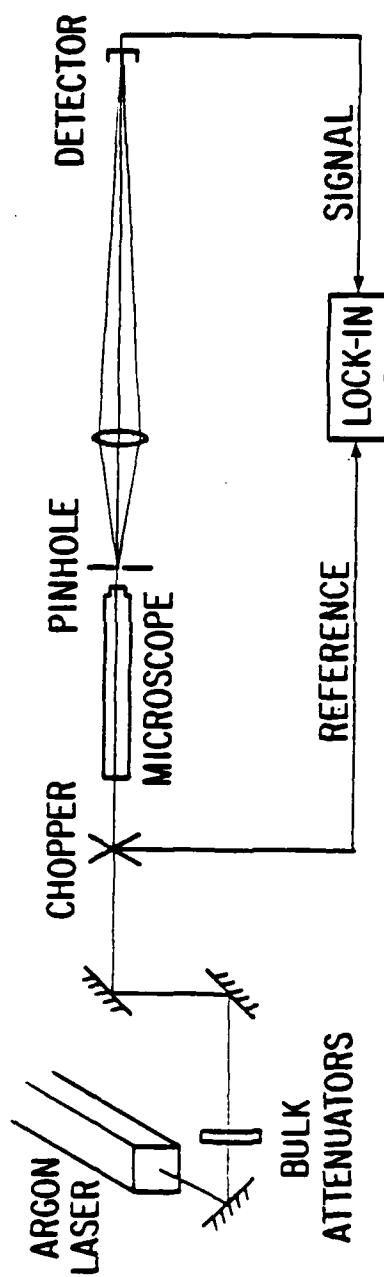


Fig. 34. Setup used to perform beam scan.

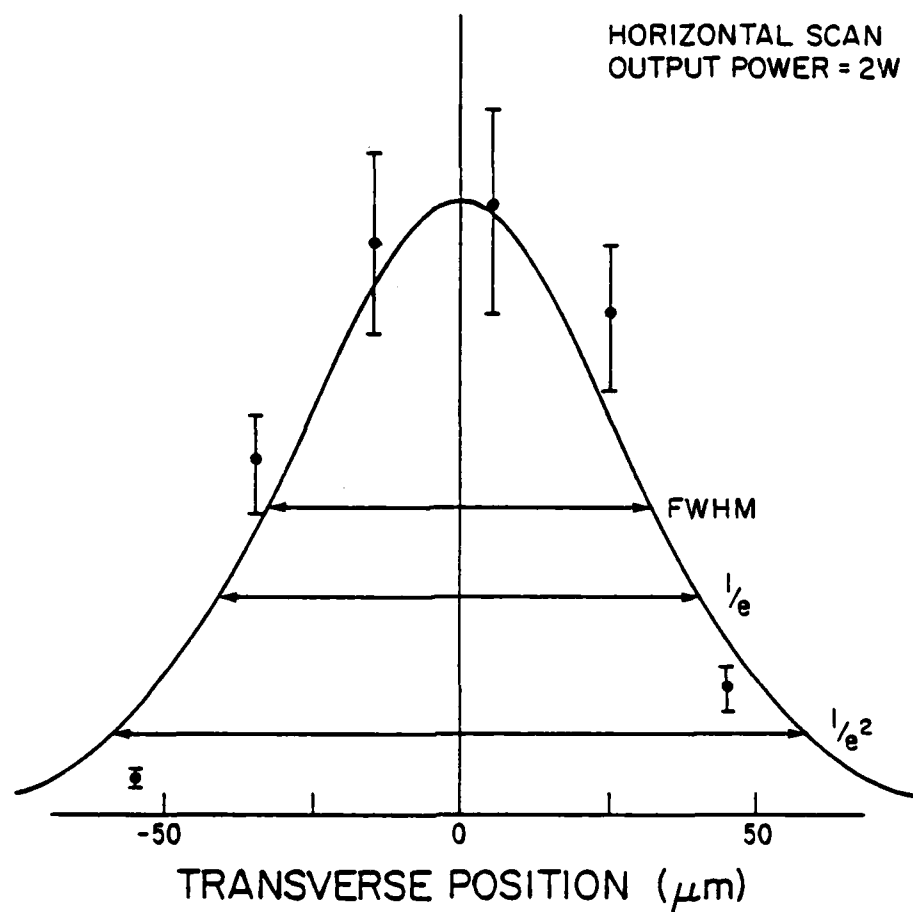


Fig. 35. Special profile of focused laser beam Gaussian fit at $1/e^2$ width of $115 \mu\text{m}$.

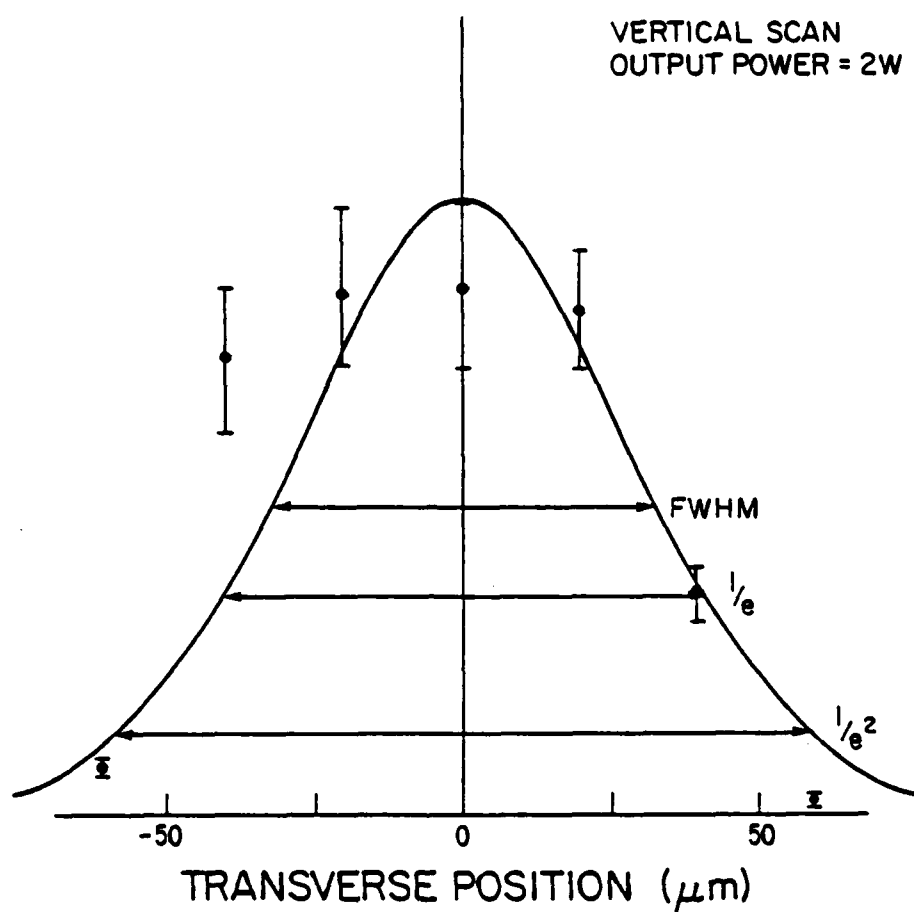


Fig. 36. Spacial profile of the focused laser beam. Solid line represents a Gaussian at $1/e^2$ width of 120 μm .

convolution of the pinhole with the focused laser beam. The result of this convolution is to enlarge the measured beam diameter by about 1%, which is negligible compared to other sources of error in the experiment.

It was found that at different power levels the beam shape changed slightly. This fluctuation was responsible for most of the uncertainty in the beam radius and hence the fluence levels as well. Alignment of the laser beam through the microscope was extremely difficult. Any misalignment resulted in an odd-shaped beam profile. Although care was taken to preserve the alignment during damage testing, a change in output power caused the laser beam to propagate in a slightly different direction. This necessitated a realignment of the optics and microscope, and undoubtedly resulted in a beam shape different from the beam scans.

To determine total power in the laser after transversing the microscope, the relative beam intensity was measured by the detector and compared to the signal detected when the microscope was removed. Figure 37 plots the lock-in reading with and without the microscope in the laser beam path for various output powers. As can be seen, a loss of light intensity of the beam in traversing the microscope resulted. This loss was linear with output power up to about 2.0 W. At this power level, losses in the microscope increased drastically because of high scatter or misalignment. Figure 38 correlates the fluence of the focused beam at the focal point to the total output power of the laser. The power density on-axis of the spatial profile of the focused beam is

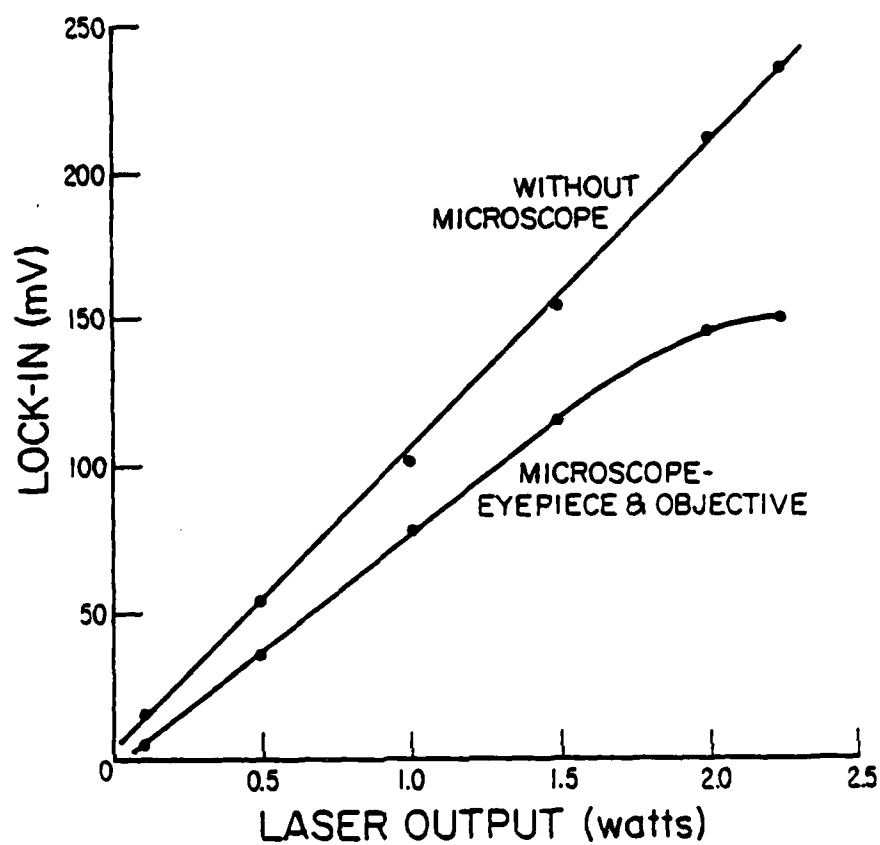


Fig. 37. Intensity loss of laser beam traversing the microscope.

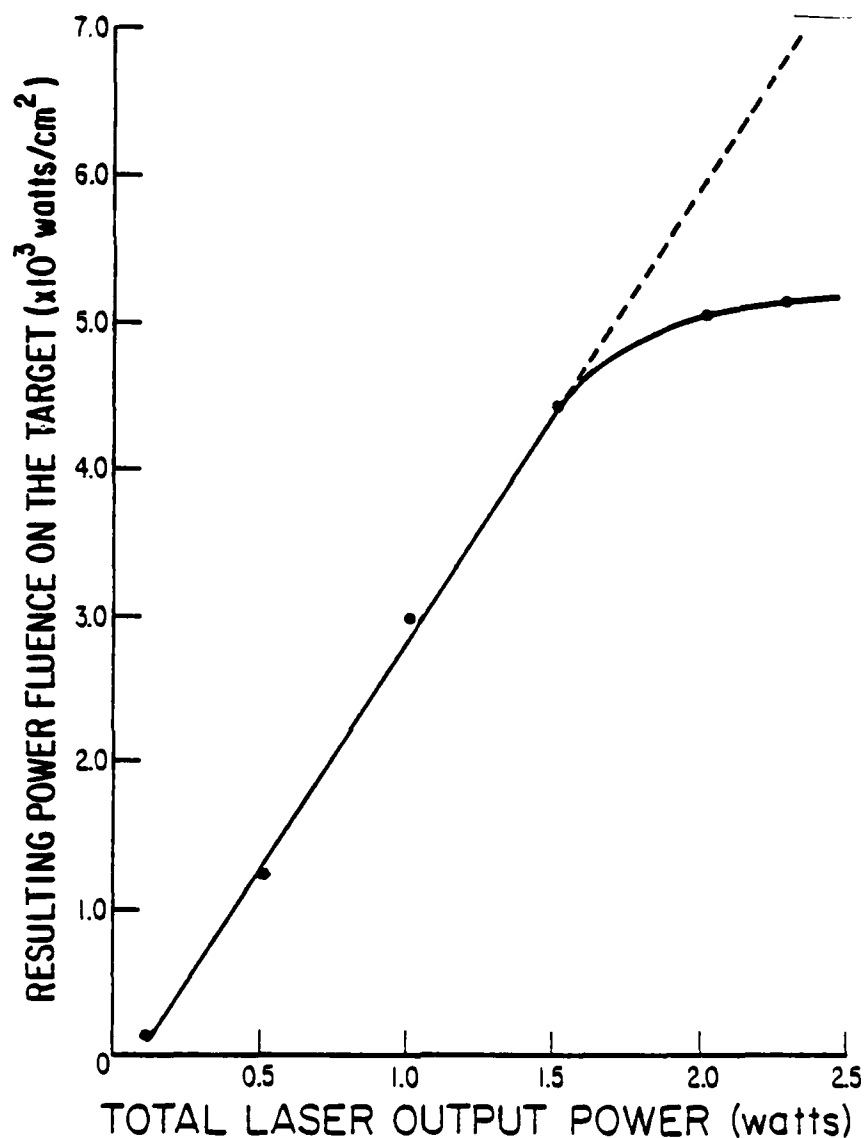


Fig. 38. Calibration plot of power fluence on the target as determined by laser output power.

referred to as the beam fluence. The fluence values in Fig. 38 were found by determining the power loss of the beam traversing the microscope (from Fig. 38) plus a 5% scatter loss at each relay mirror directing the beam from the laser into the microscope. The energy values were then divided by the calculated beam area at the $1/e$ radius of 80 μm . Inspection of Fig. 38 shows that fluence on the target increased linearly with total output power up to about 1.5 W. The deviation of the curve in Fig. 38 from a linear calibration is a good estimate of the uncertainty in the laser beam fluence for various output powers.

Beam scans and intensity measurements were not taken during laser damage testing. Since the CW output of the laser was relatively constant, the fluence at the target during testing was determined by comparing laser output power to the calibrated fluence determined by Fig. 38.

On-axis beam scans through the focused beam waist were made to determine the focal distance of the laser beam from the microscope objective. The pinhole was positioned near focus and the microscope translated slightly to defocus the beam. Orthogonal scans were then made at a number of out-of-focus positions. Inspection of these results, plotted in Fig. 39, show that the beam intensity is relatively constant within $\pm 5 \mu\text{m}$ of the waist position. The beam waist was located 0.535 cm from the microscope objective and about 0.4 mm behind the position where the eye sees focus. This was important, since it was convenient to first focus the microscope onto the test sample by direct

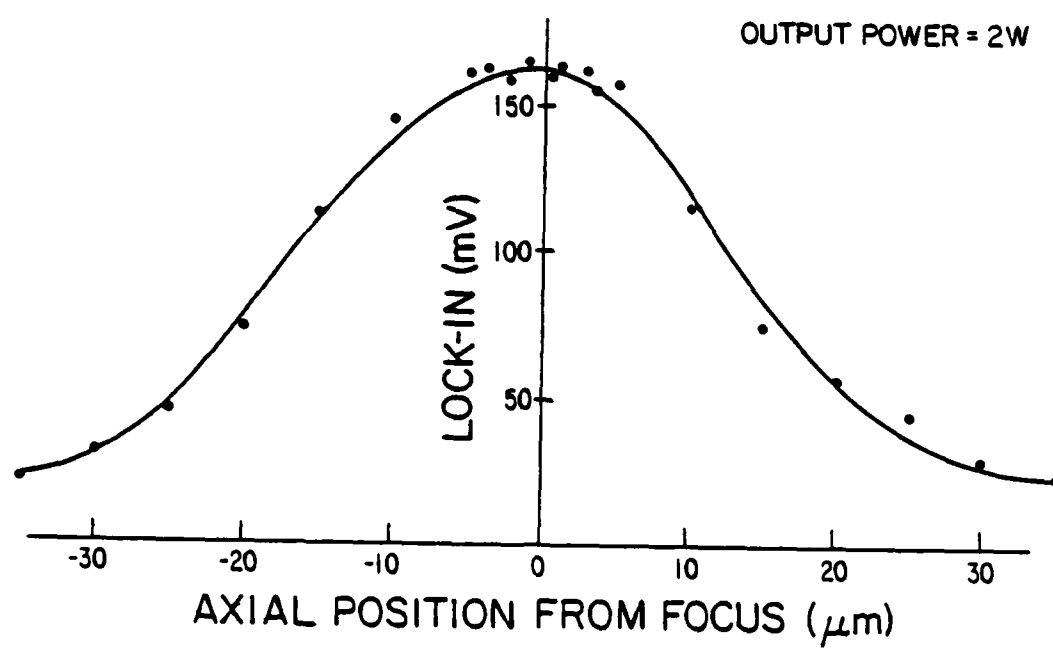


Fig. 39. On-axis scans through focus.

viewing and then to adjust the sample to the focal position of the laser beam.

In summary, because of the limited time available to do the actual damage testing, beam scans could not be performed every time the laser output power was changed. Characterization of the focused laser beam was made prior to laser damage testing by pinhole beam scans. The beam profile at 2.0-W output power was found to be Gaussian with a $1/e^2$ waist diameter of 115 μm . Although the output power of the laser remained fairly steady over long periods of time, deviation of the beam path as the output power was changed together with the difficulty in aligning the beam along the axis of the microscope prevented determination of a unique beam profile.

CHAPTER 4

LASER DAMAGE TESTING

Procedure

The setup used to perform the damage testing was described in Chapter 3 and is illustrated in Fig. 32.

The test procedure used began with viewing the test sample through the microscope and adjusting the monochromator to give the best contrast in transmission between moisture patches or other defects and the defect-free portions of the filter. The site to be damaged was then centered in the microscope and moved to the beam waist formed by the microscope. The visible scatter of the laser beam from the test sample increased when the beam was focused on the sample; fine adjustment of focus was made by maximizing the scatter. In the latter part of the experiment a scatterometer was added; it consisted of a chopper and a silicon-diode detector, enclosed in a box with one small opening for the detector. The detector and reference signals were sent into the lock-in amplifier.

Because of the small size of the adsorption sites and pit defects, centering the focused laser beam was difficult. However, scattered laser light increased noticeably when the beam was centered on these defects. The procedure employed was to scan the sample at low power (≈ 0.1 W) looking for a significant increase in scattered light. After viewing this site through the microscope, the laser output power

would be increased and damage testing initiated. Subsequent laser damage at high power on large scatter points confirmed this positioning technique. This technique of scanning the surface at low power may have inadvertently resulted in a cleaning effect. Multiple-shot pulsed irradiation of optical components at laser intensities below threshold has been shown to increase the damage threshold of the material (Porteus, Faith, and Allen 1983). However, it is not felt that low power CW radiation resulted in a cleaning or annealing effect.

Damage thresholds were determined largely by trial and observation. The laser output power was initially set at low values of about 0.1 to 0.5 W, and the sample irradiated for various durations, beginning usually at 30 sec and increasing to 2 to 5 min. Following exposure to the laser beam, the irradiation site was viewed through the microscope to determine if damage occurred. If damage at that particular site did not occur, the sample was translated to a new site, and exposed to a higher power for increasing intervals.

Because positioning the laser beam at pit defects or adsorption sites was tedious, it was convenient to leave the sample at one position and increase the output power until damage occurred. Some conditioning or annealing of the site may have occurred and the damage threshold, therefore, may have been influenced by previous laser exposures.

If difficulty was experienced in damaging the sample, the damage sequence was then initiated at high power (2.0 W). If damage occurred, the exposure time or output power was reduced. Exposure times and fluence levels were varied to relate defect damage to both the fluence

and duration of the laser exposure. For some exposures, a site, once damaged, was irradiated further to record the growth of the damage site.

While attempting to damage certain defect sites, it was observed that the amount of scattered laser light off the sample varied not only with fluence level but also with the type of defect. From this observation it was thought that the relative amount of scattered light may be related to the damage threshold. Later on in the experiment the scattered light level was measured by the scatterometer.

Data and observations for each test run are shown in Tables 2 and 3 for the ZnS/cryolite and $\text{ZrO}_2/\text{SiO}_2$ samples respectively. A test run represents consecutive exposures at one site. For each test run, the type of site irradiated (clear, moisture patch, penetration site, or pit) is given along with the fluence level, duration of exposure, and scatter level. If laser damage is noted, it represents damage that was observable through the microscope.

Both samples were aligned normally to the laser beam. Since the characteristic wavelengths for the ZnS/cryolite and $\text{ZrO}_2/\text{SiO}_2$ samples were 496 nm and 538 nm respectively, both were detuned to the incident radiation of 514 nm. We have seen that for a detuned filter, the electric field intensities move outward from the spacer layer into the reflector stack with the result that the filter behaves more like a reflector. The effect of detuning on laser damage is not known.

Observations

Sample D-21-4

The effects of laser irradiation on sample D-21-4 were investigated in 43 test runs. Because damage did not generally occur at

low power levels at defect-free or moisture patch areas, the initial power level was set at 2.0 W. Since most of the test runs were conducted before the scatterometer was installed, only a qualitative value of scatter is noted. In contrast to sample 760-21-5, there appeared to be no correlation between the amount of scatter observed prior to damage and laser damage threshold. For example, in Run 15 very high scatter was observed, whereas in Run 14, a relatively low amount was noted. However, the filter was damaged in Run 14 and not in Run 15. Nonetheless, when damage did occur, a large amount of scatter was evident.

Runs 14, 18, 23, 30, and 33 investigated the growth of the damage spot due to consecutive exposures. Generally, the spot failed to grow at a particular fluence level while increasing the duration of exposure. The damage spot did enlarge, however, when the power level was increased. Figure 40 plots the growth in diameter of damage site No. 18, created on an adsorption site defect as the output power and exposure duration are increased.

A further observation is that when damage occurred, it appeared almost immediately after exposure to the laser beam. An immediate increase in scatter that overloaded the detector was noted. Damage was verified by observation through the microscope. Most damage sites were on the order of 20 μm in diameter. However, for Runs 25 and 30 (Fig. 41), damage craters of 150 μm and 50 μm , respectively, resulted.

In only one test run was a shift in the peak wavelength observed because of irradiation at a fluence less than that needed to cause

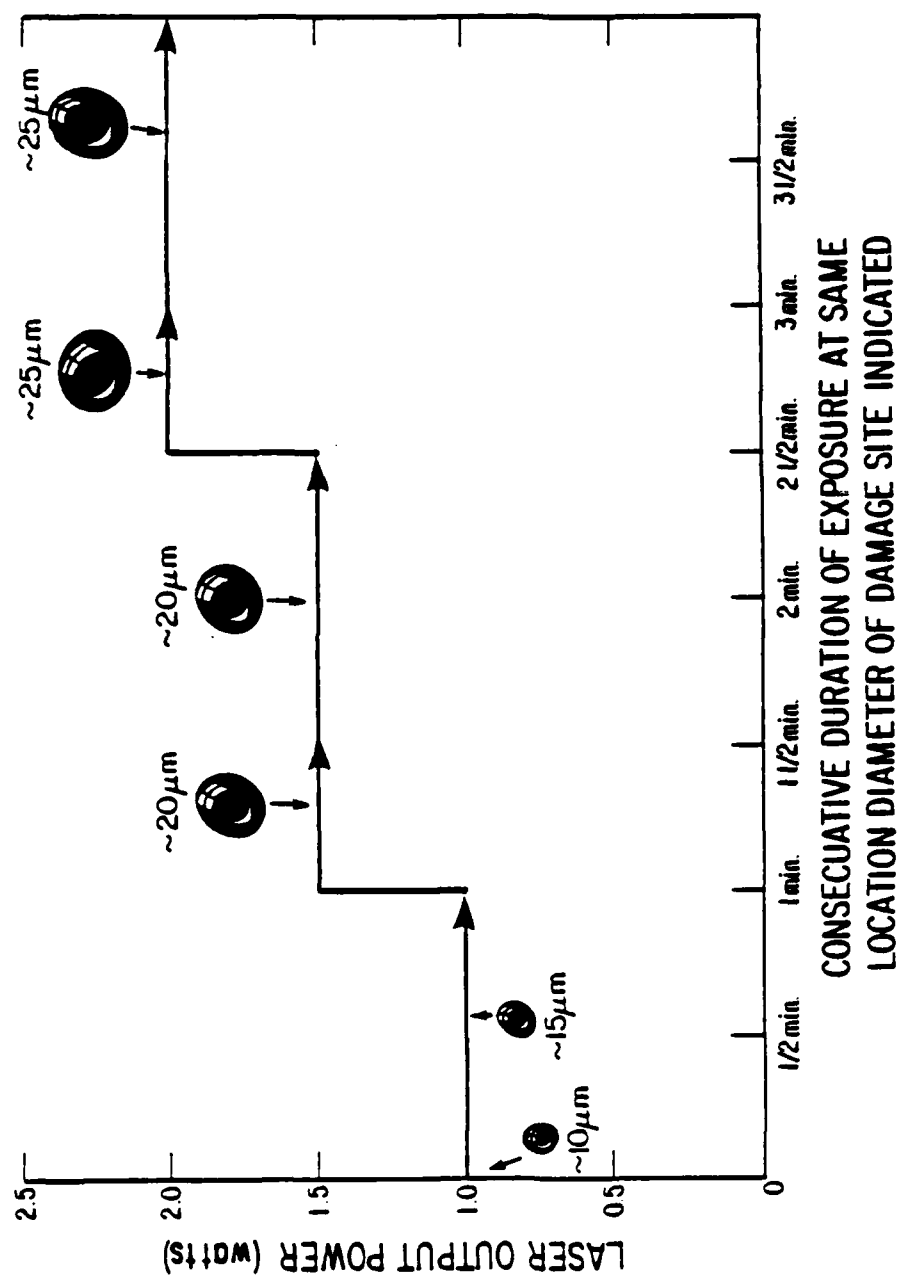


Fig. 40. Enlargement of damage site with continual irradiation for consecutive duration of exposure at same location diameter of damage site indicated
usample D-21-4, Run. No. 18.

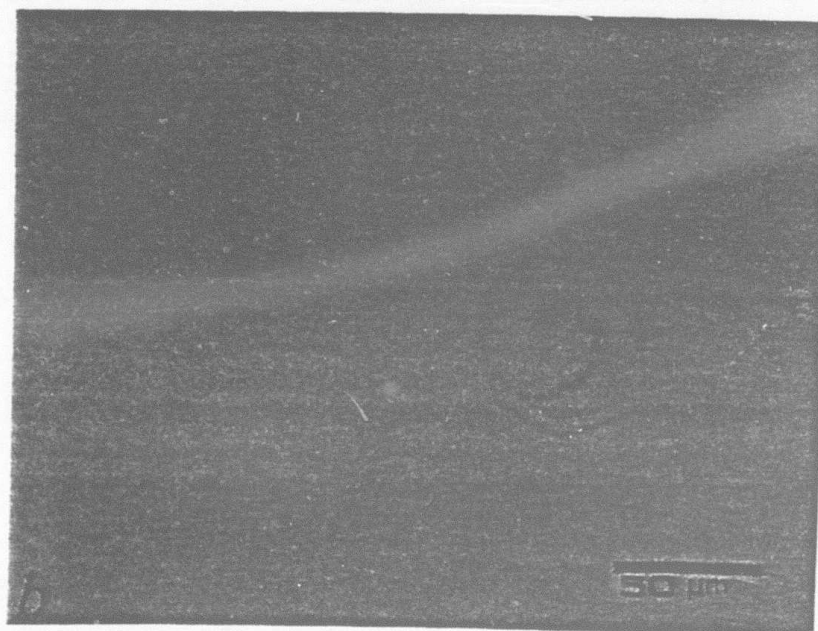
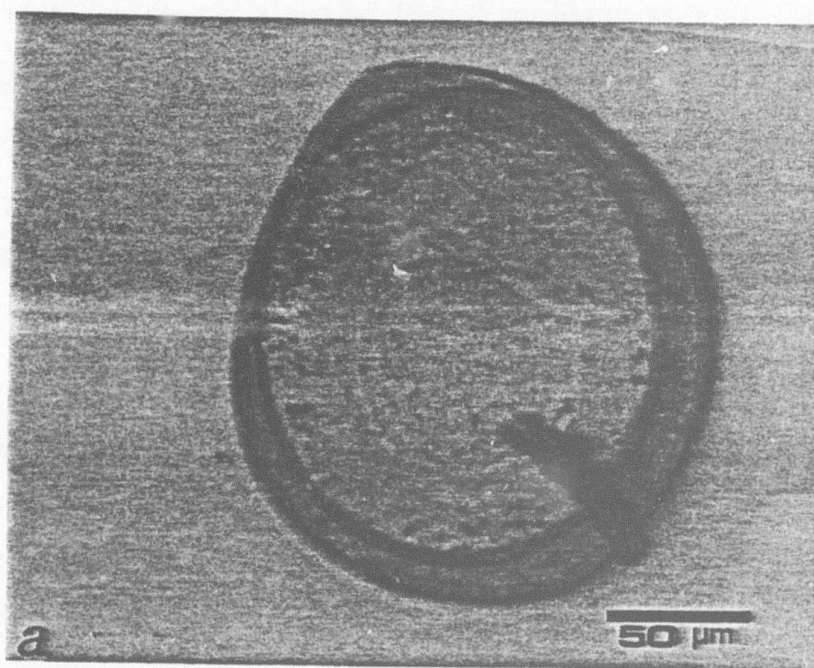


Fig. 41. Laser damage for a) Run. No. 25, and b) Run No. 30.

damage. This occurred in Run 31 where a pit defect that the laser failed to damage showed the characteristic shift in transmission wavelength indicative of a moisture adsorption patch. In all other cases the shift in peak wavelength caused by moisture adsorption was uninfluenced by exposure to the laser beam. Moisture did penetrate into the film in some cases after damage had occurred.

In Runs 4, 9, 18, and 23, the sample was translated during exposure to a damaging fluence level. It was found that in this situation the damage threshold was far below the threshold at which damage was initiated. Results of Run 23 are illustrated in Fig. 42. Although the absorption site initially was damaged at 2.0 W output power, a power level as low as 1.25 W could sustain damage as the sample was slowly translated across the laser beam.

Shown in Fig. 43 are photographs taken in monochromatic light of damage resulting in Runs 18 and 23. Nomarski micrographs of the same areas are shown in Fig. 44. Notice the circular areas in the Nomarski photos, which may indicate a surface height variation, correspond to the moisture patches detailed in Fig. 43.

Sample 760-21-5

Sample 760-21-5 was subjected to 22 test runs. Scatter measurements were recorded for most of the runs. The amount of scatter, as measured by the lock-in, should be compared to the background detector reading to indicate the relative amount of scattered light detected. During the low power (0.1 W) scans across the sample, scatter increased significantly at absorption sites, as seen for Runs 7

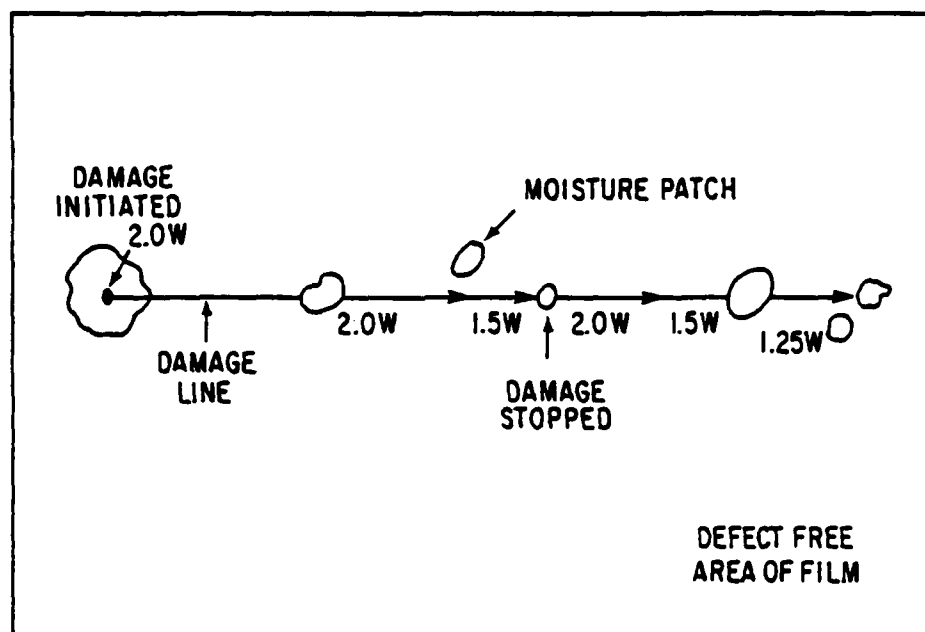


Fig. 42. Translation of sample D-21-4 in Run No. 23 during exposure to damaging irradiation indicating thresholds needed to sustain irradiation.

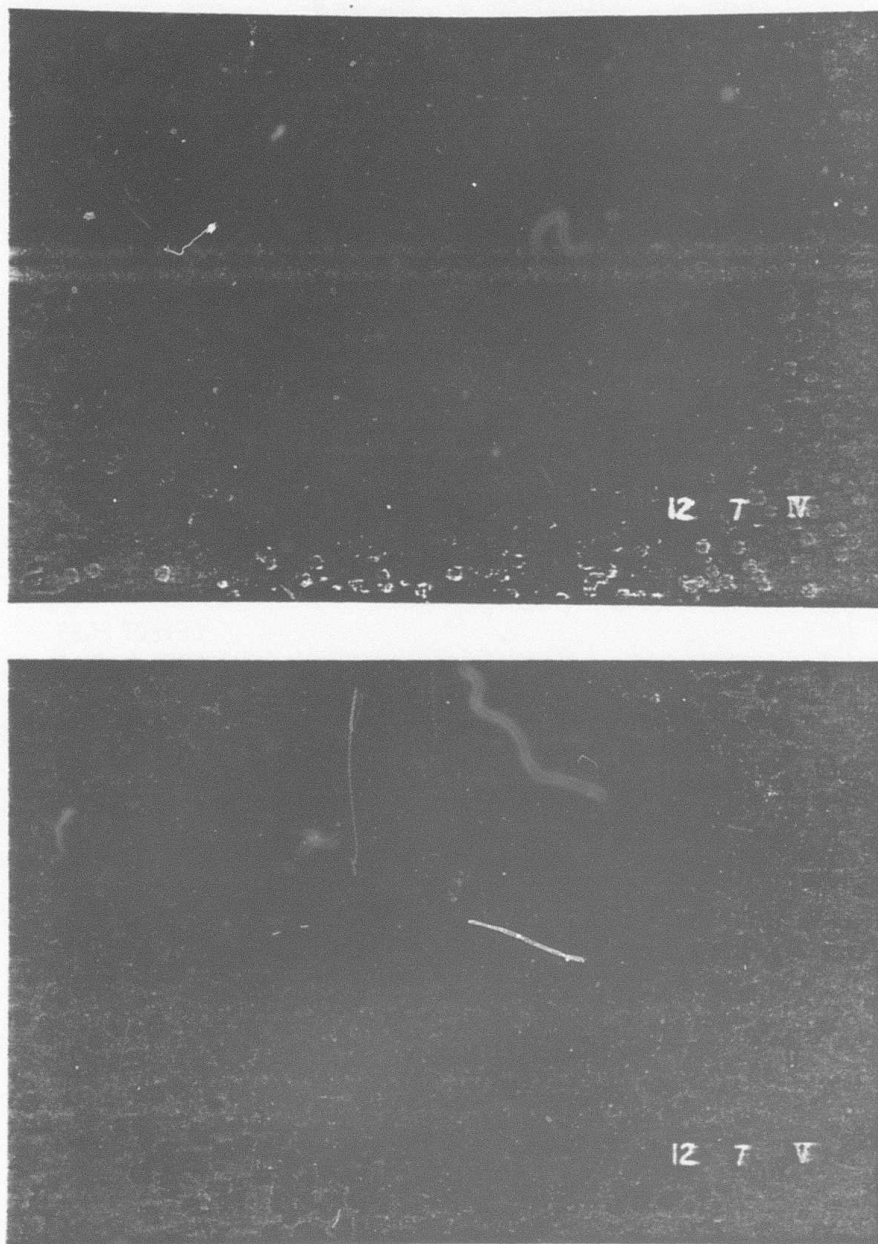


Fig. 43. Damage while sample was translated in:

- a) Run No. 18, $\lambda = 509$ nm
- b) Run No. 23, $\lambda = 480$ nm.

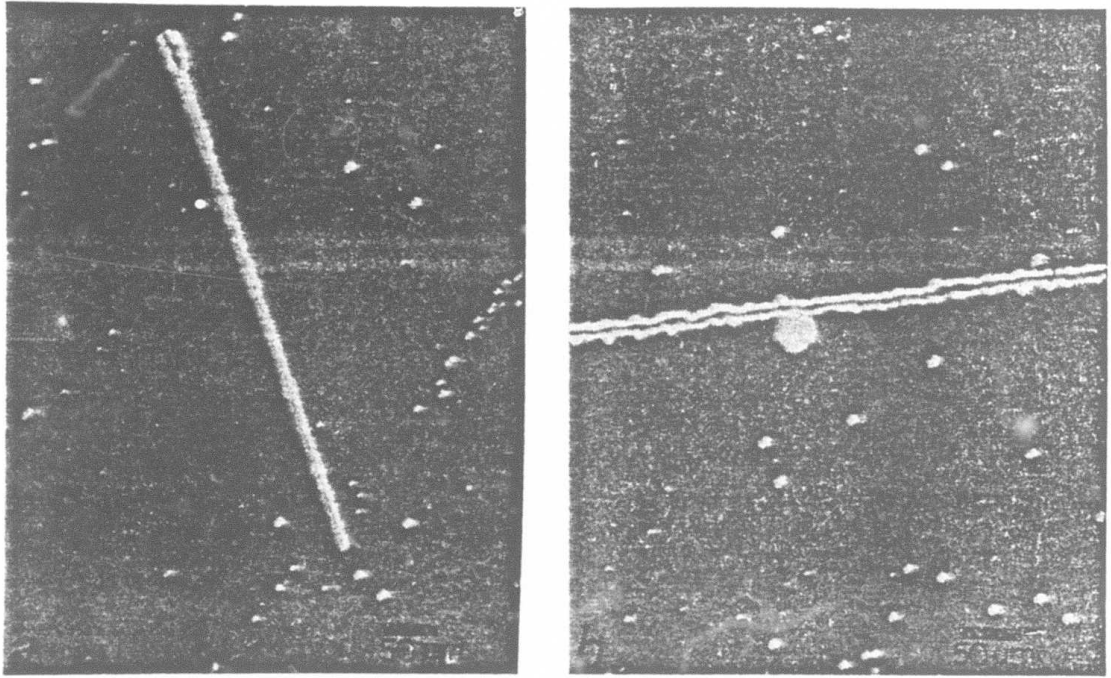


Fig. 44. Nomarski micrographs of the damage sustained in a) Run No. 18 and b) Run No. 23, taken at Naval Weapons Center, China Lake, California.

and 13; for these runs, the amount of scatter was 12 and 2.6 times the background level, respectively. Scatter seems to correlate with damage threshold for the runs examined, since Run 7 damaged at a relatively low level of 0.5 W and No. 13 could not be damaged until 2.0 W output power. This relation of scatter below threshold to the threshold level does not appear to hold for the clear areas of the filter. Once damage occurred, however, the scatter increased dramatically, as was expected.

Damage occurred for Sample 760-21-5 at the moisture absorption sites and moisture patches as well as defect-free areas of the filter. Damage threshold values varied greatly from one site to the next. The diameters of the initial damage sites were from 10 to 20 μm and increased with continual irradiation. Photographs of some damage sites on this sample are shown in Fig. 45. Run 12 was particularly interesting. In this run a defect-free area was irradiated and damaged. Immediately following exposure, a moisture patch was observed centered on the damage site.

Summary

Observations may be summarized as follows:

1. Scatter laser light was greater at adsorption sites or pit defect sites than at clear or moisture patches of the film.
2. Scatter increased drastically when damage occurred.
3. When damage did occur, it occurred instantaneously.
4. Not all defect sites could be damaged.
5. Initial diameters of the sites damaged ranged from 20 μm to 40 μm . Continual irradiation at the same power level did not

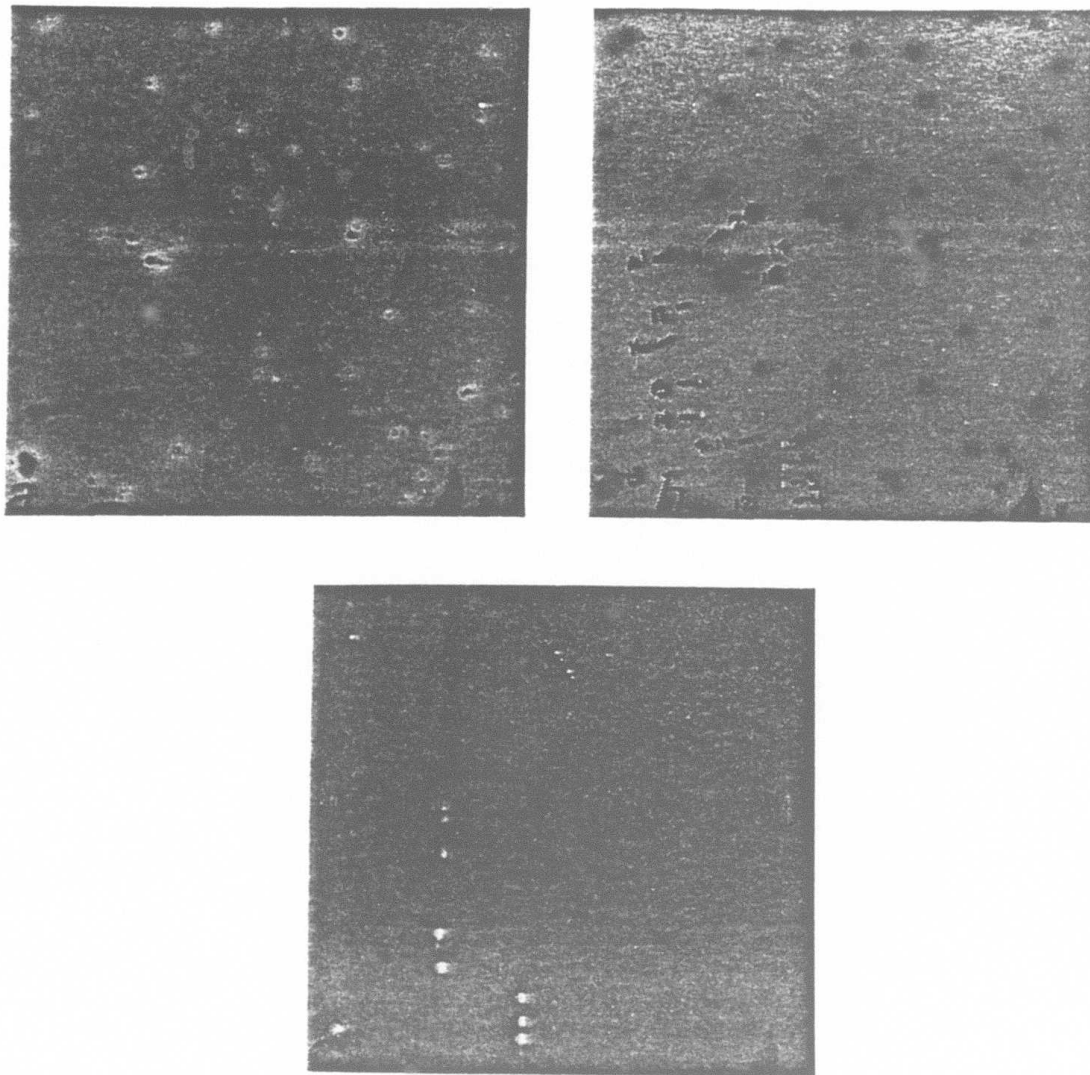


Fig. 45. Damage sites on the $\text{ZrO}_2/\text{SiO}_2$ sample (760-21-5).
a) $\lambda = 553$ nm.
b) $\lambda = 524$ nm.
c) $\lambda = 600$ nm.

Position of irradiation for each run indicated in b.

increase the damage area in sample D-21-4. When the power level was increased, however, the damage site increased in area. In contrast, continual irradiation at the same power level did enlarge damage site areas on sample 760-21-5.

6. Damage, once initiated, could be sustained at much lower fluence as the sample was translated.
7. The wavelength shift caused by moisture in the film occurred in only one test run as the result of laser irradiation short of threshold.

CHAPTER 5

RESULTS AND ANALYSIS

50 % Damage Threshold

Inspection of the experimental data presented in Tables 2 and 3 show a wide range of fluence levels causing damage to a particular defect. This distribution suggests that the structure of defects is varied and complex and cannot be completely characterized by the simple method used for this experiment.

There is no one accepted method of analyzing laser damage data. In some instances where a ranking or absolute damage levels are important, the thresholds reported are the lowest fluences that produce observable damage (Marrs, et al. 1981). This is also the technique used in large spot laser damage testing with few data points. Laser damage data is also expressed in terms of the 50% laser damage threshold (Seitel, Frank, Marrs, and Williams 1983). The 50% damage threshold is an estimation of the peak intensity required to cause damage with a 50% probability. This definition is convenient experimentally but is useful only in the evaluation of relatively defect-free films or when the damaging fluence levels do not fluctuate greatly from site to site.

In dealing with materials that exhibit a distribution in the fluence levels at which selective damage occurs, the 50% threshold represents the mean of a damage distribution, and the standard deviation of the 50% threshold indicates the extent of the damage frequency

Table 2. Laser Damage Measurements on ZnS/Cryolite Filter Sample D-21-4.

Run	Defect Irradiated	Output Power (W)	Power Fluence (10^3 W/cm ²)	Duration of Exposure	Scatter	Results
1	Moisture Patch	2.40	7.0	1 min 2 min	Low	—
2	Clear Area	2.40 2.40	7.0 7.0	1 min 5 min	Low	—
3	Clear Area	2.40	7.0	1 min	Low	—
4	Adsorp Site	2.40	7.0	10 sec	Low	Immed Damage
5	Moisture Patch	2.40	7.0	2 min	Low	—
6	Pit	2.40	7.0	30 sec	Low	Damage (20 μ m)
7	Clear	2.40	7.0	1 min	Low	—
8	Moisture Patch	2.40	7.0	1 min	Low	—
9	Adsorp Site	2.30	6.8	Immed	High	Damage Trans Sample
10	Adsorp Site	2.40	7.0	Immed	High	Damage
11	Adsorp Site	2.30	6.8	30 sec 30 sec	Low	— —
12	Moisture Patch	2.30	6.8	1 min 1 min	Moderate	— —
13	Adsorp Site	2.40	7.0	Immed	High	Damage
14	Moisture Patch	0.50 0.50 0.80 0.80 1.50 1.50 2.00 2.00 2.40	1.4 1.4 2.3 2.3 4.5 4.5 6.0 6.0 7.0	30 sec 1 min 30 sec 1 min 30 sec 1 min 30 sec 1 min 30 sec	Low Low Low Low Low Low Low Low Low	— — — — — — Damage 20 μ m Same Size Enlarged to \approx 30 μ m Same Size
15	Numerous Adsorption Site Areas	0.50 0.50 1.00 1.00 1.50 1.50 2.00 2.00 2.40 2.40	1.2 1.2 3.0 3.0 4.5 4.5 6.0 6.0 7.0 7.0	30 sec 1 min 30 sec 1 min 30 sec 1 min 30 sec 1 min 30 sec 1 min	Very High	—

Table 2 (continued). Laser Damage Measurements on Zns/Cryolite Filter Sample D-21-4.

Run	Defect Irradiated	Output Power (W)	Power Fluence (10^3 W/cm ²)	Duration of Exposure	Scatter	Results
16	Pit Defect	1.00	3.0	30 sec	Low	
		1.00	3.0	1 min	Low	
		2.00	6.0	30 sec	Low	
		2.00	6.0	1 min	Low	
		2.40	7.0	30 sec	Low	
		2.40	7.0	1 min	Low	
17	Pit Defect	2.20	6.5	30 sec	—	
		2.20	6.5	1 min		
		2.40	7.0	30 sec		
		2.40	7.0	1 min		
18	Adsorp Site	1.00	3.0	30 sec	Very High	Damage = 10 μ m
		1.00	3.0	1 min	Very High	= 15 μ m
		1.50	4.5	30 sec	Very High	= 20 μ m
		1.50	4.5	1 min	Very High	Same
		2.00	6.0	30 sec	Very High	= 25 μ m
		2.00	6.0	1 min 15 sec	Very High	Same
		2.40	7.0	30 sec	Very High	= 25 μ m
		2.40	7.0	1 min	Very High	Same
		2.40	7.0	Scan	Very High	Scan Cut Film
		2.00	6.0	Scan	= 160 μ m	
		1.50	4.5	Scan	Very High	Scan Cut Film
		2.00	6.0	Scan	Very High	Scan No Cut
		2.40	7.0	Scan	Very High	Scan No Cut
19	Clear	2.40	7.0	1 min	Low	—
		2.40	7.0	2 min	Low	—
20	Moisture Patch	2.40	7.0	1 min	Low	—
		2.40	7.0	1 min	Low	—
21	Pit Defect	2.40	7.0	30 sec	Moderate	—
		2.40	7.0	1 min	Moderate	—
22	Adsorp Site	2.40	7.0	30 sec	Low	—
23	Pit Defect Area	1.00	3.0	30 sec	High	Damage = 20 μ m
		1.00	3.0	30 sec	High	Same
		1.50	4.5	30 sec	High	= 40 μ m
		1.50	4.5	30 sec	High	Same
		2.00	6.0	30 sec	High	= 50 μ m
		2.00	6.0	30 sec	High	Same
		2.40	7.0	30 sec	High	Same
		2.40	7.0	Scan = 250 μ m	High	Cut Film
		2.00	6.0	Scan = 250 μ m	High	Cut Film
		1.50	4.5	Scan	High	No Cut
		2.00	6.0	Scan = 250 μ m	High	Cut Film
		1.50	4.5	Scanned at Slower Rate	High	Cut Film
		1.25	3.7	Scan	High	Cut Film Then Damage Stopped
24	Adsorp Site	2.40	7.0	15 sec	High	Damage = 20 μ m
25	Pit	2.40	7.0	15 sec	High	Damage = 150 μ m

Table 2 (continued). Laser Damage Measurements on Zns/Cryolite Filter
Sample D-21-4.

Run	Defect Irradiated	Output Power (W)	Power Fluence (10^4 W/cm ²)	Duration of Exposure	Scatter	Results
26	Pit	1.00 1.50 2.00 2.40	3.0 4.5 6.0 7.0	30 sec 30 sec 30 sec 30 sec	Low Low Low Low	—
27	Adsorp Size	1.00 1.00 1.50 2.00 2.40 2.40 (Adj Focus)	3.0 3.0 4.5 6.0 7.0 7.0	30 sec 30 sec 30 sec 30 sec 30 sec Immed.	High High High High High High	Damage 10 μ m Same Same Same Same Enlarged to 20 μ m
28	Adsorp Size	— — —	1.00 1.50 2.00 2.40	3.0 4.5 6.0 7.0	30 sec 30 sec 30 sec 1 min	Low — Low — Low — Low —
29	Adsorp Size	— — —	1.00 2.00 2.40	3.0 6.0 7.0	30 sec 30 sec 30 sec	High — High — High —
30	Adsorp Size	— — — —	1.00 1.50 2.00 2.40	3.0 4.5 6.0 30 sec	30 sec 30 sec 30 sec 30 sec	Moderate — Moderate Damage = 20 μ m Moderate Same Moderate Enlarged = 50 μ m
Background 0.005 V						
31	Pit	0.022 V	2.00 2.00	6.0 6.0	1 m 1.5 min	0.410 No Damage 0.200 Became Moisture Adsorp Size
32	Pit	0.020 V	2.00 2.00	6.0 6.0	1 min 1 min	0.300 — 0.455 —
33	Moisture Patch	0.025 V	2.00 2.00 2.00	6.0 6.0 6.0	1 min 1 min 1 min	1.097 Damage = 10 μ m 1.4 Enlarge to 20 μ m 2.0 Same
Background 0.060						
34	Clear	0.067	2.00	6.0	1 min	0.740 —
35	Moisture Patch		2.00	6.0	1 min	0.730 —
36	Clear		2.00	6.0	1 min	0.720 —
37	Moisture Patch		2.00	6.0	1 min	0.710 —
38	Clear		2.00	6.0	1 min	0.857 —
39	Clear		2.00	6.0	30 sec	3 and Rising — Immed High Scatter
40	Moisture Patch		2.00	6.0	1 min	0.785 —

Table 2 (continued). Laser Damage Measurements on Zns/Cryolite Filter Sample D-21-4.

Run No.	Defect	Low Power Scatter	Output Power (w)	Power Fluence (10^4 W/cm^2)	Duration of Exposure	High Power Scatter (Volts)	Results
41	Clear		2.00	6.0	1 min	0.70 to 1.15	— Damage = 20 μm
			2.00	6.0	1 min	to 6.00	
42	Clear		1.50	4.5	1 min	0.740	—
			2.00	6.0	1 min		—
43	Moisture Patch		2.00	6.0	1 min	0.710	—

Table 3. Laser Damage Measurements on $\text{ZrO}_2/\text{SiO}_2$ Filter Sample 760-21-5.

Run No.	Defect	Low Power Scatter (Volts)	Output Power (w)	Power Fluence (10^3 W/cm^2)	Duration of Exposure	High Power Scatter (Volts)	Results
Background Scatter 0.06 V							
1	Clear	0.20	2.00	6.0	Immed	4 Rising	Damage = 10 μm
2	Clear		1.50	4.5	10 sec	4 Rising	Damage = 10 μm
3	Clear		1.00	3.0	5 sec	4 Rising	Damage = 10 μm
4	Clear		0.50	1.4	30 sec	0.56	—
5	Clear		0.70	2.0	30 sec	0.47	Damage = 10 μm
6	Clear		0.70	2.0	30 sec	0.43	—
7	Adsorp Site	0.72	0.30	6	60 sec	1.86	—
			0.50	1.4	15 sec	3 and Rising	Damage = 10 μm
			0.50	1.4	15 sec	5 and Rising	Enlarged to 20 μm
8	Clear	0.25	0.50	1.4	30 sec	0.27	—
9	Clear		0.70	2.0	30 sec	0.34	—
10	Clear		0.80	2.3	30 sec	0.43	—
11	Clear	1.00	3.0	30 sec	0.45		
12	Clear		1.20	3.5	30 sec	0.6 and Rising	Damage = 10 μm
			1.20	3.5			
			1.20	3.5			
Background Scatter 0.050 V							
13	Adsorp Site	0.13	0.20	0.4	30 sec	0.21	—
			0.20	0.4	30 sec	0.18	—
			0.30	0.6	30 sec	0.24	—
			0.50	1.4	30 sec	0.36	—
			0.60	1.2	30 sec	0.47	—
			0.70	2.0	1 min	0.57	—
			0.80	2.3	30 sec	0.69	—
			0.90	2.6	30 sec	0.72	—
			1.00	3.0	2 min	0.8 to 1.0	—
			1.20	3.5	1 min	1.2 to 1.5	—
			1.50	4.5	1 min	1.5 to 2.0	00
			2.00	6.0	10 sec	5 Rising	Damage = 20 μm
14	Clear		2.00	6.0	15 sec	5 Rising	Damage = 20 μm
15	Clear		1.50	4.5	30 sec	3 Rising	Damage = 30 μm
16	Clear		1.00	3.0	30 sec	0.62	—
17	Clear		1.20	3.5	10 sec	2 Rising	Damage = 20 μm
18	Moisture Patch		1.0	3.0	10 sec	2 Rising	Damage = 20 μm

Table 3 (continued). Laser Damage Measurements on $\text{ZrO}_2/\text{SiO}_2$ Filter
Sample 760-21-5.

Run No.	Defect	Low Power Scatter (Volts)	Output Power (w)	Power Fluence (10 W/cm ²)	Duration of Exposure	High Power Scatter (Volts)	Results
19	Moisture		0.50	1.4	30 sec	0.27	—
	Patch		0.70	2.0	10 sec 3 Rising	Damage = 20 μm	
20	Clear		0.70	2.0	10 sec	0.8 Rising	Damage = 20 μm
21	Moisture		0.50	1.4	30 sec	0.29	—
	Patch		0.70	2.0	30 sec	1.6 Rising	Damage = 20 μm
22	Adsorp Site		0.50	1.4	30 sec	2.0	—

distribution. The wide frequency distribution in this case suggests a variation in defect morphologies.

The 50% damage threshold technique is usually employed in the analysis of pulsed laser damage data with many data points. Although the testing reported in this paper represents CW laser damage, the laser damage data at each particular defect type will first be analyzed using the 50% threshold technique.

Damage profiles for samples D-21-4 and 760-21-5 are plotted in Figs. 46 and 47 respectively using the 50% threshold technique. In these figures data is plotted for each defect type as damage occurs or does not occur at the corresponding fluence level. Precision of the threshold values is primarily determined by the step increments of fluence near threshold. Unfortunately, most of the power increments used in this experiment were too large to define the 50% threshold value precisely. The error bars indicate the highest fluence that did not cause damage and the lowest fluence that caused damage.

For the ZnS/cryolite sample (D-21-4) the clear areas and moisture patches were especially difficult to damage with the laser output power available. Although there are some anomalies in the data (damage occurs at some points at a low fluence and does not occur at other sites at higher fluence levels), we see from Fig. 46 little occurrence of damage up to $7.0 \times 10^3 \text{ W/cm}^2$. The adsorption sites and pit defects in this sample show a 50% threshold around $7.0 \times 10^3 \text{ W/cm}^2$.

The 50% damage threshold plots for the $\text{ZrO}_2/\text{SiO}_2$ sample (760-21-5), are shown in Fig. 47. Here the clear areas of the film show

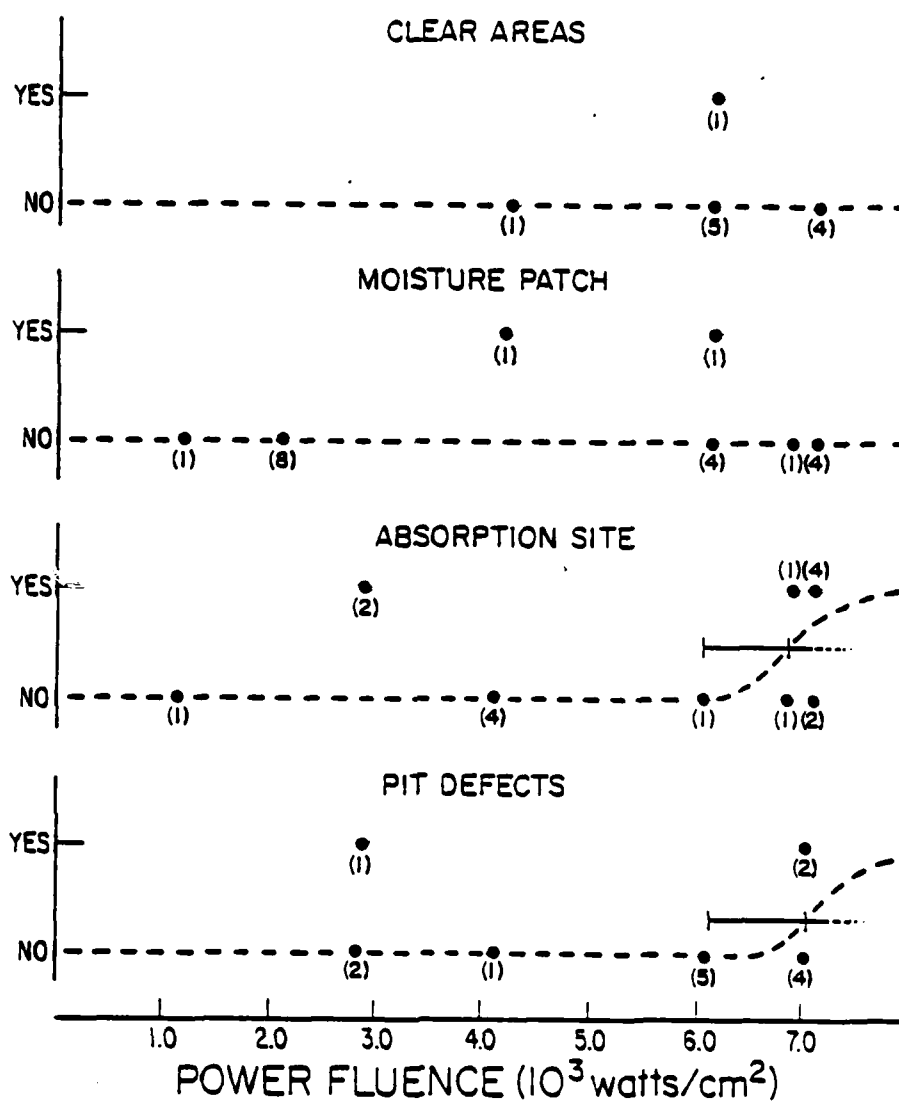


Fig. 46. 50% damage threshold plots for ZnS/cryolite sample (D-21-4). The number in parentheses indicates the number of shots at that fluence.

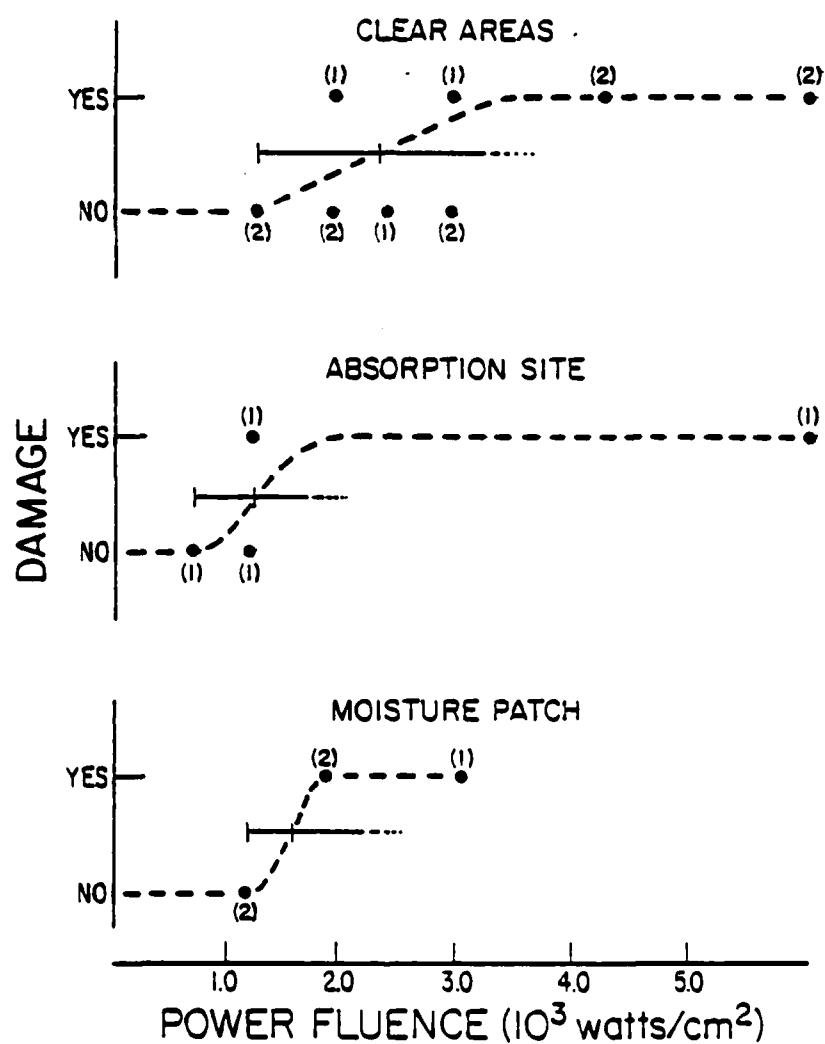


Fig. 47. Damage threshold plots for the $\text{ZrO}_2/\text{SiO}_2$ sample (760-21-5).

a 50% damage threshold of about 2.2×10^3 W/cm². The adsorption sites and moisture patches damaged at around 1.0×10^3 W/cm² and 1.5×10^3 W/cm² respectively. Results of the 50% damage threshold analysis are tabulated in Table 4.

Table 4. Approximate 50% Damage Thresholds (10^3 W/cm²).

	ZnS/Cryolite (D-21-4)	ZrO ₂ /SiO ₂ (760-21-5)
Clear Areas	>7.0	2.2
Moisture Patch	>7.0	1.5
Adsorption Site	7.0	1.0
Pit Defect	7.0	—

From the limited results we may infer that the ZrO₂/SiO₂ sample is considerably weaker in damage resistance than the ZnS/cryolite sample. Furthermore, moisture patches and adsorption sites are more susceptible to damage than clear areas in the ZrO₂/SiO₂ sample. In the ZnS/cryolite filter adsorption sites and pit defects show less damage resistance than clear areas and moisture patches.

We may speculate that the lower 50% damage threshold for the ZrO₂/SiO₂ sample is a result of the very porous structure and low packing density of the ZrO₂ layers in the filter.

Damage Onset Theory

As already mentioned, the standard deviation of the 50% threshold indicates the fluctuation in the damage distribution. However,

the shape of the distribution is not apparent from this technique. The distribution in thresholds may extend to much lower levels of irradiation, which may not have been measured directly. Since the variation in defect morphology is postulated as the cause for the distribution in the damage fluences, the damage probability distribution together with the damage onset values may be a more complete description of the influence of laser irradiation on high defect materials. Porteus and Seitel (1984) developed a technique that incorporates a theoretical relationship between damage probability and the defect distribution function to determine the damage onset value from the damage probability distribution. By redefining the threshold from 50% to 0% (damage onset), the resulting damage probability becomes laser spot-size independent. A brief description of this theory will be presented here and the damage data from Figs. 46 and 47 analyzed in terms of damage probability.

Following the theoretical development of Danileiko, et al (1981) where microdefect-dominated damage in transparent three-dimensional solids was considered, the damage probability P , for a thin dielectric film is given by

$$P = 1 - \exp \left(- \int_A dA \int_0^{\infty} f(I_d) \left\{ 1 - \exp \left[- \int_0^{\tau} w(I, I_d) d\tau \right] \right\} dI_d \right)$$

The probability of damage to a single defect during a pulse of duration τ and intensity I can be written as

$$P(\tau) = 1 - \exp \left[- \int_0^\tau w(I, I_d) dt \right]$$

where $w(I, I_d)$ represents the probability of damage per unit time. If an individual defect is assumed to have a unique, non-probabilistic damage threshold and

$$\int_0^\tau w(I, I_d) dt \gg 1 ,$$

then the damage probability becomes

$$P = 1 - \exp \left[- \int_A da \int_0^{I(xy)} f(I_d) dI_d \right] . \quad (14)$$

In this equation $f(I_d)$ is the defect ensemble function, representing the number of defects per unit area with damage thresholds between I_d and $I_d + dI_d$, and $I(xy)$ is the peak irradiance at the point x, y , rewrite Eq. 14, as

$$P = 1 - \exp \left[- \pi \int_0^{I(xy)} \int_0^\infty f(I_d) dI_d r dr \right] . \quad (15)$$

$$\text{Letting } A = \left[-\pi \int_0^{I(xy)} \int_0^\infty f(I_d) dI_d r dr \right]$$

then

$$\frac{dP}{dI_a} = -\exp[A] \frac{dI_d}{dI_a} \pi \int_0^\infty f(I_d) dI_d r dr \quad (16)$$

where $\exp[A]$ is $1 - P$.

Equation 16 can be rewritten as

$$\begin{aligned} \frac{1}{1-P} \frac{dP}{dI_a} &= -\frac{d}{dI_a} \pi \int_0^{I(x,y)} \int_0^\infty f(I_d) dI_d r dr \\ &= -\frac{d}{dI_a} \pi \int_0^I \pi \int_0^\infty f(I_a e^{-r^2/w^2}) dI r dr \end{aligned} \quad (17)$$

For the special case of a Gaussian intensity profile,

$$I = I_a \exp(-r^2/w^2) \quad (18)$$

where r is the radial position, I_a is the peak intensity, and W is the $1/e$ radius of the focal spot, we can write

$$\frac{dI}{dI_a} = e^{-r^2/w^2}$$

Eq. 17 becomes

$$\frac{1}{1-P} \frac{dP}{dI_a} = -\pi \int_0^\infty f(I_a e^{-r^2/w^2}) e^{-r^2/w^2} r dr. \quad (19)$$

Also from Eq. 18,

$$dI = I_a e^{-r^2/w^2} \left(-\frac{2r}{w^2}\right) dr$$

or

$$dr = \frac{dI}{I_a} e^{r^2/2^2} \left(-\frac{w^2}{2r}\right)$$

Finally Eq. 19 becomes

$$\frac{1}{1-P} \frac{dP}{dI_a} = \frac{\pi w^2}{I_a} \int_0^{I_a} f(I') dI' \quad (20)$$

Reintegrating on I_a gives

$$P(I_a) = 1 - \exp \left[-\pi w^2 \int_0^{I_a} [I^{-1} \int_0^I f(I') dI'] dI \right] \quad (21)$$

Equation 21 may be evaluated for specific damage models. For a degenerate ensemble, all the defects have the same damage threshold, I_0 , and $f(I_a)$ can be represented by a delta function normalized to the defect density N . Using the degenerate defect model where

$$f(I_0) = N \delta(I - I_0) \quad (22)$$

Eq. 21 becomes

$$P(I_a) = 1 - \exp \left[-\pi w^2 N \int_0^{I_a} I_0/I dI \right]$$

This relation simplifies to

$$P(I_a) = 1 - \left(\frac{I_a}{I_0} \right)^{-N\pi w^2} \quad (23)$$

The degenerate defect model and the resulting damage probability distribution are illustrated in Fig. 48. The increasing probability of damage is a result of the enlarging irradiated area and the corresponding rising probability of finding a defect within this area.

According to Porteus (1984), the degenerate ensemble model applies to many multilayer coatings damage tested at blue-green wavelength. At infrared wavelengths, the degenerate ensemble is less applicable, and the damage probability distribution may be more appropriately analyzed in terms of a power law model.

One particular nondegenerate defect model is a simple power law defined by

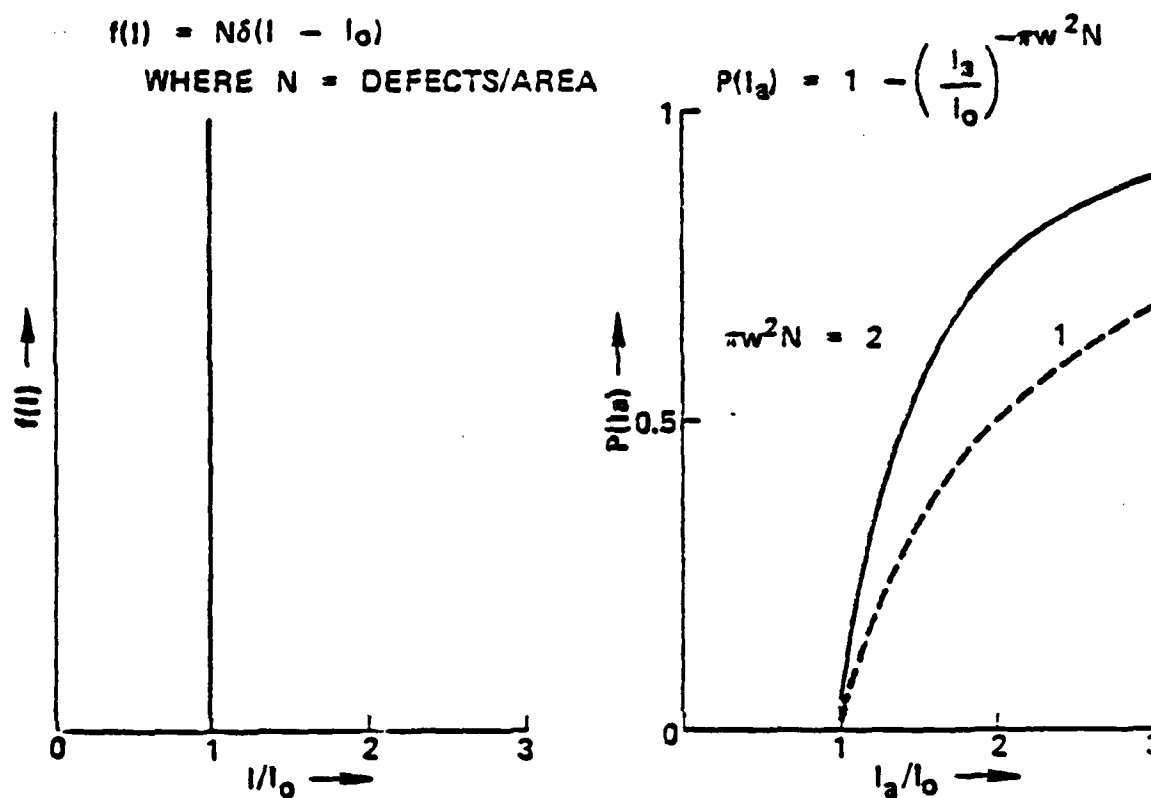


Fig. 48. Degenerate defect damage ensemble (left) and corresponding damage probability distributions (right). From Porteus et al. (1983).

$$f(I) = \text{constant} \times \begin{cases} (I-I_0)^P; & \text{for } I_0 \leq I \leq I_m \\ 0; & \text{for } I < I_0, I > I_m \end{cases} \quad (24)$$

where I_m is some maximum intensity. This case is shown in Fig. 49. Note that below the 50% damage probability, the probability distribution has a positive curve.

To analyze the data of this experiment in terms of the defect ensemble model, we must make certain assumptions concerning the technique in performing the experiment. The experimental procedure involved directing the laser beam onto adsorption sites or pit defects. Thus, each defect was irradiated close to the on-axis intensity. In the formulation of the damage probability, the spatial integral was taken over the area of the focal spot. Within the focal spot were distributed defects corresponding to the defect ensemble. To compare the damage distribution to the theoretically determined probability without biasing the results, we assume that the irradiation intensity was Gaussian, and the defect could be located anywhere within the focal spot of the beam. Of course, this assumption need not be made for the clear area or the moisture patch damage area.

The laser damage data from this experiment is plotted in Figs. 50 and 51 in terms of damage frequency, which is the percentage of shots at a particular fluence level in which damage occurred.

Fitting the damage probability distribution to the damage frequency data for the degenerate defect ensemble involves two parameters, the defect density N , and the onset value, I_0 . There is no simple algorithm for determining the onset value. It can be estimated

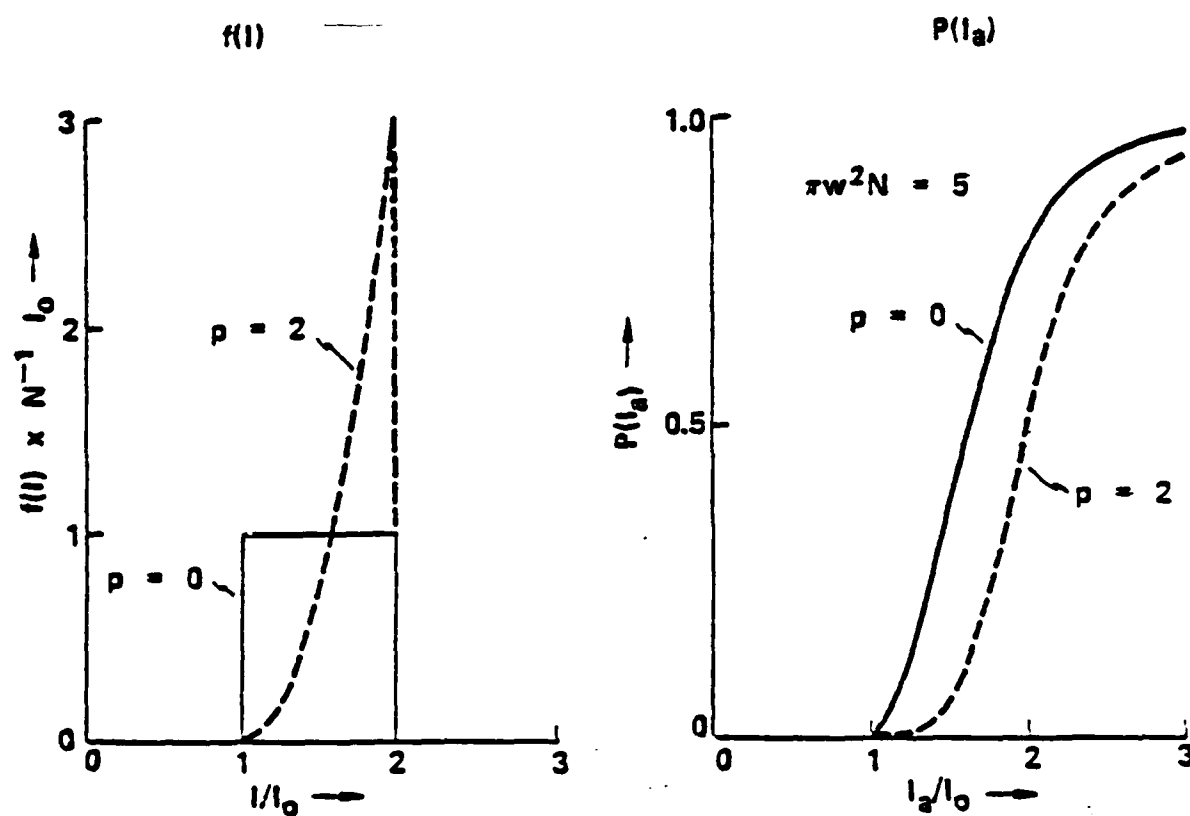


Fig. 49. Power-Law defect damage ensembles (left and corresponding probability distributions (right). From Porteus et al. (1983).

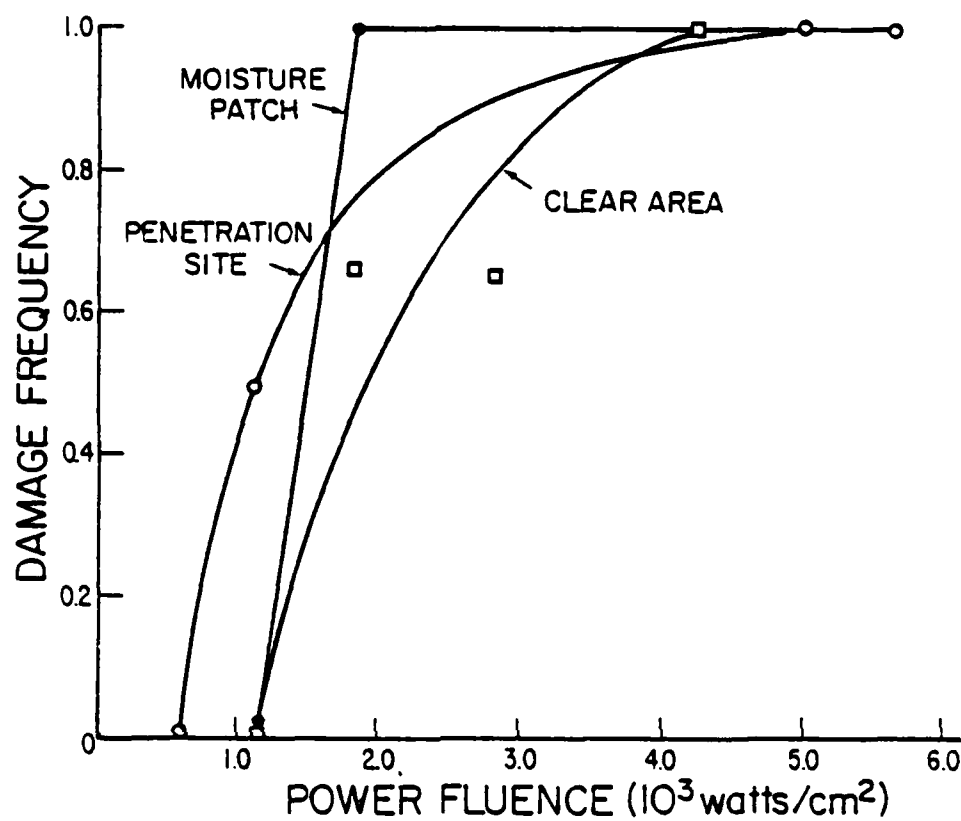


Fig. 50. Damage frequency plot for the ZrO_2/SiO_2 sample (760-21-5).

- Clear area
- Moisture adsorption site
- Moisture patch

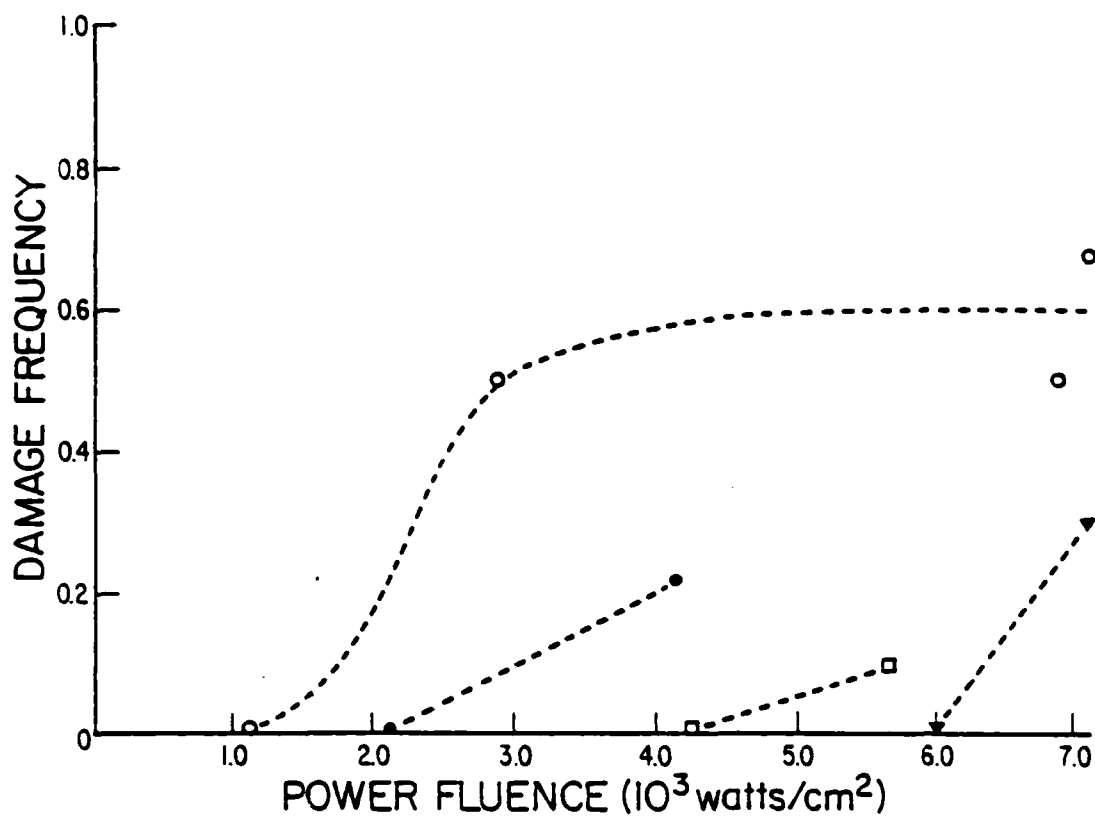


Fig. 51. Damage frequency plot for the ZnS/cryolite sample (D-21-4).

- Adsorption site
- ▼ Pit defect
- Moisture patch
- Clear area

by extrapolating the measured damage frequencies to zero probability. Because of the limited data available, the damage onset value was chosen to be the maximum experimentally determined fluence level at which no damage occurred.

The deviations of the 50% damage threshold represent a statistical variation of the damage data and do not reflect the absolute accuracy, which was influenced by many variables such as detector lock-in calibration and beam profile measurement. Of all possible factors, error in beam profile measurement had the greatest influence on absolute accuracy. The beam profile was most affected by alignment of beam through the microscope as laser output power was controlled. The deviation of the calculated fluence, which was based on measurement of power loss through the microscope, from a linear fit in Fig. 39 is the best estimate of instrumental error. This error is as large as 30% at a fluence of $7.0 \times 10^3 \text{ W/cm}^2$ and drops to 10% at 5.0×10^3 . The error remains at about 10% as the fluence decreases. Since the $\text{ZrO}_2/\text{SiO}_2$ sample damaged at values between 1.0 and $3.0 \times 10^3 \text{ W/cm}^2$, uncertainty in the damage onset values are determined primarily by the variation of the damage data. In the case of the ZnS/cryolite sample that damaged in the range 6.0 to $7.0 \times 10^3 \text{ W/cm}^2$, the uncertainty in the results is primarily due to the large instrumental error resulting at that high fluence level.

For the $\text{ZrO}_2/\text{SiO}_2$ sample, the damage frequency curves, Fig. 50, appear to be representative of the degenerate defect model. The damage onset values for the penetration site defects and clear areas of this

sample are $0.5 \times 10^3 \text{ W/cm}^2$ and $1.0 \times 10^3 \text{ W/cm}^2$ respectively. The damage frequency curves for these defect types rise with generally the same curvature indicating similar defect densities.

In Fig. 52, the damage frequency data for this sample is replotted in terms of the normalized (I/I_0) power fluence and compared to the theoretical probability distribution assuming a degenerate defect damage model. We see that under the assumptions made, the $N = 1$ probability curve best approximates the probability of damage to adsorption site defects. For the clear area, the best fit is made with a defect density $1 < N < 2$.

Less definite conclusions can be drawn for the moisture patch areas of the $\text{ZrO}_2/\text{SiO}_2$ filter. The damage onset value is about $1.0 \times 10^3 \text{ W/cm}^2$, identical to the clear area damage onset. Because the slope of the damage probability curve is proportional to N , we can infer that moisture patch areas contain more defects per unit area on the average, than either adsorption site defects or clear areas of the film. When the normalized damage frequency data for the moisture patch defects are plotted, Fig. 52, a theoretical approximation to the data can be attained with a defect density $N \approx 6$.

It must be emphasized that because of the limited data, these results are tentative and open to subjective interpretation. It is possible for example, to fit a curve of positive curvature on the adsorption site and defect-free damage data points, indicating a nondegenerate defect model.

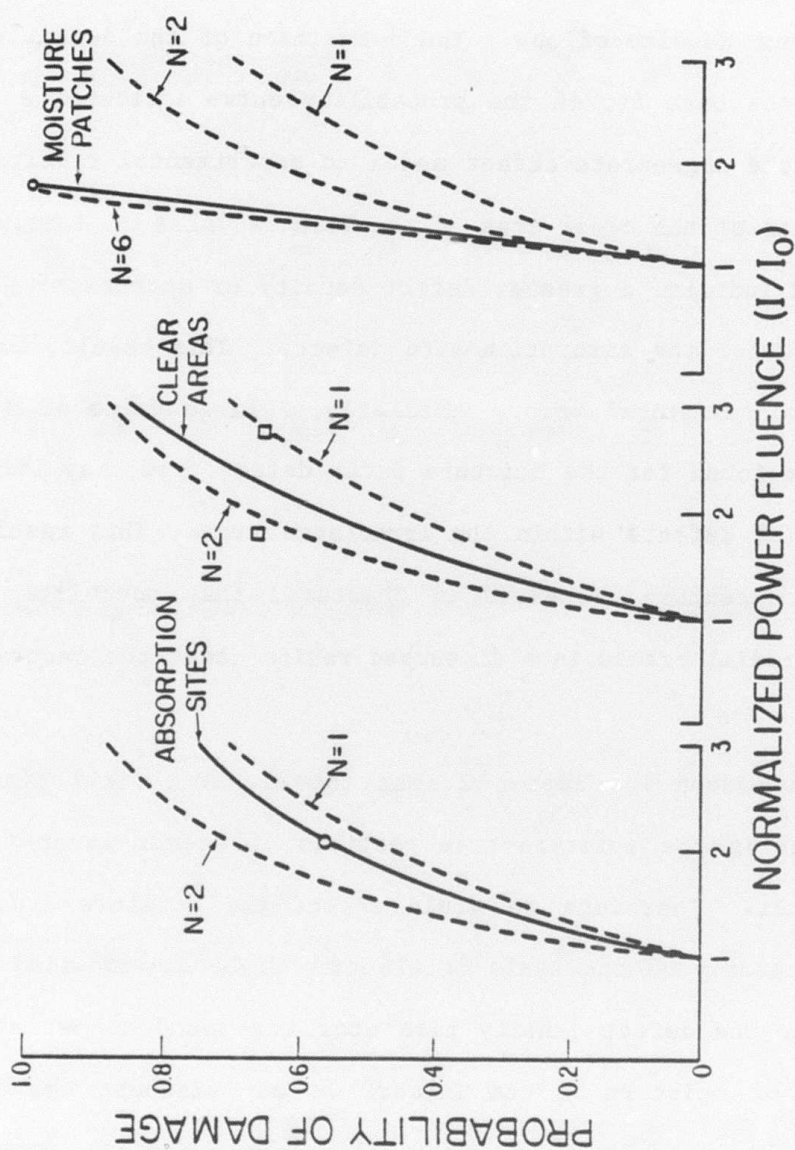


Fig. 52. Comparison of experimental damage frequency results for the ZrO_2/SiO_2 sample to theoretical probability distributions assuming a degenerate defect damage model.

The significance of the defect density parameter, N , is difficult to establish. During the laser damage experiment, only one adsorption site defect was irradiated during each exposure run. This procedure insured a defect density of one. The comparison of the defect density predicted by the best fit of the probability curve indicates a good agreement of the degenerate defect model to experimental results. For the damage data of the clear area of the film, a value of N between one and two could indicate a greater defect density or defects of greater size than that for the adsorption site defects. This result, however, may be due to statistical error. Similarly, a large value of N (about six) which was found for the moisture patch defect type, may indicate a large number of defects within the irradiated area. This result may support the contention addressed in Chapter 2 that postulates the existence of radial cracks in a disturbed region about the central defect site.

We have seen in Chapter 2 that the electric field peaks at greater values in the moisture-free portions of spacer layer for the $\text{ZrO}_2/\text{SiO}_2$ filter. Therefore we would expect the moisture areas to damage less readily on the basis of electric field distribution alone. However, since the defect density parameter was found to be larger in the presence of moisture in the filter, we may discount the direct effect of the electric field distribution on damage for this sample.

The damage frequency data for all the defect types in the $\text{ZnS}/\text{cryolite}$ filter were inadequate to establish the appropriate power law to represent the defect ensemble. Damage frequency plots for the

ZnS/cryolite sample are shown in Fig. 51. The curves do not approach the 100% line because of the difficulty of damaging the filter at the fluence levels available. A probability curve based on a degenerate defect ensemble does not seem to fit the data. A more complex defect ensemble must be postulated to reflect the damage data on the ZnS/cryolite sample. It is possible, however, to estimate onset damage values for this filter and rank the defects to damage susceptibility.

A comparison of damage onset values estimated from the damage frequency plots for both samples are tabulated in Table 5.

Table 5. Summary of Damage Onset Values and Damage Defect Models.

	ZrO ₂ /SiO ₂		ZnS/Cryolite	
	Damage Onset (10 ³ W/cm ²)	Defect Model	Damage Onset (10 ³ W/cm ²)	Defect Model
Clear Area	1.0	Degenerate N = 1	4.0	—
Adsorption Sites	0.5	Degenerate 1 < N < 2	0.5	Nondegenerate
Moisture Patches	1.0	Degenerate N > 6	2.0	—
Pit Defects			6.0	—

CHAPTER 6

CONCLUSIONS AND RECOMMENDATIONS

Vapor-deposited thin films have a columnar structure with voids or pores between the columns through which moisture may be adsorbed into the film. Many defects in dielectric coatings are a result of this microstructure. It is hypothesized that such defects in films are involved in the selective laser damage observed. The selective laser damage limits the optical performance of coatings at high laser powers. The objective of this experiment was to investigate the relationship between defects in dielectric coatings and laser damage.

Narrow-band dielectric filters were chosen as the test specimens because of their sensitivity to moisture and their observability in monochromatic light. The two types of filters used were of ZnS/cryolite and ZrO_2/SiO_2 materials. Three types of defects were assessed: moisture patches, penetration sites, and pits. These defects and the clear portions of the film were irradiated with an Argon laser at 514 nm to determine laser damage thresholds.

Evaluation of the data in terms of the damage frequency was made and compared to theoretical damage probability distributions for a degenerate defect ensemble model. Laser damage onset values were determined for the characterized defects.

Because of the limited time and resources available, a compromise had to be made between diagnostics and testing. It is not

believed that the errors resulting from the limited diagnostics are large enough to invalidate the findings.

Realizing that the results are preliminary and subject to large statistical error because of limited data, the following conclusions are drawn.

1. From the 50% damage threshold values for the types of defects investigated, the $\text{ZrO}_2/\text{SiO}_2$ film is more susceptible to laser damage.
2. Penetration sites have the lowest 50% damage threshold and damage onset values for both filter types tested.
3. For the $\text{ZrO}_2/\text{SiO}_2$ filter, the onset values for both the clear areas and moisture patches were nearly equal and were larger than penetration site defects. The steep slope, however, in the moisture patch damage frequency curve indicates a greater number of defects per unit area than in the clear portions of film.
4. Results of the measurements on the ZnS/cryolite filter are even less conclusive than that of the $\text{ZrO}_2/\text{SiO}_2$ sample. However, adsorption site defects do show less laser damage resistance than clear areas or other defects present in the film.

We may conclude that certain defects do influence laser damage in the dielectric narrow-band filters tested. Moisture penetration sites appear to be most responsible for limiting the laser damage threshold. Although the influence of other defects on laser damage is not clear, moisture patches may be weaker than moisture-free areas.

Because of the preliminary nature of the results, recommendations for further laser damage testing are made;

1. Determine the beam profile using a CCD array more accurately.
2. Characterize defects more extensively; perhaps to include Nomarski or TEM micrographs of the defect areas.
3. Obtain additional laser damage data to determine the 50% damage threshold and damage onset values more accurately.
4. Modify the laser damage facility to allow microscopic viewing of the sample in monochromatic light during laser irradiation.
5. Test filters of other materials and designs.
6. Investigate pulsed laser damage and conduct CW testing at other wavelengths.
7. Explore the effect on laser damage of the electric field distribution within the narrow-band filter; perhaps irradiate a series of filters with slightly different passbands or damage testing a filter under various humidity conditions.

LIST OF REFERENCES

- Allen, S. D., J. O. Porteus, W. N. Faith, J. B. Frank, "Contaminant and Defect Analysis of Optical Surfaces by Infrared Laser-Stimulated Desorption," H. E. Bennett, A. J. Glass, A. H. Guenther, B. E. Newnam, eds., Nat. Bur. Stand. (U. S.) Spec. Publ. 669, Jan. 1984. P. 65.
- Chain, E., "Optical Properties of Chemical Vapor Deposited Black Molybdenum Thin Films." Ph. D. Thesis, University of Arizona, 1983.
- Danileiko, Y. K., Y. P. Minaev, U. M. Nikolaev, A. V. Sidorin, Sov. J. Quantum. Electron. 11, 1445, 1981.
- Danileiko, Y. K., A. A. Manenkov, and V. S. Nechitaildo, "The Role of Absorbing Defects in the Laser Damage of Transparent Materials," H. E. Bennett, A. J. Glass, A. H. Guenther, B. E. Newnam, eds. Nat. Bur. Stand. (U.S.) Spec. Publ. 620, p. 369, Oct. 1981.
- DeSandre, L., "Bounds on the Dielectric Constant of Thin Films, Univ. of Arizona, internal report (1983).
- Epifanov, A. S., S. V. Garnov, G. V. Gomelauri, A. A. Manenkov, and A. M. Prokhorov, "Recent Progress in the Studies of Laser-Induced

Intrinsic Damage of Transparent Solids: Deterrent Lock Effect of Seid Electrons in Avalanche Ionization Process," H. E. Bennett, A. H. Guenther, D. Milam, B. E. Newnam, eds., Nat. Bur. Stands. (U.S.) Spec. Publ. 638, Sept. 1983, p. 532.

Foltyn, S. R., and B. E. Newnam, "Multiple-Shot Laser Damage Thresholds of Ultraviolet Reflectors at 248 and 308 Nanometers," H. E. Bennett, A. J. Glass, A. H. Guenther, B. E. Newnam, eds., Nat. Bur. Stand. (U. S.) Spec. Publ. 620, Oct. 1981 p. 265.

Foltyn, S. R., "Spot Size Effects in Laser Damage Testing," H. E. Bennett, A. J. Glass, A. H. Guenther, B. E. Newnam,, eds., Nat. Bur. Stand. Spec. Publ. 668, Jan. 1984. P. 368

Guenther, K. H., "Columnar and Nodular Growth of Thin Films," Proc. SPIE 346, 9, 1982.

Guenther, K. H., "Microstructure of Vapor-Deposited Optical Coatings," Appl. Opt. 23, 21, Nov. 1984 p. 3807.

Guenther, K. H., H. K. Pulker, "Electron Microscopic Investigation of Cross-Sections of Optical Thin Films," Appl. Opt. 15, 2992, 1976.

Jacobson, M. R., F. Horowitz, B. J. Liao, "Deposition Characterization and Simulation of Thin Films with Form Birefringence," Opt. Sci. Ctr., University of Arizona, 1984.

Jensen, B., "Quantum Theory of Multiphoton Free Carrier Absorption at High Intensities in Compound Semiconductors," H. E. Bennett, A. H. Guenther, D. Milam, B. E. Newnam, eds. Nat. Bur. Stands. (U.S.) Spec. Publ. 638, Sept., 1983 p. 532.

Kelly, P., D. Ritchie, P. Braunlich, A. Schmid and G. W. Bryant, "Deformation of Intense Laser Beams Tightly Focused inside NaCl: A Comparison of the Multiphoton Polaron and Avalanche Model of Optical Breakdown," H. E. Bennett; A. J. Glass, H. H. Guenther, B. E. Newnam, eds., Nat. Bur. Stand. (U.S.) Spec. Publ. 620, Oct. 1981, p. 394. Washington, D.C.

Lange, M. R., J. K. McIver, A. H. Guenther, T. W. Walker, "Pulsed Laser Induced Damage of an Optical Material with Spherical Inclusion; Influence of Thermal Properties of the Materials," H. E. Bennett, A. J. Glass, A. H. Guenther, B. E. Newnam, ed., Nat. Bur. Stand. (U. S.) Spec. Publ. 669. Jan. 1984, p. 380.

Lee, C. C., "Moisture Adsorption and Optical Instability in Thin Film Coatings," PhD Dissertation, University of Arizona, 1983.

Lowdermilk, W. N., D. Milam, and F. Rainer, "Damage to Coatings and Surfaces by 1.06 μm Pulses," H. E. Bennett, A. J. Glass, A. H. Guenther, and B. E. Newnam, eds., Nat. Bur. Stand. (U.S.) Spec. Publ. 568 Oct. 1979 pp. 391-403.

- Macleod, H. A., Thin-Film Optical Filters, American Elsevier Publishing Co. Inc. NY 1969.
- Macleod, H. A., "Some Effects of Microstructure on the Properties of Optical Thin Films," University of Arizona 1983.
- Marrs, C. D., W. N. Faith, J. H. Dancy, and J. O. Porteus, "Laser Damage Measurements at 492 nm Using a Flashlamp-Pumped Dye Laser," H. E. Bennett, A. J. Glass, A. H. Guenther, B. E. Newnam, eds., Nat. Bur. Stand. (U.S.) Spec. Publ. 638, Sept. 1983, p. 87.
- Messler, R., T. Takamori, and R. Roy, "Structure-Composition Variation in RF-Sputtered Films of Ge Caused by Process Parameter Changes," J. Vac. Sci. Tech., 13, 5 (1976) 1060.
- Movuchan, B. A., A. V. Demchieshin, "Investigation of the Structure and Properties of Thick Vacuum-Deposited Films of Nickel, Titanium, Tungsten, Alumina, and Zirconium Dioxide," Fizika Metall, 28, 83, 1969.
- Ogura, S., "Some features of the Behavior of Optical Thin Film," PhD Dissertation, Newcastle upon Tyne Polytechnic, U. K. 1975.
- Porteus, J. O., W. N. Faith, and S. D. Allen, "Laser Desorption Analysis of H₂O and Other Contaminants from Optical Surfaces," H. E. Bennett,

A. H. Guenther, D. Milam;, B. E. Newnam, Eds., Nat. Bur. Stand. (U. S.) Spec. Publ. 638. Sept. 1983, p. 273.

Porteus, J. O., J. L. Jernigan, W. M. Faith, "Multithreshold Measurements and Analysis of Pulsed Laser Damage on Optical Surfaces," A. J. Glass, A. H. Guenther, eds. Nat. Bur. Stand. (U.S.) Spec. Publ. 509, Dec. 1977, p. 507.

Porteus, J. O., and S. C. Seitel, "Absolute Onset of Optical Surface Damage Using Distributed Defect Ensembles," Appl. Opt. 23, 21 (1984) 3796.

Pulker, H. K., E. Jung, "Correlation Between Film Structure and Sorption Behavior of Vapor-Deposited ZnS, Cryolite, and MgF₂ Films," Thin Solid Films, 9, 1971 p. 57.

Richmond, D., "Thin-Film Narrowband Optical Filters," PhD Thesis, Newcastle Upon Tyne Polytechnic, U. K., 1976.

Seitel, S. C., J. B. Frank, C. D. Marrs, G. D. Williams, "Selective and Uniform Laser-Induced Failure of Antireflection-Coated LiNbO₃ Surfaces," IEEE J. Quantum Electron., QE-19, 475-479 Mar. (1983).

Soileau, M. J., "Laser-Induced Damage in Antireflection Coatings for LiNbO₃ Crystals," H. E. Bennett, A. J. Glass, A. H. Guenther, B. E.

Newnam, Eds., Nat. "Bur. Stand. (U. S.) Spec. Publ. 620, p. 800. Oct. 1981.

Svechnikov, M. B., "Radiation Strength of Dielectric Mirrors Having Layers of Different Optical Thickness," Sov. J. Opt. Tech. 48 (7), July 1981.

Temple, P. A., "Measurement of Thin-Film Optical Absorption at the Air-Film Interface within the Film and at the Film-Substrate Interface," Appl. Phys. 34 (10) p. 677, 1979.

Thornton, J. A., "Influence of Apparatus Geometry and Deposition Conditions on the Structure and Topography of Thick Sputtered Coatings," J. Vac. Sci. Tech. 11, 666, 1974.

Van Stryland, E. W., M. A. Woodall, W. E. Williams, and M. J. Soileau, "Two- and Three-Photon Absorption in Semiconductors with Subsequent Absorption by Photogenerated Carriers," H. E. Bennett, A. J. Glass, H. H. Guenther, B. E. Newnam, eds., Nat. Bur. Stand. (U.S.) Spec. Publ. 638, Sept. 1983, p. 589.

Walker, T. W., A. H. Guenther, C. G. Fry, and P. Nielson, "Pulsed Damage Thresholds of Fluoride and Oxide Thin Films from 0.26 μm to 1.06 μm ., Laser Induced Damage in Optical Materials; H. E. Bennett,

A. J. Glass, A. H. Guenther, and B. E. Newnam, eds., Nat. Bur. Stands. Spec. Publ. 568, Oct. 1979, pp. 405-416. Washington, D. C.

Zverev, G. M., G. Ya. Kolodnyi, and Yu. D. Poryardin, Kvantovaya Elektron. 5, 44(1978) [Sov. J. Quantum Electron. 8, 20 (1978)].

END